Studying time and disease using two different cell line models

William Letton

UCL

2018

Thesis submitted in fulfilment of the requirements for the degree of

Doctor of Philosophy

I, William Victor George Letton, confirm that the work presented in this thesis is my own. Where information has been derived from other sources, I confirm that this has been indicated in the thesis.

_____

William Letton

Acknowledgements

First of all I have to acknowledge and thank my project supervisors, Professor Pete Coffey, Professor David Whitmore, and Dr Amanda Carr for everything that they have done over the past four years to support and guide me. Without their combined efforts I would not be where I am now. I have learned a great deal from each of their examples, which I am confident will prove invaluable in many aspects of my life, both professional and personal.

I also want to thank members of the Whitmore, Carr and Coffey labs for their practical and social support. In addition to the many hours that Amanda Carr personally spent patiently instructing me in a vast range of research techniques, I am grateful to Kathy Tamai for introducing me to zebrafish cell culture, to Matt Hayes and Christopher Thrasivoulou, for their instruction and assistance in microscopy imaging, and to everyone who saved me a great deal of time and frustration by sharing their expertise in cell culture and molecular work. My thanks too to Naheed Kanuga, without whom I would have never have found half the reagents and equipment in the first place, and to all the support staff and administrators who worked behind the scenes.

As well as supporting me in my project work practically, there are many colleagues that were invaluable when things faltered by providing perspective, welcome distraction, and good company. My thanks go to Noémie Hamilton, Amelia Lane, Matt Smart, Ma'ayan Semo, Conor Ramsden, Kate Fynes, Britta Nommiste, Victoria Trovell, Joe Smith, Aisling Lynch, Anthony Vugler, Li Li Chen, Grazyna Galatowicz, and Yasmyn Rybak-Rajewski.

I would like to particularly thank Lena Filipkova, my fellow doctoral student and closest friend from the start of my studies, for always being there when I needed someone to talk to, and for teaching me that life is more of an art than a science.

Most importantly I am grateful to my family. Without my parents' patient advice and encouragement there would not only be no thesis to read, but no project work to write into it. They believed in me when I did not believe in myself. If I have achieved anything it is due to their guidance, support, encouragement and example.

Finally, I am grateful to the Wellcome Trust for funding my studies and UCL for hosting me as a student.

Abstract

The scientific approach of modelling uses manipulation of simpler systems in order to understand aspects of more complex ones. This method is extensively used to understand the biology of complex organisms through studying representative cells artificially cultured *in vitro*. The work presented here uses *in vitro* cell line model systems to investigate two aspects of cell biology: the coupling between the circadian clock and cell cycle, and the role BEST1 protein localisation in Autosomal Dominant Vitreoretinochoroidopathy (ADVIRC) disease.

1.

The circadian clock is an internal time-keeping mechanism that allows organisms to anticipate daily environmental changes. This mechanism operates at an organismal level as well as being intrinsic to each cell through oscillating genetic negative feedback loops. One of the many cellular functions that has been found to be regulated by the circadian clock is cell cycle progression. However, it is still an outstanding question as to whether the circadian clock drives cell cycle progression actively or whether it passively gates particular cell cycle transitions to certain times of day. In the first experimental chapter zebrafish (*Danio rerio*) cell lines are used to investigate the relationship between the circadian clock mechanism and cell cycle behaviour. This relationship is examined at a population and single cell level to address the question as to the effect of varying the circadian clock period on the timing and average length of the cell cycle output. It is demonstrated that altering the period length of the circadian oscillation affects the timing of cell cycle progression, but not the length of the cell cycle or its phases. This provides strong evidence in support of the gating theory of circadian regulation of the cell cycle. In the second experimental chapter the effects of cell density on this coupling between the circadian clock and cell cycle are considered. It is shown that this coupling is not observed in cell populations that are at low density and that are highly proliferative, providing insight into how the assay conditions used in previously published work on this coupling could be contributing to conflicting results.

2.

Bestrophinopathies are a group of retinal dystrophic diseases that share a common cause: mutations in the Bestrophin-1 (BEST1) gene, expressed in the retinal pigmented epithelium (RPE). Epithelial cell models, particularly derived from the kidney, have been used as models to study the function and dysfunction of the BEST1 protein in RPE cells through overexpression of the BEST1 gene. The results of these studies have suggested that in ADVIRC disease mutant BEST1 shows mis-splicing defects. However, this has not been supported by work using induced

pluripotent stem cell-derived RPE (iPS-RPE) cell models, raising the question as to whether the model cells used are providing accurate insights into the actual properties of native RPE.

In this section human epithelial cell lines are used to investigate the relationship between specific point mutations in the gene Bestrophin1 and the localisation within the cell of the resulting protein product. It is shown that the localisation of an ADVIRC mutant BEST1 protein depends partially on the cell line used to express it, as well as the cell culture conditions used. This suggests that the use of non-RPE model cell lines for investigating Bestrophin-1 may be leading to conclusions that do not apply *in vivo*.

Impact Statement

The experimental work and academic discussion presented in this thesis could be put to beneficial use both inside and outside an academic research setting.

In the first experimental chapter, evidence is presented in favour of the gating model of the circadian regulation of the cell cycle, specifically that the circadian clock alters the timing but not the rate of cell division. These findings increase our understanding of the adaptive role of the circadian clock in regulating cell physiology and behaviour. One potential beneficial use for this finding beyond the field of circadian biology is that control of the circadian clock phase may be a route by which cell cycle progression could be influenced. This in turn could have applications in the study and control of the cell cycle in development, regeneration, or cancer progression. The experimental protocol and analysis techniques developed in this chapter can also be used more broadly in the field of circadian biology to study clock outputs in live cells under continuous circadian entrainment.

In the second experimental chapter, cell density is shown to affect the circadian clock regulation of the cell cycle that was investigated in the first chapter. It is shown how the same experiment performed at different densities could result in a different set of results and conclusions.

Beyond circadian biology, there are broadly-applicable insights that can be generalised from these two chapters. The first is that the behaviour of cells at a population level may emerge from unexpected behaviour at a single-cell level, and that the understanding of fluctuating or periodic changes in cell state requires consideration of the internal state of individual cells. Second, that cell density represents an overlooked factor that could in principle be the hidden variable causing conflicting results from otherwise similar experimental protocols.

The third experimental chapter considers the modelling of retinal disease *in vitro*, and so has more potential short-term benefit outside of an academic setting. Research into the mechanisms of human disease has obvious potential benefits for human health, but the primary insight from the work presented in this chapter relates to the methodology of this research. The results presented suggest that use of different model cell lines to investigate the function of the protein Bestrophin-1 could lead to conflicting results that are not representative of what occurs *in vivo*.

List of Abbreviations

µM	micro-Molar
4PBA	4-Phenylbutyrate
AA	Amino Acid
ADVIRC	Autosomal Dominant Vitreochoroidopathy
AMD	Age-related Macular Degeneration
AML	Acute Myeloid Leukemia
AMP	Adenosine Monophosphate-activated Protein
AMPK	Adenosine Monophosphate-activated Protein Kinase
ANOVA	Analysis Of Variance
AOFVD	Adult-Onset Foveomacular Vitelliform Dystrophy
ARB	Autosomal Recessive Bestrophinopathy
ARMD	Age-Related Macular Degeneration
ARPE-19	Adult Retinal Pigment Epithelial cell line-19
ATP	Adenosine Triphosphate
AVI	Audio Video Interleave
AVMD	Adult-onset Vitelliform Macular
BD	Best disease/Best's disease
BMAL	Brain and Muscle ARNT-Like
BMD	Best Macular Dystrophy
BrdU	Bromodeoxyuridine
BSA	Bovine Serum Albumen
BVMD	Best Vitelliform Macular Dystophy
C1QTNF5	C1Q and Tumor Necrosis Factor related protein 5
Ca^{2+}	Calcium ion
CaC current	Calcium-activated Chloride current
$CaCl_2$	Calcium Chloride
CC	Choriocapillaris
CDC25	Cell Division Cycle 25
CDK	Cyclin-Dependent Kinase
cDNA	complementary Deoxyribonucleic Acid
CDT1	Chromatin licensing and DNA replication factor
cGMP	Cyclic Guanosine Monophosphate
CJL	Chronic Jet-Lag
CKI	Casein Kinase I
Cl-	Chloride ion
CLK	Clock (gene)
CLOCK	Circadian Locomotor Output Cycles Kaput
cm	Centimetre
CMV	Cytomegalovirus
CNTF	Ciliary Neurotrophic Factor
CO_2	Carbon Dioxide
CRALBP	Cellular Retinaldehyde-Binding Protein
CRISPR	Clustered Regularly Interspaced Short Palindromic Repeats
CRX	Cone-Rod Homeobox
CRY	Cryptochrome
CRY1	Cryptochrome1
CRY2	Cryptochrome2

Ct	Cycle threshold
DAPI	4’,6-diamidino-2-phenylindole
DCT	DOPAchrome Tautomerase
DD	Dark-Dark
ddH_2O	Double-Distilled Water
DEPC	Diethyl Pyrocarbonate
DMEM	Dulbecco`s Modified Eagle Media
DMSO	Dimethyl Sulfoxide
DNA	Deoxyribonucleic Acid
dNTP	deoxyribose Nucleotide Triphosphate
DPBS	Dulbecco’s Phosphate Buffered Saline
DTT	Dithiothreitol
DYRK1A	Dual-specificity tyrosine phosphorylation-regulated kinase 1A
EBP	ERM Binding Protein
EDTA	Ethylenediaminetetraacetic Acid
EF1α	Elongation Factor 1-alpha
EMT	Epithelial to Mesenchymal Transition
EOG	Electro-Oculogram
EOSRD	Early-Onset Severe Retinal Dystrophy
ERG	Electroretinogram
ES cell	Embryonic Stem cell
ESE	Exonic Splice Enhancer
ES-RPE	Embryonic Stem cell-derived Retinal Pigment Epithelium
FAC sorting	Fluoresence Activated Cell Sorting
FBS	Foetal Bovine Serum
FDR	False Discovery Rate
FFT-NLLS	Fast Fourier Transform Non-Linear Least Squares
FGF	Fibroblast Growth Factor
fRPE	foetal Retinal Pigment Epithelium
FUCCI	Fluorescence Ubiquitination-based Cell Cycle Indicator
G	Relative Gravity
G0	Growth phase 0
G1	Growth phase 1
G2	Growth phase 2
G418	Geneticin
gDNA	genomic Deoxyribonucleic Acid
GFP	Green Fluorescent Protein
GSK-3β	Glycogen synthase kinase 3-beta
H^+	Hydrogen ion
H_2O	Water
H3	Histone 3
hBEST1	human BEST1
HBS	HEPES Buffered Saline
HCl	Hydrochloric Acid
HEK293	Human Embryonic Kidney cells 293
HEPES	4-(2-hydroxyethyl)-1-piperazineethanesulfonic acid
HSD	Honest Significant Difference
IE	Immediate-Early
IGF	Insulin-like Growth Factor

iPSC	Induced Pluripotent Stem Cell
IRBP	Interphotoreceptor Retinol Binding Protein
K^+	Potassium ion
KCl	Potassium Chloride
kDa	kiloDaltons
KRT8	Keratin 8
LB	Luria Broth
LCA	Leber Congenital Amaurosis
LD	Light-Dark
LEDGF	Lens Epithelium-Derived Growth Factor
LL	Light-Light
L-ORD	Late-Onset Retinal Degeneration
LP	Light Peak
LRAT	Lecithin Retinol Acyltransferase
LTR	Long Tandem Repeat
M	Mitosis
mBEST1	mouse BEST1
MCS	Multiple Cloning Site
MCT1	Monocarboxylate Transporter 1
MDCK cells	Madin-Darby Canine Kidney cells
MERTK	tyrosine-protein kinase MER
MESA	Maximum Entropy Spectral Analysis
mg	milligram
Mg^{2+}	Magnesium ion
MITF	Melanogenesis Associated Transcription Factor
ml	Millilitre
mm	millimetre
mRNA	messenger RNA
MTSEA	2-aminoethylmethane
mV	milliVolt
Na^+	Sodium ion
Na_2HPO_4	Disodium Hydrogen Phosphate
NaCl	Sodium Chloride
NaF	Sodium Fluoride
NaOAc	Sodium Acetate (CH3COONa)
NCAM	Neural Cell Adhesion Molecule
NEAA	Non-Essential Amino Acids
Neo	Neomycin
NEO^R	Aminoglycoside phosphotransferase
NF1	Neurofibromatosis type 1
NIH	National Institute of Health
nm	nanometres
NONO	Non-POU domain-containing octamer-binding protein
NPD1	Neuroprotectin D1
^oC	Degrees Celcius
OCA2	Oculocutaneous Albinism 2
OLS	Ordinary Least Squares
OS	outer segments
OTX1	Orthodenticle Homeobox 1

OTX2	Orthodenticle Homeobox 2
PAS	Per-Arnt-Sim
PBS	Phosphate Buffered Saline
pBSK	BluescriptSK plasmid
PCNA	Proliferating Cell Nuclear Antigen
PCR	Polymerase Chain Reaction
PEDF	Pigment Epithelium-Derived Factor
PER	Period
PFA	Paraformaldehyde
pH	power of Hydrogen
pH3	phosphor histone H3
PMSF	phenylmethane Sulfonyl Fluoride
PO_4	Phosphate
PP2A	Protein Phosphatase 2A
PRPF	Pre-MRNA Processing Factor
qPCR	quantitative Polymerase Chain Reaction
Rb	Retinoblastoma
RCS rat	Royal College of Surgens rat
RFP	Arg-Phe-Pro protein
ROR	Retinoic acid receptor-related Orphan Receptor
RP	Retinitis Pigmentosa
RPE	Retinal Pigment Epithelium
RPE65	Retinal Pigment Epithelium-specific 65 kDa protein
RPM	Revolutions Per Minute
RRE	Rev Response Element
RT-PCR	Real-Time PCR
RU5	Moloney MLV and murine sarcoma virus LTR
RVD	Regulatory Volume Decrease
S	Synthesis
SCAM	Substituted-Cysteine Accessibility Method
SCF	Skp-Cul1-F-box
SCN	Suprachiasmatic Nucleus
SDS	Sodium Dodecyl Sulfate
shRNA	short hairpin Ribonucleic Acid
SOC medium	Super Optimal broth with Catabolite repression
SUMO	Small Ubiquitin-like Modifier
SV40	Simian vacuolating Virus 40
T	Period length
T4 PnK kinase	T4 Polynucleotide Kinase
TIM	Timeless
TMAP	Torrent Mapping Alignment Program
TMD	Transmembrane Domain
TMM	Trimmed Mean of M-values
TMT-opsin	Teleost Multiple Tissue-opsin
TrCP	Transducin repeat Containing Protein
Tris	2-Amino-2-(hydroxymethyl)-1,3-propanediol
TRP-1	Tyrosinase Related Protein-1
TRPM1	Transient Receptor Potential Cation Channel Subfamily M Member1

TRPM3	Transient Receptor Potential Cation Channel Subfamily M Member3
TRPV	The transient receptor potential cation channel subfamily V
TTFL	Transcription-Translation Feedback Loop
TYR	Tyrosinase
UCL	University College London
UV	Ultraviolet
VEGF	Vascular Endothelial Growth Factor
VGCC	Voltage-gated Ca^{2+} channel
VMD	Vitelliform Macular Dystrophy
VMD2	Vitelliform Macular Dystrophy
VRAC	Volume-Regulated Anion Channel
YFP	Yellow Fluorescent Protein
ZO-1	Zona Occludens-1
ZT+A1A6:A208	Zeitgeber Time

Table of Contents

Table of Figures

Table of Tables

Chapter 1 – Introduction and aims of this thesis

This thesis will introduce, present, and discuss two separate projects over three experimental chapters. The first project uses a zebrafish embryonic cell line to investigate the well-established coupling between the circadian clock and cell cycle machinery. Specifically the first experimental chapter aims to address the question as to whether the circadian clock is an active 'driver' of the progression of the cell cycle or whether it 'gates' cell cycle progression to particular times of day. The data presented in this chapter has been published elsewhere in a paper addressing the same question(Laranjeiro et al. 2018).

The second experimental chapter extends the methodologies developed in the first chapter to investigate the effects of cell density on the coupling of the circadian clock and cell cycle. The aim of this chapter is to assess cell density as a meaningful hidden variable in the circadian regulation of the cell cycle, and then use this framework to provide plausible and testable explanations for apparently contradictory results in the published literature.

The second project, and third experimental chapter, investigates the effect of introducing Bestrophinopathy patient mutations into the gene Bestrophin-1 through overexpression in epithelial cell line models. The aim of this chapter is to address the question as to whether contradictory results in the published literature as to the effects of specific mutations are due in part to the choice of cell line model.

The two projects use different species and cell lines to address questions related to distinct areas of cell biology. However, both use *in vitro* cellular models to attempt to answer these questions. A model is only useful if it replicates the significant properties of the more complex system about which one is trying to draw conclusions. Therefore the final aim of this thesis is to actively consider what properties of these models, and others in the published literature, may be unrepresentative of the organ or organism-level biological systems that they are being used to represent.

Chapter 2 – The effects of varying the period of entrainment of the circadian clock on cell cycle dynamics using a light-entrainable zebrafish model cell line

2.1 Introduction to the circadian clock and its regulation of the cell cycle

2.1.1 Circadian clocks

Organisms do not just passively respond to daily changes in their environment but actively anticipate them. Even when kept in constant conditions many aspects of behaviour and physiology continue to show daily rhythms of around 24 hours. This internal timekeeping is known as the circadian clock, the word itself being derived from the Latin '*circa*' and '*dies*' or 'around a day'. This clock has been found to regulate a vast array of behavioural and physiological processes in organisms across the tree of life. The focus of this chapter is the circadian clock regulation of just one of these: the cell cycle.

In this introduction the circadian clock will first be introduced conceptually, and then the cellular mechanism that regulates this timekeeping will be introduced. From there the cell cycle will be introduced and what is known about the circadian regulation of the cell cycle will be presented. Two contrasting theoretical models of this regulation will then be presented: The driving model and the gating model. Finally the zebrafish, *Danio rerio*, will be introduced as a unique model organism for studying circadian clock regulation of the cell cycle.

2.1.1.1 Adaptive functions of the circadian clock

Almost every eukaryotic organism studied shows some form of circadian clock mechanism and behaviour. This clock mechanism and function can be completely disrupted through targeted mutation without rendering an organism inviable. Therefore because clock function is not essential for life but is still so widespread, it must confer major adaptive advantages in a huge range of niches. Cyanobacteria also show circadian clock function and gene expression(Kondo et al. 1993). Circadian function has not been convincingly shown for non-cyanobacterial bacteria(Maniscalco et al. 2014), but may exist in archaebacterial cells(Whitehead et al. 2009).

Broadly speaking, the core function of the circadian timekeeping mechanism is to keep track of time internally such that external changes can be anticipated. The adaptive advantage of this is to enable an organism to anticipate changes in its environment in order to optimise its behaviour or physiology.

The most fundamental environmental rhythms are changes in the physical environment such as light intensity, ultraviolet light exposure, and temperature. The circadian closure of plant stomata to prevent excess water loss is a circadian response to the external abiotic factor of temperature(Holmes & Klein 1986). Circadian regulation of the efficiency of nucleotide repair in human fibroblasts(Bee et al. 2015), and sensitivity to ultraviolet light (UV) damage in the flagellate *Euglena*(Bolige et al. 2005) are likely adaptations to midday sunlight exposure.

Interactions of organisms with each other also follow circadian rhythms. For example prey species may use the cover of darkness for foraging and finding a mate.

Interactions between cells, tissues, and organs within a single organism may also vary in circadian fashion. For example, liver genes involved in processing of nutrients have been shown to be rhythmic in mice(Kornmann et al. 2001), peaking at the start of the active feeding phase. Partitioning in time also appears to occur between enzymes involved in biochemically opposed processes in the same tissue, such as the expression of glycogen synthase and glycogen phosphorylase in rat liver(Ishikawa & Shimazu 1980).

2.1.1.2 Defining characteristics of circadian clocks

2.1.1.2.1 Circadian systems free-run under constant conditions

What differentiates circadian rhythmicity from a direct environmental response that shows a daily rhythm? A behaviour or physiological variable that continues to show oscillations of around 24 hours when the organism is kept under constant conditions can be said to be circadian. Under these constant conditions the circadian clock is said to be free-running.

2.1.1.2.2 Circadian systems are entrained by an external stimulus

Outside of artificial constant conditions circadian oscillations are entrained by particular external stimuli, most commonly sunlight. An entraining stimulus is known as a zeitgeber, or 'time-giver'. Why is entrainment necessary? Free-running circadian clock periods are never exactly equal to 24 hours and so entrainment is necessary to maintain a stable phase-relationship between the external time and internal time.

Stimuli other than light can operate as zeitgebers in an organism or tissue-dependent manner. For example, feeding can be used to entrain tissues of the liver,(Stokkan et al. 2001) kidney, heart and pancreas of mice and decouple them from the phase of entrainment of other tissues(Damiola et al. 2000). Feeding can also entrain tissues of the zebrafish gut(Peyric et al. 2013). Small temperature changes are also sufficient to entrain some mammalian cells(Brown et al. 2002), and in flies even mechanical stimulation can be used as a zeitgeber(Simoni et al. 2014). Unless otherwise stated the zeitgeber referred to throughout this document will be light exposure.

To demonstrate entrainment of the circadian clock by a periodic stimulus such as light, temperature, or feeding schedule, it is not sufficient to merely demonstrate rhythmic output with the same period as the stimulus input. For true entrainment the periods should be equal with a stable, unique phase angle (which will differ between zeitgebers and species)(Pittendrigh & Daan 1976b). In addition, once released from entrainment the phase progression of the output should be predictable from the releasing phase of the input. If these conditions are not

fulfilled then this suggest a degree of direct response, or 'masking', is occurring. Often both entrainment and masking occur together, and the amount of masking seen may itself vary in a circadian manner(Mrosovsky 1999; Reebs 1994).

Artificial entrainment periods that differ from the natural 24 hours (T-cycles) can be used to illuminate whether true entrainment is occurring. Under entrainment the driven period becomes the same as the driver. There is a stable, unique phase angle between the zeitgeber and circadian clock for each length of T-cycle. However if the phase angle remains constant between T-cycles, then this suggests that the output is a direct response to the input, in other words masking.

2.1.1.2.3 Circadian systems are temperature-compensated

Biochemical reactions show a higher rate of reaction at higher temperatures. However, the oscillation of the circadian clock must not significantly speed up or slow down with temperature fluctuations. This is important functionally because even if an entraining zeitgeber is present to keep the period of the clock stable, a faster or slower running clock would alter the phase angle between parts of the cycle and the external time, compressing or expanding parts of the cycle relative to each other. Thus, in addition to the ability to free-run with a period close to 24 hours and the ability to be entrained by an external zeitgeber, the third key defining property of a circadian clock is that it is temperature-compensated(Pittendrigh 1960; Tsuchiya et al. 2003). Generally clock systems appear to be slightly over-compensated(Hastings & Sweeney 1957). It is not currently known how temperature compensation occurs, although there are theories(Kidd et al. 2015; Kurosawa & Iwasa 2005). These include thermal destabilisation of clock components or their dimers counteracting increased reaction rates; balancing of transcription and degradation rates; temperature-dependent splicing, as seen to occur in *Neurospora*(Diernfellner et al. 2005); or temperature-sensitive post-translational modifications to core clock components such as phosphorylation(Shinohara et al. 2017) or sumolation(Hansen et al. 2017).

2.1.1.3 Phase-response curves

A key feature of circadian entrainment, in contrast to masking, is that the response of the circadian system to the stimulus is dependent on the phase the circadian system is currently in. Thus a light-pulse of 15-minutes given to a free-running rodent in otherwise constant conditions(Pittendrigh & Daan 1976b) will either shift its pattern of activity to occur earlier (phase-advance), later (phase-delay), or leave it unaffected. These responses can be plotted into a phase-response curve, which illustrates the continuously varying response to a particular entraining stimulus and can be used to predict the outcome of particular stimulus patterns.

An appropriate phase-response distribution will mean that a stable phase angle can in theory be maintained even if the intensity and duration of the entraining stimulus varies (for example

between summer and winter conditions)(Pittendrigh & Daan 1976c; Daan & Aschoff 1975). Whether this is adaptive at a species level would depend on what aspects of the daily environmental change are most relevant to survival. For example, for a prey species active in the first few hours after dusk, maintaining a stable activity phase-angle to midday could be less important than maintaining a stable activity phase angle with sunset. A long free-running period combined with a predominately advancing phase response distribution would results in dawn tracking, while a short free-running period combined with a predominately delaying phase response distribution would result in dusk tracking. However, despite the pleasing simplicity of this dawn/dusk tracking model the comparison of the lengths of free-running periods of day-active and night-active animals does not provide much support(Johnson 1999).

As a model for the effects of zeitgeber stimulus on clock outputs, the phase-response curve can be useful to explain some features of circadian entrainment. Below light will be used as the example zeitgeber.

Figure 2.1A shows an idealised diagram of a typical type 1 phase-response curve. The curve itself would be produced from a series of individual points, each showing the effect of a pulse of light on the phase of the output. Thus the curve shows where in the circadian cycle light produces a phase-advance (above the dotted line), or a phase-delay (below the dotted line). The x-axis shows circadian phase and the y-axis shows phase response to a stimulus at that phase. The part of the curve that lies on the dotted line is the 'dead zone' where no phase-response is seen.

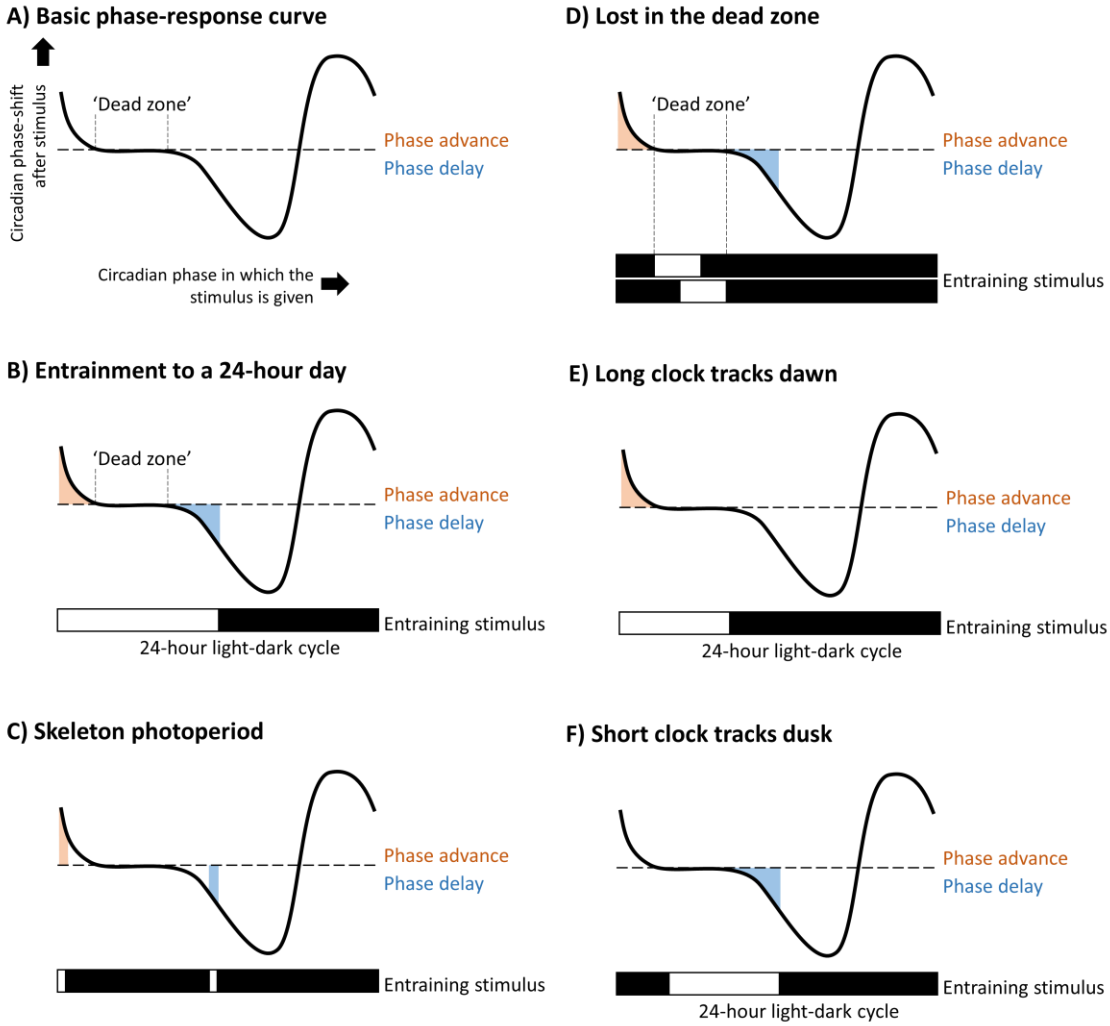

Figure 2.1 The phase-response model of circadian entrainment. A) An idealised typical type 1 phase-response curve. B) A phase advance and phase delay cancel to produce a stable entrainment. C) Entrainment through skeleton photoperiods explained through balancing phase advance and phase delay. D) A short photoperiod and a24-hour circadian clock period combine to produce an unstable phase-relationship. E) Mis-matching of a long free-running period and shorter entraining period are compensated by net phase advance. F) Mis-matching of a short free-running period and longerentraining period are compensated by net phase delay

Figure 2.1B shows how the phase-response curve relates to a 24-hour 12:12 light:dark entrainment scheme. Below the phase-response curve is the entraining light cycle. Here the assumption is that the free-running clock period is the same as the entraining zeitgeber, 24 hours. Thus the total phase advance and phase delay must cancel out for stable entrainment to occur, the red and blue areas between the phase-response curve and the axis have equal area. If the clock phase were slightly early then more light would fall during the phase-delay zone and less during the phase-advance zone. Thus the clock period would lengthen slightly and gradually return to the stable phase-relationship. The reverse would occur if the clock phase were slightly

late. This response is seen during jet-lag, where over a series of days the disrupted phase-relationship between clock and zeitgeber is corrected.

In this way the circadian clock can be seen as a homeostatic mechanism, maintaining the phase-relationship between the internal circadian phase to the external zeitgeber phase.

Figure 2.1C shows how this phase-response curve model can explain 'skeleton' photoperiods, where the light stimulus is only given for a short time at the beginning and end of the usual light cycle(Pittendrigh & Minis 1964). Here it can be seen that so long as the blue phase-delay and red phase-advance areas are equal then stable entrainment will still be maintained.

Free-running circadian periods are never exactly 24 hours. **Figure 2.1D** shows why this could be considered an adaptive feature rather than a lack of accuracy. The figure shows two entraining photoperiods with short light cycles relative to the dead zone. Because the entirety of the stimulus falls within the dead zone then no correction occurs and the phases of the clock and the zeitgeber can drift apart. Depending on the length of the light period relative to the dead zone this drift could cover several hours. By being reliably shorter or longer than the natural entraining light period of 24 hours, circadian clocks avoid this deadzone by daily correction. This is shown in **Figure 2.1E+F**, which show a long-running clock in a stable phase-relationship through a daily phase-advance and a short-running clock in a stable phase-relationship through a daily phase-delay.

A consequence of the need for correction is that the phase-relationship will change. For example a clock output period that is two hours shorter than the entraining stimulus period will need two hour's worth of net phase-delay, while one that is two hours longer will need two hours of net phase-advance. This will mean that the stable state for those two conditions will involve a different phase-angle relationship between the clock output and entraining stimulus, as can be seen by comparing **Figure 2.1E+F**. This predicts that a short-clock organism will show earlier clock output activity than a long-clock organism of the same species. This is exactly what is seen using *tau* mutant hamsters(Ralph & Menaker 1988) and in flies(Hamblen-Coyle et al. 1992).

Just as a stable zeitgeber with a 24-hour period can entrain circadian outputs with a range of free-running periods, a circadian output can be entrained to a range of zeitgeber periods (known as T-cycles). In this case the stable phase-relationship will be found that induces the appropriate net phase advance of delay to stretch or compress the free-running clock output to the length of the entraining zeitgeber period. It can immediately be seen from the phase-response curve that there is a maximum amount of phase-advance or phase-delay that can be achieved in a particular system, which will limit the range of T-cycles to which the circadian output can be entrained. This will vary according to the shape and amplitude of the phase-response curve, as

well as the free-running period of the clock output. It can also be seen that under different T-cycles the phase-relationship between the circadian output and the entraining stimulus will vary, which would not be the case with a direct (masking) response.

It must be noted that phase-response curves are not the only way of representing circadian entrainment. For example, the velocity-response curve model(Pittendrigh & Daan 1976a; Taylor et al. 2010) is very similar to the phase-response curve model in practice. Conceptually a phase-response can be thought of as a special case of the velocity-response where the phase-shift is instantaneous, discrete rather than continuous. Biologically speaking any phase-shift in the clock would be brought about through altering the chemistry of the feedback loop and so would take time. An exception would be if a portion of the clock phase was skipped entirely, perhaps through the loss of the usual peak expression of a core component through increased inhibition. Inevitably any perturbation to the free-running clock oscillation will affect some components of the clock mechanism before others, for example a light pulse influences *Cryptochrome* expression in zebrafish, which then influences other clock components(Tamai et al. 2007). Thus one runs into the limitations of the metaphor of a mechanical biological clock.

2.1.2 Circadian clock organisation and hierarchy in vertebrates

In the last few decades much research has been done to elucidate the mechanisms of circadian function across a range of species.

2.1.2.1 Hierarchical organisation of the circadian clock in vertebrates

The circadian clock of vertebrates is primarily entrained by daylight. In mammals this entrainment occurs from the eye, via the retinohypothalamic tract(Moore & Lenn 1972), to a small nucleus of the hypothalamus called the Suprachiasmatic Nucleus (SCN). Destruction or removal of this nucleus eliminates circadian rhythmicity of locomotor activity(Stephan & Zucker 1972; Moore & Eichler 1972), and transplantation of the nucleus from one individual to another is sufficient to restore behavioural rhythms in genetically arrhythmic animals(Sujino et al. 2003), with the free-running period of the donor(Ralph et al. 1990). The SCN therefore functions as a central pacemaker, determining the circadian variations seen in downstream behaviour and physiology through a cascade of hormonal release and neural projections to brain regions such as the nearby hypothalamus(Kalsbeek et al. 2006; Van Der Beek et al. 1997; Dai et al. 1998; Buijs et al. 2003).

The body temperature of birds and mammals is circadian(Aschoff 1983). Human blood pressure shows daily rhythms(Millar-Craig et al. 1978). Mice show circadian rhythms of insulin resistance, and clock-disrupted mice have been shown to be prone to obesity and metabolic disease (Shi et al. 2013; Turek et al. 2013). Shift work in humans appears to correlate with metabolic diseases(Karlsson et al. 2001; Karlsson et al. 2003) and cardiovascular diseases(Ellingsen et al.

2007). Daily rhythms in physiology and responses to drugs(Mormont & Levi 2003) and chemotherapy agents(Li et al. 2013) have led to calls for more work investigating the efficacy for chrono-therapeutics, treatments optimised according to time of day(Lévi et al. 2007). There also appears to be circadian variation in fear conditioning in mice(Eckel-Mahan et al. 2008), and cognitive function in humans(Wright et al. 2012).

2.1.2.2 Peripheral circadian clocks

Intrinsic circadian rhythmicity is not restricted to the SCN in vertebrates. It is now known that all cells contain their own intrinsic circadian clock(Balsalobre et al. 1998; Welsh et al. 2004; Yoo et al. 2004; Whitmore et al. 2000). Therefore the SCN might be more accurately be thought of as both a master pacemaker and as an internal zeitgeber, necessary for entraining the cells of the body and keeping tissues and organs appropriately synchronised. For example, liver circadian output is only partially rescued in Clock-deficient mutant mice by restoration of SCN Clock function(Hughes et al. 2012). In mouse liver the expression of core clock gene *Per2* is driven by a combination of cell-intrinsic oscillators and systemic cues(Kornmann et al. 2007).

2.1.2.3 Tissue-specific clock output

As tissues and organs fulfil vastly different functions in the body and at different times of day, it is not surprising that the downstream clock-regulated gene expression differs between them. Liver genes involved in the processing of nutrients were shown to be rhythmic in mice(Kornmann et al. 2001), and daily cycles were found in hundreds of transcripts that were mostly specific to the liver or SCN(Panda et al. 2002; Akhtar et al. 2002). Analysis of the mouse liver proteome suggests that up to 20% of soluble proteins show some level of circadian control(Reddy et al. 2006). Around 8-10% of expressed genes in both the mouse heart and liver were found to be circadian, with very little overlap(Storch et al. 2002). In a recent study of mice 45% of protein-coding genes were shown to have circadian oscillation in at least one of the tissues examined(Zhang et al. 2014).

2.1.3 The cellular mechanism of the circadian clock

2.1.3.1 The transcription-translation feedback loop

Investigation of the animal circadian clock genetic machinery began in fruit flies. These forward genetic screens identified mutations and genes that could disrupt circadian clock rhythmicity or alter the length of the free-running period. For example, three mutants that affected clock period of activity and pupa eclosion were found and tracked to the same genetic locus(Konopka & Benzer 1971). The gene responsible was cloned in 1984 and is now known as *period*(Bargiello et al. 1984).

Gradually a picture emerged of a set of core 'clock' genes that oscillated in a transcription-translation feedback loop (TTFL). Core transcription factors promote the expression of

repressive elements that inhibit their own expression(Lowrey & Takahashi 2004).The molecular basis of the circadian clock in vertebrates was found to have a very similar basis as in the fruit fly, with several orthologous genes operating, such as the mammalian *Clock* and drosophila CLK(Allada et al. 1998), the mammalian *Cry* and Drosophila CRY, and the mammalian *Timeless* and insect TIM(Chi et al. 2017).

Figure 2.2, taken from Mohawk *et al.,* 2012(Mohawk et al. 2012), shows the main components of the two TTFL arms in the mammalian clock. The core clock effectors are the transcription factors CLOCK and BMAL1(Vitaterna et al. 1994; King et al. 1997). These heterodimerise to effect transcription of downstream clock targets as well as the PER family and CRY family proteins(Gekakis et al. 1998; Kume et al. 1999). CRY and PER dimerise, and after phosphorylation of PER they translocate to the nucleus and inhibit the CLOCK-BMAL1 transcriptional activity and thus their own transcription(Kume et al. 1999; Sato et al. 2006). CRY proteins are necessary for normal circadian expression of Per1 and Per2 in the SCN(Vitaterna et al. 1999) and mice lacking both CRY1 and CRY2 show complete loss of circadian rhythmicity(Van Der Horst et al. 1999). Mice lacking both PER1 and PER2 paralogues also do not show circadian rhythmicity(Zheng et al. 2001).

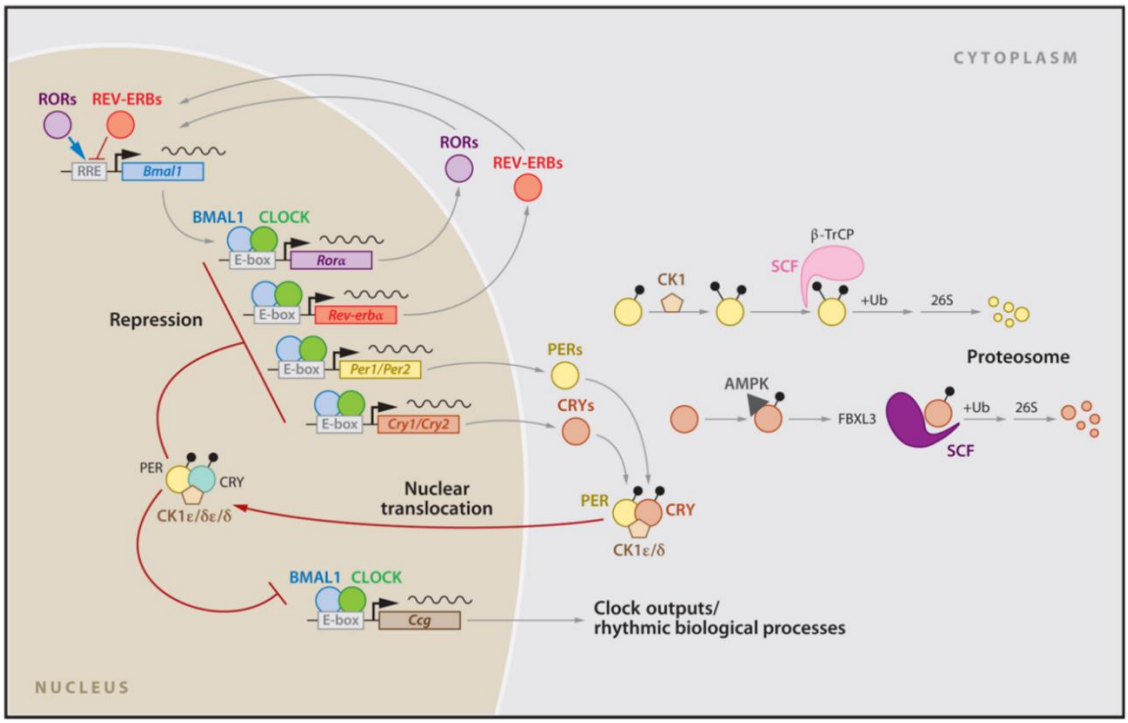

Figure 2.2 The Transcriptional-translational feedback loop (TTFL) of the vertebrate circadian clock. Figure taken from Mohawk *et al.,* 2012. The two primary feedback loops are shown. 1) BMAL1-CLOCK heterodimers promote transcription of the PER and CRY family genes. PER and CRY proteins dimerise. And translocate back into the nucleus to repress their own transcription and other BMAL1-CLOCK transcription factor activity. Outside of the nucleus post-translational phosphorylation of CRY and PER leads to their

eventual degradation. 2) CLOCK-BMAL1 also promotes the transcription of Rev-erbα and RORα, which repress and promote transcription of BMAL1 respectively.

Cytoplasmic PER and CRY are each phosphorylated by casein kinase I (CKI)(Ralph & Menaker 1988; Lowery et al. 2000; Akashi et al. 2002) and AMP kinase (AMPK)(Lamia et al. 2009) respectively, which targets them for ubiquitination and degradation by BetaTrCP(Eide et al. 2005) and SCF^{Fbxl3} respectively(Busino et al. 2007; Godinho et al. 2007; Siepka et al. 2007). Thus the processes of PER and CRY transcription-translation and degradation oscillate in opposition.

Meanwhile a second feedback loop is in operation. CLOCK-BMAL1 also effects transcription of the *ROR* family(Sato et al. 2004) and *REV-ERB* family genes(Preitner et al. 2002). Once translated, these proteins compete for RORE binding sites(Guillaumond et al. 2005) and promote(Sato et al. 2004; Akashi & Takumi 2005) or repress(Preitner et al. 2002) *BMAL1* expression respectively.

This picture is a simplification. Clock function is also affected by non-redundancy among the component paralogues. For example, mouse CRY2 has a functionally different C-terminal tail than CRY1, which is phosphorylated by DYRK1A, which primes for phosphorylation by GSK-3β, and which leads to degradation(Kurabayashi et al. 2010). Also *Ror* family genes show tissue-specific expression(Guillaumond et al. 2005), which will affect activation of Bmal1 transcription.

2.1.3.2 Post-translational modifications

Apart from the phosphorylation and ubiquitination of CRY and PER proteins, there is emerging evidence that other post-translational modifications play a role in regulation of the TTFL. In mouse liver, circadian rhythms in H3 histone acetylation in the promoters of *PER1*, *PER2*, and *CRY1* have been shown(Pacha & Sumova 2013), as well as changes in PER transcriptional repression due to changes in histone methylation(Brown et al. 2005), and regulation of *BMAL1* expression via CLOCK-induced SUMOylation(Cardone et al. 2005). SUMOylation also appears to be involved in the regulation of circadian clock period and temperature compensation in the plant *Arabidopsis thaliana*(Hansen et al. 2017).

2.1.3.3 Non TTFL clock mechanisms

There is gathering evidence that the TTFL is not the only circadian timekeeping system possible. The three core Kai proteins of the cyanobacterial clock mechanism have been shown *in vitro* not to require transcription for their circadian oscillations in phosphorylation(Nakajima et al. 2005), suggesting that the TTFL is not a necessary component in biological timekeeping systems.

More recently the dogma of the core transcription-translation feedback loop clock mechanism in eukaryotic cells has been challenged by the discovery of circadian oscillations independent of TTFL. Human red blood cells (which lack nuclei and therefore transcription) have been shown to exhibit circadian cycles in the redox potential of the antioxidant proteins peroxiredoxins(O'Neill

et al. 2011; O'Neill & Reddy 2011). This 'redox clock' persists in constant conditions, is entrainable, and is temperature-compensated.

2.1.4 The cell cycle

The cell cycle is the process by which one cell becomes two. DNA and cellular components are replicated and partitioned and the cell divides. It is the fundamental basis of all cellular reproduction and in multicellular organisms its regulation is absolutely critical for embryogenesis, growth, maintenance and repair. Cancer is at its core a disease of the cell cycle. Of the six 'acquired capabilities of cancer' identified by Hanahan(Hanahan et al. 2000), four (self-sufficiency in growth signals, insensitivity to anti-growth signals, evading apoptosis, and limitless replicative potential) relate specifically to a dysregulated cell cycle. To avoid pathology a cell must divide when, and only when, it is appropriate. In multicellular organisms tissue homeostasis relies on a controlled balance of cell death and replacement.

2.1.4.1 The eukaryotic cell cycle

During each complete cell cycle a cell must perform specific functions exactly once and in the correct order. Conceptually the process is broken down into sequential stages, separated by checkpoints where progress halts until exacting conditions are met.

2.1.4.2 What happens in each stage of the cell cycle?

The cell cycle is divided into four sequential phases: G1, S, G2 and M. The two phases G1 and G2 are termed the growth phases, where cells conspicuously increase in volume, producing new proteins and organelles. In terms of duration in time, G1 and G2 can be split differently between cell types. For example some mammalian cell lines show a complete lack of G1 phase(Liskay 1977). In this case any growth is restricted to G2 phase. The cells of early Drosphila and Xenopus embryos, which are dividing but not growing, show no G1 or G2 phase, with cells passing between S phase and mitosis without delay. G1 phase is where cells are sensitive to external growth factors and contains what is known as the restriction point, where either the irreversible decision is made to progress through the cell cycle, or the cell remains in a quiescent state termed G0(Satyanarayana & Kaldis 2009), reviewed by Matson & Cook, 2017(Matson & Cook 2017). In some cells G0 quiescence is permanent, others can re-enter the cell cycle when conditions change.

During S phase DNA is replicated. Here helicase proteins unwind the supercoiled DNA and duplication is carried out by DNA polymerases from specific origins of replication spaced along the chromosomes, reviewed in Brosh, 2013(Brosh 2013). Each origin must be replicated only once to produce a single accurate copy of each chromosome. Histone synthesis must also occur so that the new daughter can be coiled correctly.

During M phase the duplicated DNA is physically segregated across the cell, which then divides into two new cells. It is divided into six stages. During prophase the nuclear envelope is broken down, the chromosomes condense and microtubule spindle fibres form. During prometaphase the spindle fibres attach to the chromosomes at the centromere. In metaphase the chromosomes are aligned midway between the centrosomes. In anaphase the centromeres divide and the chromosomes are segregated to each centrosome at opposite ends of the cell. During telophase the nuclear membrane reforms around each set of chromosomes, the chromosomes de-condense, and the spindle fibres break down. Finally during cytokinesis the cell membrane pinches between the two nuclei and the cell splits into two.

2.1.4.3 The regulation of cell cycle progression – cyclins and cyclin-dependent kinases

The classic model of cell cycle progression is that it occurs through sequential expression of Cyclin-Dependent Kinases (CDKs) and partner cyclin proteins. These then form complexes and the serine-threonine kinase activity of the CDK is activated. For example, during G1 CDK4 and CDK6 are expressed, which both form complexes with members of the cyclin D family. These phosphorylate proteins of the retinoblastoma (Rb) family, inhibiting them from repressing the activity of E2F family transcription factors. E2F activation promotes transcription of a suite of genes necessary for the progression in S phase(Weinberg 1995; Dyson 1998).

The cyclins and Cdk protein families associated with each cell cycle stage in animals are shown below. These are conserved between yeast cells and mammalian cells.

Cell cycle stage or transition	**Cyclin family**	**Cyclin-dependent kinase**
G1	D	4-6
G1-S	E	2
S	A	2
S-G2	A	1
M	B	1

2.1.4.4 Inhibitors of cell cycle progression

Progression of the cell cycle is regulated via repressive elements that inhibit the activity of CDK complexes, such as association with P16(Serrano et al. 1993), P27(Toyoshima & Hunter 1994), and p21(Xiong et al. 1993; Harper et al. 1993) or phosphorylation by the kinase WEE1(Parker & Piwnica-Worms 1992; Parker et al. 1992). These in turn are targets of other proteins, such as those involved in DNA damage and repair. There are also cell cycle regulating proteins, such as CDC25 phosphatases, that activate CDK1 complex activity(Potapova et al. 2009).

This classic model(Morgan 1997) was undermined by the discovery that CDK1 alone is sufficient to drive the cell cycle in mammalian cell lines, with no other CDKs present(Santamaría et al. 2007), through activation by multiple cyclin families as is seen in budding yeast(Bloom & Cross 2007). Further work with knock-out mouse models revealed that the full range of CDKs and cyclins appear to regulate the cell cycle during development and show tissue-specificity of growth defects when absent. To an extent some CDKs and cyclins appear able to compensate for the loss of another, depending on their expression timing, localisation, and kinase activity. For example knockout of CDK2 in mice lead to reduced body size and failure to complete prophase I during meiosis(Berthet et al. 2003; Ortega et al. 2003). CDK4 and CDK6 appear to be able to partially compensate for each other, with single mutant animals viable, but double mutants dying during late-stage embryogenesis(Malumbres et al. 2004). Knockout of any individual D-Cyclin produces viable mice, but knockout of all three causes death at E16.5. Reviewed by Satyanarayana & Kaldis, 2009(Satyanarayana & Kaldis 2009).

2.1.5 Circadian regulation of the cell cycle

A daily rhythm in cell division was shown in rat gut epithelium as far back as the 1940s(Bullough 1947). However, a direct causal link between the circadian clock and the timing of cell division was not demonstrated until much later, first in single-celled eukaryotes, such as the dinoflagelle *Gonyaulax polydra*(Sweeney & Hastings 1958), *Chlamydomonas*(Straley & Bruce 1979), photoinduction sensitive timing in *euglena*(Hagiwara et al. 2002), *and* mating timing in *Paramecium*(Karakashian 1968).

Circadian cell cycle rhythmicity has also been shown to occur in cyanobacteria(Mori et al. 1996; Yang et al. 2010). So far it is not known if any archaebacteria show circadian regulation of the cell cycle, though a cyanobacteria-like circadian system appears to be present in at least one species(Maniscalco et al. 2014).

The adaptive advantage of the circadian clock regulation of cell cycle timing is not clear. Some explanations point to external physical factors such as ultraviolet light exposure, and how appropriate timing of cell cycle progression could avoid DNA damage(Bolige et al. 2005). This is supported by the close evolutionary relationship between the core clock protein Cryptochrome and light-activated photolyases found in plants and animals, some of which activate DNA repair in a light-dependent manner(Todo et al. 1996; Cashmore et al. 1999; Todo 1999). However, this explanation could not apply to the rhythms in cell cycle seen in non-light exposed internal organs such as the human liver, or why cell cycle rhythms can peak at different times in different tissues such as the brain and the gut(Laranjeiro et al. 2013). In this case an internal synchronisation explanation could be offered – for example the avoidance of DNA damage from reactive oxygen species, or partitioning tissue function and repair.

2.1.5.1 Mechanisms of coupling

As already detailed, the circadian regulation of gene expression is both extensive and tissue-specific. Amongst the genes known to show circadian expression in mammalian cells are those involved in the regulation of the cell cycle.

Wee1 is a tyrosine kinase that inhibits M phase entry through phosphorylation of CDK1 and inactivating the CDK1-CyclinB1 complex. *WEE1* has 3 E-box promoter elements that are recognised by the CLOCK-BMAL1 transcription factors. The cell division rhythm of regenerating mouse livers is lost in *WEE1* mutants(Matsuo et al. 2003).

Non-POU domain-containing octamer-binding protein (NONO) has been shown to associate with PER proteins in mouse(Brown et al. 2005), to bind to the cell cycle regulatory protein p16-Ink4a, and to be necessary for its circadian rhythmic expression(Kowalska et al. 2013). Loss of either NONO or PER leads to a loss of circadian p16-ink4a activation and circadian expression, and a loss of mitotic rhythmicity in mouse fibroblasts.

The expression of the cell cycle regulator p21 is rhythmic in mouse liver(Gréchez-Cassiau et al. 2008). Via two conserved RREs in its promoter it is activated by RORα and inhibited by REV-ERBα, and so is directly downstream of the circadian clock, showing a loss of rhythmicity in *Bmal1*$^{-/-}$ knockout mice.

2.1.5.2 A role for circadian clock disruption in cancer

If circadian regulation of cell cycle timing is an adaptation to reduce DNA damage by repressing cell cycle progression during certain times of day, then circadian clock disruption might be expected to be associated with an increase in mutation, cancer growth and metastasis.

2.1.5.2.1 Mouse studies of the role of circadian dysfunction in cancer

Disruption of the core clock mechanism in mice has been associated with effects on tumour formation and growth. Destruction of the SCN central pacemaker in mice leads to increased growth of transplanted tumour lines(Filipski et al. 2002). This increase in growth can also be achieved through a chronic jetlag (CJL) treatment(Filipski et al. 2004; Wu et al. 2012). CJL has also been shown to increase the number of hepatic tumours forming after carcinogen exposure(Filipski et al. 2009), an effect that is also seen if both copies of the PER2 regulatory PAS domain are mutated(Mteyrek et al. 2016). These treatments are associated by a downregulation of the tumour-suppressor *P53* and an upregulation of the oncogene *C-MYC* (Filipski et al. 2006). In mouse the promoter region of *C-MYC* contains E-box elements and its expression is deregulated in *PER2* mutant mice(Fu et al. 2002). These mice also show increased tumour development after irradiation. Mice that lack both *PER1* and *PER2*, both *CRY1* and *CRY2*, or one

copy of *BMAL1* show increased tumour development with or without radiation induction, an effect that is replicated through CJL(Lee et al. 2010).

However, other studies have reported a lack of impact of clock disruption on cancer-related phenotypes, or even a potential protective phenotype. *CRY1* and *CRY2* knockout mice showed no effect on radiation-induced tumour incidence or associated mortality(Gauger & Sancar 2005). Overexpression of *PER2* in mouse carcinoma lines reduced proliferation and altered apoptosis-related gene expression, including upregulation of *P53*(Hua et al. 2006). Induction of *PER2* in NIH 3T3 cells caused growth inhibition and cell cycle arrest(Gery et al. 2005). Cry mutation reduced cancer onset and increased lifespan in *P53*-deficient mice(Ozturk et al. 2009).

Clock disruption has also been associated with age-related phenotypes. *BMAL1*-deficient mice show some age-related pathologies such as reduced lifespans, sarcopenia, cataracts, fat and organ tissue loss(Kondratov et al. 2006). *PER1-*, *PER2-*, or *CLOCK*-deficient mice do not show predisposition to tumour formation, but do show apparent radiation-induced acceleration of aging phenotypes(Antoch et al. 2008; Antoch et al. 2013). This apparent inconsistency with previous work was attributed to possible effects of the background of the mouse lines used and consideration of mouse sex differences.

Together these results suggest that the role of clock disruption on cancer initiation and growth, apoptosis, and ageing are likely context-dependent – varying according to the nature of the clock disruption and the background of the model system used. The clock mechanism could become 'stuck' in a variety of configurations or non-standard oscillatory loops. In addition disrupted clock configurations may affect DNA mutation, tumour initiation, tumour growth and metastasis in different ways.

Stimulation of clock rhythmicity using dexamethasone, forskolin or heatshock appeared to reduce proliferation rates in mouse tumour models, though it is not clear if these treatments were directly linked to clock function, nor whether clock rhythmicity was stimulated at a single cell level or that the cell population was synchronised by the treatment(Kiessling et al. 2017).

2.1.5.2.2 Humans studies of the role of circadian dysfunction in cancer

Disrupted clock function has been found in human tumour samples and cell lines. Disruption of *PER1*, *2*, and *3* expression was found in >95% of human breast cancer cells relative to nearby cells(Chen et al. 2005). A lower expression of *CRY1* and *CRY2* was seen in human gliomal cells relative to nearby cells(Luo et al. 2012). Downregulated *PER1* expression was found in endometrial carcinoma samples(Yeh et al. 2005). High levels of the Timeless (TIM) protein in breast tumour samples were associated with a poorer prognosis(Chi et al. 2017).

Disrupted circadian rhythms were seen in cultured prostate cancer cells, and *PER1* was downregulated in prostate cancer samples. Overexpression of *PER1* in cultured prostate cancer cells reduced proliferation and induced apoptosis(Qi et al. 2009). Low expression of *PER1* was found in small cell lung cancer cell lines, which showed growth reduction when expression was forced(Gery et al. 2007). *PER2* expression levels were reduced in samples of acute myeloid leukemia (AML) cells and in lymphoma cell lines. Overexpression of Per2 in the K562 myelogenous leukemia line inhibited growth and promoted cell cycle arrest and apoptosis(Gery et al. 2005; Sun et al. 2010).

Long-term night shift work or rotating shift work has been found to be statistically associated with breast cancer risk(Davis et al. 2001; Megdal et al. 2005; Schernhammer et al. 2001), colorectal cancer(Schernhammer et al. 2003), and non-Hodgkin lymphoma(Lahti et al. 2008). However, in these cases it is not clear if it is the circadian disruption that is the causal factor. It is also not clear if the key variable is nightshift work or the phase-disruption from switching to and from night and day shift schedules(Haus & Smolensky 2006).

2.1.6 Two models of circadian regulation of the cell cycle

The observations of circadian rhythmicity of cell cycle timing have led to two broad models of circadian regulation of the cell cycle: Gating and Driving(Bieler et al. 2014; Destici et al. 2011; Feillet et al. 2015)

The gating model conceptualises circadian regulation of the cell cycle as a number of gates, i.e. periods of time during the circadian cycle when specific cell cycle events are permitted to occur. The number of these gates per circadian cycle and the points of regulation of the cell cycle are unclear, though it appears that both the G1-S and M transitions show circadian regulation. It could also be possible that multiple gates for M transitions could exist within a single circadian cycle, as suggested for NIH 3T3 rat fibroblasts(Nagoshi et al. 2004). The gating hypothesis considers circadian regulation of the cell cycle as another kind of checkpoint.

According to the driving model, the circadian clock couples to the cell cycle in 1:1 phase-locked state. During each circadian period the cell cycle progresses through an entire cycle and the phase-relationship is constant. Phase-locking has been demonstrated in cyanobacteria(Yang et al. 2010), transitioning from a 1:1 to a 2:1 ratio as cell cycle rates increased. In NIH 3T3 rat fibroblasts(Feillet et al. 2014; Bieler et al. 2014), 1:1 phase-locking has been reported, but driven by reverse-coupling, with the cell cycle phase determining clock phase rather than the other way around. It was also demonstrated that artificially lengthening the circadian clock period using a CRY2 shRNA knockdown did not affect cell cycle length, supporting this reverse-coupling.

Another study using the NIH3T3 cell line found no relationship between the circadian phase and M transitions at all(Yeom et al. 2010). Work in a lung carcinoma cell lines also concluded a lack of phase-locking of M transition timing(Pendergast et al. 2010).

Fundamentally the fact that cell cycle events in tissues are observed to occur at particular phases of the circadian clock implies a gating effect, while the exact 1:1 phase-locking demonstrated in rat fibroblasts *in vitro* suggests that that the circadian clock is regulating the length of the cell cycle itself. An alternative explanation for the 1:1 phase-locking is that the cell cycle is affecting the circadian period, i.e. reverse-coupling(Bieler et al. 2014). However there appears to be no evidence of this occurring at a tissue level, or any adaptive reason why it would occur. In the discussion of this chapter the results presented in the next section will be used to present a testable hypothesis for these apparent contradictions.

2.1.7 Zebrafish as a vertebrate circadian model

One notable flaw in the *in vitro* mammalian cell modelling of circadian systems is the lack of constant entrainment protocols. Cells can be synchronised using treatments such as serum shock, but there is currently no protocol to provide a constant zeitgeber.

The Zebrafish (*Danio rerio*) is a commonly used animal model for genetics, embryology, regeneration and disease modelling. They are small, easy to maintain, have short generation times and large number of offspring, are genetically easy to manipulate and have a fully sequenced genome, and show external development of their transparent larvae.

Zebrafish have also become a unique tool for studying vertebrate circadian clocks at the tissue and cellular level. Unlike mammals, which have a top-down hierarchical circadian organisation based on the SCN central pacemaker, zebrafish show a decentralised clock organisation, with tissues and individual cells being sensitive to direct light entrainment(Whitmore et al. 1998; Whitmore et al. 2000; Carr & Whitmore 2005; Tamai et al. 2007; Vallone et al. 2004; Carr et al. 2006). This is similar to the case of *Drosophila* flies, which also show direct light entrainment of tissues and cells(Jeffrey D. Plautz, Maki Kaneko, Jeffrey C. Hall 1997).

In zebrafish cells, light exposure induces transcription of both *CRY1a* and *PER2*(Hirayama et al. 2007; Vatine et al. 2009), with hydrogen peroxide appearing to act as a secondary messenger. Although the photoreceptor responsible for this is not yet known, currently the best candidates are (TMT)-opsin, of which there are multiple paralogues(Davies et al. 2011; Fischer et al. 2013) and which is widely expressed in zebrafish tissues(Moutsaki et al. 2003), or melanopsin, which is essential for the entraining light sensitivity of photoreceptive retinal ganglion cells in mice(Hattar et al. 2003; Panda et al. 2003), although in fish and mice melanopsin appears to be primarily localised to the retina(Bellingham et al. 2002).

Transfection of zebrafish melanopsin or (TMT)-opsin into light-insensitive Somalian cavefish *Phreatichthys andruzzii* partially rescues the light-inducible gene expression otherwise absent in this species(Cavallari et al. 2011). It seems likely that there are multiple light-input pathways and these may be cell-type dependent.

Zebrafish organs, tissues, tumours and cell lines therefore show a unique advantage over those of other models in that they can be directly, easily and continually entrained by artificial lighting. While the circadian clocks of mammalian cells can be synchronised through pulses of the adenylate cyclase activator forskolin(Aurélio Balsalobre et al. 2000) and the synthetic glucocorticoid dexamethasone(A. Balsalobre et al. 2000), through serum-pulsing(Balsalobre et al. 1998; Akashi & Nishida 2000), or even merely through changes in culture medium(Kaeffer & Pardini 2005), these treatments do not continuously entrain a population. In addition, changes in medium are likely to affect cell cycle progression, particularly of cells in G1, which are sensitive to external growth factors. The effect of forskolin and dexamethasone on cell physiology and cell cycle progression are not well known. Forskolin has been shown to reduce proliferation of human T-cells(Rodriguez et al. 2013).

2.1.7.1 Clock regulation of the cell cycle in zebrafish

As in mammalian tissues and cells, regulation of the cell cycle by the circadian clock is also seen in zebrafish. In adult fish daily cell cycle rhythms have been seen in intestine(Peyric et al. 2013), brain(Laranjeiro et al. 2013), and in epidermal cells during fin regeneration(Idda et al. 2012).

Circadian rhythmicity in S-phase entry is also seen in developing embryos exposed to a daily light cycle(Dekens et al. 2003). Rhythms in both S-phase and M-phase entry are also seen in an *in vitro* cell line, PAC2, derived from developing embryos(Dekens et al. 2003).

In zebrafish gut the cell cycle regulators *CyclinB1*, *CyclinB2*, *CDC2*, *WEE1*, *p21*, *PCNA*, *CDK2* and *CyclinE1* all showed at least some circadian rhythmicity in expression after light entrainment(Peyric et al. 2013). The zebrafish PAC2 cell line also showed circadian expression of *CyclinB1*, *CyclinB2*, and *CDC2* under light entrainment, but not in *WEE1* or *WEE2*(Tamai et al. 2012). In contrast, in zebrafish Z3 cells *WEE1* expression was induced following a light pulse(Hirayama et al. 2005).

In addition, when lighting entrainment was maintained but the zebrafish were starved the circardian rhythmicity in expression of *CyclinB1 and CyclinB2* in the gut was lost, with expression falling to very low levels. Cell division fell to low levels even as the expression of the core clock gene *PER1* remained unchanged(Peyric et al. 2013). This suggests that the circadian regulation of cell cycle timing in the gut is dependent on the context of a fed condition.

Oscillation was seen in the expression levels of the cyclin-dependent kinase inhibitor *p21* in both larval tissues and PAC2 cell lines(Laranjeiro et al. 2013). Oscillation was also seen in the zebrafish *p21* paralogue *p20*, the expression of which was seen at different levels and in different tissues to *p21*. Expression of *p20* was dominant in the larval brain and peaked 6 hours earlier than *p21*, which was more prevalent in the gut. Remarkably, the peak of S-phase transition coincided with the trough of whichever of *p20* or *p21* was more highly expressed, meaning that the phase-relationship between the circadian clock and cell cycle was tissue-specific. The peaks in S-phase were around 9 hours earlier in the brain than the intestine. What the adaptive reason for this is, and whether it also applies to adult fish, is unknown. It could support the theory that circadian regulation of the cell cycle can occur in order to optimise internal physiology rather than anticipate external cues. It also suggests that the assumption cannot be made that different tissues, or cells within a tissue, will show the same strength or timing of clock regulation of the cell cycle.

2.1.7.2 PAC2 cells as a model system

Zebrafish cells then show directly light-entrainable circadian clock machinery and clear clock regulation of cell cycle timing, although the exact form of the regulation appears to be context-dependent. Together this makes them an ideal model system to investigate the coupling between the circadian clock and the cell cycle, particularly in addressing the question of whether clock progression is gating or driving cell cycle progression.

The timing of mitosis in the zebrafish PAC2 cell line, derived from 24-hour old zebrafish embryos(Whitmore et al. 2000), is regulated by the circadian clock machinery(Tamai et al. 2012). The timing of mitosis does not respond to light alone when a *CLOCK1* dominant negative construct is expressed and persists in constant darkness, confirming that is regulated by the clock. The transcription of the cell cycle regulators *CyclinB1, CyclinB2 and cdc2* are rhythmic under light entrainment and persist in DD. This is largely reduced in the *CLOCK1* dominant negative cells.

In contrast to what has been found in mouse liver(Matsuo et al. 2003), zebrafish gut(Peyric et al. 2013), and zebrafish Z3 cell line(Hirayama et al. 2005), *WEE1* and *WEE2* did not show rhythmic expression in entrained zebrafish PAC2 cells(Tamai et al. 2012). This suggests that the regulation of M phase timing is occurring through different mechanisms in different cell lines. In the zebrafish cells circadian *CyclinB1* expression peaked at the mitosis peak. Zebrafish *CyclinB* has E-box and E'-box regulatory elements and an imperfect RRE in its promoter region, but mutation of some or all of these elements does not affect the observed rhythms. This suggests circadian regulation of *CyclinB1* is occurring through another mechanism(Tamai et al. 2012).

Constant light supressed clock oscillation and cell proliferation. The expression of *CyclinB1*, *CyclinB2* and *cdc2* was also supressed, a suggested cause of the inhibition of proliferation through suppression of M-phase entry(Tamai et al. 2012).

A picture has thus emerged of a circadian regulation of the cell cycle that is dependent on the context of species, tissues, cell line and even feeding state. The question remains as to what extent this regulation is driving or gating.

Further work using the PAC2 zebrafish line has been done to probe this question(Laranjeiro et al. 2018). In the first section of this paper it was demonstrated that the rhythm of percentage of cells in S-phase, as well as luciferase expression driven from the promoters of the cell cycle regulator p21 and the cell cycle protein Cyclin B1, all rapidly re-entrain to a reversed light-dark cycle. The expression rhythms for p21, p20, and Cyclin B1 promoters were shown to match period to the core clock factor Per1 when entrained to T-cycles of 32, 24, 20, and 16 hours, each with a unique phase-angle under varying T-cycle lengths. Rhythms in percentage of cells in S-phase were also shown to entrain to 32, 24, 20, and 16 hour photoperiods, again with unique phase-angles in each case. Together this confirmed the strong circadian control over cell cycle progression in this cell line, but did discriminate between a gating mechanism and a driving mechanism.

If the driving hypothesis is correct then it would be expected that the shorter entraining period would lead to a shorter cell cycle period and therefore to an increase in proliferation. However, proliferation was not found to significantly change between entraining light cycle periods of 8, 16, 24, or 32 hours. This suggests that gating was more likely occurring in this system. However, it is still possible that driving was occurring, but that cells were dropping out of the cell cycle or dying, thus balancing out the increase in proliferative rate.

To investigate this the cell cycle transitions needed to be looked at on a single-cell level, which formed the second part of the paper and the results section of this chapter. A reporter system exists for the fluorescence monitoring of cell cycle transitions in mice known as the Fluorescence Ubiquitination-based Cell Cycle Indicator (FUCCI) system(Sakaue-Sawano et al. 2008). The FUCCI reporter system has a wide range of applications, including the study of cell-cycle progression during vertebrate development(Sugiyama et al. 2009), hormonal signalling in cell cycle checkpoints(Manila et al. 2018), and stem cell heterogeneity and differentiation(Calder et al. 2012; Singh et al. 2015; Roccio et al. 2013; Lian et al. 2014). This system has also been adapted to function in zebrafish PAC2 cells(Downey et al. 2011).

The FUCCI system consists of an Azami-Green fluorophore fused to the ubiquitination domain of GEMININ and a Kusabira-Orange fluorophore fused to the ubiquitination domain of CDT1. As

CDT1 is degraded during SG2M and GEMININ is degraded during G1, transfected cells show red signal during G1 and green signal during SG2M.

2.2 Project aims

In the introduction to this chapter research has been presented investigating the regulation of the cell cycle by the circadian clock. This process appears to be somewhat cell-type, tissue, and species specific and may involve multiple points of regulation at both the G1-S transition and the M-phase transition. In addition, there is conflicting evidence regarding the resulting cell behaviour of this regulation. Whether the circadian clock gates or drives the cell cycle is not a trivial question: quite apart from the potential implications for cancer incidence and treatment, the regulation of the cell cycle is crucial to the repair and homeostasis of tissues throughout the body.

How can gating be distinguished from driving in a model system? One way in which gating and driving can be distinguished is by altering the period of the circadian oscillation. The driving model predicts that this would cause alteration in the period of the cell cycle at a single-cell level, while the gating model predicts that this would only affect the timing of cell cycle events on average for the population.

Using a light-entrainable zebrafish cell line it is possible to alter the period of the circadian oscillation by using artificial lighting periods of different lengths (T-cycles), for example 16 hours light and 16 hours darkness. Combining this with the FUCCI cell cycle reporter it is possible to measure the cell cycle lengths of individual cells while they are under entrainment and answer the following question: To what extent do cells that are entrained to different length T-cycles show different cell cycle dynamics? The aim of this chapter is to answer this question.

2.3 Materials and methods

2.3.1 Zebrafish cell lines and maintenance

Zebrafish cell lines were cultured in Leibovitz's L15 medium (Gibco, Gaithersburg, MD, USA) supplemented with 15% foetal bovine serum (FBS, Biochrom AG, Berlin, Germany), 50µg.ml^{-1} gentamycin (Gibco), and 50U.ml^{-1} penicillin/streptomycin (Gibco, Gaithersburg, MD, USA). Cells were incubated in thermostatically controlled waterbaths at 28^{o}C with atmospheric oxygen and carbon dioxide concentrations and fed every 2-6 days.

The zebrafish cell line used for light cycle experiments was PAC2 (RRID:CVCL_5853), derived originally from a 24 hour-old embryo.

Cells were split by washing with phosphate-buffered saline (PBS), incubating in trypsin for up to five minutes, then resuspending in medium and transferring to a new culture vessel.

2.3.1.1 Zebrafish PAC2-FUCCI cells

The FUCCI system consists of an Azami-Green fluorophore fused to the ubiquitination domain of zebrafish Geminin and a Kusabira-Orange fluorophore fused to the ubiquitination domain of zebrafish Cdt1. As Cdt1 is degraded during SG2M and Geminin is degraded during G1, transfected cells show red signal during G1 and green signal during SG2M.

Here we use a zebrafish embryonic cell line (PAC2) transfected with Fluorescent Ubiquitination-based Cell Cycle Indicator (FUCCI) plamids. The FUCCI reporter used in this work has been described previously(Downey et al. 2011), where it was also used in the PAC2 cell line.

To create the PAC2-FUCCI line used in this chapter, PAC2 cells were transfected through electroporation (Neon® Transfection System, Thermofisher Scientific), and then fluorescence activated cell (FAC) sorted for positive fluorescence, plated individually and grown into clonal lines. The PAC2-FUCCI cell line was produced by Kathy Tamai.

2.3.1.2 Zebrafish cell line freezing and thawing

Cells were frozen down by first detaching using a trypsin incubation, followed by dilution with standard culturing medium, centrifugation at 1100RPM for 5 minutes and resuspension in L15 medium supplemented with 30% serum and 10% DMSO. Frozen cell stocks were stored at -80^{o}C in standard cell culture cryovials. Cells were thawed by taking the cryovial from -80^{o}C and placing it at 28^{o}C until it had thawed. The cells were then resuspended in culture medium in a 15ml falcon tube and spun at 300G for 3-5 minutes. The medium containing the freezing medium was removed and the cells were resuspended in 7ml of culture medium and transferred to a 25cm^{2} culture flask and incubated at 28^{o}C.

2.3.2 Assessing the cell cycle reporter function of the PAC2-FUCCI cell line

The PAC2-FUCCI cell line was defrosted and recovered in L15 medium for several days. Cells were then viewed using a fluorescence microscope to confirm the expression of both the red (Kusabira Orange) and green (Azami Green) fluorophores in the population. The cells were then plated onto a 35mm plastic cell culture dish and left to attach overnight. The dish was then sealed with Parafilm® and imaged using an Olympus inverted confocal microscope over a series of several hours to check that cells underwent the fluorescent colour changes that were expected as they transitioned through the cell cycle: red for G1 and green for S+G2+M. These are detailed in **Figure 2.3A** and can be found in the published material for the creation of this zebrafish-specific reporter system(Sugiyama et al. 2009). The microscope used was an inverted confocal to allow imaging of live cells from below. It was also contained within an environmental control box, which allowed the temperature to be maintained at 28^{o}C, a typical temperature for the culture of zebrafish cell lines. This was considered essential as, although cellular circadian clock function is well temperature-compensated, changes in temperature have been robustly shown to function as an entraining stimulus in a large variety of organisms both *in vivo* and *in vitro*. Examples include Drosophila(Zimmerman et al. 1968), Neurospora(Liu et al. 1998), chick cells(Barrett & Takahashi 1995), mammalian cells(Brown et al. 2002) and most relevantly zebrafish(López-Olmeda et al. 2006).

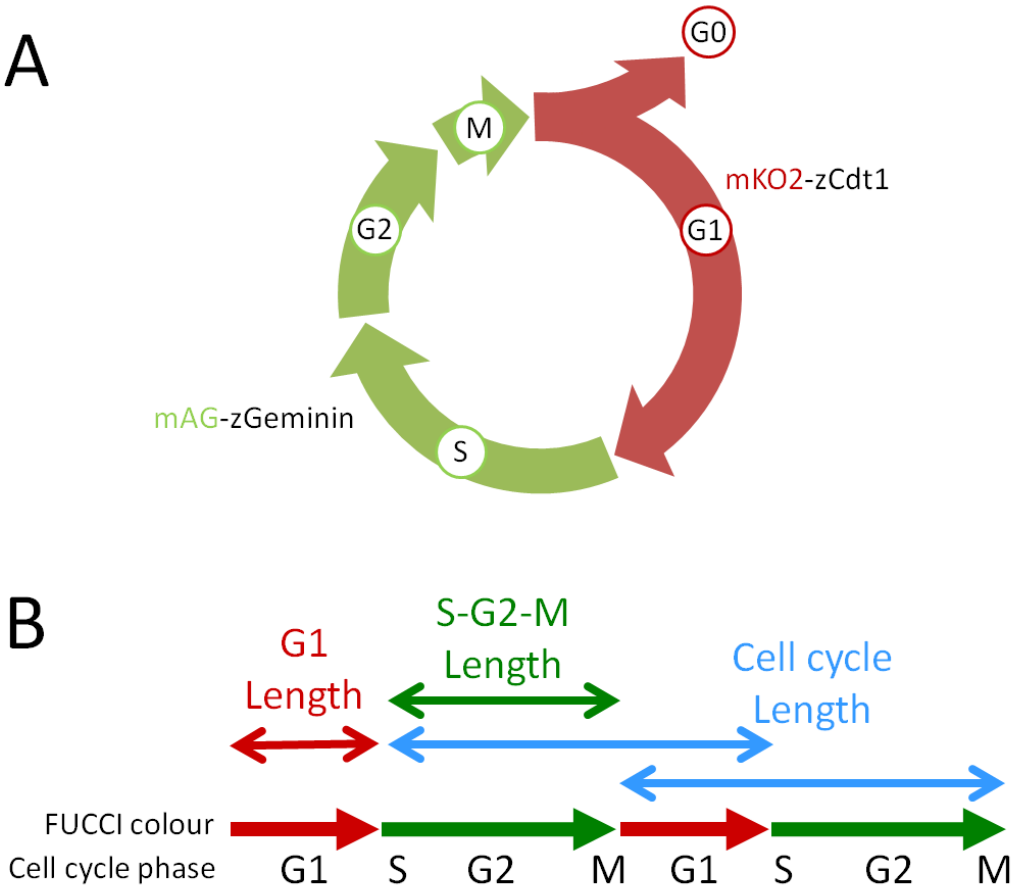

Figure 2.3 Schematics of how the FUCCI reporter was used to identify cell cycle phase transitions and to measure the length of cell cycle phases. (A) An illustration of the changes in reporter colour shown during the cell cycle. Monomeric Kusabira Orange2 (mKO2) produces a red fluorescence during G1. Monomeric Azami Green (mAG) produces a green fluorescence in S-G2-M. (B) An illustration showing how G1 length, S-G2-M length and cell cycle length data was extracted by following individual cells through timelapse movies.

Through observation it was confirmed that the dual fluorescence FUCCI reporter was expressed in the cells at the times that were expected, with cells changing from red to green, dividing, and becoming red again. Several time-lapse imaging sets were taken using the inverted confocal microscope for preliminary analysis. Examples of frames from these a timelapse can be seen in **Figure 2.4**.

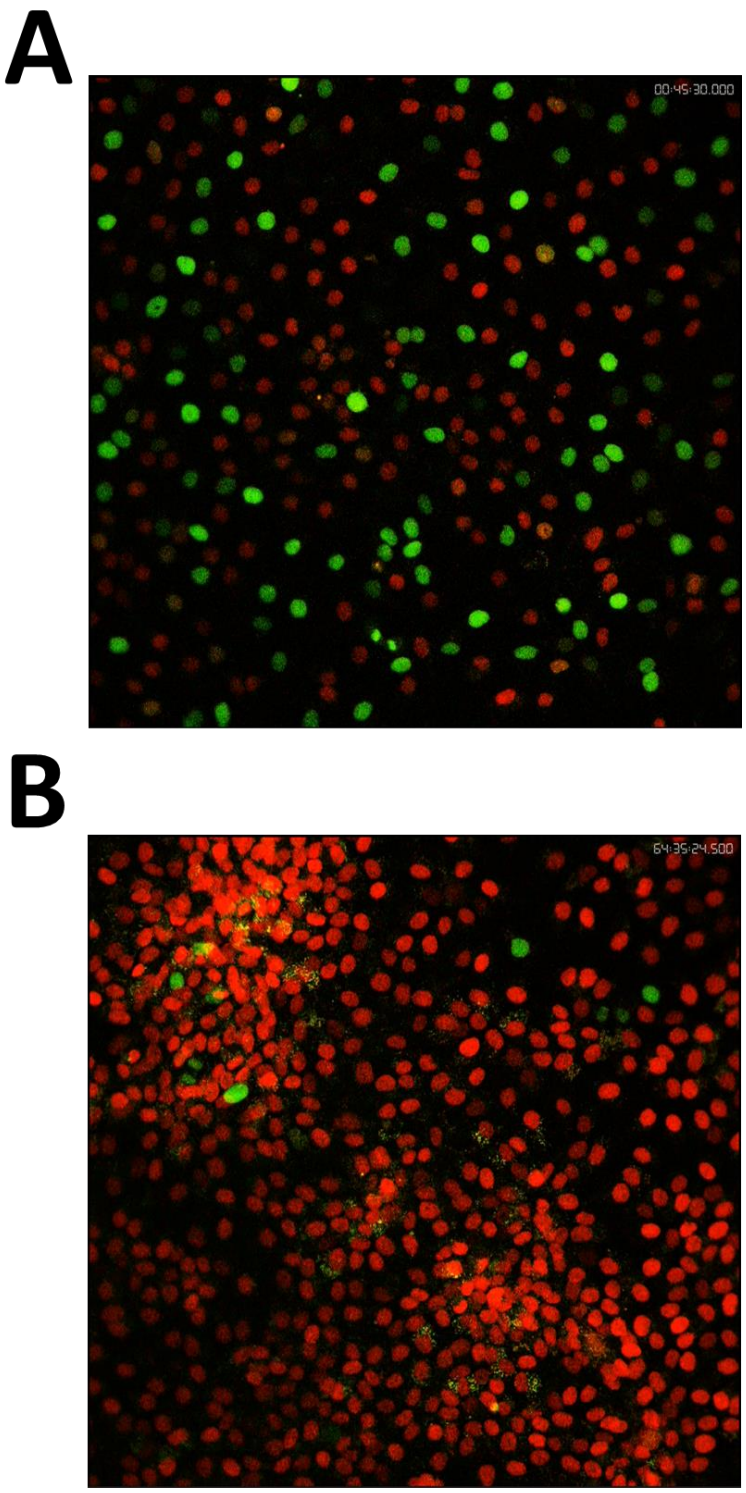

Figure 2.4 Example frames from a confocal timelapse of PAC2-FUCCI cells. A) At 0.25 hours. B) At 64.58 hours. Red staining shows nuclei in G1 – positive for Kusabira Orange2, Green staining shows nuclei in SG2M – positive for Azami Green.

2.3.2.1 Evaluation of using a confocal microscope for the time-lapse imaging

Inspection of the time-lapse image series revealed multiple issues with this protocol as a method of collecting data for analysis of a large number of single cells.

1. The field of view, even at only 10x magnification, contained only a few hundred cells. Of these only a fraction would undergo cell cycle phase transitions during the imaging run. Based on previous work looking at clock to cell cycle coupling we expected to need many hundreds of data-points to identify trends reliably.
2. Even when images were taken every half hour, cells would move across the plastic substrate between time-points. This was particularly the case when cell density was low. This lead to three issues:
    a. Cells would move in and out of the field of view at the edges. As any cell that did this even once during the time-lapse could not be followed with certainty this further reduced the number of cells suitable for analysis.
    b. The nuclear fluorescent signal of the cells would move in the z axis as well as x and y. This made following the signal more difficult. In particular, towards the ends of time-lapses the nuclear signal would often be out of the focal plane that was set at the start. This was hypothesised to be due to either drift in the focal plane during imaging, or due to a change in cell morphology as they became denser with cells having a larger height to width ratio.
    c. Tracking individual cells required being able to identify the same cell nuclear signal between time-points with a high degree of certainty. At low cell density this was difficult due to the high motility of the cells. At high cell density this was difficult due to the closeness of the cells to each other. A higher temporal resolution of time-points made this easier, but required more frequent irradiation of the cells with the ultraviolet laser light, which was considered undesirable.
3. As previously stated, zebrafish cells are light sensitive and the circadian clock of the PAC2 cell line used in this study is efficiently entrained by exposure to relatively low intensity artificial lighting. This means that during imaging of an entrained cell population the ambient light must be strictly controlled. This was achievable through turning off the lights in the room that housed the confocal microscope, but this method was not robust against the lights being turned back on by an unaware third party. This happened frequently, despite posters on the door designed to raise public awareness.
4. The fluorophore signals, particularly the Azami Green, were not strong. This meant that background signal in the images was higher than would have been ideal and that higher illumination intensities or longer exposure times were required.
5. At high density the cells tended to start to form multi-layered structures, which interfered with the ability to distinguish individual nuclei. In addition the cells would become partially autofluorescent at high density, interfering with identification of the weak true signal.
6. Time-lapses of several days would be required for the entrainment assays that were planned. However, the longer the programmed time-lapse was the more likely the z focal plane would change relative to the nuclear signal and become unusable. In addition the confocal microscope was a popular and well-used piece of equipment that was rarely available for long periods of time.

2.3.2.2 Evaluation of using the plate-reader for the time-lapse imaging

Based on the above concerns alternate imaging protocols were investigated. A fluorescence plate reader would also allow long time-lapse imaging and temperature control, and offered multiple advantages over the confocal setup.

1. The plate reader used an automated x-y stage and so could be programmed to image multiple locations on a plate at each time-point. This allowed for an effectively infinite field of view up to the surface area of a standard rectangular cell culture plate. This would allow orders of magnitude more data to be collected in parallel during each imaging run.
2. The plate reader was not a confocal system and so the z-axis focal plane was much thicker than for a confocal microscope. For this assay this was ideal as it kept the cells more reliably in focus throughout the imaging run.
3. Unlike the confocal microscope, the plate reader contained the culture plate within the body of the microscope, away from external light.
4. The plate reader was kept in its own small room. Therefore while it was in use there was no reason for a third party to enter and switch on lights.

The most significant of these advantages was the vastly increased field of view that could be achieved through imaging multiple areas of the plate at each time-point. This would not only allow for more data to be collected per imaging run, but also allowed the partial solving of another issue. Instead of plating only fluorescent PAC2-FUCCI cells and having to track them all as they grew, moved, and divided in close proximity to each other, we were able to dilute the fluorescent cells with non-fluorescent PAC2 cells. This made it significantly easier to follow an individual cell.

The plate reader showed two disadvantages for these assays compared to the confocal microscope:

1) The images generated from the plate reader showed a smaller signal to noise ratio than did the confocal. This was likely due to an increased thickness of culture plastic, larger depth of field, and lower sensitivity of the plate reader camera sensor.
2) The fact that the plate was kept within the body of the microscope during imaging was an advantage to avoid contamination by external light, but also prevented the deliberate illumination that was necessary to maintain circadian entrainment.

The low signal to noise ratio was compensated for through changing the contrast of each channel of the time-lapse movie generated. The lack of illumination was compensated for by including a 'journal' step in the image sequence of the software that opened the loading door in between imaging time-points. This allowed entrainment to be continued during the imaging run using the same fluorescent desk lamp as was used during the pre-imaging entrainment. To prevent temperature changes a thin sheet of glass was placed over the loading door during imaging runs.

Example frames from timelapses generated by the plate reader are shown in **Figure 2.5** and individual cell cycle transition examples are shown in **Figure 2.6**.

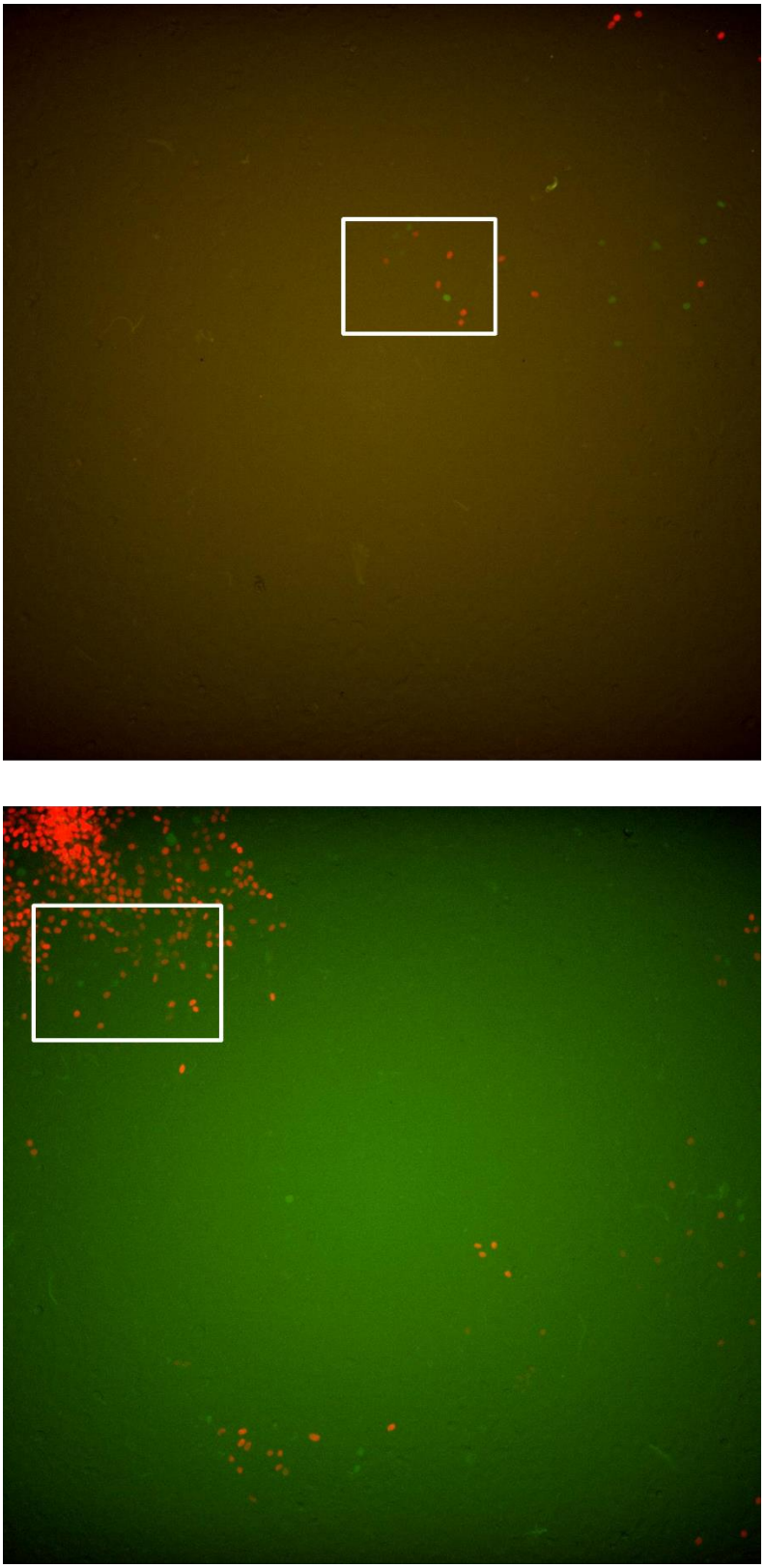

Figure 2.5 Example frames from two time-lapses taken from different wells in the same plate. FUCCI PAC2 cells appear as either green or red nuclei mixed in at 2% with non-fluorescent PAC2 cells. White boxes mark the regions shown in the next figure.

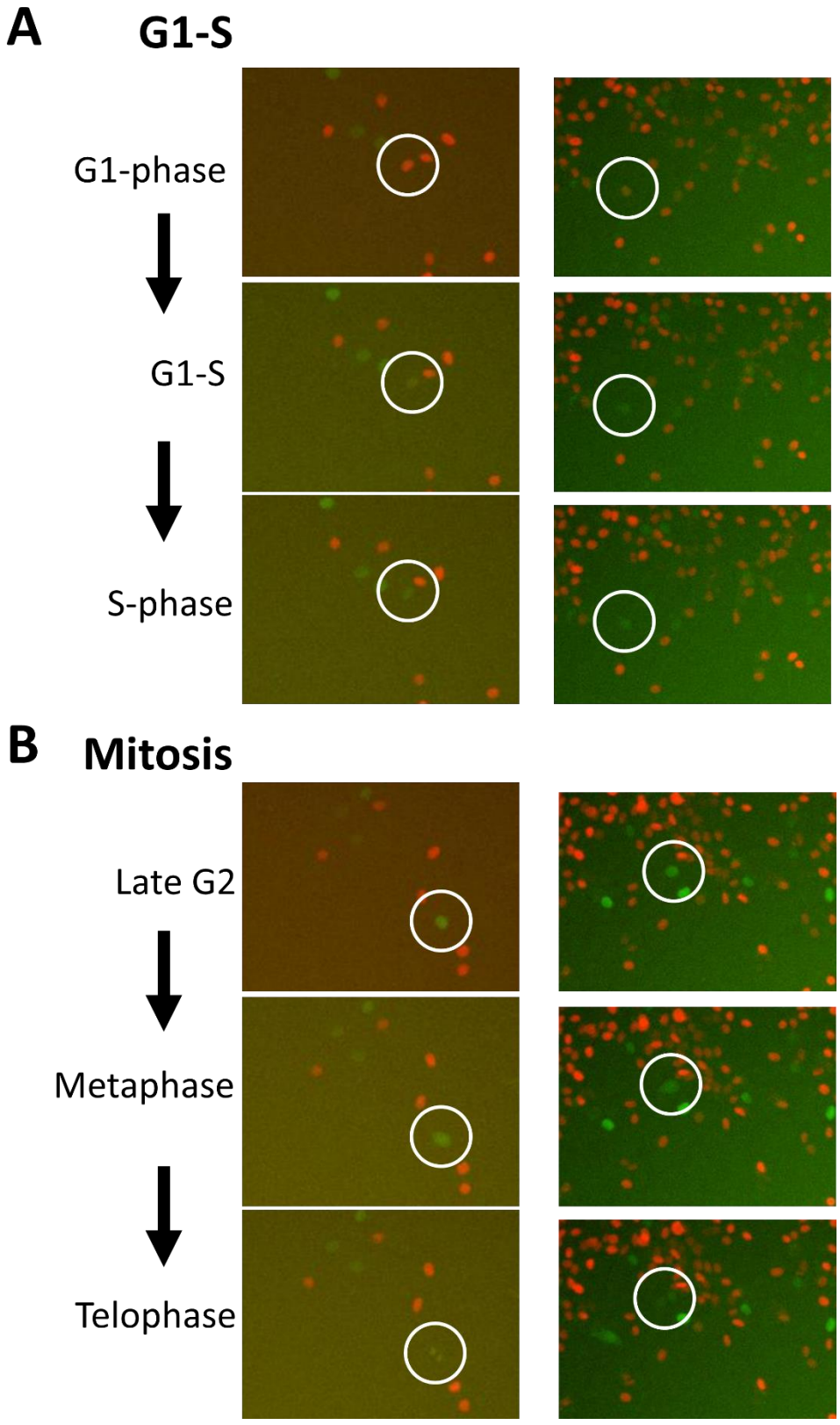

Figure 2.6 Example cell cycle transition events assayed using the FUCCI reporter in PAC2 cells. FUCCI PAC2 cells appear as either green or red nuclei mixed in at 2% with non-fluorescent PAC2 cells nuclei are red in G1-phase and green in S-phase, G2-phase, and M-phase. A) Two examples of three consecutive frames showing transition from G1-phase to S-phase. B) Two examples of three consecutive frames showing transition from G2-phase to M-phase (mitosis).

2.3.3 Cell plating and light entrainment

Cells were split 1:2 or 1:3 three days before plating for time-lapse experiments so as to be actively growing. On the day of plating the cells were trypsinised for 5 minutes, resuspended in L15 and counted using a haemocytometer.

Fluorescent PAC2-FUCCI cells were mixed with non-fluorescent PAC2 cells at 2% or 4% to allow resolution of individual cells in dense culture. These mixed cultures were plated in 24-well plastic cell culture plates without coating, 0.5ml per well. Exterior wells were left empty of cells as survival of cells in exterior wells appeared to be lower during long periods of culture. Empty wells were filled with L15 medium or PBS to assist temperature and humidity buffering.

The plate was placed inside a waterproof plastic container and left for 1-2 hours for the cells to adhere before being moved into a 28^{o}C waterbath inside a darkroom. The plate was incubated for 4 days in the 28^{o}C water bath under an entraining white light cycle. The light source used was a standard desk lamp with a fluorescent bulb, typically 11 Watts, controlled by a programmable timer. The timing was arranged so that the cells would be in the light phase of the entrainment cycle when the time-lapse was started, thus avoiding accidental light pulses during the dark phase.

2.3.3.1.1 Time-lapse imaging

A fluorescence plate reader, ImageXpress Micro XL Widefield High Content Screening System (Molecular Devices, Sunnyvale, CA, USA), was used for the time-lapse imaging. The plate reader was preheated to 28^{o}C 30 minutes before imaging was started. The plate was moved to the fluorescence plate imager inside the waterproof plastic container and transferred as quickly as possible to avoid changes of temperature. Parafilm® was used to seal the plate, preventing evaporation during imaging and further buffering temperature changes. The access door of the fluorescence plate reader was covered with a pane of transparent glass to allow illumination of the cells while preventing heat loss. The plate reader took between 5 and 8 minutes per time-point to image the whole plate. Using custom journals within the Metaxpress5.0 software the machine was programmed to open the opaque door above the plate between time-points for either 30 minutes if the imaging interval was 40 minutes or 57 minutes if the imaging interval was 65 minutes. This allowed continued light entrainment of the cells during the imaging run. During the time-lapse imaging the light cycle was continued using a single lamp close to the access door.

Laser-based autofocus was used to identify the bottom of the wells and then a manual offset was used to focus on the cell nuclei. Varying exposure times were used, typically between 400

and 750 milliseconds for both the 555 (red) and 488 (green) channels. Six non-overlapping locations were imaged in each well. Images were taken using the 10x objective.

2.3.3.2 T-cycle experiments

For the T-cycle experiments, cells were plated at 180,000 cells.ml^{-1}, 90,000 cells.cm^{-2}. Cells were entrained using a light cycle of either 16 hours (8 hours light: 8 hours dark), 18 hours (9 hours light: 9 hours dark), 24 hours (12:12), or 32 hours (16:16). These cells were then imaged every 40 minutes for 72 hours.

2.3.4 Video analysis

The time-lapse images for each channel were exported from the software as .AVI video files and then the red and green channel for each AVI file were combined using ImageJ software. Brightness and contrast were adjusted for each channel to allow visibility of the faint nuclear signal.

2.3.4.1 Cell cycle transition counts

Cell cycle transition data were collected by eye from the resulting time-lapse movies in ImageJ. G1-S was defined as a loss of the nuclear Kusabira-Orange signal. M was defined as the splitting of the nuclear Azami-Green signal into two nuclei. This is shown in **Figure 2.3B**.

There were several reasons why the analysis of phase transitions and phase and whole cycle lengths was performed by eye:

- The signal from the FUCCI dual reporter was relatively weak compared to the background signal from the plastic culture plate and cell culture medium. The Azami-Green signal in particular was barely above background at times.
- Detritus from dead cells or medium precipitation produced an auto-fluorescent signal that was trivial for a human analyser to ignore.
- The G1 Kusabira-Orange signal was generally lost for several frames at the G1-S boundary before the Azami-Green signal was seen. Similarly at mitosis there was a significant drop in signal as Azami Green was lost and Kusabira Orange gained.
- Depending on the density of the culture there were often quite large movement of cells between frames such that the fluorescent signal for a cell would not overlap with its location in the previous frame.
- The operation of opening the opaque access door between time-points to allow continued entrainment also involved the mechanical unclipping and re-clipping of the plate within the plate reader. This caused slight changes in plate position that manifested as a ‘shaky’ time-lapse movie.

Cell tracking software relies on targets with high signal that do not move significantly between frames, cross paths, or lose signal for periods of time. The time-lapse videos produced in this chapter suffered from all three of these issues and more. Even after brightness and contrast adjustment a human would struggle to follow a single cell throughout the time-lapse without

experience. Often, comparison with multiple adjacent cells over many frames was necessary to track a cell through the cell cycle, and this was considered to be beyond the plausible ability of commercial cell-tracking software, let alone plugins for ImageJ.

2.3.4.2 Cycle and phase length analysis

By following each cell through a time-lapse movie it was possible to extract data for the interval between successive cell division events as well as the lengths of phases within the cell cycle. Cell cycle length was defined as the interval between two mitotic events (splitting of a red nucleus into two) or as the interval between the entry to S-phase (change of nuclear fluorescence from red to green) in mother and daughter cells. G1 length was measured as the interval between mitosis and S-phase. SG2M length was measured as the interval between S-phase and mitosis.

In all cases cells were excluded if the transition appeared abnormal, producing more than two daughter cells, daughter cells of an abnormal size, or daughter cells which immediately died or became autofluorescent.

2.3.5 Quantitative PCR

2.3.5.1 RNA extraction

RNA extraction was performed inside a fume hood due to the toxicity of the TRIzol® (Invitrogen) reagent used. The cell culture medium was aspirated from the cells, Phosphate Buffered Saline (PBS) was added to wash and then also aspirated. 1ml of TRIzol® reagent was added to each well of a 6-well plate or to a T25 flask. The TRIzol® was left for 1 minute and then the cells were scraped off the plastic culture surface using a standard cell scraper. The detached cell clumps in TRIzol® were transferred to a 1.5ml Eppendorf tube and immediately frozen at -80^{o}C until needed.

200µl of chloroform was added at room temperature. The Eppendorf was vortexed for 15 seconds and incubated at room temperature for 2 minutes. It was then spun at 12,000G for 15 minutes at 4^{o}C. The upper aqueous layer was transferred to a fresh Eppendorf and 500µl of isopropanol was added. The solutions were mixed by inverting the tube and incubated at -20^{o}C for at least an hour.

The Eppendorf was spun at 12,000G for 20 minutes at 4^{o}C. The supernatant was removed and the pellet washed with 1ml of 75% ethanol diluted with water. The Eppendorf was vortexed and spun at 7,500G for 5 minutes at 4^{o}C. The supernatant was removed and the Eppendorf spun quickly again to collect liquid residue, which was also removed. The pellet was allowed to air-dry and then re-suspended in 20-50µl of sterile water. After thorough mixing the RNA concentration was measured using a nanodrop Spectrophotometer. RNA was kept at -20^{o}C for short-term storage and -80^{o}C for long-term storage.

2.3.5.2 cDNA synthesis

3µl of the RNA sample with the lowest concentration was used for cDNA synthesis, and the volume other samples were adjusted to be the same RNA mass and made up to 3µl with DEPC-treated H_2O. All reactions were made in standard RNase-free PCR tubes. 1µl of DNase buffer (Promega) and 1µl of RNase-free DNase (Promega) was added. This was incubated at 37^oC for 30 minutes. 1µl of DNase stop solution (Promega) was added. This was incubated at 65^oC for 10 minutes.

For the cDNA synthesis reaction the SuperScript III First-Strand Synthesis kit (Thermofisher) was used. 1µl of oligo$(dT)_{20}$ (50µM) primers and 1µl annealing buffer were added. This was incubated at 65^oC for 5 minutes, placed on ice for 1 minute, then collected by brief centrifugation. 10µl of 2X first-strand reaction mix was added. 2µl of SuperScript III/RNaseOUT enzyme mix was added. Tubes were flicked to mix and collected by brief centrifugation. This was incubated at 50^oC for 50 minutes. The reaction was inactivated at 85^oC for 5 minutes and then chilled on ice. 1µl of *E.coli* RNase H (2units/µl, Promega) was added. This was incubated at 37^oC for 20 minutes. cDNA samples were stored at -20^oC until use.

2.3.5.3 Quantitative PCR

cDNA samples were diluted to 10% concentration with H_2O prior to use in quantitative PCR. For quantitative PCR Power SYBR Green Master Mix (ThermoFisher Scientific) was used. 12.5µl of MasterMix, 9.5µl ddH_2O, 1µl cDNA, 1µl forward primer and 1µl reverse primer were combined in each well of a 96-well as per the manufacturer's protocol. The Mastermix and water were combined first and mixed. This was then split, the cDNA added, and mixed again. This was then pipetted onto the plate. Primer pairs were mixed and then added to the plate as well. Plates used were MicroAmp™ Fast Optical 96-Well Reaction Plate, 0.1 ml (ThermoFisher). These were sealed with MicroAmp™ Optical Adhesive Film (Thermofisher).

The RT-PCR was performed using a StepOnePlus™ Real-Time PCR System (Applied Biosystems™), according to the manufacturer's protocol.

2.3.5.4 Data analysis

The relative expression values for the assayed genes in each sample were calculated using the ΔΔCt method(Livak & Schmittgen 2001), as below.

The StepOne™ software v2.3 calculated the cycle threshold (Ct) values for each well according to automatic settings. All samples-primer combinations were plated in triplicate so a mean of the three Ct values was taken. From these Ct values was then subtracted the geometric mean of three reference genes (also in triplicate), which were considered stable across treatments.

ΔCt = Ct (target gene) – Ct (reference gene geometric mean)

These values were then subtracted the ΔCt of a reference sample, in this case at the first time-point.

ΔΔCt = ΔCt (of each sample) – ΔCt (reference sample)

This gave a relative expression level for each target gene such that relative expression between time-points could be seen. 95% confidence intervals were also calculated using the StepOne™ software v2.

2.3.5.5 List of primers for quantitative PCR

Gene	**Forward Primer (5'-3')**	**Reverse Primer (5'-3')**
β-Actin	CGCAAATACTCCGTCTGGAT	GGGCCAGACTCATCGTACTC
EF1-α	CAGCTGATCGTTGGAGTCAA	TGTATGCGCTGACTTCCTTG
18s	TCGCTAGTTGGCATCGTTTATG	CGGAGGTTCGAAGACGATCA
PER1	ATCCAGACCCCAATACAAC	GGGAGACTCTGCTCCTTCT
CRY1a	AGGCTTACACAGCAGCATCA	CTGCACTGCCTCTGGACTTT

2.3.6 Statistics

2.3.6.1 One-way Analysis of Variance (ANOVA)

This was used when comparing cell cycle length and phase length values between treatments. Calculations were performed using Microsoft Excel and the resulting values were checked by inputting the data into [http://www.socscistatistics.com/tests/anova/default2.aspx].

2.3.6.2 Post-hoc Tukey honest significant difference (HSD) test

This was used when comparing phase length values between treatments after a significant difference had been indicated by the one-way ANOVA. The critical q value was found using [http://www.vassarstats.net/tabs.html#q]. Calculations were performed using Microsoft Excel and the resulting values were checked by inputting the data into [http://astatsa.com/OneWay_Anova_with_TukeyHSD/].

2.3.7 BioDare2 periodicity analyses

Periodicity analysis was conducted using the online platform BioDare2 [https://biodare2.ed.ac.uk] using raw cell cycle transition count data. Two periodicity analysis methods were chosen that work on different principles(Zielinski et al. 2014). This would give greater confidence in the estimated periods, which was considered particularly important as the datasets were subject to considerable noise and total number of cycles to be analysed was generally low.

Both periodicity methods described below perform linear de-trending before analysing.

2.3.7.1 Fast Fourier Transform Non-Linear Least Squares (FFT-NLLS)

This analysis starts with a model of a cosine and then uses a non-linear least squares algorithm to determine the parameters of phase amplitude and period that most closely fit the given data. This is iterated with more cosine elements added until adding an extra one does not improve the fit. From these cosine elements the period is chosen based on the expected range.

This analysis gives confidence levels for period, phase and amplitude by altering these values until the model fit is significantly changed. FFT-NLLS is reported to function well with short and noisy datasets and is a commonly used analysis for circadian data.

2.3.7.2 Maximum Entropy Spectral Analysis (MESA)

This analysis uses a completely different method from FFT-NLLS to determine period and so is recommended to be used in conjunction to improve confidence in results. This method relies on the assumption that the value of a datapoint is predictable based on the values of the datapoints that precede it over some length of time, combined with some element of noise. A spectrum of the frequency of time delays that have the highest prediction coefficients produces estimates for the period of the data. This method also does not assume a waveform shape of the data and is effective for very short time samples of oscillations relative to the period length.

2.4 Results

2.4.1 Introduction to chapter and how it will be laid out

In this Results section the experimental question of: "to what extent do cells that are entrained to different length T-cycles show different cell cycle dynamics?" will be addressed using the techniques presented in the Materials and Methods section.

In brief, a zebrafish embryonic cell line transfected with a fluorescent cell cycle reporter was used to investigate the effect of varying the circadian entrainment period on the cell cycle output. Cells were cultured for 4 days under entraining light cycles of different periods, for example 12hours light:12hours dark or 16hours light:16 hours dark. These cells were then continuously imaged over three days to assay for cell cycle transitions.

2.4.2 Quantitative clock gene expression comparison between the PAC2 and PAC2-FUCCI cell lines

The PAC2-FUCCI line was created through transfection of PAC2 cells with the dual FUCCI reporter plasmid system, as detailed in the Materials and Methods section.

It was unlikely but possible that the FUCCI vectors could have integrated into locations in the genome that disrupted clock function in a major way. Therefore a quantitative polymerase chain reaction (qPCR) experiment was performed to assess for the presence and timing of core clock gene oscillation, comparing the PAC2-FUCCI sub-population against the source PAC2 population.

Cells were incubated in 6-well culture plates (with a growth area of 9.6cm^2 per well) under a 24-hour entraining light cycle for 4 days and then a sample of each cell line was taken every four hours for 24 hours while the cells were kept in constant darkness, corresponding to ZT 0, 4, 8, 12, 16, 20. The RNA was extracted and cDNA synthesised. qPCR experiments were performed using a StepOnePlus™ Real-Time PCR System. Triplicate technical repeats were performed for each sample-primer pairing. The expression levels of 3 ubiquitously expressed endogenous control genes were used as standard controls. These were: the 18s ribosomal subunit, elongation factor 1-alpha (EF1α), and β-actin. Full experimental details and primer sequences are given in the Materials and Methods section.

The results are shown in **Figure 2.7**. Starting with the upper graph displaying *PER1* expression data it can be seen that the broad expression pattern is similar between the PAC2 and the PAC2-FUCCI lines. However, the FUCCI expression peak is at time-point 1 while the PAC2 expression peak is at time-point 6. However, the 95% confidence interval bars suggest that the certainty of the relative levels of the time-points, particularly for the PAC2 data, is not high. The amplification profiles for the *PER1* samples in this experiment showed late amplification relative to the control

genes. This in turn suggests very low absolute levels of *PER1* mRNA in the samples, which is likely the reason for the broad confidence intervals.

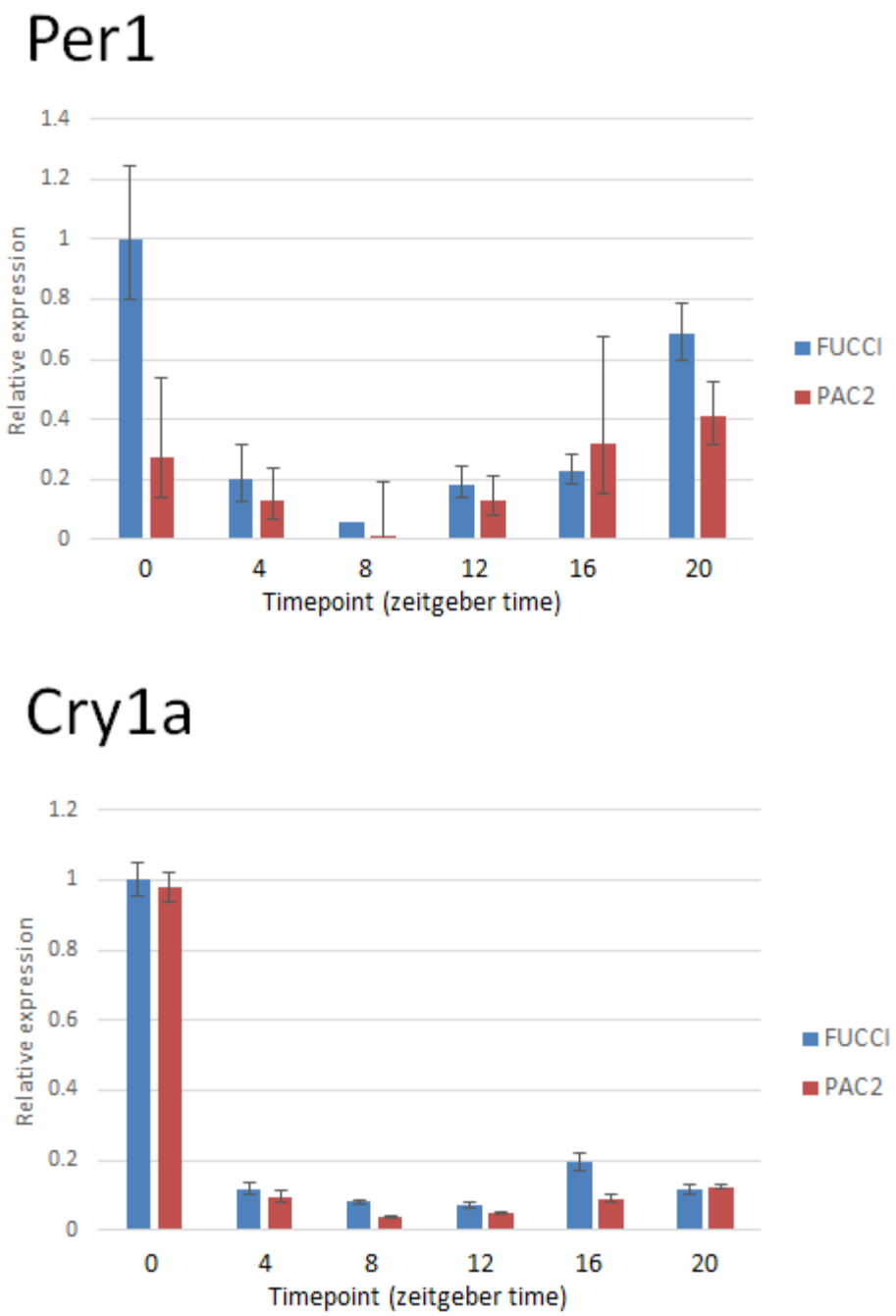

Figure 2.7 Quantitative PCR relative gene expression data for PAC2 and PAC2-FUCCI cells entrained to a 24-hour light-dark cycle and then harvested every 4 hours over a 24-hour period of constant darkness, starting at ZT 0, 4, 8, 12, 16, and 20. The upper panel shows expression of the core clock gene Period1, the lower shows expression of the core clock gene Cry1a. Both are shown relative to the FUCCI sample at timepoint 1. Error bars represent 95% confidence intervals based on three technical measurements. Note that timepoint 3 for Per1 expression in the FUCCI line has no error bars as only one technical measurement produced amplification.

The data is in agreement that the trough for *PER1* expression is at time-point 3. Note however that the FUCCI bar for time-point 3 has no error bars. This is due to the fact that two of the three technical repeats showed no amplification at all during the course of the protocol. Again, this is likely due to the late amplification, in turn due to low absolute expression of the *PER1* gene. The peak of Per1 expression for both lines lies near the ZT 0/24, which is in agreement with Per1 promoter-driven luciferase expression experiments for the PAC2 cell line(Laranjeiro et al. 2018).

Moving on to the lower graph. This shows relative *CRY1A* expression for the two cell lines. Here the error bars are much smaller, which reflects greater agreement between technical repeats, which is likely due to the fact that the absolute levels of *CRY1A* mRNA were generally higher than *PER1*. There is also much better agreement between the two lines, with a very clear peak at timepoint 1.

Taken together these qPCR data suggest that the clock entrainment is functioning in the PAC2-FUCCI line, though caveats remain as to the biological relevance of this highly derived *in vitro* cell line.

2.4.3 24-hour light entrainment produces measurable rhythms in cell cycle progression at the population level

An imaging run using a T24 entrainment period (24 hour period, 12h light:12h dark) was used to generate 102 timelapse movies from a single 24-well plate of fluorescent PAC2-FUCCI cells mixed with non-fluorescent PAC2 cells. Images were taken every 40 minutes over 72 hours, generating 108 frames in each movie. 40 minutes was considered appropriate for high temporal resolution while also keeping the number of frames appropriate for analysis. Before imaging, the cells were entrained in culture to the T24 light cycle for four days. Previous experimentation suggested that four days of entrainment would be more than sufficient to entrain and synchronise the population circadian clock rhythmicity(Whitmore et al. 2000). During imaging the entrainment was maintained by opening the opaque plate reader door as detailed in the methods section.

Each movie was then analysed manually frame-by-frame using ImageJ. ImageJ is described by its developers as an "open source image processing program designed for scientific multidimensional images"(https://imagej.nih.gov/ij/). Cell cycle transition events were defined according to which frame of the video they occurred in. For example, if a division event occurred between frames 23 and 24 then the event would be recorded as occurring in frame 24. No events were recorded for frame 1 as there was no previous frame to compare to. Typically only a dozen events were recorded per time-lapse at each location due to the small number of fluorescent cells, though occasionally there were many more or none at all. Example frames from these

time-lapse videos can be found in the Materials and Methods, as well as examples of cell cycle transition events.

2.4.3.1 Cell cycle transition population data

The data from this T24 entrainment experiment was used to generate the scatterplots show in **Figure 2.8**. This figure demonstrates the effect of the moving averaging that was performed on the data. The raw plots show a predictable amount of noise in their trends given the small number of data points in each of the 110 time bins (typically around ten per bin). Performing the moving average in the lower plots allowed a better visual demonstration of the period of the oscillations. The averaging has only been used for more convenient visualisation; for periodicity analysis using BioDare2 and all statistical analysis the raw data was always used. In subsequent figures showing phase transition timing the data will be displayed in this way. Seven frames was chosen for the moving average as it balanced improved visualisation of the peak and trough timings with avoiding excessively reducing their amplitude. At the bottom of the figure the same data is shown with both the G1S and M transitions on a single graph. The background colour represents the entraining light cycle, with the light section corresponding to lights on and the dark to lights off. From this it can be seen that the M-phase transition peak occurs around the dark to light transition while the G1S transition peak occurs around the light to dark transition.

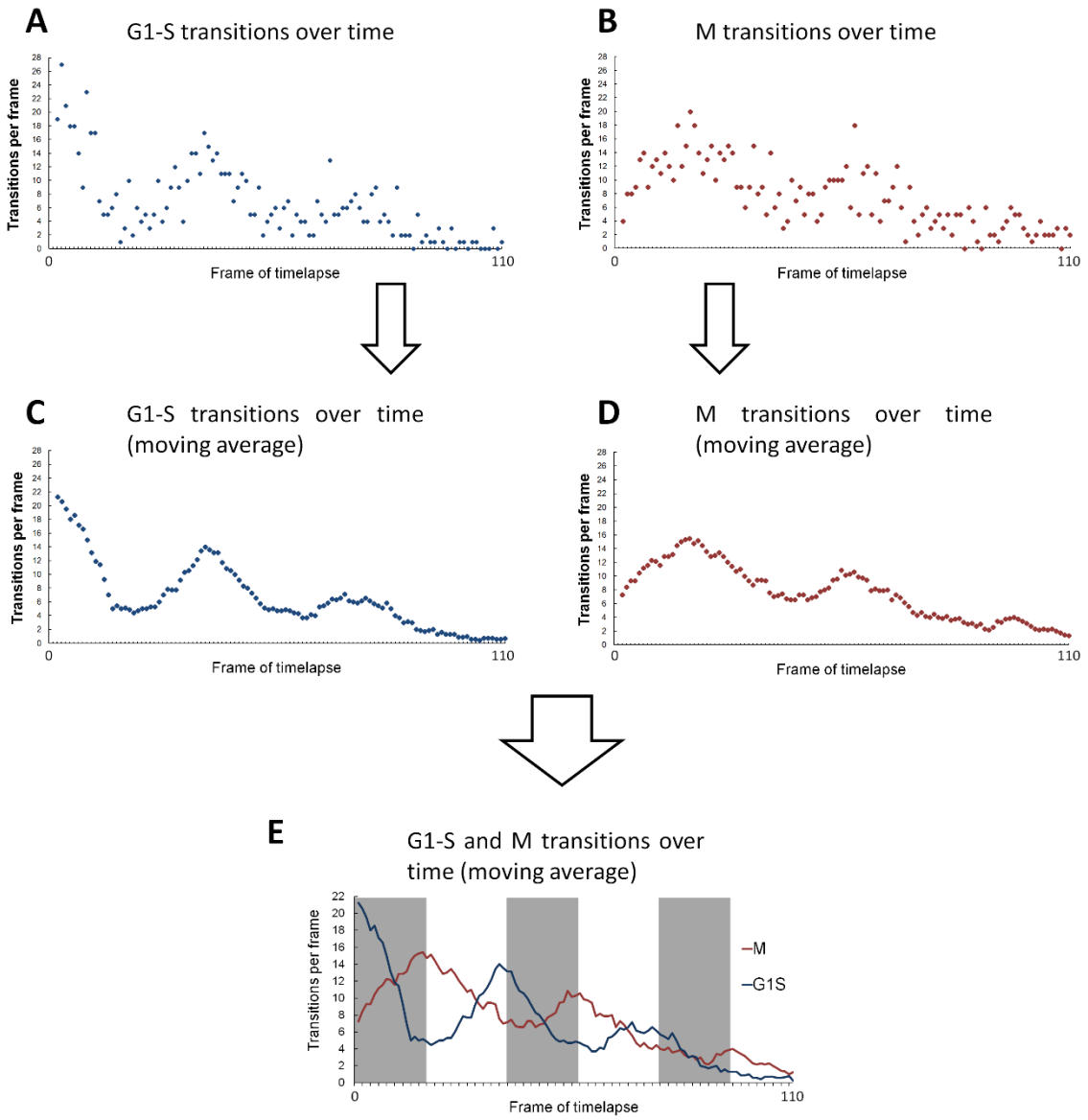

Figure 2.8 FUCCI cell cycle phase transtion data from a T24 72-hour timelapse. X-axes show the frame of the timelapse at 40-minute intervals and Y-axes show the count of transitions per frame. G1-S transitions are shown in blue, M transitions are shown in red. (A) Raw counts for G1-S transitions (n=708). (B) Raw counts for M transitions (n=804). (C) G1-S transition counts with a 7-point moving mean. (D) M transition counts with a 7-point moving mean. (E) Data from C and D redisplayed as a combined line graph. Dark areas represent the dark periods of the entraining light cycle, which was 12hours light and 12 hours dark.

2.4.3.2 Biodare and periodicity analysis

The raw data for this T24 entrainment experiment was uploaded to BioDare2(Zielinski et al. 2014). This software is described by its developers as being for "fast period analysis, timeseries processing and aesthetic visualizations" and can be found at: (https://biodare2.ed.ac.uk).

The Biodare2 software was used to perform periodicity analyses on the dataset as outlined in the Materials and Methods section. FFT-NLLS and MESA periodicity analysis were both used as they generate period values through completely different methods, and so their agreement

strengthens confidence in the period values given. The estimated period values that were produced by the analysis are shown below.

Using FFT-NLLS:

G1-S period is **24.61** hours

M period is **25.7** hours

Using MESA:

G1-S period is **25.68** hours

M period is **25.78** hours

All of these values are greater than the 24-hour period of the entraining light cycle that was applied prior to the imaging and maintained during the imaging. In addition the MESA analysis gives a G1S period that is 1.07 hours longer than that given by the FFT-NLLS analysis. It should be noted that periodicity analyses performs better with data that contains larger numbers of full cycles. The T24 T-cycle data covers only three cycles of the entraining light stimulus. Thus the deviation of these period values from the expected 24 hours could be a real effect of the experimental protocol, or it could simply be due to noisy data covering only three entrainment cycles.

The BioDare period analyses can also give an estimate of the confidence in the output period values for some forms of analysis including FFT-NLLS. However, this is mostly applicable for datasets containing multiple traces for each condition and so is not applicable to this dataset.

2.4.3.3 The population data of cell cycle transitions under a T24 entrainment is consistent with previously used cell-cycle assays

Other assays have previously been used to assess cell cycle transition timing in the zebrafish PAC2 cell line under a T24 light entrainment protocol. Thus they can be directly compared to the FUCCI reporter data shown in **Figure 2.8**.

Bromodeoxyuridine (BrdU) incorporation staining of DNA synthesis during S-phase gives a peak time for S-phase between ZT9 and ZT12, just before the light to dark transition(Laranjeiro et al. 2013; Laranjeiro et al. 2018). (ZT, or Zeitgeber time, refers to the phase of the entraining stimulus). The FUCCI data puts peak G1S transitions just before the light to dark transitions also. The same paper found that expression of the cell cycle inhibitor p21 is lowest at ZT9, before the light-dark transition, which again is consistent as p21 inhibits S-phase entry. Phosphor histone H3 (pH3) staining puts the peak of M-phase at just before the dark to light transition(Tamai et al. 2012). This also appears to closely match the M-phase peak seen in the FUCCI data.

For the FUCCI assays presented in this chapter the change in nuclear fluorescence from red to green has been used to define the timing of the G1 to S transition as CDT1 is degraded and GEMININ is no longer degraded. Note that the BrdU staining indicates the timing of DNA synthesis, which will occur throughout S phase. Therefore one would expect the BrdU peak to occur slightly after the G1S FUCCI peak, depending on the length of S-phase. However, neither assay possesses the temporal resolution to determine this one way or another.

For these FUCCI assays the splitting of the green FUCCI signal in two has been used to define the timing of M phase. More accurately the splitting of the green signal defines the reforming of the nuclear membrane around the separated chromosomes in telophase just prior to cytokinesis at the end of M-phase. pH3 staining marks condensed chromatin, which will be present from prophase through to telophase. However, as M-phase as a whole takes only around an hour to complete in vertebrate cells the likely peak difference between the pH3 staining and FUCCI green signal splitting will be less than an hour. The resolution of the pH3 staining and FUCCI datasets is not high enough to resolve a difference at this level.

Therefore the PAC2-FUCCI reporter system gave population rhythms for cell cycle progression that are consistent with two other cell cycle assays that used completely different mechanisms. This is a good indication that the FUCCI reporter was working as expected.

2.4.4 Clock to cell cycle coupling occurs at a range of entraining periods

Having confirmed that the FUCCI cell cycle reporter was working as expected and that the imaging protocol could produce appropriate data for the experimental question, the experiment was now extended to include T-cycles with entraining light periods that differed from the natural 24 hours.

To investigate the effect of varying T-cycle length on the cell cycle dynamics the time-lapse imaging experiment was repeated for cells entrained to T16, T18, and T32 length light cycles. The light and dark parts of the entraining cycles were always equal in lengths, so 8:8 for T16, 9:9 for T18, 12:12 for T24, and 16:16 for T32. The experimental protocol was otherwise identical. The resulting time-lapse movies were analysed in exactly the same way as the T24 ones, with 102 produced per plate. The results are shown in **Figure 2.9**.

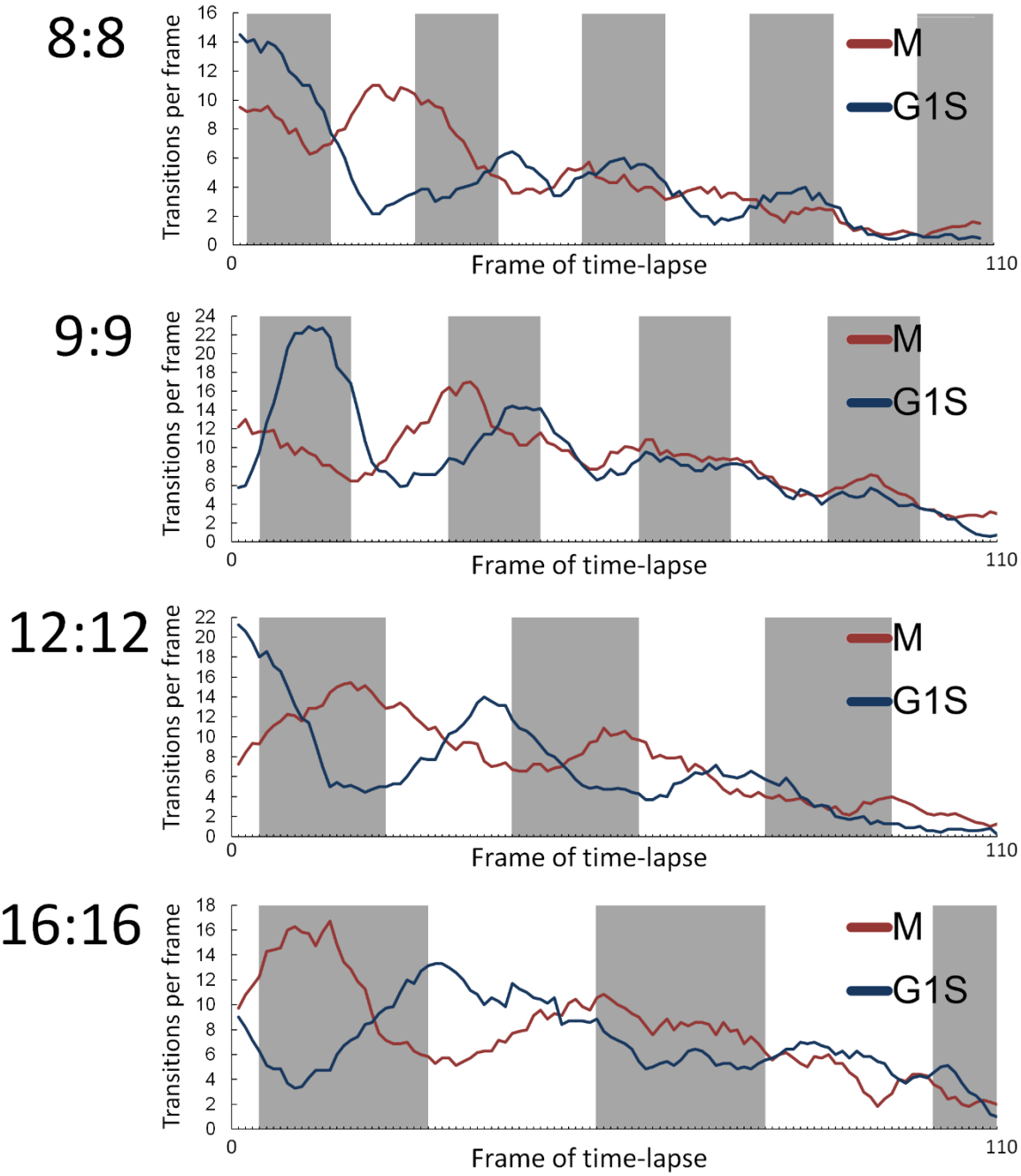

Figure 2.9 FUCCI cell cycle phase transition data from cells maintained under differing T-cycles. X-axes show the frame of the time-lapse at 40-minute intervals and Y-axes show the count of transitions per frame. To the left of each graph is shown the entraining light cycle (8:8 means 8 hours light and 8 hours dark, etc.) G1-S transitions are shown in blue, M transitions are shown in red. Dark areas represent the dark periods of the entraining light cycle. The number of datapoints for each graph is shown below. For 8:8, G1-S n=468, M n=515. For 9:9, G1-S n=947, M n=939. For 12:12, G1-S n=708, M n=804. For 16:16, G1-S n=765, M n=841.

Looking at **Figure 2.9**, the T16 data do not appear to show stable rhythms in either G1S or M phase transitions. The T18 show moderate rhythm for G1S, a less good rhythm for the M and lacks a clear anti-phasic relationship between the two. The T32 showed clear daily rhythms for

both G1S and M transitions that were anti-phasic. The FFT-NLLS and MESA analyses for T32 produced M periods that were very different and divergent from the entraining period (39.29 and 22.90 hours respectively), which suggests that too few complete cycles were present in the data for the periodicity analyses.

The raw counts for all the datasets were uploaded to the online software BioDare2. The software performed a period analysis for all datasets using FFT-NLLS and MESA analyses. The results are shown in **Figure 2.10**. This kind of analysis works better for more full oscillation cycles than were present in these 72 hour datasets, and so the results should be interpreted with some caution, but the results nonetheless support the idea that the entrainment had produced cycles of approximately the expected period.

		Estimated period (hours)	
T cycle	Cell Cycle Transition	FFT NLLS	MESA
16	M	27.51	15.94
	G1-S	16.44	32.74
18	M	20.99	21.16
	G1-S	18.39	18.86
24	M	25.70	25.78
	G1-S	24.61	25.68
32	M	39.29	22.90
	G1-S	34.21	28.90

Figure 2.10 Period estimates of cell cycle transition timing for PAC2-FUCCI cells entrained under different T-cycles. T cycle - The period of the entraining light stimulus. Cell Cycle Transition - The phase progression being measured using the FUCCI reporter. Either mitosis (M) or from G1 to S-phase (G1-S). FFT NLLS and MESA - The two periodicity analyses used to generate the estimated period from the transition data.

The T16 data, which appears visually in **Figure 2.9** to be the least stably entrained, also presented problems for the period analysis, with the FFT-NLLS method giving an M period of 27.51 hours. In addition, the MESA method gave a G1-S period of 32.74 hours. A visual inspection of the T16 graph in **Figure 2.9** suggests that the blue G1-S trace does not appear to have a stable phase relationship to the entraining light stimulus. The first peak is before the start of the first dark phase, the second is during the early light phase, and the third is in the mid-late dark phase. One possibility is that harmonic entrainment is occurring to some extent, with the population partially entrained to a 16-hour day and partially to the 2x multiple 32-hour day. This idea is

supported by the MESA output G1-S period of 32.74 hours, which is almost exactly double the entraining period.

The T18 G1-S periods are approximately the expected length, at 18.39 and 18.86. The estimated period values for the M transitions though were much higher, at 20.99 and 21.16. Visual inspection of the corresponding graph in **Figure 2.9** suggests an unstable phase relationship between the T18 G1-S and M waveforms and supports the idea that the M rhythm is not in a stable phase-relationship with the entraining stimulus.

The T24 periods came out at within 2 hours of 24 hours for both G1-S and M transitions with both analysis.

The T32 periods came out higher than the expected 32 hours for the FFT-NLLS analysis (34.21 and 39.29 hours for G1-S and M respectively) and lower than the expected 32 hours for the MESA analysis (at 28.90 and 22.90 hours for G1-S and M respectively). This is likely due to the fact that the 72 hours of the time-lapse only covered 2.25 entraining cycle lengths of 32 hours, limiting the ability of either method to produce an accurate period.

For the following analysis these T16, T18, T24 and T32 datasets will be used to answer the experimental question: to what extent do cells that are entrained to different length T-cycles show different cell cycle dynamics?

2.4.5 Entraining T-cycle period affects the phase-angle between the entraining light stimulus and the output timing of the cell cycle

Above it has been shown that the T24 FUCCI cell cycle transition data closely matches the rhythm peaks seen using two separate assays, BrdU and pH3 staining. How does this vary for the T16, T18 and T32 datasets?

Examining **Figure 2.9** a notable feature of the four T-cycle datasets is that that peaks of M and G1S rhythms do not occur in the same part of the light-dark cycle, i.e. the phase angle of these peaks differs relative to the entraining light stimulus.

Looking first at the peak of G1-S transitions: T16 does not appear stable, but T18, T24 and T32 all have G1-S peaks that occur at stable but different times during the light-dark cycle. T18 occurs during the mid-to-late dark phase, T24 occurs during the late light phase, and T32 occurs during the early light phase. The results of BrdU assay mentioned earlier put the T32 S-phase peak in the mid-light phase also, consistent with this FUCCI data(Laranjeiro et al. 2018).

Looking at the peak of M transitions: T16 again does not appear stable and neither does T18, but T24 and T32 have M peaks that occur at stable but different times during the light-dark cycle. T24 occurs during the late dark phase whereas T32 occurs during the early dark phase.

These differences are consistent with the known effects of varying T-cycles on the dynamics of the circadian clock, where the driven rhythm phase-lags the driving rhythm less (or leads by more) the longer the T-cycle is relative to the free-running period of the free-running clock machinery(Pittendrigh & Daan 1976a). Generally speaking, this results in the driven output (in this case cell cycle transitions) occurring earlier in the light-dark cycle the longer the period of that cycle is, as is seen in **Figure 2.11**.

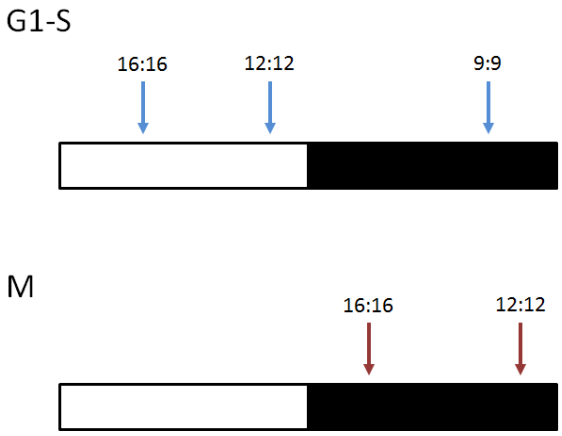

Figure 2.11 Approximate circadian timing of peak cell cycle transition timing under differing T-cycles. The white and black bar indicates the entraining light cycle of light and dark. In each T cycle condition this cycle would be different lengths. Above each bar is shown the approximate timing of peak transitions for G1-S (top) and M (bottom) during the light-dark cycle. Above each arrow is shown the T cycle photoperiod in hours, for example '16:16' indicates a 32 hour day of 16 hours light and 16 hours dark.

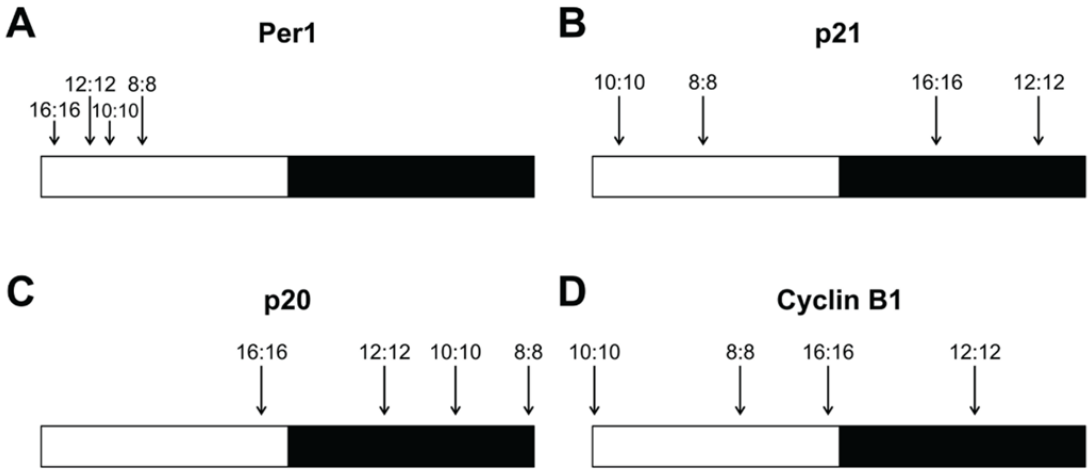

Figure 2.12 T-cycle entrainment modulates the timing of peak expression of clock-related genes. Taken from Iaranjeiro *et al.*, 2018. The white and black bar indicates the entraining light cycle of light and dark. In each T cycle condition this cycle would be different lengths. Above each bar is shown the approximate timing of peak expression of a luciferase reporter driven by the promoter of the core clock gene Per1 or the clock-regulated cell cycle regulators p21, p20, and Cyclin B1.

Figure 2.11 shows the approximate peaks of G1-S and M transitions for this T cycle data. The data for the T16 (8:8) G1-S and M transitions and the T18 (9:9) M transitions are not included as they did not appear to show a stable phase-angle to the entraining light stimulus.

Figure 2.11 can also be compared to published data of luciferase expression driven by the promoters of cell cycle regulators regulated by the circadian clock in PAC2 cells, as shown in **Figure 2.12**, adapted from Laranjeiro *et al., 2018*(Laranjeiro et al. 2018). Here it can be seen that increasing the period of the entraining T-cycle shifted the peak of the driven expression to earlier in the light-dark cycle. Of note is that p21 peaks in the early-mid dark under T32 entrainment, and middle-late dark under T24 entrainment. This lies almost exactly in antiphase with the peaks of G1-S transition shown in **Figure 2.11**. This would be expected as p21 inhibits s-phase entry.

Similarly the peaks of Cyclin B1 promoter-driven expression for T24 entrainment and T32 entrainment in **Figure 2.12** lie shortly before the peaks in M-phase transitions in **Figure 2.11**. This also makes sense as Cyclin B1 is expressed prior to mitosis and promotes early mitotic events.

As detailed in the introduction, the fact that these cell cycle progression rhythms show different phase angles to the entraining stimulus under different T-cycles is an indication that these are rhythms that are truly entrained rather than merely light-driven. The response of the clock phase to the external zeitgeber stimulus will be to advance, delay, or to be insensitive, depending on the current phase it is already in. Therefore entrainment to a longer period length, for example the 32-hour T-cycle, will occur by shifting of the phase angle between the driving light stimulus and the driven clock response such that more of the clock phase that is delay-sensitive to the light stimulus lies during the light stimulus and/or less of the clock phase that is advance-sensitive to the light stimulus lies during the light stimulus. Thus because different phases of the circadian cycle have different sensitivities and responses to external zeitgeber stimuli, at each entraining period length there will be a different and unique phase relationship between the entraining stimulus and the resulting clock phase. If this were not the case in the data, and for example the G1-S transitions always rose to a peak after the dark-light transition regardless of entraining period length, that would suggest that the driven oscillation was due to an acute effect of the light stimulus rather than true entrainment.

2.4.6 Comparing population-level and single-cell data in the time-lapse T-cycle datasets – changing the entraining t-cycle period length does not change cell cycle length or cell cycle phase length

The T18, T24 and T32 datasets all show rhythms in both G1S and M transitions at a population level that appeared to be similar in period to the entraining light stimulus. They also had different phase angles relative to the entraining light stimulus from each other, which is what

would be expected from an entrained rhythm. The entraining light cycle was therefore influencing the timing of cell cycle phase progression.

Based on the data presented so far the question still remains as to whether this influence on cell cycle phase progression is due to coupling or gating. By comparing the population-level cell cycle rhythms with behaviour of the individual cells in the same time-lapse datasets it is possible to distinguish between these two possibilities in this model system.

2.4.6.1 Extracting single-cell cell-cycle phase length data from the T-cycle time-lapses

In order to consider both population rhythms and single-cell behaviour the T-cycle movies were reanalysed. This time instead of recording transition events and the frame in which they occurred, individual cells were followed throughout the time-lapse and those that transitioned through an entire cell cycle were recorded. Cell cycle length was defined either M-to-M or G1S-to-G1S, as already shown in **Figure 2.3**. The same was done for G1 lengths (M-to-G1S) and SG2M lengths (G1S-to-M). When the exact frame of transition was not clear an average of the plausible range was taken. This was typically two or three frames at most. If a cell passed through enough phases of the cell cycle that it had both an M-to-M and G1S-to-G1S length within the time-lapse then whichever came first was recorded.

The length of the SG2M phase is far shorter than either G1 or the whole cycle. This meant that far more cells went through an entire SG2M phase during the time-lapse than an entire G1 or an entire cell cycle. For this reason the number of cells counted for SG2M length was capped at 100 per T-cycle experiment. Similarly there were more than 100 full G1 events in the T24 dataset, and again the number counted was capped at 100.

The mean cell cycle length values are shown in **Figure 2.13**. The mean cell cycle length for all four T-cycle conditions lies between 41 and 46 hours. Thus in none of the four cases does the cell cycle length match the entraining circadian cycle length of 16, 18, 24, or 32 hours. Nor does it match any of the periods of oscillation of the M or G1S rhythms in the population data.

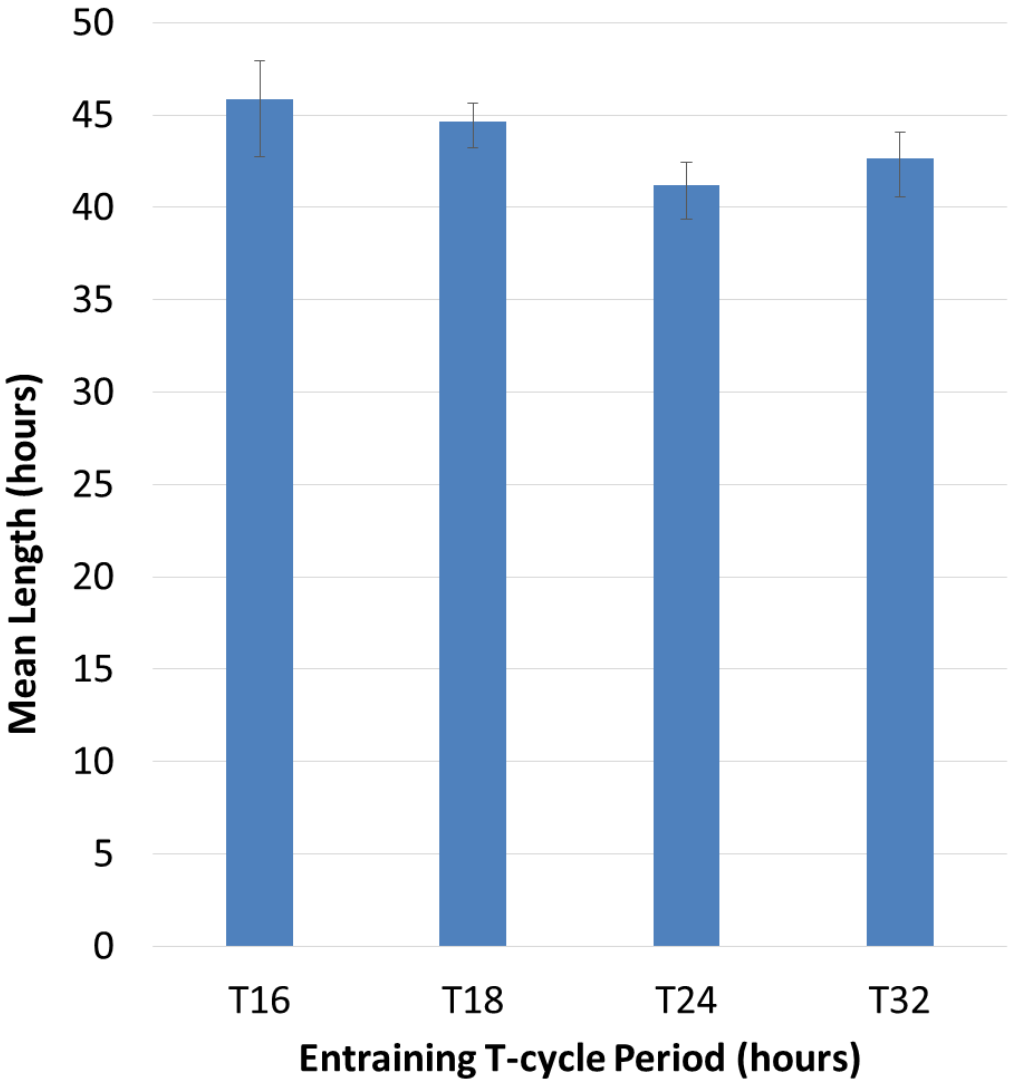

Figure 2.13 Cell cycle lengths under different entraining T-cycles. Each bar displays the mean whole cell cycle length measured for each T-cycle dataset. Cell cycle length was measured as the G1S-G1S interval or M-M interval. Error bars represent the s.e.m. A one-way ANOVA analysis found no significant difference between means at $p<0.05$.

For G1 lengths and SG2M lengths only the T18, T24, and T32 data is shown as the T16 raw time-lapse data was lost due to human error before the analysis was performed. G1 length data is shown in **Figure 2.14** and SG2M length data is shown in **Figure 2.15**. All mean length data is also summarised in **Table 2.1**.

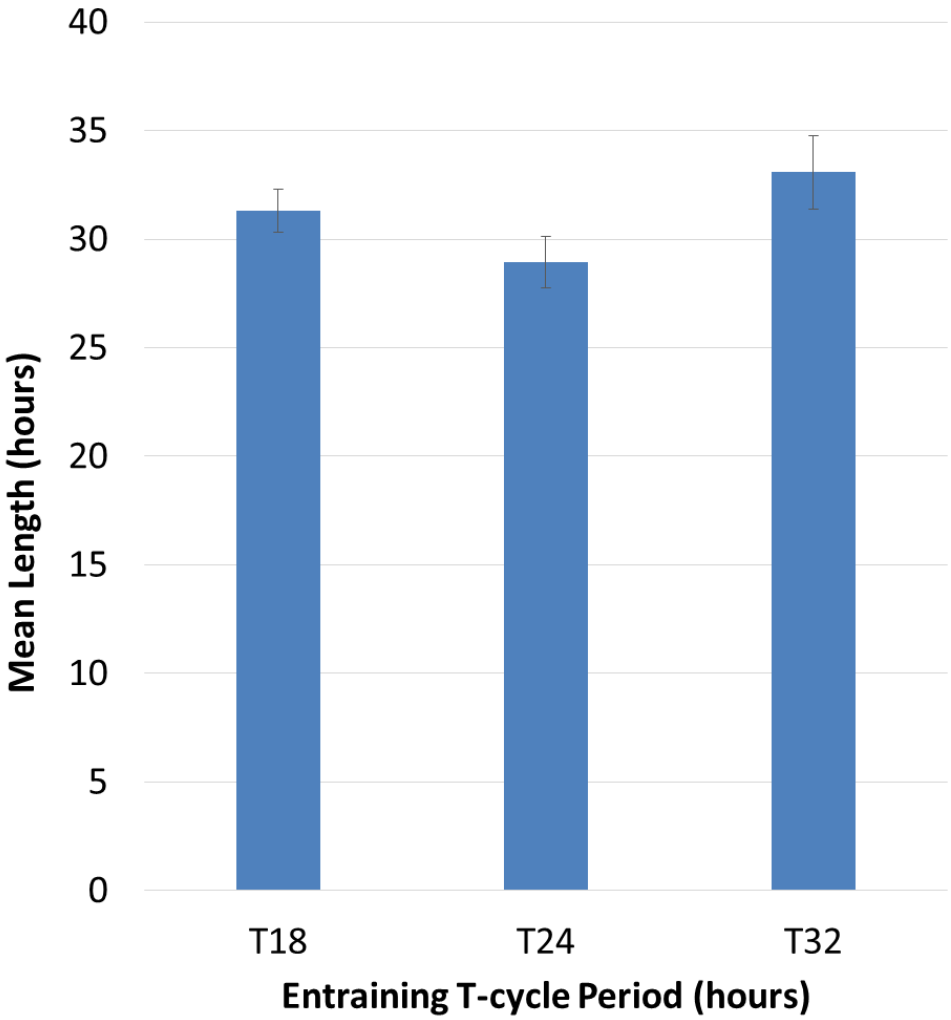

Figure 2.14 G1 lengths under different entraining T-cycles. Each bar displays the mean G1 length measured for each T-cycle dataset. Error bars represent the s.e.m. A one-way ANOVA analysis found no significant difference between means at $p<0.05$.

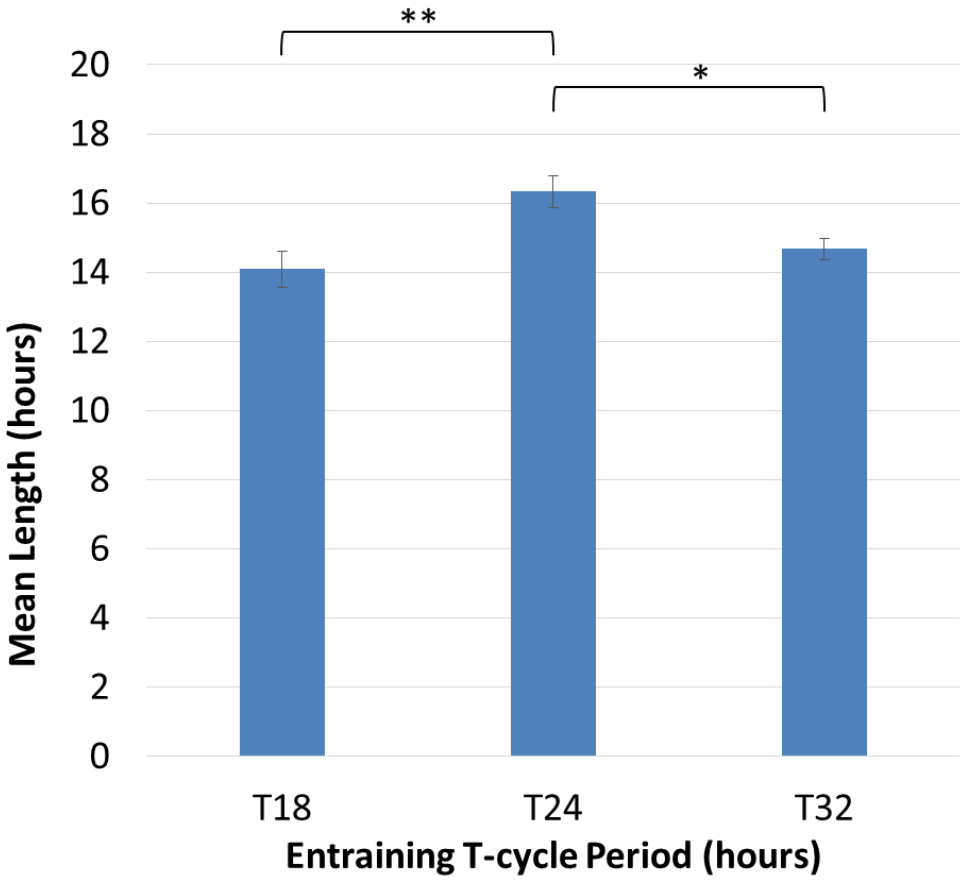

Figure 2.15 SG2M lengths under different entraining T-cycles. Each bar displays the mean SG2M length measured for each T-cycle dataset. Error bars represent the s.e.m. Significant differences between values according to a post-hoc tukey honest significant difference test are bracketed (*p<0.05, **<p<0.01).

		Entraining T-Cycle			
		T16	T18	T24	T32
Cell cycle	mean	**45.85**	**44.67**	**41.19**	**42.67**
	standard deviation	11.01	9.92	8.86	9.59
	n	28	107	51	46
G1	mean		**31.31**	**28.93**	**33.08**
	standard deviation		11.57	11.82	14.87
	n		142	100	78
SG2M	mean		**14.09**	**16.33**	**14.67**
	standard deviation		5.16	4.59	3.01
	n		100	100	100

Table 2.1 Cell cycle phase lengths under different entraining T-cycles. Mean measured values are shown in bold and are given in hours.

The mean phase lengths for G1 lie between 28 and 34 hours. This does not equal the phase delay between the M peaks and G1S peaks for the three T-cycles, which are between 12 and 15 hours. The mean phase lengths for SG2M lie between 14 and 17 hours, which is closer to the phase-delay between G1-S and M peaks. However the mean SG2M length does not increase with increasing T-cycle period.

Figure 2.16 shows the distribution of cell cycle length values for each dataset (T16, T18, T24, T32). Here the cell cycle length data have been sorted into 6-hour bins and then plotted as bar charts. 6 hours was chosen in order to balance resolution with having sufficient data-points in each bin. As the length data is not truly continuous, falling at discrete intervals of 40 minutes (for example 26.00 hours, 26.67 hours, 27.33 hours), a bin size of 6 hours meant that each bin is be exactly 6/(2/3)=9 data intervals wide.

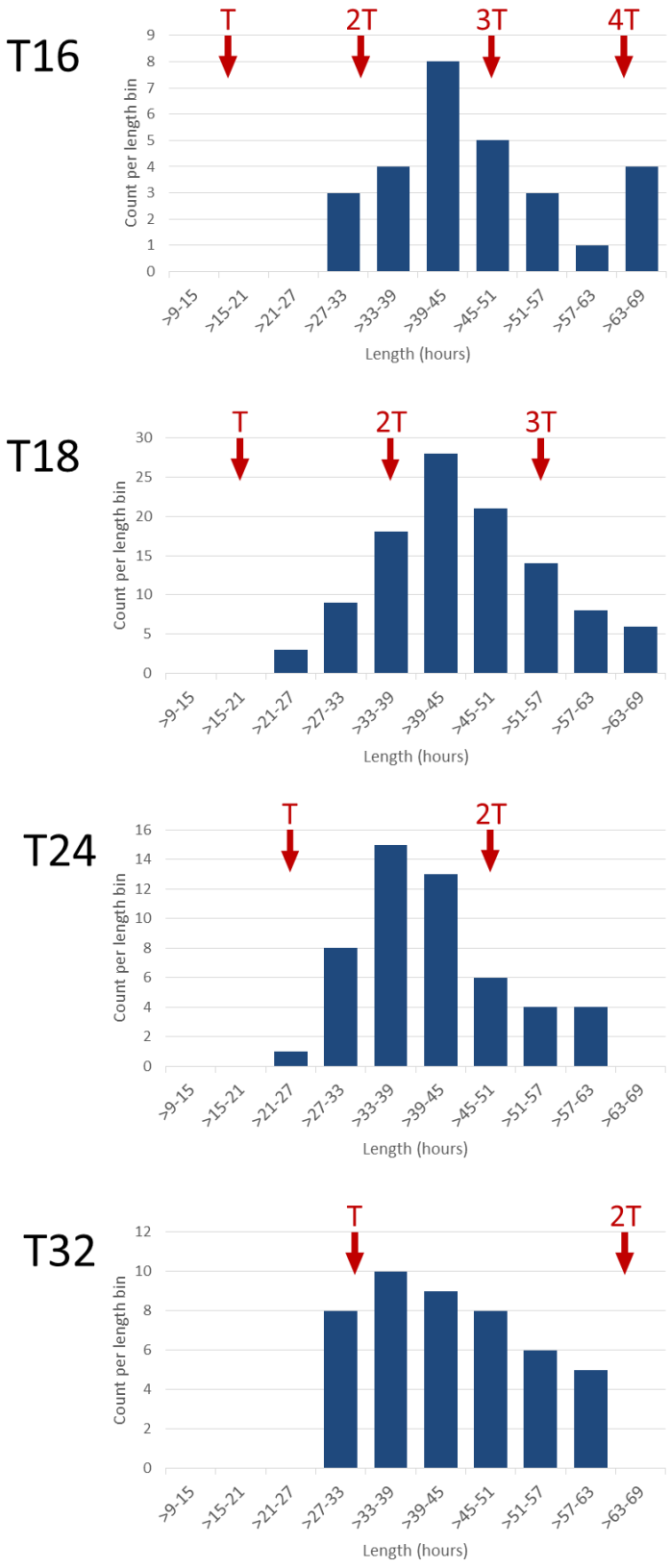

Figure 2.16 Distribution of cell cycle length data for each T-cycle exposure group. The data was grouped into bins of 6 hours and plotted for each T-cycle exposure. The y-axis shows total number of data values that fell into each bin, and is different for each treatment group. The red arrows denote where along the x-axis cell cycle lengths equalling to the entraining light cycle period (T) or equalling a multiple of the entraining light cycle period (T, 2T, 3T, and 4T) fall.

It can be seen that all three T-cycle datasets show a broad distribution of cell cycle length values and there is no one value for 'cell cycle length'. There is some suggestion that the distribution for the T16 data differs in shape from that of the T18 and T32 data, with a hint of a bimodal distribution with peaks at 39-45 hours and a second one at 63-69 hours. However the number of counts per length bin are so low that this merely suggestive. The red arrows in the figure show the entraining period length (T) or multiples of it (2T, 3T, 4T). It can clearly be seen that in none of the four T-cycle cases does the distribution centre at T or a multiple of T.

Figure 2.17 shows a similar set of bar graphs for G1 length. Here the bins are 4 hours wide. 4 hours was chosen in order to balance resolution with having sufficient data-points in each bin. As the length data is not truly continuous, falling at discrete intervals of 40 minutes (e.g. 26.00 hours, 26.67 hours, 27.33 hours), a bin size of 4 hours meant that each bin is be exactly 4/(2/3)=6 data intervals wide.

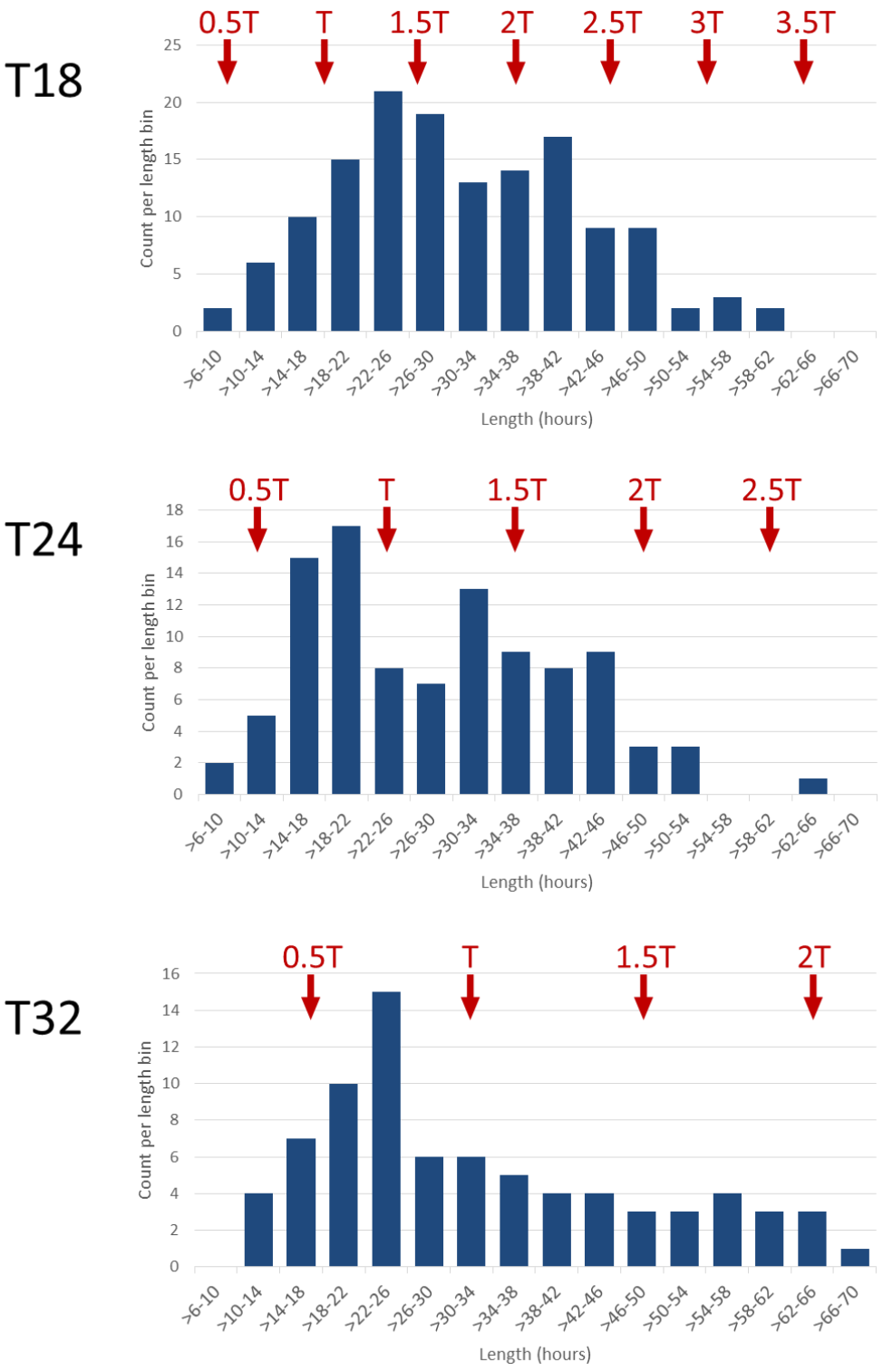

Figure 2.17 Distribution of G1 length data for each T-cycle exposure group. G1 length was defined as the M-G1S interval. The data was grouped into bins of 4 hours and plotted for each T-cycle exposure. The y-axis shows total number of data values that fell into each bin, and is different for each treatment group. The red arrows denote where along the x-axis G1 lengths equalling to half of the entraining light cycle period (0.5T) or equalling a multiple of half the entraining light cycle period (T, 1.5T, 2T, 2.5T, 3T, and 3.5T) fall.

It can be seen again that there is a broad distribution of length values for each dataset (T18, T24, T32). Here the red arrows show half the entraining period length (0.5T) or multiples of it (T, 1.5T, 2T, etc.). These were added as the phase relationship between the G1-S and M transition traces in **Figure 2.9** are roughly anti-phasic. For example for the T24 data the phase-delay between the M peak and the G1-S peak is around half the period, so 12 hours. From **Figure 2.17** there is no compelling suggestion that any of the three distributions peaks at around the half-period length or period length. However, in the case of the T18 data there is a suggestion of a bimodal distribution with peaks around 26 and 40 hours. 26 hours is very close to 1.5x the 18-hour period length. The suggestion of a bimodal distribution is also seen in the T24 graph, with peaks around 20 and 34 hours. The T32 data does not show a second peak, but does show significant positive skew.

Figure 2.18 shows a similar set of bar graphs for SG2M length. Here the bins are 2 hours wide. 2 hours was chosen in order to balance resolution with having sufficient data-points in each bin. As the length data is not truly continuous, falling at discrete intervals of 40 minutes (e.g. 26.00 hours, 26.67 hours, 27.33 hours), a bin size of 2 hours meant that each bin is be exactly 2/(2/3)=3 data intervals wide.

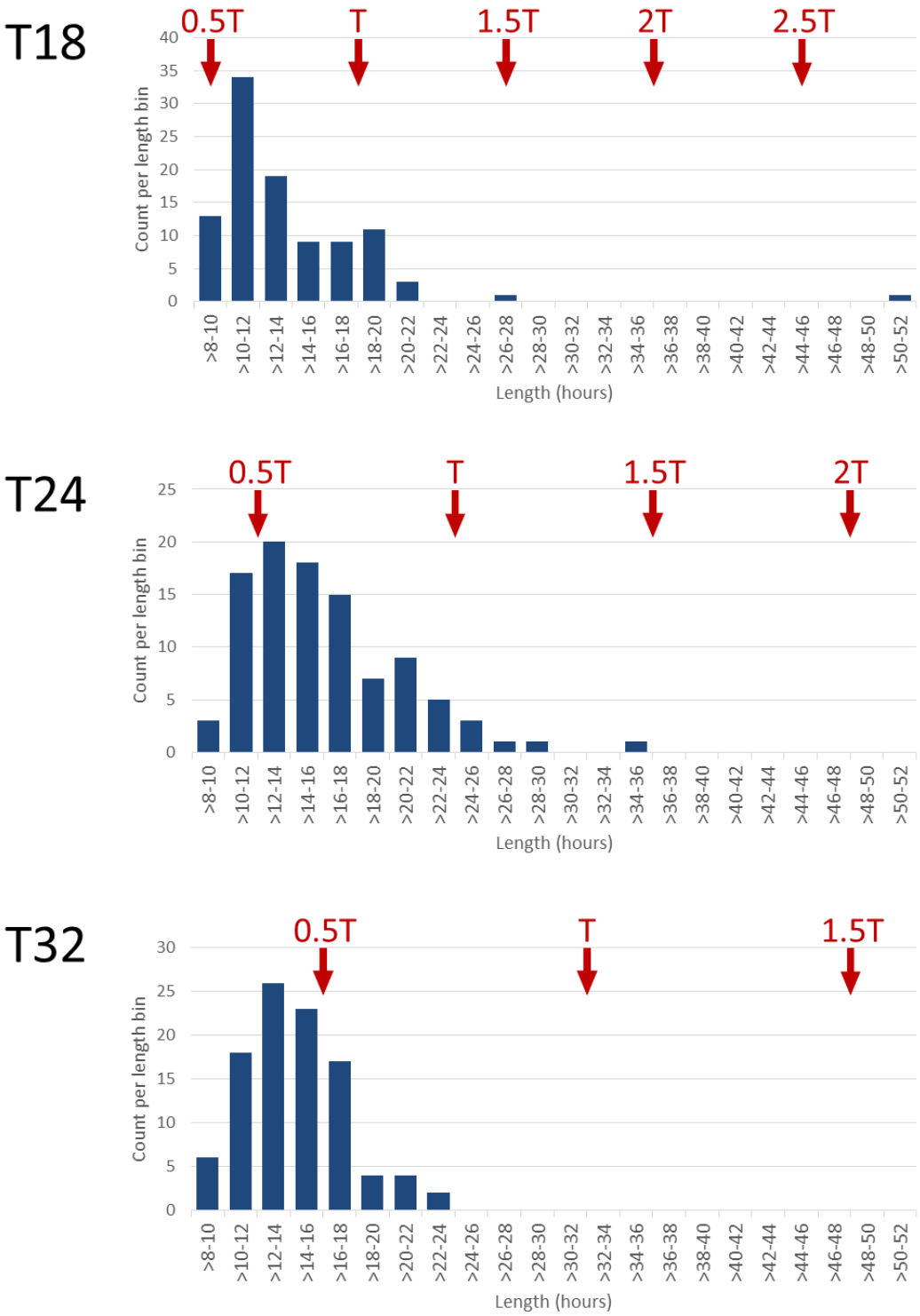

Figure 2.18 Distribution of SG2M length data for each T-cycle exposure group. SG2M length was defined as the G1S-M interval. The data was grouped into bins of 2 hours and plotted for each T-cycle exposure. The y-axis shows total number of data values that fell into each bin, and is different for each treatment group. The red arrows denote where along the x-axis SG2M lengths equalling to half of the entraining light cycle period (0.5T) or equalling a multiple of half the entraining light cycle period (T, 1.5T, 2T, 2.5T, 3T, and 3.5T) fall.

The SG2M graphs in **Figure 2.18** show some positive skew, with outliers to the right of the distributions of the T18 and T24 data. However, it must be remembered that length values are limited by the 72-hour time-lapse duration and so extreme high outliers are more expected for the relatively shorter SG2M data than for the whole cycle and G1 data. Here the peaks of the three distributions lie quite closely to the 0.5T red arrows. However, the T18 peak lies to the right of the 0.5T arrow, the T24 peak lies just to the right of the 0.5T arrow, and the T32 peak lies to the left of the 0.5T arrow. This is exactly what would be expected if the distribution peaks were independent of period length.

As with the G1 data there is small suggestions of second peaks in the T18 and T24 data at 19 and 22 hours respectively.

From this data it is clear that the change in period of the cell cycle oscillations shown in the population data is not reflected in the mean length of the cell cycle in the single cell data. Nor does the M-to-G1S interval equal the mean G1 length, nor does the G1S-to-M interval equal the mean SG2M length. This suggests that the oscillations of the circadian clock and cell cycle are not coupled in a 1:1 ratio. There is also no suggestion that they are coupling in a 2:1 or 3:1 ratio, though this assay is unlikely to be sensitive enough to reveal this. Certainly the 18 hour T-cycle is not driving a greatly shorter cell cycle, G1 length, or SG2M length than the 24 hour T-cycle or the 32 hour T-cycle.

That being said, there is a suggestion that in the case of whole cycle length under T16, G1 length under T18 and T24, and SG2M length under T32 that the data does not show a single peak value.

With that broad visual qualitative analysis in mind, there do appear to be differences between the mean values for cell cycle length, G1 length and SG2M length for these datasets. For example the mean cell cycle length for T16 is 45.84 hours, 4.62 hours longer than the mean cell cycle length for T24. These differences were assessed formally using a one-way Analysis Of Variance (ANOVA), as detailed in the Materials and Methods section. Details of the analysis can be found in the Appendix and the results are summarised in **Table 2.2**.

Treatment groups	Data type	Statistical test	F statistic	Tukey HSD Q statistic	Degrees of freedom	p-value	Significance
T16, T18, T24, T32	Whole cell cycle length	One-way ANOVA	2.0913		3, 228	0.1022	Insignificant
T18, T24, T32	G1 length	One-way ANOVA	2.4833		2, 317	0.0851	Insignificant
T18, T24, T32	SG2M length	One-way ANOVA	7.1488		2, 297	**0.0009**	*** p<0.001
T18, T24	SG2M length	Tukey HSD		5.1516	297	**0.0010**	** p<0.01
T18, T32	SG2M length	Tukey HSD		1.3339	297	0.6046	Insignificant
T24, T32	SG2M length	Tukey HSD		3.8177	297	**0.0200**	* p<0.05

Table 2.2 Results of the statistical analyses performed on the T-cycle cell cycle and phase length data. The top half of the table shows the results of the One-way ANOVA performed between all treatment groups of each data type. Based on the significant result for SG2M length a *post-hoc* Tukey HSD test was performed pairwise between each treatment group of the SG2M length dataset. Statistically significant p-value results are shown in bold.

The ANOVA found no significant difference in cell cycle length between the treatment groups T16, T18, T24 and T32 at $p<0.05$. The ANOVA also found no significant difference in G1 length between the treatment groups T18, T24 and T32 at $p<0.05$. Therefore the null hypotheses that there is no difference in mean cell cycle or G1 lengths cannot be rejected based on this data.

The ANOVA found a significant difference in SG2M length between the treatment groups T18, T24 and T32 at $p<0.001$. To investigate the nature of this difference a Post-Hoc Tukey Honest Significant Difference (HSD) test was performed on the SG2M length datasets as detailed in Materials and Methods. Details of the analysis can be found in the Appendix.

The difference between the SG2M length of T18 and T32 was found not to be significant at $p<0.05$, but the difference between the SG2M length of T18 and T24, as well as T24 and T32 were found to be significant at $p<0.01$ and $p<0.05$ respectively. This means that based on this data the null hypothesis that there is no difference between the mean SG2M lengths can be rejected.

2.4.6.2 Does T-cycle period affect cell cycle phase length?

The data displayed above presents a slightly mixed picture. The entraining light cycles produce rhythms in cell cycle progression that appear to be equal to the entraining period. This is supported by previous work using BrdU staining and similar entrainment protocols. The measurements of cell cycle length, G1 length, and SG2M length suggest that the mean values for these do not match the entraining period or multiples of it. However, the significant differences between the SG2M lengths of T18 vs T24 and T24 vs T32 require some kind of explanation.

What is it that the results of the ANOVA analysis actually show? A statistical test uses data derived from a sample along with certain assumptions to produce probabilistic statements about the properties of two or more populations. Here cells have been sampled from populations incubated under differing light T-cycles and compared using the ANOVA test. However, while many cells have been sampled from each T-cycle dataset, only one T-cycle dataset has been produced per T-cycle period. Therefore the statistically significant differences seen between mean SG2M lengths apply only to the population of each dataset. In effect, therefore, it can be stated with some confidence that the mean SG2M length differs between these particular three plates kept and that the plates were kept under different T-cycles, but not whether that difference in means was due to the difference in T-cycle or some other difference between these plates. In order to make a statistical statement about PAC2 cells kept under different T-cycles in general this imaging protocol would have to be repeated multiple times with different plates for each T-cycle. Using that expanded dataset a statistical test could then say something about the effect of T-cycle period on PAC2 cells incubated on plates in general.

2.4.7 Conclusion to the chapter and what was presented

In this section the experimental question of: "to what extent do cells that are entrained to different length T-cycles show different cell cycle dynamics?" was addressed using the Materials and Methods presented in the previous section. It was found that the population rhythms of M-phase and G1-S could be entrained to different periods (T-cycles), matching the period of the entraining light cycle. An analysis of the cell cycle lengths of individual cells found no significant differences between T-cycle treatments.

2.5 Discussion

2.5.1 Introduction to this discussion

In this section the experimental results presented in the previous section will be reviewed and placed in the context of circadian theory and other published work. The experimental question of: "to what extent do cells that are entrained to different length T-cycles show different cell cycle dynamics?" will be answered and compared to other recently published findings.

2.5.2 Main experimental findings

The zebrafish FUCCI cell line was derived from the commonly-used PAC2 cell line. To assay whether the production of the FUCCI line had compromised the oscillations in core clock gene expression, a qPCR was performed and this found that the expression of core clock repressors *PER1* and *CRY1A* oscillated in the FUCCI line closely in phase with the oscillations seen in the PAC2 line.

Having validated both the reporter system and the imaging protocol, a time-lapse of cells under a 24-hour entrainment protocol was conducted. The analysis of this dataset revealed rhythms in cell cycle transitions G1-S and M that were consistent with BrdU and PH3 staining methods in the PAC2 cell line(Laranjeiro et al. 2013; Tamai et al. 2012). This strongly suggests that this FUCCI reporter system and time-lapse imaging protocol represents a valid methodology for the investigation of cell cycle dynamics in this zebrafish cell line.

In order to address the experimental question as to what extent the entraining light cycle period affects cell cycle dynamics, the experiment was then extended to include non-natural day-lengths of 16, 18, and 32 hours. Visually these entrainments produced rhythms in cell cycle progression that were consistent with what had been previously reported with BrdU staining and circadian regulated cell cycle regulator promoter-driven luciferase expression(Laranjeiro et al. 2018), as well as previous theoretical and experimental T-cycle work(Pittendrigh & Daan 1976a).

Entrainment could occur over a range of T-cycle periods, but rhythms broke down under particularly short cycles of 16 hours. The program BioDare2 was used to assess the periods of the cell cycle transition data. Despite the noisy data and low number of oscillations, the periodicity analysis supported the assessment that the cell cycle progression rhythms were of approximately the same period as the entraining light cycle.

Having determined that the G1-S and M cell cycle progression were rhythmic, followed the entraining T-cycle periods (with the exception of the T16 time-lapse), and were driven by entrainment rather than masking, the experimental question could now be addressed using the four T-cycle datasets. This question was: to what extent do cells that are entrained to different

length T-cycles show different cell cycle dynamics? This was a simple case of reanalysing each time-lapse and recording the duration between definable points during the cell cycle progression of individual cells.

This analysis found that mean cell cycle lengths do not follow the entraining T-cycle length and that shorter entraining T-cycles do not cause shorter mean cell cycle lengths. In addition, the mean lengths of G1 phases did not follow the M to G1S peak interval. Mean SG2M lengths for T18, T24 and T32 did lie somewhat close to the G1-S to M peak interval, however changing the length of this interval through changing the T-cycle length did not appear to systematically affect SG2M length, suggesting that this was coincidental. This all strongly suggests that cell cycle progression is not phase-locked with circadian clock progression and that shorter entraining T-cycles do not lead to a reduction in cell cycle length, G1 length, or SG2M length.

Examining the distribution of cell cycle lengths under T16, T18, T24 and T32 entraining photoperiods failed to provide evidence that clustering occurs around the entraining period or multiples of it. There was some suggestion in the case of the T16 data of a bimodal distribution of cell cycle lengths, but this is based on only four outlying data-points. The G1 and SG2M length data also contained suggestions of multimodal distributions, though again based on relatively small datasets.

2.5.3 Discussion of experimental findings

The experimental question that drove the research in this chapter was: to what extent do cells that are entrained to different length T-cycles show different cell cycle dynamics?

As detailed in the Introduction there are two primary models of circadian cell cycle rhythmicity. The first is that the circadian clock is driving the cell cycle through its phase transitions and the second is that the circadian clock gates cell cycle phase progression to certain times of day. Like most simplified dichotomous models their true value lies in framing questions and experiments that distinguish between them. One prediction of the driving model is that speeding up or slowing down the rate of circadian clock progression will alter the rate of cell cycle progression. By using this zebrafish model system it was possible to entrain cells through non-chemical means to different T-cycles, confirm that the rhythm periods of the cell cycle transitions were altered, and confirm that the rate of cell cycle progression was unaffected, all within the same population of cells.

These data support the Gating hypothesis – that the circadian clock influence on the cell cycle is specific to the timing of cell cycle phase progression (here assessed at the G1-S transition and the M transition) and does not influence the inherent rate of cell cycle progression. Perhaps it would be more accurate to speak of a “biasing” effect rather than a “gating” effect, as there is

no evidence from this data that the clock is acting as a checkpoint, but rather modulating the probability that a cell will progress through G1-S or M at a particular clock phase. (With that said, under different entraining T-cycles the mean values for cell cycle length, G1 length and SG2M length were not identical. An analysis of variance followed by a Tukey Honest Significant Difference statistical test found significant differences between the SG2M lengths of T24 and T18 and between T24 and T32. Because only one plate was used per T-cycle condition the statistically significant difference could be due to a T-cycle effect or some other difference between the plates. These differences will be the subject of the next experimental chapter.)

From an evolutionary perspective a lack of driving is not surprising. Cell cycle progression is extremely tightly controlled and it is hard to think of a reason why clock progression *per se* would affect the mean rate cell cycle progression, whereas some control of the timing of progression of particular phases has potential adaptive advantage, such as reducing DNA damage through ultraviolet exposure or reactive oxygen species generation.

This result appears to be at odds with recent published research that found robust 1:1 phase-locking between the circadian clock and cell cycle(Bieler et al. 2014; Feillet et al. 2014). However, on closer comparison these results are not only compatible, but together offer plausible explanations for unexpected findings and suggest avenues for future investigation.

In general terms phase-locking is defined as a system of two interacting oscillators having a common frequency and a fixed relative phase. It requires close natural frequencies and strong enough coupling. Both papers used NIH 3T3 mouse fibroblast cells, which have an average cell cycle length in serum-rich culture of around 22 hours(Bieler et al. 2014), compared to a free-running period of around 25 hours of the circadian clock(Nagoshi et al. 2004). Thus the cell cycle period and the free-running circadian clock period were quite similar. In addition, mitosis has been shown in this cell line to phase-shift the circadian clock, shortening the free-running period(Nagoshi et al. 2004; Bieler et al. 2014). Thus it is not surprising that phase-locking occurs is this model system. What is more surprising is the finding that reverse coupling (cell cycle progression affecting the circadian clock phase) was found to be predominant(Bieler et al. 2014).

In fact the effect of mitosis on clock phase was found to be a little more complex, and is worth discussing. This phase-shifting of the circadian clock by mitosis depended on the circadian phase in which it occurs(Bieler et al. 2014). Recall from the introduction that entrainment of the circadian clock by a zeitgeber is characterised by a phase-dependent effect of the stimulus(Pittendrigh & Daan 1976b). However, while in general mitosis was found to shorten the circadian period (a phase-advance), a very early division was found to lengthen the circadian

period (a phase-delay). This is the inverse of what would be expected for a 'natural' entraining zeitgeber stimulus and immediately predicts two effects in a system of this kind.

Firstly, because early divisions are found to phase-delay the clock, an already phase-delayed cell will tend to be increasingly phase-delayed until it phase-skips. In fact a degree of phase-skipping was seen in otherwise 1:1 phase-locked cells(Feillet et al. 2014), exactly as would be predicted. The exact degree of this phase-skipping would depend on the relative mean periods of the two oscillators, their period distributions, and the phase-response distribution of the clock to a mitotic stimulus.

The second prediction is more relevant to the results that have been presented here. Above it has been suggested that the 1:1 phase-locking seen in NIH 3T3 cells is due to the special case of a slightly shorter cell cycle than circadian period and a general tendency of mitotic events to phase-advance the circadian clock. What then would be the effect of having a longer cell cycle period than circadian clock period? In this case mitotic events should still generally phase-advance the circadian clock, but the clock is already shorter than the cell cycle so no phase-locking should occur. The phase-delay caused by mitotic events very early in the clock phase should only amplify already phase-delayed clocks, which would also not promote phase-locking. To the knowledge of this writer, the question of whether phase-locking is lost as cell cycle length increases significantly above free-running circadian length has not been directly addressed experimentally.

Additionally, there is an important caveat to be made about the finding that reverse-coupling predominates in this system. As pointed out(Feillet et al. 2014), these experiments were performed using unentrained cells. Thus it is impossible to say how strong an entraining stimulus from a zeitgeber would have to be in order to overcome the phase-shifting effects of mitosis on the circadian clock. This could well vary with the identity and strength of zeitgeber and would have to be addressed systematically. Typically, mammalian cell circadian clock phases are synchronised *in vitro* using a single pulse stimulus such as serum pulse. This synchronisation approach would not be appropriate in this case as the question relates to the relative strength of the disruption due to cell cycle progression and continuous entraining stimulus. A light-entrainable zebrafish cell line would be an appropriate model system for investigating this.

In any case the above gives two good reasons to expect different results from the experiments that have been presented in this chapter: namely the use of entrained cells and the use of a cell line with a vastly higher cell cycle period than circadian period. It is also entirely possible that mammalian and teleost circadian clocks and cell cycles show different coupling dynamics.

The question certainly remains open as to whether coupling or reverse-coupling predominates *in vivo*. The experiments presented here do not assay for clock phase and so the effect of mitosis phase-shifting the circadian machine cannot be measured. However, this disruption was demonstrably not enough to prevent circadian rhythmicity in cell cycle transition, which is downstream of clock rhythmicity. One objection could be that it is possible that the rhythmic light stimulus could be affecting cell cycle progression directly. However, there is no evidence to suggest that such a mechanism exists. In addition, given that the different T-cycle traces show different phase-angles between the light stimulus and cell cycle output, one would have to invoke a mechanism not only for direct light to cell cycle sensitivity, but also a mechanism for clock-independent cell cycle entrainment in a population with individual cell periods that are not equal to that of the entraining stimulus.

2.5.4 Future directions

So far in this chapter the discussion of experimental results has raised multiple questions. Here these questions and others will be briefly considered in terms of the experimental work that would address them.

2.5.4.1 Does having a significantly shorter cell cycle period affect the biasing of cell cycle progression timing?

In the previous section it was hypothesised that the 1:1 phase-locking seen in two studies that used NIH 3T3 cells was dependent on the specific case of a clock-advancing effect of mitosis and a cell cycle period shorter than the circadian clock free-running period. An obvious experimental approach to address this question would be to use a cell line with a cell cycle period approximately the same as the free-running circadian clock length and then modulate it through changing the serum levels or temperature.

In fact an experiment of this kind has been performed using the immortalised rat1 fibroblasts(Yeom et al. 2010). Here temperature changes were used to alter the length of the cell cycle relative to the circadian clock (which is of course temperature-compensated). However, the authors found no phase-relationship between circadian oscillations and the timing of G2-M, as assayed through the expression of Cyclin B1 promoter-driven luciferase. This was the case at all assayed temperatures.

The authors suggest that either there is no coupling between the circadian clock and the cell cycle in this cell line, or that the process of immortalisation has disrupted this coupling. Based on the data presented here and in the following chapter this author would add a third possibility: that cell density was too low for coupling of the circadian clock to M transitions to occur. Indeed the authors plated cells at 5,000 cells per 35mm culture dish, which is approximately 550 cells

per cm^2, far lower than the 90,000 cells per cm^2 used in the experiments presented in this chapter.

By mixing the reporter cells with identical cells that do not carry the reporter, their protocol could be adjusted to include higher cell densities while still allowing the luciferase signal to be measured. Alternatively the imaging protocols described in this chapter could be modified to include a zebrafish cell line with a shorter mean cell cycle period.

2.5.4.2 How does mitosis affect clock phase under entrainment conditions?

The most surprising finding of the coupling studies discussed above that examined clock to cell cycle coupling in NIH 3T3 cells was that reverse-coupling predominated, i.e. that the cell cycle had more influence on the clock phase than *vice versa*.

Biologically this seems to make little sense. If the function of the circadian clock is to maintain a constant phase-relationship to a predicable external stimulus such as sunlight then what could be the function of a phase-shifting effect of mitosis? One theory is that it could be to produce heterogeneity in proliferating cell populations or stem cell niches(Brown 2014). Alternatively the phase-shifting could be an unavoidable consequence of cell cycle progression with no adaptive value. This could be due to the changing of transcriptional rates during the cell cycle(Gottesfeld & Forbes 1997), pausing of transcription during mitosis(Gottesfeld & Forbes 1997), changes in the concentration of core circadian proteins when the cell divides(Nagoshi et al. 2004), or disruption of Per and Cry protein localisation during breakdown and reformation of the cell nucleus.

The question is how much this phase-shifting affects clock function *in vivo* under entrained conditions. Specifically, what is the relative strength of a physiologically relevant zeitgeber and the disruption caused by the cell cycle? A study of regenerating mouse liver, where an estimated 70% of cells were cell cycling, showed unimpaired circadian clock oscillations at a tissue level(Matsuo et al. 2003).

This is an important question because clock disruption is frequently seen in cancers and cancer cell lines, but without an idea of the relative strength of entraining zeitgebers and phase-shifting due to proliferation, it is hard to be certain of the causal direction.

Any answer to this question will necessarily be specific to a particular species, cell type, growth niche, zeitgeber identity, and zeitgeber strength. However, it would provide a useful reference point for more specific questions. An experimental protocol to address this at a single-cell level would require a way to measure clock progression and cell mitosis, such as a Rev-Erbα::Venus fluorescent reporter(Feillet et al. 2014), and an entrainable cell line such as the zebrafish PAC2 cell line used here, which can be continuously entrained using light.

2.5.4.3 Do cells show intrinsic variation in their coupling between clock and cell cycle?

From the results presented here the circadian clock appears to bias G1-S and M transitions to occur at particular times during the day. However, this means that there are always some cells that are transitioning from G1 to S or from G2 to M at the 'wrong' time of day. The question remains as to whether there is variation between cells as to how obedient they are to the influence of the circadian clock. Some cells may always transition at clock-approved times while others proceed according to their own schedule.

One way to address this question would be to follow a cell through several divisions and correlate its cell cycle transitions in terms of their proximity in time to the 'correct' time as dictated by the circadian clock. If closeness of fit of one transition is predictive of closeness of fit of the next then this would suggest that there is an internal state of the cell (which may change over time) that determines its obedience. If one transition is not predictive of the next then this would suggest the biasing occurs equally to cells in the same conditions.

This experiment would require cells to pass through multiple cell cycles, and thus much longer time-lapses or a cell line with a shorter cell cycle would be necessary.

The question would still remain as to whether those cells are ignoring their own clock or whether their clock entrainment is disrupted. To address this a dual clock and cell cycle reporter system would be required.

2.5.4.4 Do these result generalise to other cell types, in vivo conditions, and other organisms?

Zebrafish cells were used for the experiments presented here because they can be easily and continuously entrained by light(Whitmore et al. 2000). As has been discussed, there is evidence to believe that the coupling between the circadian clock and cell cycle shows different dynamics under entrained and free-running conditions. Thus the use of zebrafish or other light-sensitive fish model cells may be necessary to investigate this. The question will remain over the applicability of zebrafish *in vitro* cell work to other organisms such as mammals, or even to cell behaviour *in vivo*.

Fluorescent live-imaging of tissue explants and even the transparent larvae of zebrafish is possible, and FUCCI zebrafish lines already exist and can be used to track individual cells(Sugiyama et al. 2009). Thus the results presented here and any generated while addressing the questions posed above could be compared between cell lines and live tissues.

It may also be possible to allow non-light-entrainable cells to respond to light through coupling an optogenetic input into the usual entrainment pathway of that cell type. However, this would require a thorough evaluation of relative zeitgeber strength in order for the results gained using such cells to be considered applicable to physiological situations.

Given the vast differences in cell cycle behaviour of cells in the body, both during development, during adult homeostasis, and during pathology, it is likely that the nature of the coupling between the circadian clock and cell cycle also varies. Studies in cell lines will therefore produce effects and general principles that can be considered when looking at a specific situation, but the temptation to generalise must be resisted.

2.5.5 Conclusions

In this discussion the experimental results presented in this chapter have been reviewed and placed in the context of circadian theory and other published work.

The experimental question of: “to what extent do cells that are entrained to different length T-cycles show different cell cycle dynamics?” has been answered, finding that in this model system clock phase biases cell cycle timing for G1-S and M transitions and that clock period does not appear to affect cell cycle length, G1 length, or SG2M length. This appeared to be in contradiction to other studies which found phase-locking between the circadian clock and cell cycle. However, this contradiction was resolved, at least hypothetically, by considering the specifics of each experimental protocol.

Chapter 3 – The effects of cell density on the coupling between the circadian clock and the cell cycle using a light-entrainable zebrafish model cell line

3.1 Introduction

The previous chapter aimed to answer a specific question about the effect of altering the circadian period on the length of the cell cycle of individual cells. It was found that there appeared to be no effect of entraining period on cell cycle length or G1 length, supporting the Gating model of circadian regulation of the cell cycle. However, there was a small but statistically significant difference between the SG2M lengths of the different T-cycle conditions. It was considered likely that this difference was due to the variation of a control variable between experiments, and cell density was hypothesised to be this variable.

3.2 Project aims

The experimental work presented in this chapter was conducted with the aim of answering the question: Is density the hidden variable that explains the difference in SG2M length? This was approached through deliberate variation of the cell density in an imaging protocol mostly identical to those outlined in the previous chapter.

3.3 Methods

3.3.1 Variable-density experiments

For the variable density experiments, a mastermix was made with the PAC2-FUCCI cells mixed at 2% with PAC2 cells. This was then pipetted into the first well of the 24-well plate and then a lower volume into each successive well (i.e. 500µl, 470µl, 440µl…50µl, 20µl, 0µl). L15 medium was then added to each well in order to make up the volume to 500µl and the well contents were pipetted up and down to encourage even plating. Cells were entrained using a light cycle of 24 hours (12:12) and then imaged every 65 minutes for 120 hours. Cells were plated at a range of densities from 150,000 cells.cm^{-2} down to 0 cells.cm^{-2} on a 24-well plate.

Each time-lapse generated 102 time-lapse movies (6 locations in each of 17 wells). The movies were analysed in the same way as detailed in the previous chapter.

3.3.2 Statistics

3.3.2.1 Two-tailed Welch's t-test

A two-tailed Welch's t-test (unequal variances t-test) was used when comparing cell cycle and phase lengths between two cell density treatments. Calculations were performed in Microsoft Excel and the resulting values were checked by inputting the data into [https://www.graphpad.com/quickcalcs/ttest1/].

3.4 Results

3.4.1 Cell density – is it a true independent variable?

A plausible explanation for the small but statistically significance in the SG2M length measurements is that a control variable in the experimental protocol was not identical between the three T-cycle experiments. Contact inhibition between cells and lack of culture space are both known to inhibit cell cycle progression, therefore it was hypothesised that differences in cell density could be having an effect on cell cycle dynamics and would explain the small differences that were seen.

Possible causes of differences in cell density at the time of plating include:

- Differences in the number of cells plated due to counting or pipetting errors.
- Uneven deposition of cells in the wells, leading to denser and less dense areas.
- Differential growth during the entrainment phase due to after-effects of the plating protocol, such as stress due to trypsin treatment or pipetting to mix.
- Small differences in plate properties such as surface smoothness.

3.4.2 Cell density affects cell cycle length and the relative length of G1 and SG2M lengths within it

Rather than repeat all three T-cycle experiments from the previous chapter to see whether these significant differences were reproduced, it was decided to test the effects of deliberately varying the density of the cells. To that end an experiment was set up according to the same protocol as before. This time, however, the volume of cells added to each well was varied systematically to give a gradient of cell density across the plate. Extra medium was then added to each well to make the total medium volume the same in all wells. Cells were plated on a 24-well plate at a range of densities from 150,000 cells.cm^{-2} down to 0 cells.cm^{-2}. For reference, the T-cycle experiments in the previous chapter were plated at 90,000 cells.cm^{-2}.

This plate was then incubated on a T24 light entrainment before imaging, again for four days. This time the time-lapse was run for 5 days (120 hours) rather than 3 days. This was so that effects of changes in cell density during the imaging could also be considered, in addition to the effects of differences in cell density between the wells. The interval between time-points was increased from 40 minutes to 65 minutes so that the total number of time-points would remain the same. The resulting time-lapse movies were analysed as before.

The population results of this are shown in **Figure 3.1**. Here it can be seen visually that the G1S and M phase transitions show the expected oscillations with a 24hour period. The peaks of the G1S rhythm occur at the light-dark transition and the peaks of the M rhythm occur at the dark-light transition, which is consistent with the previous T24 T-cycle experiment.

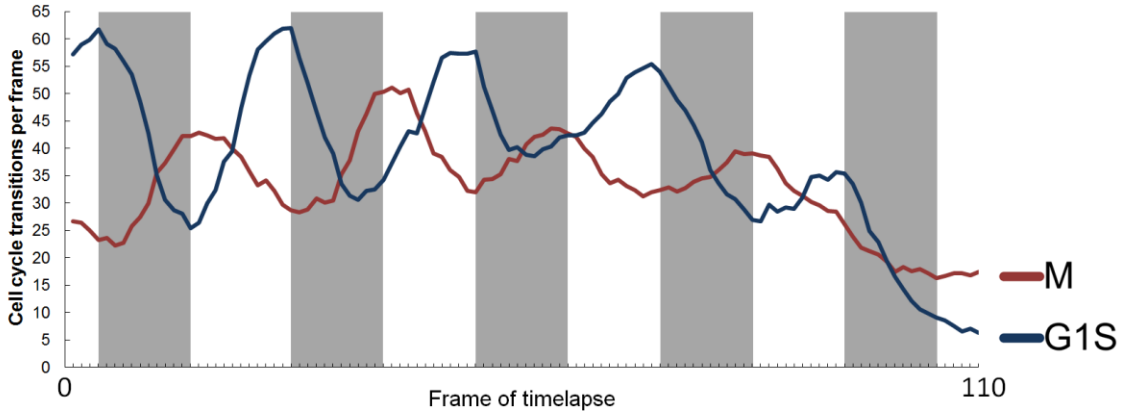

Figure 3.1 FUCCI cell cycle phase transition data from cells maintained at variable density under a 12:12 entraining light stimulus. X-axes show the frame of the timelapse at 65-minute intervals and Y-axes show the count of transitions per frame. G1-S transitions are shown in blue, M transitions are shown in red. Dark areas represent the dark periods of the entraining light cycle, which was 24 hours long.

A BioDare2 periodicity analysis support the 24-hour entrainment, the results of which are shown in **Table 3.1**. The FFT-NLLS analysis estimates the M and G1-S periods at slightly over 24 hours, 25.19 hours and 24.08 hours respectively. The MESA analysis estimates the M and G1-S periods at slightly under 24 hours, 23.64 hours and 23.34 hours respectively.

		Estimated period (hours)	
T cycle	Cell Cycle Transition	FFT NLLS	MESA
24 hours, variable density	M	25.19	23.64
	G1-S	24.08	23.34

Table 3.1 Results of BioDare2 FFT NLLS and MESA periodicity analysis of the T24 variable density time-lapse experiment.

The analysis for cell cycle length, G1 length, and SG2M length gave results shown in **Figure 3.2**, alongside the equivalent values for the T24 fixed density experiment from the T-cycle experiments. More data was generated than was required for the analysis so a range of imaging locations were analysed at random rather than the entire dataset.

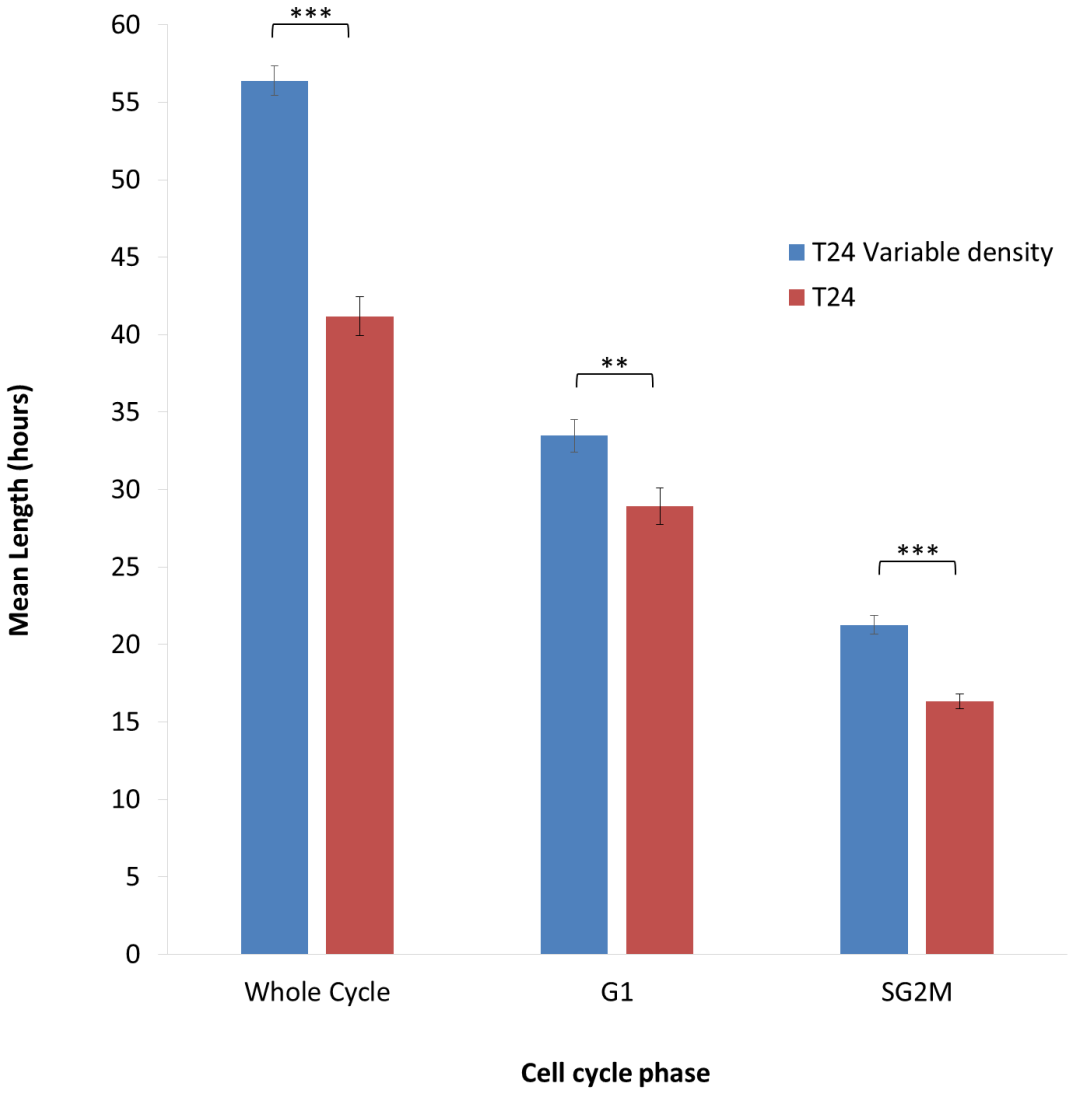

Figure 3.2 Graph comparing cell cycle and phase length mean averages for the T24 variable density dataset (blue) and the T24 single density dataset (red). Error bars represent standard error of the mean. Significant differences according to a two-tailed Welch's t-test are bracketed (*p<0.05, **<p<0.01, ***p<0.001).

For the variable density T24 data the mean cell cycle length is 56.4 hours. This is more than fifteen hours longer than the mean of 41.19 that was generated from the fixed density T24 experiment. However, there are three *a priori* reasons why this difference is not surprising.

- Firstly, the time-lapse is 120 hours rather than 72 hours, which allows cell cycle lengths of between 72 and 120 hours to be included in the analysis that would have been cut off of the distribution of the 72-hour time-lapse.
- Secondly a shorter time-lapse will be enriched for shorter cell cycle length values regardless of how many hours long it is. This is because as time runs out at the end, only shorter and shorter complete cycles can fit in before the end to be included in the analysis. For example, 40 hours before the end of the time-lapse cell cycles lengths of

40 hours or less will be included, whereas 20 hours before the end of the time-lapse only lengths of 20 hours or less will be included.

- Thirdly the frame length for the variable density experiment is 65 minutes instead of 40 minutes. As all phase lengths have to round up to an integer value of frames this will result in a slight increase in length estimates up to a maximum of 25 minutes.

Both of the first two reasons will have a greater effect the larger the measured phase length is relative to the length of the time-lapse. Looking again at **Figure 3.2** it can be seen that the difference in cell cycle length between the variable density and fixed density datasets is greater than the difference between the G1 lengths or the SG2M lengths, exactly as would be predicted.

In the case of comparing the T24 72-hour time-lapse data and the T24 variable density 120-hour time-lapse data it is easy to demonstrate the first two effects.

3.4.2.1 Accounting for the effects of the longer time-lapse on cell cycle length measurements

In the T24 variable density dataset there are 61 of the 295 cell cycle lengths (20.7%) that have a value of over 72 hours. If they are removed from the analysis then the mean cell cycle length falls from 56.4 hours to 50.3 hours.

In addition to this all data-points that finish after 72 hours into the time-lapse can be removed (e.g. a 40 hour cell cycle length where the first division was at 50 hours and the second at 90 hours would be excluded). This excludes a further 121 data-points (52% of what's left). In effect the time-lapse frames past 72 hours have been completely ignored. The mean cell cycle length then falls to 45.8 hours. This is much more similar to the mean value for the T24 T-cycle experiment, which was 41.2 hours. Even this smaller difference of 4.6 hours needs accounting for.

The T24 variable density experiment was plated with cell densities that lie either side of the plating density for the T24 T-cycle experiment. If the hypothesis that the cell density is affecting cell cycle progression is correct, then the 4.6 hour difference in mean cell cycle lengths could be due to the cells being on average denser or more dilute at the time of imaging. 7 wells were plated at a higher densities than in the T-cycles and 11 were plated at lower densities. By splitting the data into these two groups the averages for the higher and lower densities becomes 48.1 and 45.6 hours respectively. Therefore, although the higher density cells have a 2.5 hour longer cell cycle length on average than the lower density cells, both of these values are higher than the 41.2 hour average cell cycle length seen in the T24 T-cycle experiment. This suggests that some other variable than density is to blame for the difference in averages. It seems likely that this variable is one of those listed previously, i.e. cell plating variations, uneven deposition of cells, differential growth, or plate surface variability.

This analysis can be repeated for the G1 and SG2M length data.

For G1 lengths the mean for the 120-hour variable density experiment is higher than for the T24 T-cycle experiment (33.5 hours vs 28.9 hours), a difference that becomes less pronounced once the time-lapse is artificially shortened to match the 72hour T24 dataset as described above (25.4 hours vs 28.9 hours). Once the remaining data is split into those wells that were plated at higher density than the T24 T-cycle and those that were plated at lower density, the effect of density appears even greater than for the whole cycle, with a 9.5 hour difference between the dense and dilute G1 average lengths. Unlike for the cell cycle lengths as a whole, the high and low density G1 lengths lie either side of the average G1 length in the T24 T-cycle experiment, meaning that the T24 T-cycle experiment and the T24 variable density experiment are consistent with each other.

For SG2M lengths the mean for the 120-hour variable density experiment is higher than for the T24 T-cycle experiment (21.3 hours vs 16.3 hours), a difference that becomes less pronounced once the time-lapse is artificially shortened to match as described above (19.0 hours vs 16.3 hours). Once the remaining data is split into those wells that were plated at higher density than the T24 T-cycle and those that were plated at lower density the effect of density appears even greater than for the whole cycle, with a 6.3 hour difference between the dense and dilute SG2M average lengths. Unlike for the cell cycle lengths as a whole, the high and low density SG2M lengths lie either side of the average SG2M length in the T24 T-cycle experiment, meaning that the T24 T-cycle experiment and the T24 variable density experiment are consistent with each other.

All this summarised in a **Figure 3.3**. Here it can be seen that if the variable density data is split into wells that were plated more densely or less densely than the fixed density data then the G1 lengths and SG2M lengths lie either side of the fixed density length. This is what would be expected if cell density is systematically affecting phase length. The equivalent data for the whole cell cycle does not show this pattern, with both the higher and lower density data having a larger mean cell cycle length than the fixed density data.

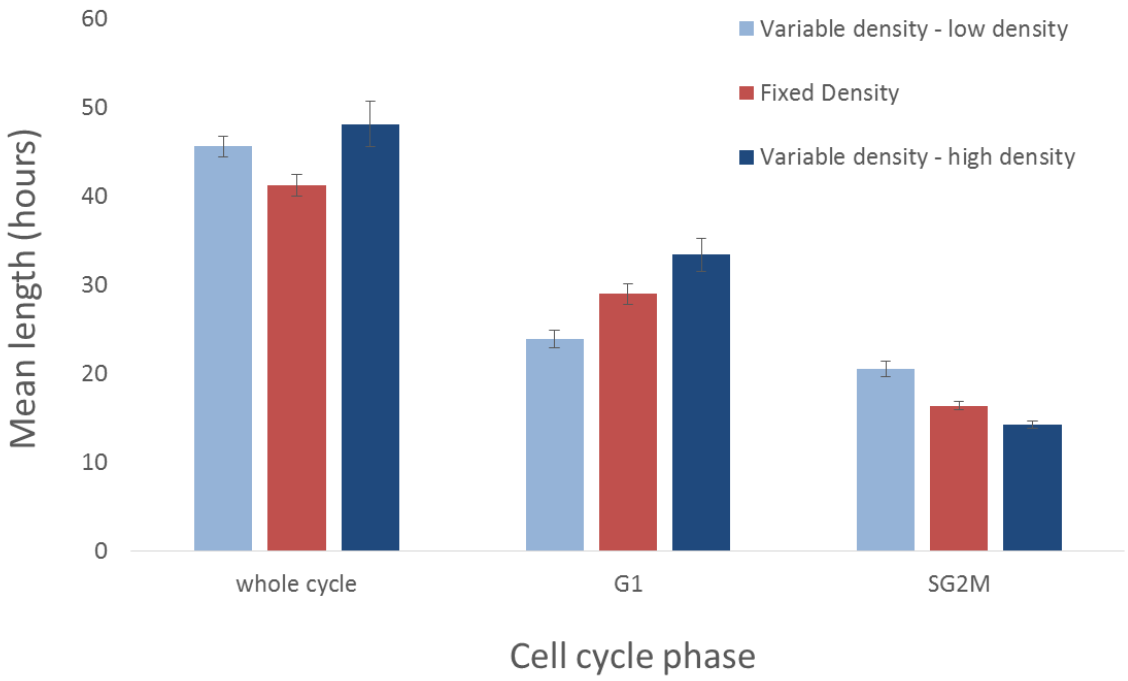

Figure 3.3 Graph comparing mean cell cycle and phase length data from the fixed density T24 experiment with the variable density T24 experiment. The T24 variable density dataset was artificially cut-off at 72 hours to be equivalent in length to the T24 fixed density dataset. This data was then split into wells that had been plated more densely than the fixed density experiment (dark blue) and wells that had been plated at lower density than the fixed density experiment (light blue). The fixed density data is shown in red. The means are plotted above. Error bars represent standard error of the mean.

3.4.2.2 Considering the full-length variable density dataset

Together this data suggested that cells plated at higher density have a longer cell G1 length, shorter SG2M length and a slightly longer overall cell cycle length. However, more can be done using this variable density T24 dataset than merely comparing it to the fixed density T24 dataset. From here the variable density T24 data will not be compared to the fixed density T24 data. Thus the entire 120-hour variable density dataset, can be used. This is summarised in **Figure 3.4**.

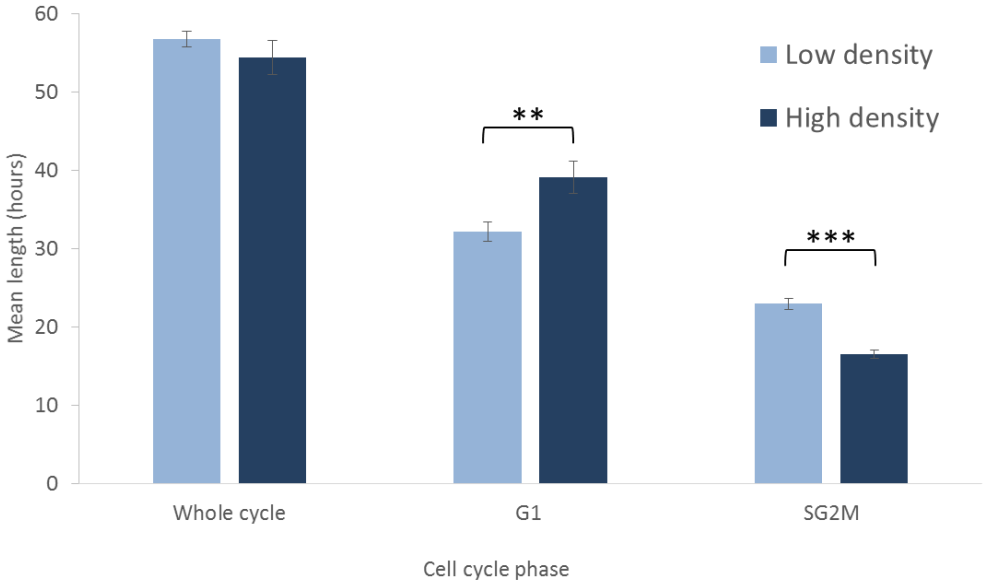

Figure 3.4 Graph comparing mean cell cycle and phase length data from the variable density experiment, split into dense and dilute plating. The T24 variable density dataset was used up to the full 120hours of the time-lapse. This data was then split into wells that had been plated at higher density than the fixed density experiment and wells that had been plated at lower density than the fixed density experiment. The means are plotted above. Error bars represent standard error of the mean. Significant differences according to a two-tailed Welch's t-test are bracketed (*p<0.05, **<p<0.01, ***p<0.001).

Comparing **Figure 3.3** and **Figure 3.4** three things become apparent:

1) The mean lengths for all measured values are higher if the entire 120-hour dataset is used rather than cutting it off at 72 hours. This is to be expected based on the reasoning given in the previous section.
2) The pattern for G1 and SG2M remains the same, with the low density condition giving shorter G1s and longer S2GMs and the high density condition giving longer G1s and shorter SG2Ms.
3) The pattern for the whole cycle lengths is reversed between the 72-hour and 120-hour subsets. In the 72-hour subset the high density condition gives slightly longer mean cell cycle lengths (48.10 vs 45.56 hours), while in the 120-hour subset the high density condition gives shorter mean cell cycle lengths (54.35 vs 56.71 hours). Although small, this difference highlights that the length of the time-lapse is an important consideration when comparing data and making assumptions about the true distribution of cell cycle and phase length values in a population.

3.4.2.3 T-tests comparing phase lengths between denser and less dense plated cells

A two-tailed Welch's t-test for unpaired samples with unequal variances was performed on the 120-hour variable density T24 data, comparing cell cycle and phase lengths between the dense and dilute conditions. The result was a highly significant difference in SG2M lengths ($p<0.0001$),

a significant difference in G1 lengths ($p<0.01$), and a non-significant difference between whole cycle lengths ($p>0.5$). The results of these statistical tests can be found in the Appendix.

A Welch's t-test was used because the variances of the samples were unequal between the dense and dilute condition. This was particularly the case for the SG2M data.

3.4.2.4 Using a longer time-lapse does not affect the conclusions drawn in the previous chapter about the distributions of cell cycle and phase lengths

Figure 3.5 shows the distribution of cell cycle length and phase length values for the variable density T24 dataset. For this experiment the interval between time-points was 65 minutes instead of the 40 minutes used in the T-cycle experiments. This means that the smallest bin size that will fit a whole number of frame intervals in is 13 hours, 13/(65/60)= 12 frames. However, 13 hours is too long for a bin interval. A smaller bin sized could have been used, but this would have resulted in unequal numbers of length intervals falling into adjacent bins. Instead the data in this figure is given in terms of time-lapse frames, with the bins containing 6, 4, and two frame intervals for whole cycle length, G1 length, and SG2M length respectively. The use of frames instead of hours as a unit of time is appropriate in this context as distribution shape and relationship to entraining period are of primary interest in this figure.

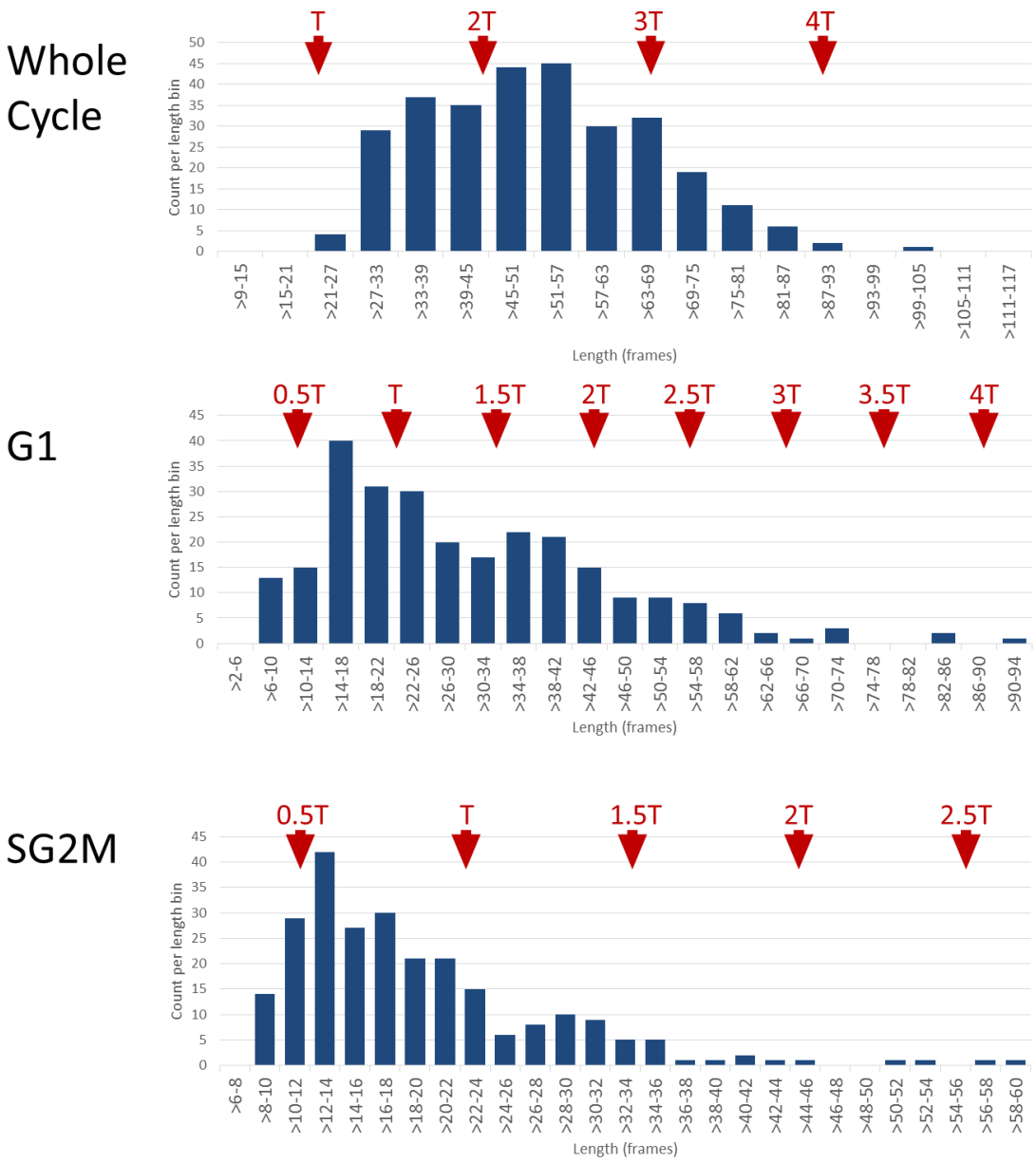

Figure 3.5 Distribution of cell cycle lengths, G1 lengths, and SG2M lengths for cells plated at variable density and entrained to a T24 light cycle. Phase length data was grouped into bins of 6, 4, and 2 frames for whole cycle, G1, and SG2M respectively and plotted. The y-axis shows total number of data values that fell into each bin. The red arrows denote where along the x-axis cell cycle lengths equalling to the entraining light cycle period (T) or equalling a multiple of the entraining light cycle period (T, 2T, 3T, and 4T) or half multiple (0.5T, 1.5T, 2.5T etc.) fall. Note that one frame is 65 minutes, or 1.083 hours.

It can be seen that the distribution for the whole cell cycle length shows a large range and does not appear to show a peak at the entraining period value of 24 hours or multiples of it.

The distributions for the G1 length data and SG2M length data show large ranges with some positive skew. In neither case does the distribution appear to show peaks at integer or half-

integer values of the entraining period, although the SG2M distribution does show some suggestion of a bimodal distribution, peaking at around 16 hours and 32 hours.

3.4.3 Considering the effect of cell density in more detail

So far these data have been looked at in a limited way. These data were split into 'dense' and 'dilute' plating only relative to the density of the fixed density T-cycle plating, which was chosen arbitrarily to begin with. In the T24 variable density experiment cells were plated at 17 distinct densities, which allows a more detailed analysis. For the following analysis the entire 120-hour variable density T24 dataset was used.

3.4.3.1 Consideration of the appropriate independent variable to use for this dataset

To set up the variable density T24 experiment the plating density of the cells was systematically varied. Thus the plating density of the cells has been used above as the independent variable for this data, with the cell cycle, G1, and SG2M lengths being the dependent variables. The question can be asked, however, as to what the variable of 'plating density' represents in terms of the question of this experiment. With this in mind it is reasonable to ask whether plating density is the most appropriate choice for the independent variable.

It is well known that achieving a homogeneous plating density of cells in culture is nearly impossible, with cells tending to cluster around either the centre or the edge of the well. As each well was imaged in multiple locations there could easily be significant differences in cell density between time-lapses taken from the same well. It would seem more appropriate to measure density at the time the time-lapses were actually taken, after the four-day entrainment period, and also specifically for each imaged location rather than for each well as a whole. Due to the fact that the fluorescent FUCCI-PAC2 cells were mixed with non-fluorescent PAC2 cells it is not possible to directly measure cell density using the time-lapse images, but if homogeneous mixing is assumed then the number of fluorescent cells in the starting frame of each time-lapse should closely approximate total cell density.

The question of to what extent plating density predicts measured density through counting of fluorescent cells can be addressed through linear regression analysis. **Figure 3.6** shows scatterplots relating three measures of cell density that can be produced using the variable density dataset. All imaged locations are used for this analysis, a total of 101 non-adjacent locations (16 wells of 6 sites, and 1 well of 5 sites).

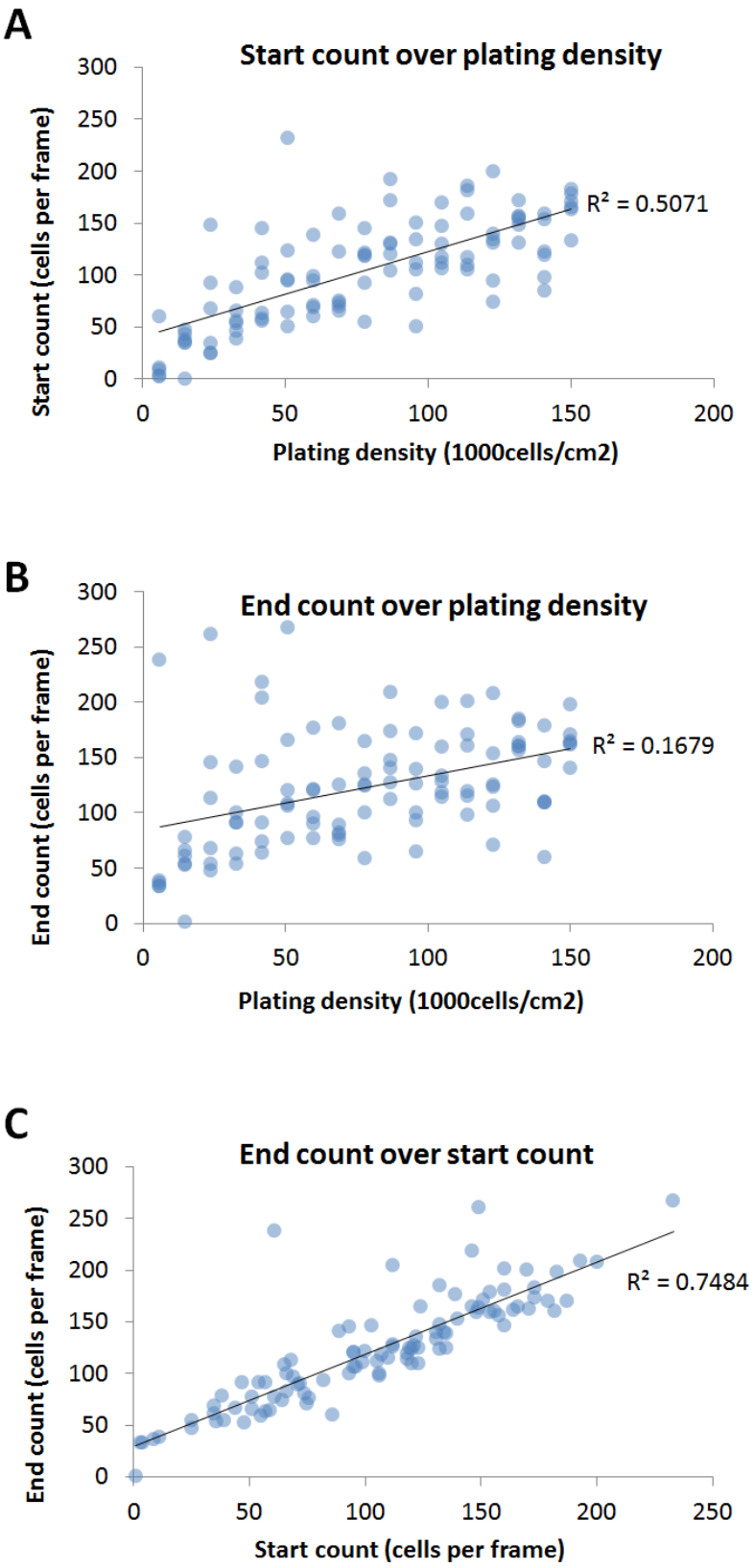

Figure 3.6 Regression graphs comparing plating density, measured starting density at the onset of imaging, and measured ending density at the offset of imaging. (A) Starting count plotted against plating density. (B) Ending count plotted against plating density. (C) Ending count plotted against starting count. Linear trendlines were added using Microsoft Excel and used to calculate R^2 values, which are shown at the top right of each graph.

Here “Plating Density” is the target cell density per cm^2 of culture area at the time of plating, based on using a haemocytometer to count samples of the PAC2 and PAC2-FUCCI cells before mixing and plating. “Starting Count” is the number of fluorescent cells counted in the first frame of the time-lapse at a given imaging location. “Ending Count” is the number of fluorescent cells counted in the last frame of the time-lapse at a given imaging location. There is a four-day delay between plating and starting count (while the cells were entrained with light), and a five-day delay between starting count and ending count (while the time-lapse imaging was performed).

The R^2 values for the coefficients of determination of these ordinary least squares (OLS) regression lines can be compared. Looking at **Figure 3.6A** it can be seen that if starting count is plotted over plating density then the linear regression R^2 value is 0.5071. Thus plating density and measured starting density of the time-lapse through counting fluorescent cells are not very well correlated.

This correlation is even weaker when ending count is plotted over plating density, **Figure 3.6B**, with a R^2 value of 0.1679. This suggests that over time the ability to predict current cell density from starting cell density falls.

It can also be seen from **Figure 3.6C** that the R^2 coefficient between starting count and ending count is 0.7484, which is much higher than the 0.5071 between plating density and starting count. The delay in time between plating density and starting count is only four days, whereas the delay in time between starting count and ending count is five days. Therefore the fact that the correlation is higher between starting count and ending count than between plating density and starting count suggests that the passing of time is not the only reason why these measurements of cell density diverge over time. This supports the idea that plating was not homogeneous, either in density, in cell mixing, or both.

The above regression analysis is certainly not conclusive as to which measure of cell density would be most appropriate to use as the independent variable for analysing the effect of cell density on cell cycle phase lengths. Arguments could be made for using plating density, or starting count, or ending count, or an average of starting or ending count. Meaningful conclusions cannot be drawn without confidence in the independent variable data values. Thus in the next section the data for cell cycle length, G1 length, and SG2M length will be considered from the point of view of using multiple of these estimates of the independent variable ‘cell density’.

There is one further independent variable that could be considered: cell proliferation rate. Although the experimental protocol was not designed with proliferation rate in mind, it would be expected that there would be some relationship between cell density and cell proliferation and between proliferation rate and cell cycle dynamics. As such it is worth considering here.

A proliferation index can be calculated simply by taking a ratio of the ending count to the starting count. A site with 50 cells at the start and 100 at the end would therefore have a proliferation index of 100/50 = 2.

Figure 3.7 shows a graph of proliferation index over plating density. From this graph several things can be seen:

- The lower the plating density is the higher the proliferation rate is. This is not unexpected as contact inhibition generally inhibits cell proliferation.
- The vast majority of the values for the proliferation index lie between 1 and 2, meaning that the number of fluorescent cells less than doubled over the 5-day time-lapse.
- All of the proliferation indices above 3 were found in the well with the very lowest plating cell density.
- A power law trend-line has an associated R^2 value of 0.6699, which suggests that plating density predicts the proliferation rate between 4 and 9 days better than it predicts starting count (R^2=0.5071). Note that if a power law trend-line is fitted to the scatterplot of starting count over plating density the R^2 value is 0.5983, so this difference is only partially due to the use of a power trend line instead of a linear trend line. Details of R^2 values for different variables and trendlines can be found in the Appendix.
- The range of proliferation index values for the lowest plating density is much higher than the other plating densities. This is likely due to the fact that the total starting and ending counts for these sites are that much lower and so variability is relatively higher.

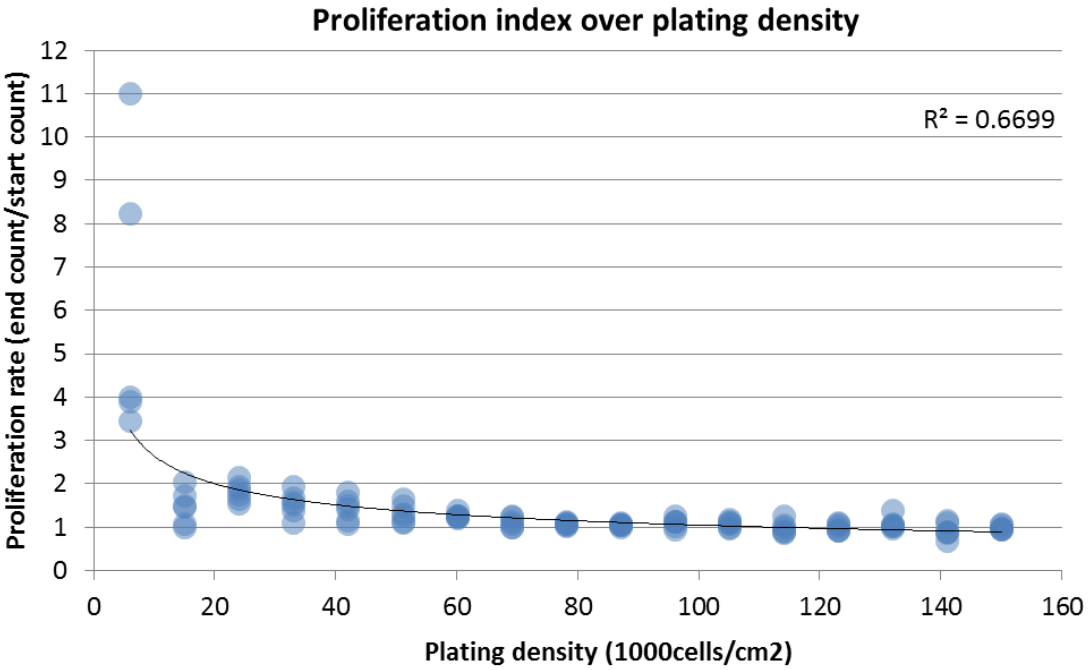

Figure 3.7 Regression graph plotting proliferation index over plating density for the T24 variable density time-lapse. A power trend line was added using Microsoft Excel and used to calculate the R^2 value, which is shown at the top right of the graph.

Based on the above analysis it seems that dividing ending count by starting count produces an index of proliferation that is more closely correlated to plating density that either start count or end count are alone (or indeed averaged, which produces a linear trend line R^2 value of 0.3344 and a power R^2 value of 0.409). It seems like that this is due to fluorescent cell counts not being representative of local cell density. In any case, the proliferation index will be considered alongside measures of density as a valid independent variable in the following sections.

3.4.3.2 What is the effect of varying cell density on the cell cycle lengths and phase lengths?

Figure 3.8 shows the cell cycle lengths, G1 lengths, and SG2M lengths plotted against the plating density, the starting count, and the proliferation index for that well. Together this forms a 3x3 grid of nine graphs. A linear trend-line has been added to each graph to indicate the broad trends of the data. However, it can be seen that the relationships are more complex than simple linear correlations.

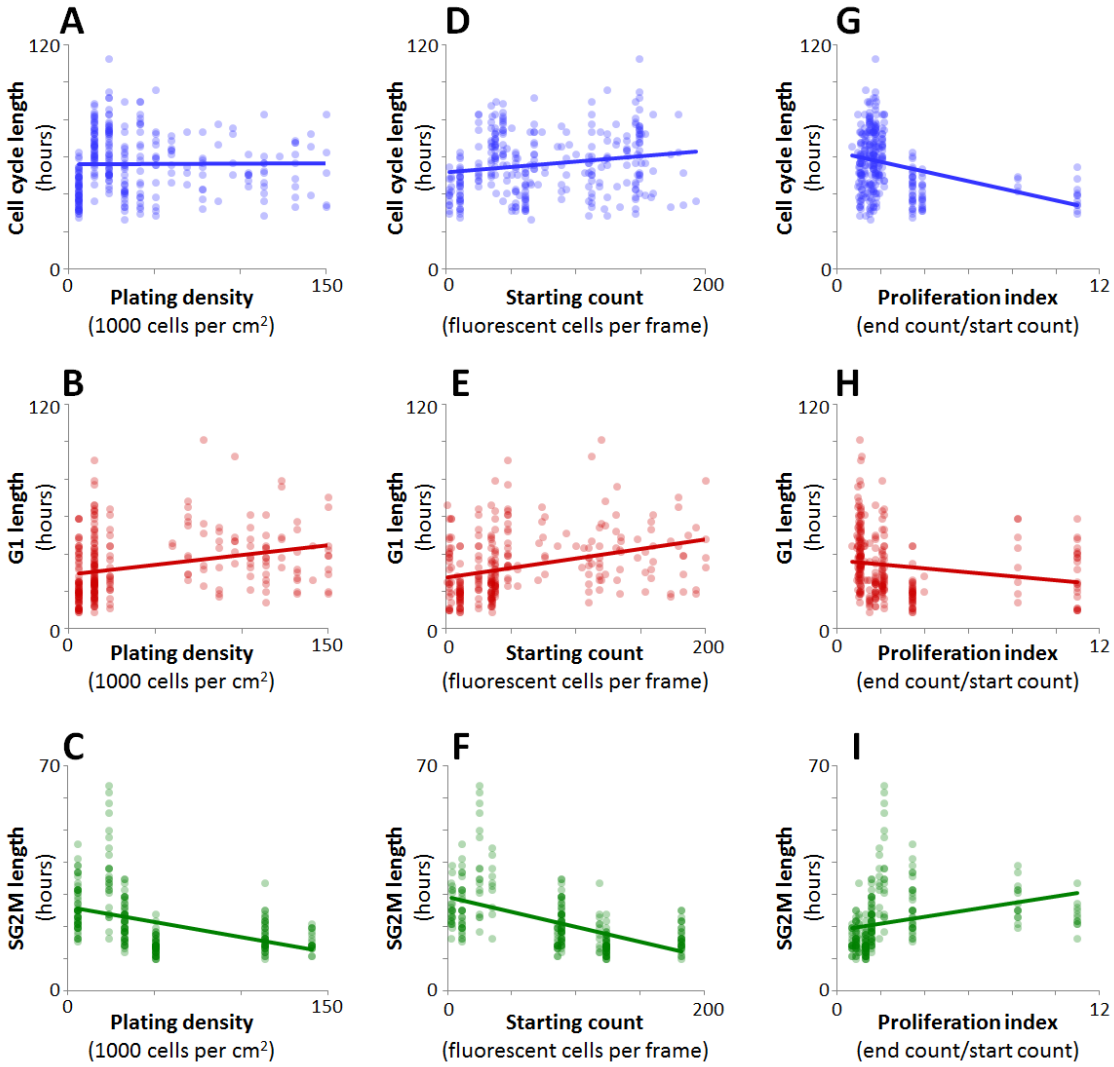

Figure 3.8 Graphs plotting cell cycle length, G1 length, and SG2M length values against three measures related to cell density. Each column displays length data plotted against a single independent variable and each row displays length data for a single class of cell cycle phase length measurement. Linear regression lines have been added to indicate broad trends.

Looking first at the cell cycle and phase length data plotted against plating density (the leftmost column) it can be seen that:

- Looking first at graph A, which plots cell cycle length over plating density, it can be seen that for most plating densities there is neither a trend for increased or decreased whole cell cycle length. However, at the lowest densities on the left there is a bump in the data, with the lower densities showing an increase in cell cycle length and the very lowest density well showing a decrease in cell cycle length. Thus the difference in mean cell cycle lengths between the cells plated at 6,000 cells.cm^{-2} and those plated at 15,000 cells.cm^{-2} is 25.24 hours. This could be due to some difference in behaviour between cells that are so dilute as to have no cell-cell contact vs cells that are just dense enough to form clusters.

- Moving on to graph B, the G1 length data again shows the shortest lengths at the lowest plating densities. The trend on the right hand side of the graph is less clear, but suggest perhaps a slight decrease in length with increasing plating density.
- On graph C the SG2M length data shows the longest lengths at the lowest densities. Again there is the suggestion of a bump in the data, with cells plated at 24,000 cells.cm^{-2} having a mean 10.55 hours higher than those plated at 6,000 cells.cm^{-2} and 15.05 hours higher than those plated at 33,000 cells.cm^{-2}.

These trends can now be compared to the graphs where lengths have been plotted against measured starting density (middle column):

- Graph D of cell cycle length plotted against starting count shows a similar bump in values towards the lower end of the density distribution to graph A. After this the trend is a weakly positive correlation, in contrast to the very weakly negative correlation when plotted against plating density on graph A.
- Graph E of G1 length plotted against starting count shows a similar weak positive correlation to graph D of G1 length plotted against plating density.
- Graph F of SG2M length plotted against starting count shows a similar pattern to SG2M length plotted against plating density on graph C, with lower densities having higher lengths and with a bump in the data at low densities.

Finally the graphs plotting lengths against proliferation index (righthand column) can be considered:

- Graph G of cell cycle length plotted against proliferation index shows that the sites with the lowest proliferation indices tend to have longer cell cycles relative to the sites with high proliferation indices.
- Graph H of G1 length plotted against proliferation index shows that the sites with the very lowest proliferation indices tend to have longer G1 lengths.
- Graph I of SG2M length plotted against proliferation index shows that the sites with the lowest proliferation indices tend to have shorter SG2M lengths.

All three datasets suggest that the greatest differences are between the least densely plated cells and the rest. The broad trend seems to be that as cells become denser G1 lengthens and SG2M shortens, with peak cell cycle length at an intermediate density (hence the bumps on the left side of the distributions).

Regarding proliferation index, the most highly proliferative cells have shorter G1 phases, longer SG2M phases, and shorter overall cell cycle lengths.

3.4.4 Cell density affects cell cycle rhythm periods

The variable density dataset can also be used to answer the question as to what happens to the population rhythms of cell cycle progression as the cell density changes.

In **Figure 3.9** the G1-S and M transition data for the T24 variable density time-lapse is shown again, the same set of data as **Figure 3.1**. Here though the data has been split. On the top row

the data has been split into the 54 highest density sites and the 47 lowest density sites (these numbers are not equal because there were six sites for each plating density and so they could not be split down the middle). On the middle row the data has been split into the 51 sites with the highest starting count and the 50 sites with the lowest starting count. On the bottom row the data has been split in the 51 sites with the lowest proliferation index and the 50 sites with the highest proliferation index.

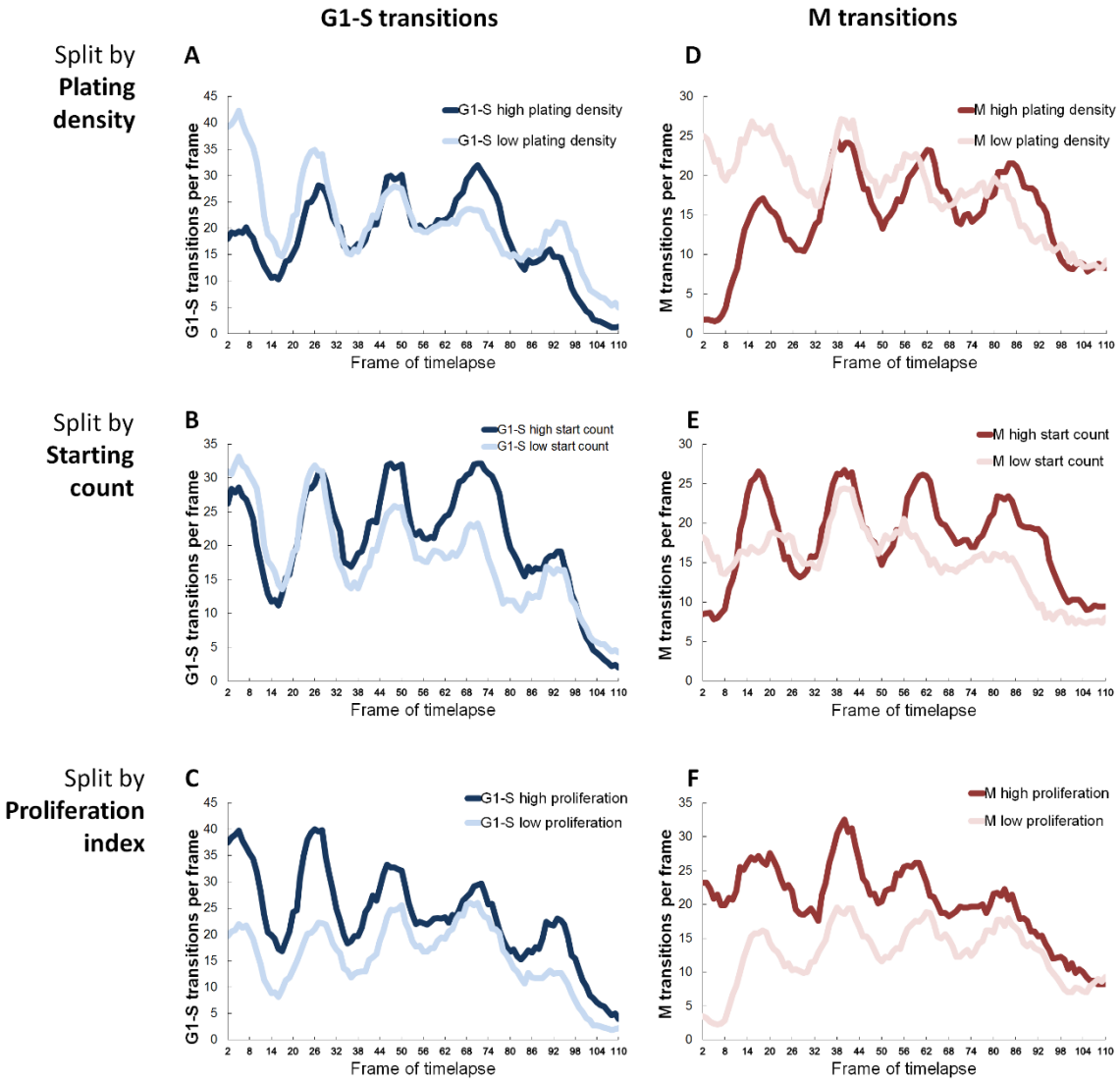

Figure 3.9 FUCCI cell cycle phase transition data from cells maintained at variable density under a 24-hour entraining light stimulus. The data has then been split into high or low plating density (top row), start count (middle row), or proliferation index (bottom row). X-axes show the frame of the time-lapse at 65-minute intervals and Y-axes show the count of transitions per frame. G1-S transitions are shown in blue, M transitions are shown in red. All data were subject to a 7-point moving averaging before plotting. G1-S high plating density n=1971, G1-S low plating density n=2301, G1-S high start count n=2276, G1-S low start count n=1996, G1-S high proliferation index n=2566, G1-S low proliferation index n=1706, M high plating density n=1612, M low plating density n=2010, M high start count n=1960, M low start count n=1662, M high proliferation index n=2234, M low proliferation index n=1388.

Looking first at the three graphs, A, B, and C, of G1-S transitions on the left hand side of **Figure 3.9** it can be seen that splitting the data does appear to have some small effects on the amplitude of the oscillations. This is particularly the case for the plating density graph A, where the low plating density trace starts out with higher amplitude oscillations than the high plating density trace, and gradually falls to having a lower amplitude.

The M transition graphs on the right, D, E, and F, appear more interesting. Starting with graph D where M transitions are split by plating density several things can be seen. First, the amplitude of the low plating density trace is much smaller, particularly in the second half of the time-lapse. Second, the period of the oscillations appears to be slightly different, with the low plating density having a shorter period than the high plating density. This can be seen in the fact that the first two peaks are quite closely aligned while the last two are not.

Moving to graph E, split by starting count, a very similar pattern is seen, with lower amplitude oscillations in the case of the low starting count trace and oscillation peaks that do not align.

Finally graph F is split by proliferation index and shows the reverse pattern for amplitude, with high proliferation having a lower amplitude than low proliferation. This is consistent with graphs D and E above it if one expects low cell density to correlate with a high rate of proliferation. The two traces appear to have similar periods, however, without the noticeable difference shown in the two graphs above.

The question of whether splitting the data according to plating density, starting density, or proliferation rate, results in altered periods can be assessed rigorously by using BioDare2 to generate periodicity estimates for each trace. This is summarised in **Table 3.2**. The BioDare2 estimated period results for the whole dataset are shown as well as the results of the data split according to high and low plating density, high and low starting count, and high and low proliferation index. Next to the estimated period results are the results shown as a percentage change relative to the whole dataset. These have been coloured to show larger percentage increase in period in darker red and larger percentage decrease in darker blue. The grey boxes show where the analysis was unable to produce a reasonable period value based on the data.

			FFT NLLS		MESA	
Transition	Split by	High or low	Estimated period (hours)	Length relative to whole dataset (%)	Estimated period (hours)	Length relative to whole dataset (%)
G1-S	Whole dataset		24.08		23.34	
	Plating density	High	23.97	-0.46	23.46	0.51
		Low	24.07	-0.04	23.40	0.26
	Starting count	High	24.28	0.83	23.52	0.77
		Low	23.91	-0.71	23.20	-0.60
	Proliferation index	High	23.95	-0.54	23.28	-0.26
		Low	23.95	-0.54	23.48	0.60
M	Whole dataset		25.19		23.64	
	Plating density	High	25.79	2.38	24.84	5.08
		Low	21.68	-13.93	22.20	-6.09
	Starting count	High	25.51	1.27	24.46	3.47
		Low	143.7*	*	21.52	-8.97
	Proliferation index	High	22.25	-11.67	22.32	-5.58
		Low	25.21	0.08	24.48	3.55

Table 3.2 Period estimates of cell cycle transition timing for PAC2-FUCCI cells entrained under a T24 light cycle, split according to three estimates of cell density. Total cell cycle transition data was arranged by plating density, starting count, or proliferation index and then split into high or low values for those variables. Split datasets were analysed using BioDare2 periodicity analysis FFT NLLS and MESA and the results are shown above. Cells are colour-coded, darker red for longer periods than the reference, darker blue for shorter periods than the reference. *The FFT NLLS periodicity analysis was unable to produce a period estimate in this case.

Looking at the table there are several features of note. It can be seen that splitting the data does not make much difference to the period estimates for the G1-S rhythms. The largest percentage change is +0.83%, which corresponds to 0.2 hours, or 12 minutes.

The period estimates for the M rhythms, however, seem to be much more greatly affected by splitting the data. The largest change here is -13.93%, which corresponds to 3.51 hours.

Starting with plating density it can be seen that the high plating density half of the data gives a longer period than the whole dataset while the low plating density half of the data gives a shorter period than the whole dataset. The difference between the two halves of the dataset for the FFT-NLLS analysis is 4.11 hours and for the MESA analysis it is 2.64 hours.

For starting count the FFT-NLLS analysis was unable to produce a reasonable period estimate for the low starting count half, but the high starting count half is higher than the whole data value. For the MESA analysis the data shows the same pattern as for plating density, with high starting count giving a longer period and low starting count giving a shorter period. The difference is 2.94 hours.

For proliferation index the pattern is reversed, with the high proliferation half giving a lower period estimate and the low proliferation half giving a higher period estimate, as one would expect high proliferation rate to be correlated with low cell density. The period length estimate differences for high vs low proliferation rate are 2.96 hours and 2.16 hours for FFT-NLLS and MESA respectively.

Put together this periodicity analysis supports the visual interpretation of **Figure 3.9** that the period of M transition rhythms appears to be dependent on some function of density and/or proliferation rate, with denser, less proliferative cells having a longer period.

3.4.5 Cell density/proliferation rate affects clock to cell cycle coupling

Above it was demonstrated that splitting the cell cycle transition timing data into high or low plating density, starting count, and proliferation index suggests that density and/or proliferation rate affects clock to cell cycle coupling – particularly in the amplitude and period of M transitions.

When analysing the cell cycle and phase length data earlier it was found that, once the data was plotted on scatter plots against the cell density/proliferation rate, the greatest differences were found between the very most dilute (or highest proliferating) cells and the rest of the dataset. It seems possible therefore, if not likely, that the same would be true of the phase transition timing data. One way of examining this would be to split the data into smaller bins such as deciles. However, the fewer data-points there are in each bin the harder it would be to see the patterns through the noise, and as was seen for the FFT-NLLS analysis for the low starting count M data in **Table 3.1**, the BioDare periodicity analysis already struggles with the data merely split into two.

Instead in **Figure 3.10** the data in is displayed in the same layout as **Figure 3.8**, as six heat-maps that show visually the entire dataset. Each horizontal line of pixels represents a single location in the time-lapse experiment, ranked according to plating density, starting count, or proliferation index for both G1-S transitions (left) and M transitions (right). There are 101 locations in total so each heat-map is 101 pixels high. Each time-lapse has 110 time-points so each heat-map is 110 pixels wide. In effect then the x-axis of the heat-map shows time while the y axis shows either plating density, starting count, or proliferation index.

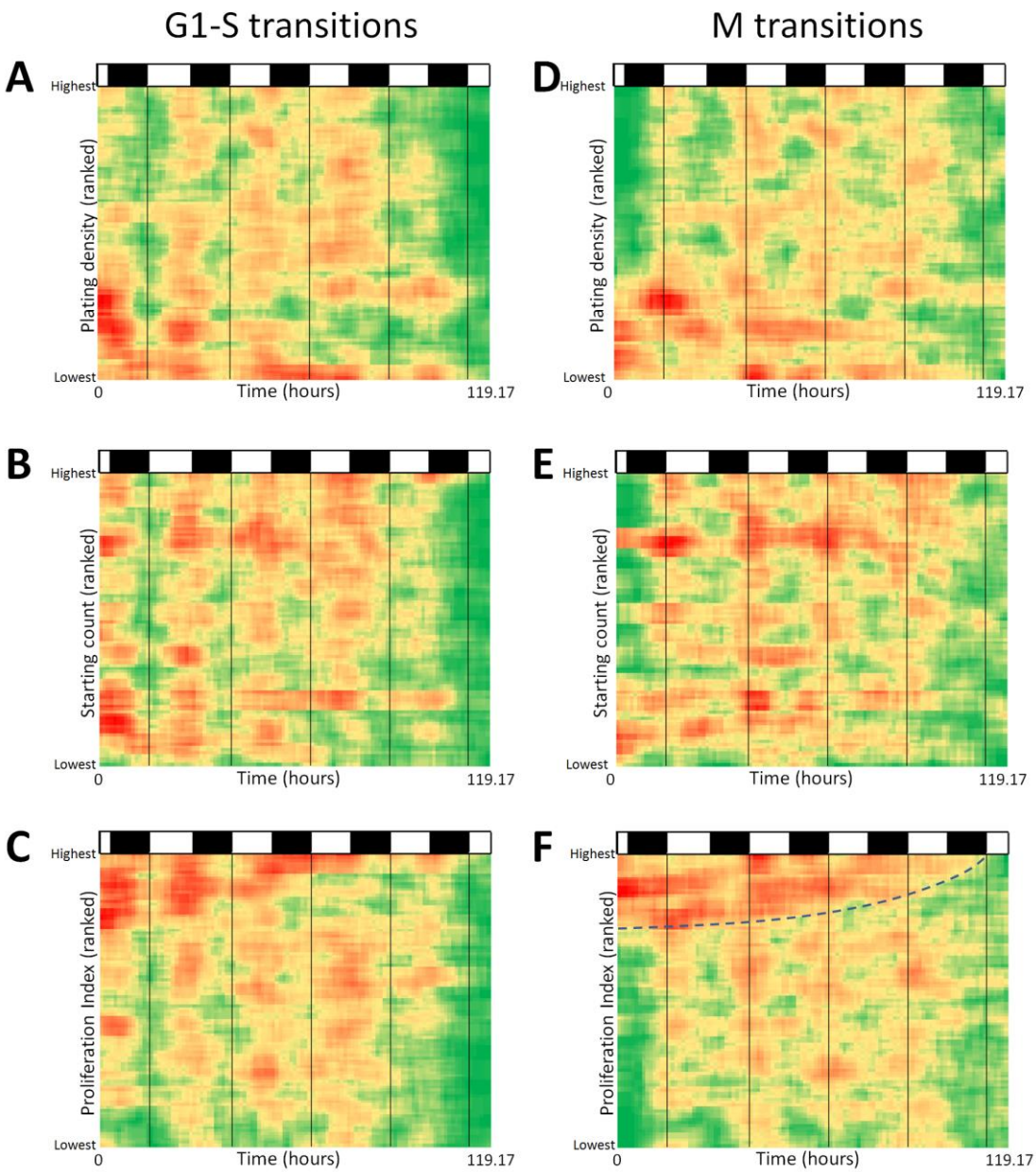

Figure 3.10 Heat maps displaying cell cycle progression timing for PAC2-FUCCI cells entrained under a T24 light cycle and then imaged for five days. Each row of the heat-maps represents the count data for a single imaged location of the time-lapse (101 in total) these were then ranked according to plating density, starting count, or proliferation rate, with the highest value at the top. A five-point moving mean was then applied in the x and y axes, and the data values were substituted for a standard colour intensity gradient, with red indicating a higher value of count values and green indicating a lower value. Black and white boxes represent the entraining light cycle. The dotted line in (F) has been added to mark the boundary of a putative 'arrhythmic zone'.

The data matrix for each heat-map was then subject to a 5-point moving mean in both the x and y axis to smoothen the data. Finally the data values were substituted for a standard colour

intensity gradient, with red indicating a higher value of count values and green indicating a lower value. The black and white striped bars at the top of each heat-map represent the entraining light cycle.

Looking first at the G1-S heat-maps on the left (A, B, and C) it can be seen that there five vertical bands of redder colour in each one. These correspond to the five peaks seen in **Figure 3.1**. In each case the final vertical band is weaker than the others, which likely represents the general drop in cells entering S-phase after nine days in culture. This could be due general increase in cell density reducing proliferation, or exhaustion of cell culture medium, or some cumulative effect of five days of fluorescent imaging inside the plate-reader.

The heat-map of G1-S transitions ranked by plating density (A) appears to show a weaker banding pattern towards the bottom of the heat-map where plating density is lowest. This is also seen at the top of the proliferation index heat-map (C) where proliferation is highest. However, this effect seems rather small and could easily be due to the influence of only a small number of imaging sites at the extreme end of the distribution.

On the right the M-phase transition heat-maps (D, E, and F) also show a vertical banding pattern corresponding to the four peaks seen in **Figure 3.1.** However, it is much clearer that this banding breaks down at low plating densities (D), with the bottom quarter of the heat-map lacking a clear daily rhythm. This is also seen in the lower half of the starting count heat-map (E), and most clearly of all at the top of the proliferation heat-map (F). Here there appears to be quite a sharp dividing line between the rhythmic sites and the arrhythmic sites. The arrhythmic zone also appears to slant upwards as it moves along the time axis, which is exactly what one would expect if proliferation rate falls throughout the time-lapse.

By way of quick illustration of this arrhythmic zone, **Figure 3.11** once again displays line graphs for the G1-S and M phase transition data split by proliferation index. This time the split is uneven, with sites split between those with a proliferation index of less than or equal to 1.5 and those greater than 1.5. In effect this is splitting the top quarter of the heat-map from the bottom three quarters and recombining each into a line graph. Here it can be seen that the G1-S transition data is rhythmic in both the high and low proliferation condition. The M transition data, however, is rhythmic in the low proliferation data, but largely arrhythmic in the high.

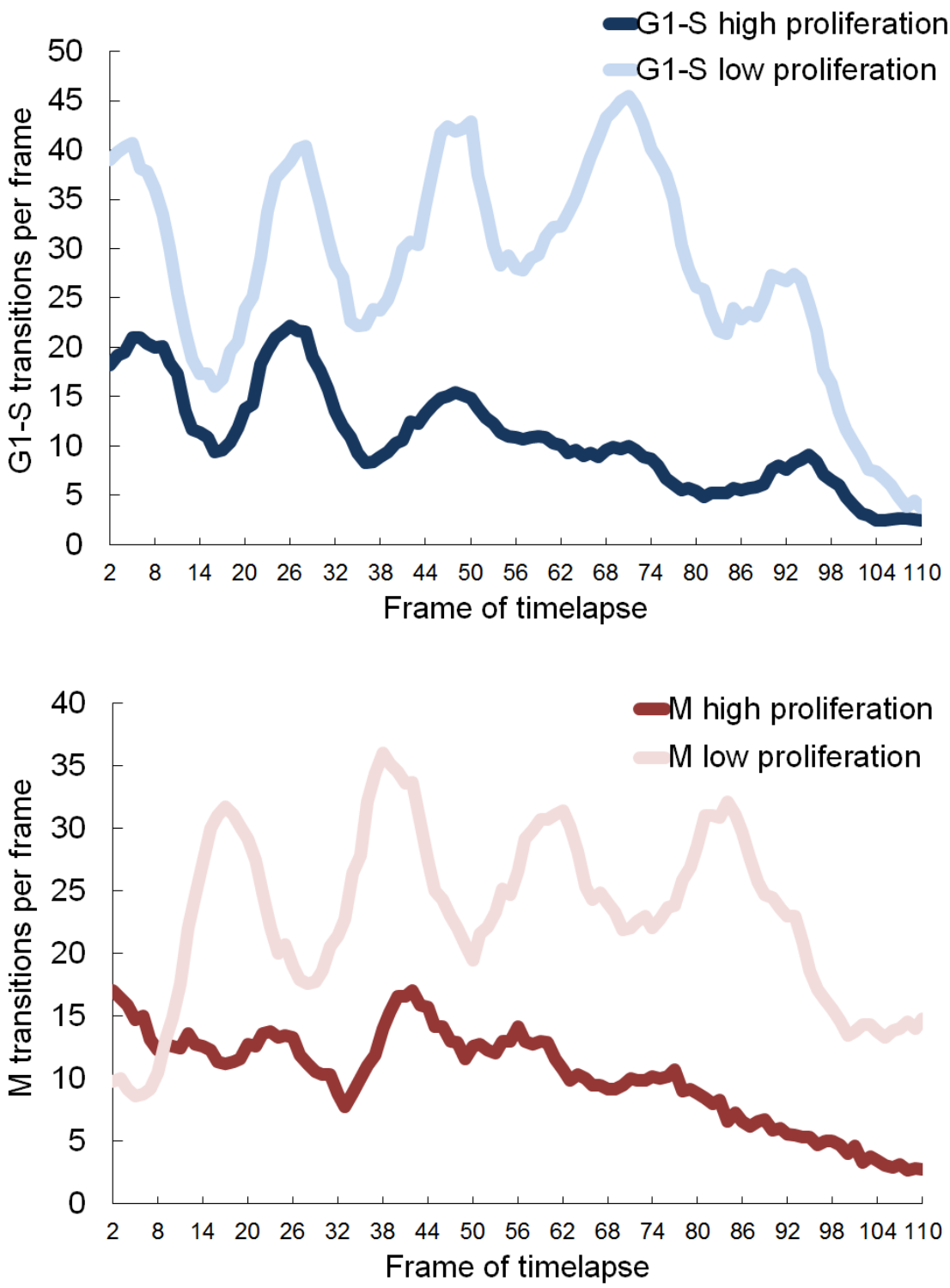

Figure 3.11 FUCCI cell cycle phase transition data from cells maintained at variable density under a 24-hour entraining light stimulus. The data has then been split into high (>1.5) or low (≤1.5) or proliferation index. X-axes show the frame of the time-lapse at 65-minute intervals and Y-axes show the count of transitions per frame. G1-S transitions are shown in blue, M transitions are shown in red. All data were subject to a 7-point moving averaging before plotting. G1-S high proliferation index n=1186, G1-S low proliferation index n=3086, M high proliferation index n=1112, M low proliferation index n=2510.

Considering period length, **Figure 3.9** and **Table 3.2** had previously suggested that G1-S period is unaffected by plating density, starting count, or proliferation index, but that M period is shorter at low plating density, low starting count, and high proliferation rate. What would that be expected to look like on **Figure 3.10**? The G1-1 vertical bands would be expected to be parallel to each other (although not necessarily exactly vertical), while the M vertical bands would be expected to diverge slightly, with a greater distance between them at the top of the plating density heat-map (D), the top of the starting count heat-map (E), and the bottom of the proliferation index heat-map (F). However, it is unclear whether that is the case.

Taken together, the data shown in above suggests that either cell density, proliferation rate, or both can affect the rhythms of cell cycle progression seen in these entrained cells. Cells that are highly proliferative and plated at lower density show smaller or absent oscillations in M-phase rhythms and appear to have a longer period of oscillation, while G1-S rhythms are largely unaffected. The implications of these results will be discussed in the next section.

3.5 Discussion

3.5.1 The aim of this chapter

The data presented in the previous chapter suggested that entraining circadian period length does not systematically affect cell cycle length, G1 length, or SG2M length. However there was a statistically significant difference found between the SG2M length in the T24 condition and the T18 condition, and between the SG2M length in the T24 condition and the T32 condition. In order to explain this it was hypothesised that variation in cell density between experiments could be a hidden variable affecting SG2M length. The experimental work in this chapter tested that hypothesis.

An experiment was therefore set up to test the hypothesis that deliberately varying the cell density in this experimental protocol could produce systematic variation in SG2M length at least as large as those seen in the T-cycle experiments. It was expected that cell cycle length and G1 length would also vary.

3.5.2 Splitting the data into high and low plating density revealed a large effect of density on cell cycle phase lengths

By splitting the variable-density data into high and low plating density there were clear effect of density on G1 and SGM2 lengths, with low density cells having shorter G1 lengths and longer SG2M lengths. These were found statistically significant according to a two-tailed Welch's t-test. These data confirmed that variations in cell density can explain the statistically significant differences in SG2M length seen between T-cycle conditions in the previous chapter.

The experimental question of this chapter had therefore been answered. However, further investigation of the data was performed to examine the effect of cell density in more detail.

3.5.3 Comparing the T24 variable-density dataset to the T24 fixed-density dataset from the previous chapter

The population cell cycle phase transition graph showed that both G1-S and M transitions continued to oscillation even after five days under imaging (and nine days total in culture), although the amplitude was not as great as was seen for the T24 T-cycle data. This could have been due to use of variable densities of cells in this experiment or differences in entraining zeitgeber strength. As was expected the longer time-lapse produced greater estimates for the mean cell cycle and cell cycle phase lengths than the shorter time-lapse in previous chapter, and it was demonstrated that these could be separated from the effects of varying cell density. The distributions of length for the cell

3.5.4 Proliferation rate is more closely correlated with plating density than either the starting count or ending count of cells in the time-lapses

The data that was collected for the variable density experiment fell into 17 distinct plating densities, ranging from 150,000 cells.cm^{-2} down to 0 cells.cm^{-2}. Therefore this range was then considered in more detail than just splitting into high and low density.

The most appropriate measure of cell density was investigated, as there were several available from the data. In addition to those an index of proliferation rate was considered, based on ratios of counted cells at the start and end of the time-lapse movies. Proliferation index turned out to correlate better with plating density than either start count or end count alone. As it would have seemed negligent to ignore information on the proliferation of cells when considering cell cycle dynamics, the proliferation index was included in the subsequent analysis. For the most part the use of plating density or proliferation rate as independent variables produced results that were the inverse of each other. This supports the intuitive link between density and proliferation that one would expect in a cell line affected by contact inhibition.

3.5.5 Splitting the data further more finely by density revealed more nuance in the effect of density on cell cycle dynamics

The consideration of the measured proliferation rate of the varied plating densities showed that only the most dilute well of the 17 plated contained cells that were particularly highly proliferating, an observation that would not have made based on count data alone.

Plotting individual cell cycle and phase length data against plating density, starting count and proliferation index agreed with the assessment that higher densities were associated with shorter SG2M lengths and longer G1s. The effect of density on the whole cell cycle length was less clear: a linear regression against plating density gave an almost horizontal linear best fit, while a linear regression against starting count showed a slight increase. It was clear though that high proliferation rate was associated with much shorter average cell cycle rates.

Overall the scatterplots convincingly supported a strong role for density and proliferation rate in the length and phase lengths of the cell cycle. The relationship appears to be non-linear. However, an experiment with more accurate measures of cell density and greater number of data would be required to further investigate these patterns.

3.5.6 Splitting the data further more finely by density revealed more nuance in the effect of density on the coupling between the circadian clock and cell cycle

The cell cycle phase transition data for the variable density dataset had been used to merely confirm that cell cycle progression entrainment had occurred. Now this data was looked at in more detail to examine whether cell density (or proliferation rate) was affecting this entrainment.

The surprising answer was that cell density and proliferation rate did affect the cell cycle progression rhythms. Not only did more dilute and more highly proliferative cells show lower amplitude oscillations in M transitions, but these oscillations showed shorter period lengths. Further investigations employing heat-map matrices revealed a zone of high proliferation where M transitions seemed effectively arrhythmic. These effects did not seem to occur for G1-S transitions to the same extent.

3.5.7 Future directions

3.5.7.1 Which of cell density and proliferation rate is affecting circadian clock to mitosis coupling?

In the discussion above plating density and proliferation rate have mostly been considered together as they showed significant correlation and appear to be largely two sides of the same coin in terms of the results presented. However it seems likely that proliferation rate is the variable that is key to explaining the results seen. It is an important question to answer though, particularly as the correlation between density and proliferation rate is cell-type specific and likely to also be very different outside a static 2-dimentional cell culture environment.

This could be investigated through manipulation of cell proliferation at matching densities, for example using varying serum concentrations(Feillet et al. 2014), or temperature(Yeom et al. 2010).

In addition scratch assays could be performed. Here a tool is used to scratch an artificial wound in a confluent monolayer of cells. In this scenario cells are still confluent on one side, but also proliferate quickly to fill the gap, thus having both high density and high proliferation.

3.5.7.2 Investigating the effects of density on G1-S and M transition entrainment

The fact that M transition rhythms are density-dependent while those of G1-S rhythms are not in the same cells is curious, but not totally unexpected. It suggests that these transitions are regulated separately. This separate regulation is also supported by the fact that if only one of these transitions was clock-regulated and the other passively followed it then the phase-delay between G1-S peaks and M peaks or M peaks and G1-S peaks would equal the average length of SG2M or G1 respectively, which does not happen in any condition presented here. This is also entirely consistent with previous work that showed that clock regulation of cell cycle transitions occurs via particular cell cycle regulators for G1-S and M.

This does have implications for research on circadian clock regulation of the cell cycle and circadian clock biology in general. In the variable density data presented here the lowest density most highly proliferative sites showed effectively no rhythm for M transitions. Thus had this been the only density that had been considered then the results and conclusions would have been quite different, namely that M transition timing is not clock-regulated in this cell line. Had

G1-S transitions not been considered alongside M transitions then it would have been concluded that the clock and cell cycle are not coupled in this cell line.

There is reason to believe that this is not merely speculation. Generally, cell density for *in vitro* experiments is chosen based on convenience. In the case of circadian studies dense cells are commonly used for population experiments while extremely dilute cells are used for single-cell experiments. Thus the contradiction between papers that report clock regulation of the cell cycle and those that don't could conceivably be due to the cell density they chose.

The results present here suggest disruption of clock regulation of M-phase timing at high proliferation rates. However, it could be the case that this high proliferation is in part due to a weaker influence of the clock-mediated cell cycle repression. Removal of the putative clock-regulated cell cycle inhibitor NONO produced higher rates of proliferation(Kowalska et al. 2013). RNA-mediated knockdown of p21, also a circadian inhibitor of cell cycle progression(Ogryzko et al. 1997; Gréchez-Cassiau et al. 2008), leads to an increase in proliferation rate.

If significant proportion of changes in proliferation rate are due to alteration in expression of cell cycle regulators with circadian influence then weakening or strengthening of the circadian influence may be a general mechanism for modulating proliferation rate. If this is the case then it would be expected that highly proliferative cells will show a lack of circadian timing of cell cycle progression across cell types and species.

The key question is to whether high proliferation is disrupting clock-to-cell cycle coupling or whether the loss of clock-mediated repression of cell cycle progression is contributing to the high proliferation.

3.5.7.3 When and how does the switch from arrhythmic to rhythmic mitosis occur? What causes it?

Based on the heat-maps presented in this chapter there appears to be quite a marked transition between arrhythmic and rhythmic M transitions at a critical proliferation rate. In fact as the data had to be subjected to a moving average to smoothen it before plotting it is possible that the transition is even more marked that appears.

To further investigate the nature of this transition more accurate methods for measuring local cell density would be required. Light-imaging could be used to more accurately determine the total number of fluorescent and non-fluorescent cells present. However, this risks phase-shifting the clock. Alternatively the number of cell cycle transition events relative to the number of cells could be used as a measure of proliferation rate that is independent of cell density. Alternatively density or proliferation rate could be measured by comparing the cell currently being assayed

with its neighbours and its distance to them, as is commonly used in automated single-cell analysis.

From there the zeitgeber strength could be varied. If a stronger zeitgeber reduces or eliminates the arrhythmic zone then this suggests that it is due to clock disruption. If it does not then this suggests that it is due to changes in the regulation of mitosis.

If the arrhythmic zone is confirmed then the next step would be to assay for clock-regulated M-transition regulators and see if expression levels or rhythms are density-dependent. *WEE1* would seem a likely candidate(Matsuo et al. 2003; Peyric et al. 2013), as would *NONO*(Kowalska et al. 2013). However, in PAC2 cells the expression of *WEE1* and *WEE2* wasn't found to be rhythmic(Tamai et al. 2012). It is quite possible that clock regulation of the cell cycle occurs via different regulators in a cell- and species-dependent manner.

3.5.7.4 How does density/proliferation rate affect the phase-angle between the clock and the cell cycle?

One unexpected finding of the results presented here is that the period of M transition peaks appears to differ between the dense and dilute sites, with lower density sites having shorter periods. Two explanations for the shorter period lengths of M transitions at low density could be:

Theory 1: Cell cycle progression disrupts entrainment of the circadian clock

The lower density cells, which show greater proliferation, are being repeatedly clock phase-advanced by their mitotic events, despite the entraining zeitgeber. This explanation is consistent with the clock phase-advance due to mitosis that is seen in NIH 3T3 mouse cells(Bieler et al. 2014), that were discussed in the previous chapter. It also offers an explanation of why the traces start in phase and appear to move out of phase over time – the zeitgeber strength is weaker during the imaging than during the entrainment. This could be due to lower light intensity or interference due to laser illumination during imaging. The effect of zeitgeber strength on these results would be simple to test through altering or removing the light intensity during imaging.

A prediction of this theory would be that, as mitotic events tend to phase-advance the circadian clock, the circadian clock of proliferating cells would be able to entrain to a fractionally shorter T-cycle than non-proliferating cells. Also the circadian clock of non-proliferating cells would be able to entrain to a fractionally longer T-cycle than proliferating cells. However, this effect could well be too weak to be seen with standard assays. A more direct approach would be to use markers for both the circadian clock and cell cycle and compare the cells under entrained and unentrained conditions.

This theory leaves unexplained why G1-S transitions do not show the same disruption, as the clock of those cells should also be phase-advanced by mitotic events.

Theory 2: The phase-angle between the circadian clock and mitosis changes with density

The phase-angle between the circadian clock and mitosis in entrained cells changes as cell density changes and the cells in the low density 'half' change in density over the time-lapse more than the cells in the high density 'half'. This change in phase-angle could be caused through change in expression of clock-regulated cell cycle proteins involved specifically in the mitotic checkpoint. This would be analogous to the differences in G1-S to clock phase-angle seen between zebrafish tissues expressing predominately p21 or p20(Laranjeiro et al. 2013). Both p21 and p20 show circadian expression, but at different phase-angles to the zeitgeber time. This theory could explain why the BioDare2 periodicity analysis consistently gave higher values for M period than G1-S period in both the T-cycles and variable density experiments. It would also explain why on the T18 traces in the previous chapter the G1-S peaks appear stable with respect to light and dark phase when the M peaks do not.

3.5.8 Summary of this chapter

The experimental work presented in this chapter clearly confirmed that cell density affects SG2M length in this zebrafish cell line and so answers the question posed in the aims. However, the data presented also raises further questions about the role of cell density and/or proliferation rate in the coupling of the circadian clock and cell cycle. Although only preliminary, the data presented suggests that cell density may strongly affect the regulation of cell cycle timing by the circadian clock and may explain why studies using cells *in vitro* report conflicting findings.

Chapter 4 – The effects of Autosomal Dominant Vitreoretinochoroidopathy (ADVIRC) disease mutations on BESTROPHIN-1 localisation in epithelial model cell lines

4.1 Introduction to the Bestrophinopathies, Bestrophin-1, and ADVIRC disease

For humans, sight is the primary sense for navigating the environment. The importance of vision to our mental construction of the world is reflected in the English language through the linguistic metaphors we use daily. A new idea 'in the light of day' can 'open our eyes', while ignorance can 'blind us to the truth' and 'leave us in the dark'. An intelligent child is 'bright', 'focussed', and a 'shining' example. A boring date is 'dull', and quite possibly 'dim'. An inspiring politician has a 'vision', and we can 'see' their point. But if we are 'short-sighted', lacking 'insight' or 'foresight' then we'll always be 'looking back', 'blindsided' by 'hindsight'. When angry we 'see red', when sad we 'feel blue', when a novice shows their lack of experience we say that they seem 'a bit green' – like an unripe banana they are not quite ready.

"To suppose that the eye with all its inimitable contrivances for adjusting the focus to different distances, for admitting different amounts of light, and for the correction of spherical and chromatic aberration, could have been formed by natural selection, seems, I freely confess, absurd in the highest degree." – Charles Darwin, On the Origin of Species (1859).

The quote above is often used to suggest that even Darwin considered the human eye too intricate and complex to have been formed by natural selection. If one reads the entire passage it is clear that Darwin chose the example of the eye as the most complex biological apparatus he was aware of, yet one which still must have formed through decent with modification. (One might well argue that the brain, or even just the visual centre of the brain, appears to show such high complexity and apparent 'design' that this example would have served Darwin better. Still, as of 2018 the human brain and the consciousness that arises from it are still so poorly understood that we are embarrassingly ignorant of quite how complex it is, and so we are not sure quite how astonished we should feel about its existence.)

The eye then is the standard example of physiological complexity, and the study of visual perception is of great interest in its own right. Unfortunately the eye is also prone to degeneration and disease, which cause visual impairment and blindness. Given the importance that the sense of sight has for human psychological wellbeing, perhaps equalled only by hearing, it is not surprising that there is great clinical interest in understanding the pathologies of the eye.

This introduction will discuss a cell type of particular importance to the healthy functioning of the visual retina: the retinal pigmented epithelium (RPE). First the RPE will be placed in context in the functioning of a healthy retina, then the role of RPE in retinal pathology will be discussed. From there a collection of diseases known as Bestrophinopathies that have been causally linked to variants in Bestrophin-1, a protein expressed in the RPE cells, will be introduced. What is

known about role of the Bestrophin-1 protein in RPE function and dysfunction will then be discussed, with reference to the cellular models used for this research. Recent conflicting research results relating to the cause of pathology in the case of the specific bestrophinopathy Autosomal Dominant Vitreochoroidopathy (ADVIRC) will then be introduced, and then the aims of this projected relating to those results will be given.

4.1.1 The Retinal Pigment Epithelium (RPE)

4.1.1.1 Development of the retina and RPE

The retina, including the RPE, forms from the diencephalon, the neuroepithelium of the posterior forebrain. Following neural induction the eye field is specified, is bisected, and evaginates to form the two optic vesicles. On contact with the overlying surface ectoderm each optic vesicle is patterned into regions that will give rise to the optic stalk, neuro-retina, and RPE. From there the vesicle invaginates to form the concave eye cup. The neural retina and presumptive RPE become apposed by this folding. The lens forms from invagination of the surface ectoderm. The sclera and cornea are also derived from the surface ectoderm. This process is shown in **Figure 4.1**, taken from Adler and Canto-Soler(Adler & Canto-Soler 2007).

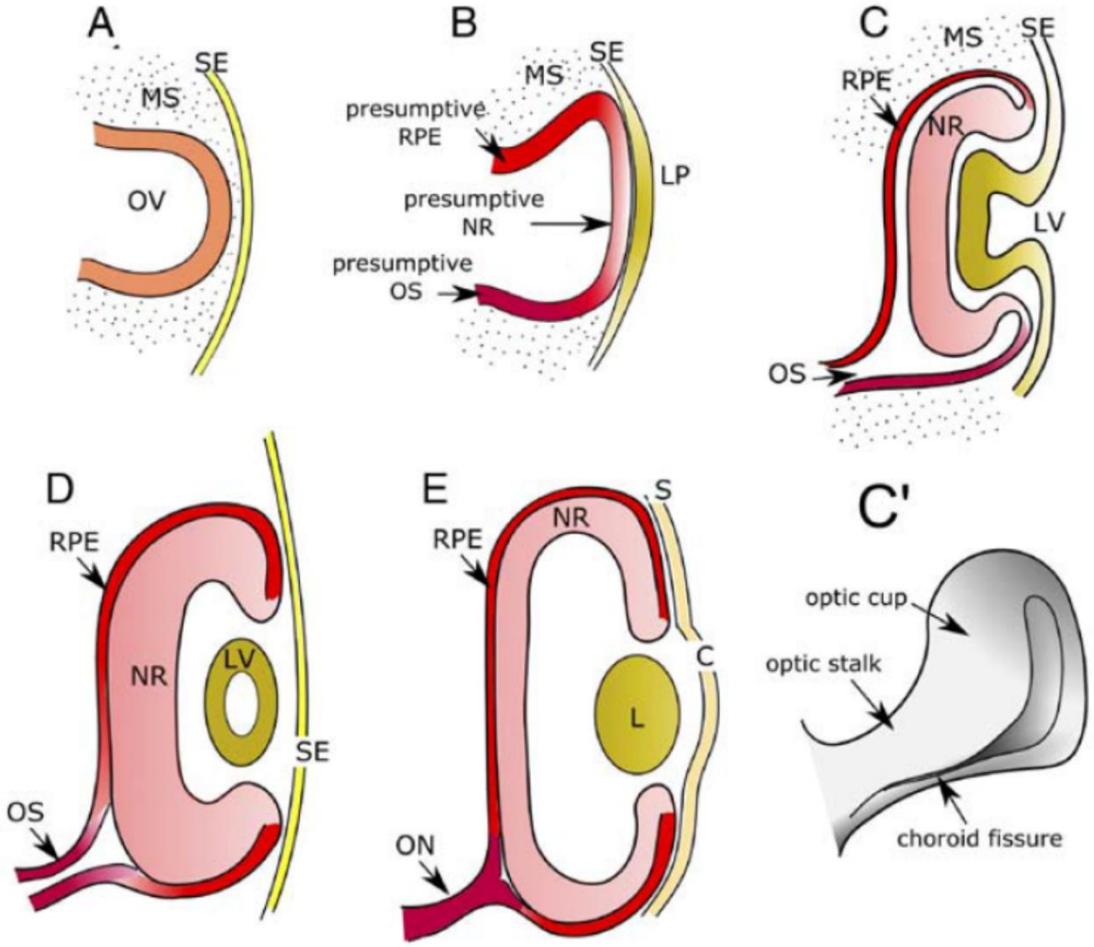

Figure 4.1 Development of the retina from the optic vesicle through folding of the neuro-epithelium. Taken from Adler & Canto-Soler, 2007. Abbreviations: C: Cornea, L: Lens, LP: Lens Placode, LV: Lens Vesicle, MS: Mesenchyme, NR: Neural Retina, ON: Optic Nerve, OS: Optic Stalk, OV: Optic Vesicle, RPE: Retinal Pigment Epithelium, S: Sclera, SE: Surface Ectoderm.

4.1.1.2 Anatomy of the retina

A cross-section diagram of the adult human retina can be seen in **Figure 4.2**, adapted from Yvon *et al.,* 2015(Yvon et al. 2015). Most apically (towards the front of the eye, the direction of incoming light) can be seen the ganglion cell layer, which transmits visual information across the surface of the retina to the optic disk. At the optic disk the nerve cells pass through the retina and project to the visual centre of the brain via the optic nerve. A small fraction of retinal ganglion cells have been found to express the photopigment melanopsin and to be photo-transductive, providing information on ambient illumination for circadian entrainment in the SCN via the retinohypothalamic tract(Berson et al. 2002) and influencing the pupillary reflex through projections to the olivary pretectal nucleus (Lucas et al. 2003)).

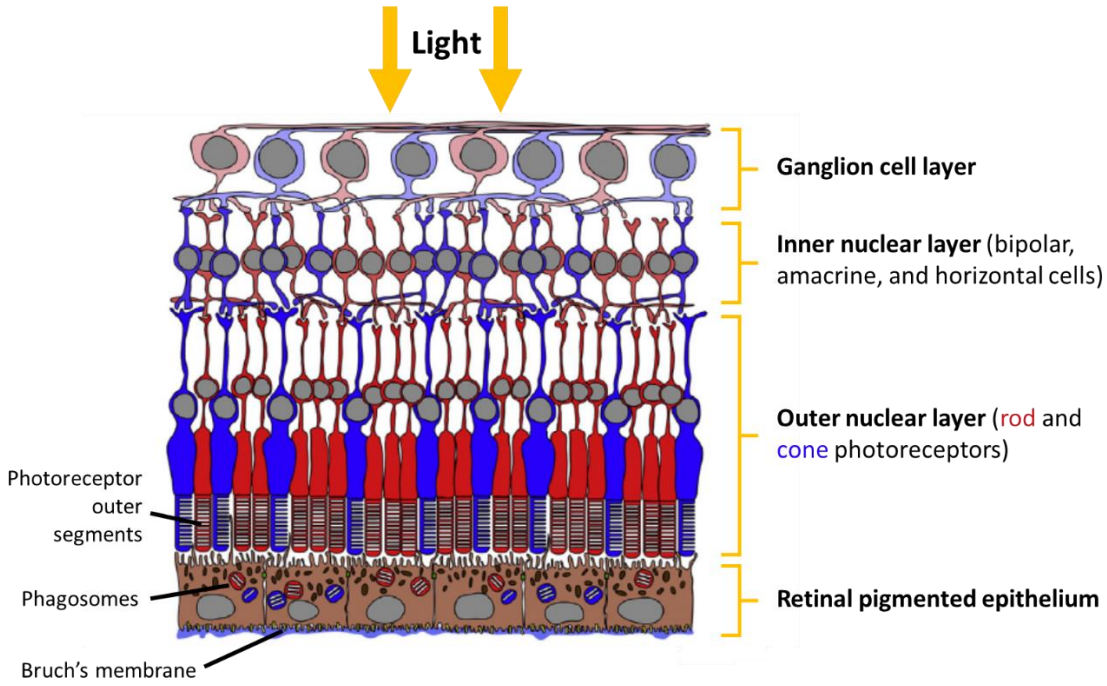

Figure 4.2 A diagram showing the layered structure of the retina, adapted from Yvon *et al.,* 2015. The retina is shown with the most apical cells at the top, towards the path of incoming light. Light passes through the ganglion cell layer and the inner cell layer and is detected in the photoreceptors of the outer nuclear layer. The retinal pigmented epithelium (RPE) lies basally to the photoreceptors

Basal to this is the inner nuclear layer that contains bipolar cells (which transmit information from the photoreceptors to the ganglion cells), amacrine cells (which are inhibitory neurons projecting to the bipolar and gangion cells), and horizontal cells (which integrate information from multiple photoreceptors and provide inhibitory feedback, allowing adaptation to ambient light levels and centre-surround inhibition which improve spatial frequency tuning)(Chaya et al. 2017).

Basal to this are the rod and cone photoreceptors that project to the bipolar cells. It is here that photo-transduction for image-forming vision takes place. Photoreceptors contain opsin photo-pigments that are based evolutionarily on G-protein coupled receptors. Within the opsin is the chromophore 11-*cis* retinal, which undergoes photo-isomerisation to all-*trans* retinal. This changes the conformation of the opsin and triggers a signal transduction cascade that results in cell hyperpolarisation. This system adapts to ambient light levels over many orders of magnitude: dark-adapted rod cells have been shown to be able to detect single photons of light(Rieke & Baylor 1998).

Below the photoreceptors is found the RPE monolayer. This layer is adhered basolaterally via integrin and fibronectin(Philp & Nachmias 1987) to an extracellular pentalaminar matrix structure known as Bruch's membrane(Booij et al. 2010). At the apico-lateral surface of the RPE

are tight, gap, and adherens junctions that keep the cells adhered and the layer impermeable, forming a blood-retinal barrier(Rizzolo 2007). Apical microvilli extend apically from the RPE around the outer segments of the photoreceptors(Anderson & Fisher 1979).

4.1.2 Functions and suggested functions of the RPE

The RPE monolayer has multiple important functions that maintain the health of the retina, particularly the photoreceptors, and thus in turn is vital to the maintenance of vision itself. Some functions, such as improving visual acuity, are hard to confirm experimentally. Others, particularly those related to ion and water balance, are likely inseparable. Here the known functions will be broken down into four broad areas: barrier function, phagocytosis of outer segments, light absorption, and contribution to the visual cycle.

4.1.2.1 The blood-retinal barrier

Much of the functional role of the RPE derives from the fact that it forms a relatively impermeable monolayer – the blood-retinal barrier. Histochemical studies in chick retinal tissues demonstrated that RPE express the tight junction proteins Zonula Occludens-1 (ZO-1), 7H6 antigen, and Occludin(Konari et al. 1995). This prevents the paracellular transport of fluid, ions and molecules between the cells(Rizzolo 2007). Patients with mutations in Claudin-19, a component of tight junctions, showed, among other pathologies, ocular defects and visual impairment(Konrad et al. 2006). Being an epithelial barrier means that the RPE is able to produce and maintain an electrochemical gradient across itself. The (Na^+/K^+-ATPase) ion pump and other ion channels maintain high Na^+ concentration at the apical side and high K^+ concentration at the basal side of the RPE. The high Na^+ concentration is important for the photoreceptor dark current that maintains the depolarised resting state of -40mV (reviewed by Gallemore *et al.*, 1997)(Gallemore et al. 1997). Bicarbonate transporters at the basal membrane prevent acidification of the sub-retinal space by photoreceptor CO_2 release(Adijanto et al. 2009).

The hexahelical membrane protein Aquaporin is expressed in human RPE cells and appears to contribute to water transport when expressed in the epithelial model cell line Human Embryonic kidney cells 293 (HEK293)(Stamer et al. 2003). This supports the hypothesis that the RPE functions in maintaining fluid balance and intraocular pressure and preventing retinal detachment. This role in fluid balance has also been hypothesised to be involved in eye growth during development, as reviewed by Rymer and Wildsoet, 2005(Rymer & Wildsoet 2005).

Being a relatively impermeable polarised monolayer, RPE can secrete growth factors and other signalling molecules apically or basally. It maintains the choriocapillaris (CC) layer of blood vessels through the secretion of Vascular Endothelial Growth Factor (VEGF) basolaterally, while preventing endothelial growth into the retina itself(Blaauwgeers et al. 1999). To actively maintain glucose levels in the retina, RPE express several glucose transporters(Takata 1996; Ban

& Rizzolo 2000). To remove lactate produced in the retina RPE express monocarboxylate transporter (MCT1) apically and MCT3 basally, a process coupled to the transport of H^+ and H_2O(Hamann et al. 2003).

RPE also secrete Pigment Epithelium-Derived Factor (PEDF) apically, which inhibits angiogenesis(Dawson 1999) and is neuroprotective for those photoreceptive cells of the retina that show expression of PEDF receptor proteins(Aymerich et al. 2001). PEDF also induces Neuroprotectin D1 (NPD1) synthesis, which is secreted apically(Mukherjee et al. 2007). Other growth factors secreted by RPE include fibroblast growth factors (FGF1, 2, and 5), transforming growth factor-β (TGF- β), insulin-like growth factor-1 (IGF-1), lens epithelium-derived growth factor (LEDGF), and ciliary neurotrophic factor (CNTF), reviewed by Strauss, 2005(Strauss 2005).

4.1.2.2 Phagocytosis of outer segments

Photoreceptor cells continuously add new outer segment discs proximal to the cell body, with the older segments moving away from the cell body until they are shed adjacent to the RPE layer(Young 1967). Outer segment turnover is slower for cones than for rods(Anderson et al. 1980). The RPE actively phagocytose these outer segments for recycling and degradation of components, thus preventing build-up of this cellular detritus(Young & Bok 1969). Phagocytosis involves a recognition/binding phase, an internalisation phase, and a digestion phase, each of which is regulated by associated proteins, while the timing of outer segment shedding by photoreceptors is influenced by light and the circadian clock. Reviewed by Mazzoni *et al.,* 2014(Mazzoni et al. 2014).

4.1.2.3 Contribution to the visual cycle

Following photo-isomerisation from 11-*cis* retinal to all-*trans* retinal as the first part of the photo-transduction cascade the visual pigment is regenerated and reused(Wald 1935; Kevany & Palczewski 2010). This process occurs in the RPE. Once all-*trans* retinal is released from the opsin photopigment it is reduced to all-*trans* retinol(Haeseleer et al. 1998) and transported across the intercellular space to the RPE. Inside the RPE, a series of enzymatic reactions regenerates the 11-*cis* retinal: esterification to retinyl ester by lecithin retinol acyltransferase (LRAT), converted to 11-*cis* retinol by RPE65(Ma et al. 2005; Jin et al. 2005), and then oxidised to 11-*cis* retinal, which is transported across the subretinal space, a process thought to be facilitated by IRBP(Landers et al. 1984). All-*trans* retinol (also known as vitamin A) from the diet is also converted to 11-*cis* retinal in the RPE. Reviewed by Tsin *et al.,* 2018(Tsin et al. 2018).

There is emerging evidence that the above cycle applies primarily to rod visual pigment, while cone visual pigment is regenerated through a different process, possibly involving Muller cells(Muniz et al. 2007). Why two different pathways might exist to complete the same chemical reaction in the same tissue is not clear.

4.1.2.4 Light absorption

RPE cells contain large apical melanosomes that contain the pigment melanin. This pigment absorbs stray light that passes through the photoreceptor layer. This is hypothesised to both reduce photo-oxidative damage(Hu et al. 2008) and also visual glare from backscatter(Wooten & Hammond 2002). Melanin pigment absorbs most efficiently at short wavelengths, which are most energetic and damaging to macromolecules including DNA. In addition melanin purified from porcine RPE showed decreased antioxidant and possible pro-oxidant function when photobleached, a process that is also believed to occur with aging(Zadlo et al. 2007; Burke et al. 2007).

4.1.3 RPE pathology

As described above, the RPE has a range of functions that serve to maintain the health and function of the retina. It is not surprising therefore that diseases of sight can commonly be traced back to a specifically RPE origin. In the case of age-related macular degeneration (AMD) cellular damage is acquired over the life-time of the individual, eventually leading to progressive loss of RPE function. In other cases dystrophic disease phenotypes have been traced to mutations in a particular gene involved in one or more specific functions of RPE. Below three pathological RPE diseases will be briefly described, before moving on to examine diseases associated with the gene Bestrophin-1 in particular.

4.1.3.1 Age-related macular degeneration (AMD/ARMD)

As of 2002 AMD was the third leading cause of blindness worldwide after cataract and glaucoma. However, it is a relatively greater burden in industrialised nations with aging populations and existing treatments for other visual diseases(Resnikoff et al. 2004), and is considered the leading cause of blindness in the over-65 age group.

As its name suggests, AMD is a late-onset disorder. It is characterised by gradual loss of central vision associated with progressive degeneration of the RPE layer in the macular region, along with degeneration of Bruch's membrane and changes to the underlying choriocapillaris. These changes precede the degeneration of the retinal photoreceptor layer. In the 'wet' form of AMD neovasularisation of the macular region is observed, for which there are several treatments intended to slow the progression of the blood vessel invasion into the retina, such laser treatment to seal leaking blood vessels and as injections of anti-VEGF agents to prevent new growth, reviewed by Bressler, 2009(Bressler 2009).For the 'dry' form AMD there are no treatments available. However, antioxidant treatment has been shown to slow progression of the disease in a minority of cases, reviewed by Gehrs *et al.,* 2006(Gehrs et al. 2006). Although there a small number genetic associations with AMD, it is generally considered a pathology of aging rather than a genetic disease(Stone et al. 2001).

Studies of the effects of aging on human retinal cells found a higher density of RPE in the fovea relative to the peripheral retina in all age groups studied(Del Priore et al. 2002; Gao & Hollyfield 1992). It was also found that photoreceptors and RPE showed a decrease in cell density during aging that maintained their relative ratios, and that age-related photoreceptor loss was higher in the peripheral retina than in the fovea(Gao & Hollyfield 1992). RPE density was found to be stable in the central macula region over different age groups despite much higher numbers of apoptotic cells being found there. It is hypothesised that the death of macula RPE may be compensated for in the early decades of life by migration of peripheral RPE inwards towards the fovea(Del Priore et al. 2002). Within this model AMD could be considered the result of the exhaustion of the ability of the RPE layer to maintain and repair itself.

4.1.3.2 Leber Congenital Amaurosis (LCA) and Early-Onset Severe Retinal Dystrophy (EOSRD)

LCA and EOSRD are broadly defined as a loss of vision that presents at birth or soon after and that is not associated with retinal lesions. Other signs include nystagmus, amaurotic pupils and reduced or absent electroretinograms. Genetic analysis has revealed over 25 associated genes, suggesting that LCA/EOSRD are a collection of genetic disease with similar clinical presentation, but potentially different primary causes. Some of the genes are involved in the visual cycle, including those expressed in the RPE, such as the retinal cycle genes LRAT and RPE65. Reviewed by Bainbridge *et al.,* 2008(Bainbridge et al. 2008).

4.1.3.3 Retinitis Pigmentosa (RP)

RP is a heterogeneous group of inherited retinal disorders with mixed heritability and characterised by rod photoreceptor death, affecting the peripheral retina first, and sometimes RPE involvement. Over 100 mutations have been linked to RP, with a diverse array of functions(Hartong et al. 2006). The RPE retinal cycle gene RPE65 is one of these, as is the receptor tyrosine kinase MERTK, which is involved in ligand binding of photoreceptor outer segments in RPE phagocytosis. Mutations in Bestrophin-1 have also been linked to cases of RP(Davidson et al. 2009).

4.1.3.4 Defining diseases

It is important to note that historically diseases have been defined based on clusters of signs and symptoms and the stage of life at which they occur. The increasing role of genetic testing and diagnosis in many diseases of the eye has revealed that frequent misdiagnosis does occur, particularly for rarer disorders, and that some disorders can be traced mutations in a single gene while others are highly polygenic. Increasingly genetic testing is being used to define patients according to the genetic basis for their disease (where one exists) rather than relying only on examination. This has the potential to significantly improve treatment options through more targeted therapy in the short and medium-term future. For example, future gene therapy

targeted at forms of LCA caused by RPE65 mutations could have therapeutic benefits for forms of RP caused by RPE65 mutation(Maguire et al. 2008; Bainbridge et al. 2008).

4.1.4 The Bestrophinopathies

Apart from AMD, the other well-defined group of diseases with a consistent RPE origin are the Bestrophinopathies, so called because they are defined by causative mutations in the gene Bestrophin-1 (*BEST1*). The exact number of discrete Bestrophinopathies is a matter of some disagreement, and depends somewhat on whether one tends towards 'lumping' or 'splitting'. This situation is not helped by the fact that the protein product of *BEST1* contains 585 amino acids, each of which could in theory be mutated to any of the 19 others, or a stop codon. This yields 11,700 unique possible single site protein mutations, not including any genetic changes that might be redundant for protein-coding but that influence mRNA transcription, splicing, degradation, or translation. In addition, the effects of any particular mutation are likely to vary depending on the genetic background (particularly the sequence of the homologous *BEST1* gene on the sister chromosome), and environmental factors. Thus, despite the fact that hundreds of unique patient *BEST1* mutations have been recorded to date, this represents only a tiny fraction of potential options. Systematic mutagenesis methodologies have been conducted *in vitro*, which have provided information on the structure and functioning of the BEST1 protein, but do not reveal what clinical effects these mutations would have. Animal models of Bestrophinopathies can bridge this gap, but it is in question to what extent they can represent the human disease state.

Although the Bestrophinopathies are united by causal mutations in the *BEST1* gene, they are nevertheless regarded as separate diseases due to the consistent and different patterns of pathology associated with each. The importance of this is three-fold. Clinically this means that likely disease progression can be predicted upon diagnosis and that any treatment can be tailored to the specific pathology present. From a research perspective, the existence of distinct Bestrophinopathies are considered likely to reflect different classes of possible disruption of the function of BEST1. Study of these difference can therefore reveal the functioning of different parts of the BEST1 protein, the understanding of which can lead to the future development of unique treatment options tailored to the mutation that the patient carries, as revealed by genomic DNA sequencing.

Below is given a brief description of four of the Bestrophinopathies: Best Vitelliform Macular Dystophy (BVMD), Adult-onset Vitelliform Macular Dystrophy (AVMD), Autosomal Recessive Bestrophinopathy (ARB), and Autosomal Dominant Vitreoretinochoriodopathy (ADVIRC).

4.1.4.1 Nomenclature of Bestrophinopathies

Many variants of Bestrophinopathy disease naming exist. BVMD is often referred to as Vitelliform Macular Dystrophy (VMD/VMD2), Best Macular Dystrophy (BMD), Juvenile Vitelliform Macular Dystrophy, Juvenile-Onset Vitelliform Macular Dystrophy, Best disease (BD), or Best's disease (BD). Depending on the author, AVMD may also be included under a broad meaning of the term "Best disease" or specifically considered as a subtype of BVMD. AVMD has been referred to as Adult Foveal Macular Dystrophy of Gass and also has significant clinical overlap with Adult-Onset Foveomacular Vitelliform Dystrophy (AOFVD), the latter of which may be due to *BEST1* mutation in some cases(Seddon et al. 2001). ADVIRC was previously known as Microphthalmia-Retinitis Pigmentosa Glaucoma and is sometimes referred to as Autosomal-Dominant Vitreochoroidopathy. This mixture of terminology for Bestrophinopathies likely reflects in part the new role that routine genetic testing is having in the diagnosis of retinal disease. To avoid misrepresentation of research results in the following sections the disease name used by the author will be used in each case. **Table 4.1** shows a summary of the alternative nomenclature.

Bestrophinopathy	Alternative names
Best Vitelliform Macular Dystrophy (BVMD)	Vitelliform Macular Dystrophy (VMD/VMD2)
	Best Macular Dystrophy (BMD)
	Juvenile Vitelliform Macular Dystrophy
	Juvenile-Onset Vitelliform Macular Dystrophy
	Best disease (BD)
	Best's disease (BD)
Adult-onset Vitelliform Macular Dystrophy (AVMD)	Best disease (BD)
	Adult Foveal Macular Dystrophy of Gass
Autosomal Dominant Vitreoretinochoroidopathy (ADVIRC)	Microphthalmia-Retinitis Pigmentosa Glaucoma
	Autosomal-Dominant Vitreochoroidopathy
Autosomal Recessive Bestrophinopathy (ARB)	-

Table 4.1 Alternative names for common Bestrophinopathies used in referenced research material in this chapter.

BEST1 mutations have also been found at low percentage in other maculopathies(Seddon et al. 2001), including AMD(Lotery et al. 2000) and RP(Davidson et al. 2009) and could represent additional kinds *BEST1* pathology that have yet to be formalised, or a subclinical *BEST1* pathology interacting with an unrelated pathology. Mutations in *BEST1* do not appear to significantly contribute to cases of AMD(Krämer et al. 2000).

4.1.4.2 Clinical appearance of Best Vitelliform Macular Dystrophy (BVMD)

BVMD, also known as Best disease, was first described in 1883 by JE Adams at Moorfields Eye Hospital(Adams 1883). After a 1905 paper by Frederich Best(Best 1905) it became known as Best Vitelliform Macular Degenration (BVMD). BVMD is a macular degeneration with a predominately juvenile onset showing autosomal dominant inheritance(Bakall et al. 2003). It is characterised by a reduced electro-oculogram (EOG) light peak to dark trough ratio (i.e. a Arden ratio(Arden et al. 1962)of less than around 1.5), but with a normal electroretinogram (ERG)(Marmorstein et al. 2002). ERG measures rapid changes in retinal nerve potential due to light exposure, while EOG measures slower changes in the standing electric potential across the RPE due to ion changes during alternate periods of light and dark adaptation(Arden & Constable 2006; Stone et al. 1992; Brown et al. 2006). Unlike Stargardt Macular Dystrophy, BVMD does not affect the rate of dark adaption of rod cells(Baca et al. 1994).

Fundus examination finds an orange/yellow 'egg-yolk' (vitelliform) lesion centred on the fovea, which may break up over time into a 'bulls-eye' lesion while visual acuity drops(Birndorf & Dawson 1973). This lesion is due to an accumulation of autofluorescent lipofuscin debris within and beneath the RPE layer(Tsunenari et al. 2003). Some patients also show subretinal fibrosis or neovascularisation of the choroid(Bitner et al. 2011; Petrukhin et al. 1998).

BVMD shows heterogeneity in age-of-onset and progression. The lesion progression is not necessarily regular through standard stages(Clemett 1991). The abnormal EOG Arden ratio appears to be more diagnostic than the maculopathy symptoms, with a small number of individuals of affected families carrying the *BEST1* mutation and showing the abnormal EOG, but without the retinal degeneration(Seddon et al. 2003). However, normal EOG light rises have been reported in individual patients with BVMD diagnosis. In some cases there is no confirmed *BEST1* mutation(Birndorf & Dawson 1973). In others cases there are confirmed *BEST1* mutations, as well as affected siblings with the same mutation that show the expected abnormal EOG(Low et al. 2011). Though most cases of BVMD occur in childhood, this is not always the case. A patient with a *BEST1* mutation who was unaffected at 51 years developed clinical Best disease at 75 years old(Mullins et al. 2005). In another case a patient with a familial Best's disease locus was shown to have no detectable sign of the disease(Weber et al. 1994). A 2011 study found that only 60% of patients diagnosed with a Juvenile Vitelliform Macular Dystrophy carried a *BEST1* mutation. This increased to 83% for a subset of those with both a family history and reduced Arden ratio of <1.6(Meunier et al. 2011). This could partially explain the heterogeneity in BVMD presentation – not all patients diagnosed with BVMD actually have a *BEST1* mutation.

Generally, cases of BVMD are associated with dominant missense mutations in *BEST1*, although cases of BVMD symptoms have been reported in patients with premature stop codons(Bitner et al. 2011) or compound heterozygosity(Zhao et al. 2012).

Because BVMD primarily affects the macular region it is the central, high acuity vision that is progressively and irreversibly lost in patients. There are currently no treatments for BVMD other than for the neovascularisation that is shared with AMD.

4.1.4.3 Clinical appearance of Adult-onset Vitelliform Macular Dystrophy (AVMD)

AVMD was first described based on nine patients in 1974(Gass 1974). Its defining features were similar to BVMD in some ways and differed in others. Similarities included: yellow subretinal lesions in the fovea; a normal ERG; a pattern of likely dominant inheritance. Differences included: a much later onset than BVMD (typically 30-50 years); visually asymptomatic or showing only visual blurring and metamorphopsia that progressed slowly such that reading vision is often maintained; sometimes small drusen in the paracentral region; normal or only mildly subnormal EOG. AVMD symptoms are generally considerably less severe than BVMD.

However, the clinical appearance varies, as does the degree of vision loss(Brecher & Bird 1990). In addition some cases of AVMD have been attributed to mutations in genes other than *BEST1*, such as peripherin/RDS(Wells et al. 1993; Felbor et al. 1997). In one study 0 of 19 AVMD patients had *BEST1* mutations and 2 of 19 had peripherin/RDS mutations(Meunier et al. 2011). In a study of 23 *BEST1* mutants associated with Best disease and 4 associated with AVMD, two of the AVMD mutations were also among the Best disease mutations(Krämer et al. 2000), suggesting that the same mutations can produce different disease manifestations depending on genetic background and environmental factors.

4.1.4.4 Clinical appearance of Autosomal Recessive Bestrophinopathy (ARB)

Autosomal Regressive Bestrophinopathy (ARB) was described by Burgess *et al.*, 2008(Burgess et al. 2008). This disorder causes loss of central vision, the absence of the EOG light rise, and a reduced ERG. Hyperopia was found in all for whom data was available, and several had shown angle-closure glaucoma. The RPE was irregular and showed scattered punctate flecks, as well as retinal oedema and subretinal fluid. The vitelliform lesions characteristic of BVMD and AVMD were never seen.

ARB was found to be recessive, with heterozygous carriers unaffected, prompting the authors to suggest that ARB represents the null best1 condition. This view was supported by the finding that when these mutant forms of *BEST1* were co-transfected along with the wild-type *BEST1* into HEK293 cells the former did not interfere with the formation of active wild-type *BEST1* channels. Since its discovery more case studies of AMD have followed, and genotyping has

supported the hypothesis that ARB represents the null phenotype(Lee et al. 2015; Davidson et al. 2010; Gerth et al. 2009).

4.1.4.5 Clinical appearance of Autosomal Dominant Vitreoretinochoroidopathy (ADVIRC)

ADVIRC was first described by Kaufman *et al.*, 1982(Kaufman et al. 1982). It is characterised by semiconfluent circumferential peripheral pigmentation. Patients also show, to various degrees, lens opacities, presenile cataracts, cells and fibrillar condensation in the vitreous, retinal arteriolar narrowing and occlusion, diffuse retinal vascular incompetence, retinal neovascularisation, choroidal atrophy, cystoid macular oedema, white punctate retinal opacities, and mild myopia. It is inherited in an autosomal dominant fashion(Kaufman et al. 1982; Blair et al. 1984; Yardley et al. 2004; Traboulsi & Payne 1993; Goldberg et al. 1989). ADVIRC has also been associated with nanophthalmos, microcornea, closed angle glaucoma, and congenital cataract(Lafaut et al. 2001; Yardley et al. 2004), suggesting a role for BEST1 in the normal development of the eye. ADVIRC patients show abnormal ERGs and very low EOGs(Yardley et al. 2004).

As with the other Bestrophinopathies, presentation varies greatly between individuals. An early report found variable presentation of ADVIRC symptoms within the same family, with neither patient showing the reduced EOG light rise(Kellner et al. 1998). However, genetic testing was not performed so it is not confirmed that *BEST1* mutation was causative. A more recent study of two siblings with confirmed *BEST1* mutations found a lack of the reduced EOG light rise in the one of the two that could be tested(Burgess et al. 2009).

4.1.4.6 Concluding notes on the Bestrophinopathies

As described above there is considerable overlap in the pathology of Bestrophinopathies and presentation varies even within families with identical mutations. For example BVMD and AVMD both show subretinal lipofuscin accumulation, retinal atrophy, and choroidal neovascularisation (something they share with AMD). The similarity of presentation coupled with variations in disease appearance and progression even between family members with known identical *BEST1* mutations means that misdiagnosis is considered to be relatively common. Thus some AMD patients may be suffering from late-onset Best disease and some patients diagnosed with a juvenile or adult onset macular dystrophy have no *BEST1* mutation and are therefore suffering from some other causative factor(Lotery et al. 2000). It also seems that an early age-of-onset is not necessarily diagnostic for BVMD, which can present later in life(Eksandh et al. 2001).

Criteria for diagnosing Bestrophinopathies also appear to vary. In one study on 60% of patients diagnosed with a juvenile or adult-onset macular dystrophy carried *BEST1* mutations(Meunier et al. 2011). There are likely other genes that when mutated give similar phenotypes to Bestrophinopathies that remain to be identified(Chen et al. 2013). Other diseases may be

confused with BVMD, such as AVMD, AMD, and bull's-eye maculopathy. Routine genetic testing should increasingly clarify which cases are actually due to *BEST1* mutations.

In the next section the research into the function of the *BEST1* gene and BEST1 protein product will be presented, relating both to healthy vision and the pathology seen in Bestrophinopathies.

4.1.5 Bestrophin-1

4.1.5.1 Identification of BEST1 as the genetic cause of Bestrophinopathies

The gene associated with BMD was first located to chromosome 11q13.(Forsman et al. 1992; Stone et al. 1992). The gene was then identified by Petrukhin *et al.,* 1998(Petrukhin et al. 1998). It was initially referred to as *VMD2* and is now commonly known as Bestrophin-1, or *BEST1*. The human genome contains four Bestrophin genes, of which *BEST1* is the most studied due to its role in degenerative eye disease.

The protein product of *BEST1* was found to be closely related to the *RFP* proteins in *C.elegans*, members of which were also found in *Mus musculus* and *Drosophia*. The protein function was unknown (*RFP* proteins were named after the invariant Arg-Phe-Pro sequence found within). Mouse (*Mus musculus)* has four bestrophins, Pufferfish (*Fugu rubripes*) has three, Drosophila (*Drosophila melanogaster*) has four, Mosquito (*Aenopheles* gambia) has two, the nematode (*Caenorhabditis elegans*) has 25(Tsunenari et al. 2003). Bestrophins are highly conserved between species for the first 300 or so residues(Qu et al. 2003). The N-terminal domain is greatly conserved, while the C-terminal domain varies much more in length and sequence(Tsunenari et al. 2003). Two of the five human disease missense *BEST1* mutations investigated by Petrukhin *et al*. were at amino acid residues where the human wild-type residue would normally be identical to the residue at that same position in all 14 of the *C.elegans* orthologues examined. This supported the view that these missense mutations were disrupting highly conserved regions and thus essential function.

The role of Bestrophins in vision appears not to be universal. Although the tissues in which Best proteins are expressed in *Drosophila* are not known, flies lacking dbest1 are viable and show photoreceptor integrity(Tavsanli et al. 2001). Loss-of-function knockdown and RNAi screens have identified a role for Drosophila Best proteins in wing morphogenesis(George et al. 2019).

Bestrophin orthologues have also been identified in bacterial genomes, suggesting a deep evolutionary history(Yang et al. 2014). It has been proposed that this family of proteins evolved as part of a pathway to compensate for acidic environmental conditions(Iyer et al. 2002).

4.1.5.2 Expression and localisation of the BEST1 protein

BEST1 is a 585 amino acid protein consisting of 11 exons and a molecular weight of around 68 kiloDaltons (kDa). It appears to be primarily expressed in RPE(Petrukhin et al. 1998; Marquardt

et al. 1998), where it localises to the basolateral membrane(Marmorstein et al. 2000; Bakall et al. 2003).

BEST1 expression in mouse RPE has been shown to require two upstream E-boxes and is regulated by the MITF-TFE transcription factor family(Esumi et al. 2007). *BEST1* expression has also been shown to be promoted by OTX1, OTX2, and CRX, which are expressed in the RPE(Esumi et al. 2009).

BEST1 mRNA was detected in the eye of developing mice by embryonic day 15, but BEST1 protein was not detected by immunofluorescence in RPE until postnatal day 10(Bakall et al. 2003). The authors suggest that this implies strong translational control of BEST1 expression. In addition the authors point out that the first detection of BEST1 protein in RPE coincided with the first detectable ERG a-waves, which are a product of the phototransduction cascade(Robson & Frishman 2014; Einthoven & Jolly 1908), suggesting functional BEST1 is adaptive from the onset of visual function.

4.1.5.3 Structure and Function of BEST1 as a membrane channel

When *BEST1* was discovered as the causative gene for BVMD nothing was known about the structure and function of the BEST1 protein. While this question is still far from settled there has been considerable research progress, particularly on the role of BEST1 as an ion channel.

As early as 1989, Cl^- channel blocking agents were found to supress or abolish the light peak in chick RPE and that this light peak was due to RPE basal membrane depolarisation(Gallemore & Steinberg 1989). This suggested that a chloride channel in the basal RPE membrane was responsible for the EOG light peak. Thus when *BEST1* was discovered to be causative for retinal diseases that involved disruption to the EOG light rise and to be localised to the basolateral RPE membrane it was considered likely that BEST1 would form or interact with some kind of chloride channel.

4.1.5.4 BEST1 as a membrane chloride channel

Expression of human, *Drosophila*, and *C. elegans* bestrophins in HEK293 cells suggested significant conductance for Cl^- (for both hBEST1 and hBEST2). This current was reduced or completely absent when h*BEST1* containing one of fifteen VMD mutations was used in place of the wildtype. Co-expression of four of these mutants with the wildtype demonstrated a dominant effect of inhibition of membrane current, consistent with the dominant nature of VMD(Sun et al. 2002). Sulfhydryl-reactive agents inactivated the current of wild-type BEST1, but not a mutant version lacking cysteine residues. This further suggested that BEST1 was itself acting as a chloride channel, rather than just interacting with one. Co-precipitation of differently tagged BEST1 proteins suggested that BEST1 oligomerised into tetramers or pentamers

(consistent with a separate study that suggested that BEST1 formed complexes of two or more(Stanton et al. 2006)). Photo-release of Ca^{2+} in HEK293 cells transfected with *BEST1* caused large Cl^- currents, suggesting BEST1 was calcium-sensitive. Introducing *BEST1* with known VMD mutations resulted in loss of this Ca^{2+}-activated Cl^- (CaC) current in some cases, suggesting a possible mechanism for some Best disease pathology. The role of Bestrophins as Ca^{2+}-activated Cl^- channels was supported by expression of two Bestrophin genes from *Xenopus laevis* in HEK293 cells, which produced large Ca^{2+}-activated Cl^- currents(Qu et al. 2003). RNA interference to two of the *Drosophila* Bests, d*BEST1* and dBest2, abolished the CaC current and overexpression of dbest1 in HEK293 cells caused a novel CaC current(Chien et al. 2006), further supporting the role of BEST1 as a Ca^{2+}-activated Cl^- channel. The mechanism could have been through direct Ca^{2+} binding to BEST1 or indirectly via another protein(Hartzell et al. 2008). Membrane-patch Cl^- currents through hBest4 are Ca^{2+}-activated, suggesting that a diffusible messenger or phosphorylation are not necessary for this Bestrophin(Tsunenari et al. 2006). In the BEST1 protein, a region found after the final transmembrane domain included five adjacent acid amino acids and an EF hand that were responsible for Ca^{2+} activation(Xiao et al. 2008), though it was still not clear if this was a direct or indirect activation.

4.1.5.5 BEST1 as a regulator of calcium signalling

Voltage-gated Ca^{2+} channels (VGCCs) allow Ca^{2+} entry based on depolarisation of the cell membrane. The resulting transient increase in intracellular Ca^{2+} then initiates cell-type specific physiological events such as muscle contraction; activation of calcium-sensitive potassium channels; neuronal excitation; changes in gene expression; and secretion of hormones, growth factors, or neurotransmitters. They are classified into L-, N-, P-, Q-, R-, and T-type, based on their response to various toxins. L-type channels are involved in contraction of cardiac, smooth and skeletal muscle, changes in gene expression, and endocrine hormone secretion (reviewed by Catterall, 2000(Catterall 2000)). Neuroendocrine L-type channels are expressed in rat RPE and are activated by the tyrosine kinases $pp60^{c\text{-}src}$, probably via the α1D Ca^{2+} channel subunit(Strauss et al. 2000). Human RPE and ARPE-19 express the TRPV channels TRPV1, 2, 3, and 4. Temperature increases or IGF-1 treatment increased VEGF-A secretion in both cell lines(Cordeiro et al. 2010).

As well as being regulated by calcium ions, *BEST1* also appeared to be involved in the regulation of calcium channels. Expression of *BEST1* in RPE-J cells changed the kinetics of L-type Ca^{2+} channels, an effect that was modulated depending on whether the *BEST1* was wild-type or a Best disease mutant. Nimodipine, an L-type Ca^{2+} channel blocker, reduced the light peak in rats without affecting the a- and b- waves(Rosenthal et al. 2006). Together this suggested that the *BEST1* involvement in generating the EOG light peak might be through regulation of calcium

channels. However, *BEST1*$^{-/-}$ knockout mice show normal light peak amplitude and no Cl^- current differences compared to *BEST1*$^{+/+}$ littermates(Marmorstein et al. 2006). Mice with a loss of function mutation in the β_4 subunit of voltage-dependent Ca^{2+} channels showed altered light peak response, and ATP stimulation resulted in a five-fold greater Ca^{2+} increase in *BEST1*$^{-/-}$ cells than *BEST1*$^{+/+}$ cells. The authors suggested that this indicates a *BEST1* role in supressing Ca^{2+} rise and therefore the light peak, and that the pathologic role of mutant *BEST1* in BMD is due to some other cellular function or interaction.

β4-subunits of voltage-dependent L-type Ca^{2+} channels show co-immuno precipitation with *BEST1* and the $Ca_V1.3$ and β4-subunits co-localise with *BEST1* in mouse RPE. BEST1 appears to regulate the number of Ca^{2+} channel subunits that localise to the membrane, and in turn the Ca^{2+} currents themselves. Mouse deficient for the $Ca_V1.3$ or β4-subunit have reduced EOG light peaks, suggesting this interaction as a mechanism for *BEST1* effecting the light peak. In addition a proline-rich motif in the C-terminus (residues 330-346) of *BEST1* was shown to be important for the co-immuno precipitation, the effects on Ca^{2+} current, and BEST1 trafficking to the membrane(Reichhart et al. 2010; Milenkovic, Krejcova, et al. 2011). However, this C-terminus region corresponds to a region with no known Bestrophinopathy mutations(Boon et al. 2009), which suggests that disruption of this region, even if it can be demonstrated to be disruptive to calcium signalling *in vivo*, is not causative for Bestrophinopathies.

Knockdown of BEST1 in porcine RPE has been shown to disrupt phagocytosis, as does blockage of voltage-gated L-type channels. $Ca_v1.3^{-/-}$ cells lacked the usual morning phagocytosis peak. Activation of TRPV channels increased phagocytosis rates while inhibition reduced them(Müller et al. 2014). Together this suggests that BEST1 regulation of Ca^{2+} signalling through physical interaction with Ca^{2+} channel subunits is involved in controlling RPE phagocytosis.

4.1.5.6 The structure of the BEST1 protein

Meanwhile, using the Cl^- currents of *BEST1* as an assay for *BEST1* function, it was possible to begin to determine the structure of BEST1 in the cell membrane. An assessment of the effects of the cysteine modification reagent 2-aminoethylmethane thiosulfonate (MTSEA) on human *BEST1* (*hBEST1)* expressed in HEK-293 cells revealed a loss of whole-cell current(Tsunenari et al. 2003). By systematic mutation of cysteine residues to alanine within the BEST1 sequence (the Substituted-Cysteine Accessibility Method(SCAM)(Karlin & Akabas 1998)) the authors were able to identify Cys-69 as necessary for this inactivation, and infer that it likely lies extracellularly. The authors also tested the effect of inserting N-Glycosylation sequences into 25 sites in the BEST1 protein. By measuring the extra protein mass due to glycosylation the authors could infer which sites lay on the inner face of the endoplasmic reticulum membrane after translation. Finally, they introduced consensus cleavage sites for the tobacco etch virus protease into 22 sites in the

BEST1 protein, used a membrane disruption and vesicle formation protocol to produce vesicles with the cytoplasmic membrane face outwards, and assayed for cleavage locations in the BEST1 sequence. These results suggested a cytosolic N-terminal terminus and C-terminal terminus, as well as at least three extracellular domains.

Hydrophobicity analysis of the amino acid sequence of *BEST1* predicted four transmembrane segments with a cytoplasmic loop between TMD2 and TMD5, so that TMD3 and 4 are actually cytoplasmic(Milenkovic et al. 2007). They also measured defects in membrane insertion in 3 of 18 BMD-related mutants they examined, suggesting this could be one cause of pathology.

Crystallography has been used to generate a model of a bacterial Bestrophin orthologue, kpBEST, a pentamer with four transmembrane helices and cytoplasmic N- and C-terminus(Yang et al. 2014). The shape of the pore formed two predicted ion permeation restrictions, and the four residues at these sites are conserved or disease-related in h*BEST1*: I76, F84 and I205 are identical between kpBest and h*BEST1*, while mutations at F80 or I205 in h*BEST1* are known to cause disease phenotypes(Davidson et al. 2009; Lotery et al. 2000). Using their bacterial Best model they identified and mutated resides mostly like to contribute to the selectivity of ion permeability. For example mutating F80I in h*BEST1* greatly reduced Cl^- permeability of the hBEST expressed in HEK293 cells. Again based on this bacterial model the isoleucine at site 205 in h*BEST1* was predicted to be the narrowest point of the ion pathway, and mutating it to the smaller Alanine greatly increased Cl^- currents, while mutating it to Glutamic Acid had very little effect. I205T is a known disease-causing mutation with decreased Cl^- conductance(Davidson et al. 2009), supporting the role of this residue in *BEST1* permeability. Based on homology to their bacterial model and the effects of their mutational assays they produced a structural model of h*BEST1* with four transmembrane regions and pentameric oligomerisation.

X-ray structure of chicken BEST1-Fab complex supported a four-transmembrane structure with pentameric oligomerisation(Dickson et al. 2014). Electron-density consistent with Ca^{2+} was found in the region of G300 to Asp304, consistent with identified Ca^{2+} binding sites and clusters of BVMD mutations(Boon et al. 2009; Caldwell et al. 1999). This crystal structure also produced insights into the nature of the channel shape, including conformational changes near the Ca^{2+} binding region under different preparations. This supports the idea of direct Ca^{2+} binding to the BEST1 protein and its role in pathology.

4.1.5.7 The current consensus on BEST1 structure and function

The exact structure and function of BEST1 are still far from settled. It is generally accepted that it is a pentameric Cl^- channel which predominately localises to the basolateral membrane of the RPE and which regulates Ca^{2+} signalling. However, there is dispute that BEST1 is responsible for

the EOG light rise. *Best1* null mice showed normal light peaks and no evidence of photoreceptor loss, although those with the W93C BVMD mutation showed some difference in light peaks and did also show accumulation of lipofuscin(Marmorstein et al. 2006). Some suspect BEST1 is a regulator of channel function rather than a channel itself(Marmorstein et al. 2009), and it may of course function as both. The use of different model organisms and cell lines, though convenient, may lead to false generalisations. Overexpression studies in non-RPE cell lines may not provide physiologically meaningful results.

4.1.5.8 Other interactions of BEST1 and other BEST proteins

Apart from the putative role as a chloride channel (possibly calcium activated), and as a regulator of calcium signalling, it is possible that *BEST1* has additional functions within RPE and elsewhere that may be disrupted in disease states. Below are presented some of these proposed roles.

4.1.5.8.1 BEST1 as an Intracellular Cl^- channel

It has been hypothesised that as well as a membrane channel *BEST1* may also function as an intracellular Cl^- channel(Hartzell et al. 2005). Other Cl^- channels are known to have both plasma membrane and internal membrane function, such as CIC-3 and CIC-7, which can be found in endosomes and lysosomes respectively, reviewed by Jentsch *et al.,* 2002(Jentsch et al. 2002). Intracellular Cl^- pumps are known to function as counterion shunts to dissipate the membrane potential that develops when H^+ ions are pumped into acidic organelles such as in the endosomal pathway, reviewed by Faundez & Hartzell, 2004(Faundez & Hartzell 2004). The luminal pH of vesicles also affects membrane trafficking and the activity of enzymes within(Mellman 1992). If *BEST1* were directly involved in the phagocytic pathway this could explain the accumulation of incompletely digested outer segments (OS) that leads to the vitelliform lesions seen in Bestrophinopathies. It has also been suggested that *BEST1* might operate as a counter-ion channel for Ca^{2+} entry into intracellular stores(Neussert et al. 2010).

4.1.5.8.2 BEST1 as a volume-regulated anion channel (VRAC)

As an example of species-level differences in BEST function, *Drosophila* BEST1 (dBEST1) appears to operate as or part of a volume-regulated anion channel (VRAC) in S2 cells, while the mouse BEST (mBEST1) appears not to in peritoneal macrophages(Chien & Hartzell 2008). Mice null for *BEST1* do not show retinal phenotypes, but do show a subfertility phenotype(Milenkovic et al. 2015), which the authors hypothesise could be due to impaired regulatory volume decrease (RVD). Expression of h*BEST1* or hBest2 in HEK293, HeLa, or ARPE-19 cells produced Ca^{2+} -activated Cl^- currents. This current could be reduced by 70-80% through using hypertonic solution to induce cell shrinkage. An effect of hypertonic solution-induced cell shrinkage on Cl^- current also occurred in mouse RPE cells. This suggested that the BEST1 contribution to anion currents could be volume-regulated(Fischmeister & Hartzell 2005).

4.1.5.8.3 Differences in chloride channel activity between different BESTs

The human genome contains four paralogous bestrophin genes(Stöhr et al. 2002), of which *BEST1* is the most studied due to its role in degenerative eye disease. The ion current properties differs between bestrophin paralogues and orthologues(Tsunenari et al. 2003). When overexpressed in HEK293 cells mBest4 only functions as a Cl^- channel when a short C-terminal motif is deleted(Qu 2006). However, hBest4 appears to produce a large Cl^- current when overexpressed in HEK293 cells(Tsunenari et al. 2006).There also appears to be a C-terminal Cl^- current self-inhibitory region in mBest3 and hBest3 and hBest2, which may also affect localisation(Qu et al. 2007). The role of the C-terminus in localisation is supported by investigations of h*BEST1* splice variant trafficking(Kuo et al. 2014).

4.1.5.8.4 BEST1 interaction with protein phosphatase 2A (PP2A)

Human and porcine *BEST1* physically associates with the β-catalytic subunit of protein phosphatase 2A (PP2A), via the C-terminal cytoplasmic domain(Marmorstein et al. 2002). BEST1 protein was found to be phosphorylated when expressed in RPE-J cells, which was increased when PP2A was inhibited.

PP2A is found in rod outer segments and has been shown to be able dephosphorylate opsin and rhodopsin(Fowles et al. 1989; Palczewski et al. 1989). In addition it has been shown to increase the cGMP sensitivity of cGMP-regulated ion channels in rod cell membrane patches(Gordon et al. 1992). This suggests a route by which BEST1 could influence the visual cycle.

4.1.5.8.5 Extra-RPE retinal expression of BEST1

A study found m*BEST1* promoter-driven expression in Muller cells during retinal development in around half of the mouse lines examined(Zhu et al. 2010). This suggests both that *BEST1* expression may not always be solely localised to the RPE in the retina, and that there may be differences between animal lines, as well as between species.

4.1.5.8.6 *BEST1* expression outside of the retina

Despite being commonly described as being expressed exclusively in the RPE, it has been suggested that *BEST1* expression occurs in many epithelial tissues other than RPE. This includes the tracheal epithelium, but not the nasal epithelium, the proximal colon, but not the distal colon, and the kidney epithelium. The authors hypothesise that *BEST1* therefore represents a component of the Ca^{2+}-activated Cl^- current in these cells, supported by knockdown of *BEST1*, but leave unexplained why in humans mutations in *BEST1* appear to only cause retinal pathology(Soria et al. 2009; Barro-Soria et al. 2008).

4.1.5.8.7 A role for BEST1 in the brain

BEST1 also appears to be expressed at some level in multiple cell types in the brain, particularly astrocytes. BEST1 is not only permeable to chloride ions, but also to the anionic

neurotransmitters GABA and glutamate and there is therefore speculation that BEST1 may be involved in a range of conditions associated with astrogliosis such as brain injury, inflammation and neurodegeneration, reviewed by oh & Lee, 2017(Oh & Lee 2017). There does not appear to be any evidence that Bestrophinopathy patients show any pathology of the central nervous system.

4.1.6 Mechanisms of Bestrophin1 pathology

As described above much more is now known about BEST1 structure and function, although there is still considerable debate and uncertainty as to which functions and interactions of BEST1 are important for retinal disease or even real in native human RPE cells. The pathways of pathology for *BEST1* and the Bestrophinopathies is very uncertain. Still, multiple possible pathogenic routes for *BEST1* mutations have been identified. As each of the main Bestrophinopathies appears to show particular characteristics this suggests that there may be a limited number of discrete pathways being affected.

4.1.6.1 Mechanisms of BVMD/AVMD pathology

Although BVMD is associated with a range of clinical features, the disease progression gives suggestions of a causative chain. The low Arden ratio appears to be the most universal feature, and can be found before any other. The vitelliform lipofuscin deposits occur next, followed by degeneration of the RPE, and then degeneration of PRs accompanied by loss of vision. The primacy of the altered Arden ratio suggests the primary pathology is an ion channel dysfunction. Many mutations associated with BVMD have been shown to affect BEST1 chloride channel function and mutations for this disease appear to cluster near the cytosolic side of the predicted transmembrane domains of the anion channel(Milenkovic et al. 2007; Guziewicz et al. 2011). The region just C-terminal to the final transmembrane domain is rich in BVMD-causing sites, but then the C-terminal third is devoid of disease-causing regions(Boon et al. 2009; Dickson et al. 2014). Some BVMD mutations have also been associated with alteration in localisation and regulation of calcium channels(Sun et al. 2002; Rosenthal et al. 2006), reviewed by Boon *et al.*, 2009(Boon et al. 2009). BMD mutant BEST1 appears to be commonly mis-localised, suggesting this as one mechanism for altered chloride channel function(Milenkovic, Röhrl, et al. 2011). As mis-localisation of mutant BEST1 has also been shown to cause mis-localisation of wild-type BEST1, presumably through oligomerisation, this also suggests a mechanism for autosomal dominance(Johnson et al. 2014).

How channel defects lead to the observed clinical characteristics of BVMD is unknown and could operate via multiple pathways simultaneously through altering the ion balance of the RPE cells. The fact that AVMD is a dominant disease suggests that mutant BEST1 subunits can affect the properties of the entire pentameric channel.

As the clinical characteristics of AVMD are very similar to BVMD, with later onset and milder symptoms, it is possible that there are a range of severities of mutational disruption of chloride channel function that can partly explain the range of severity seen(Yu et al. 2006).

4.1.6.2 Mechanisms of ARB pathology

Due to its recessive inheritance and lack of interference in wild-type BEST1 oligomerisation ARB mutants are considered likely to be the loss-of-function null condition for BEST1. This appears to be due to nonsense-mediated decay of the mRNA transcript in at least some cases(Pomares et al. 2012). In other cases mutant BEST1 appears to mis-traffic and be degraded by the proteasome, or else collect in aggresome-like bodies(Davidson et al. 2011). In another study expression of ARB mutant BEST1 in Madin-Darby Canine Kidney (MDCK) cells showed the majority mis-localised and also caused mis-localisation of wild-type BEST1(Johnson et al. 2014). As ARB is recessive, this effect of ARB mutants causing mis-localisation of wild-type BEST1 is either an effect that occurs during overexpression in MDCK cells but not native RPE, or suggests that mis-localisation does not lead to dysfunction. Mis-localisation and proteasomal degradation appears to be a common feature of ARB mutations(Uggenti et al. 2016).

ARB cases lack the Vitelliform lesions seen in BVMD and AVMD, suggesting that the lesions are a gain-of-function effect. Mullins *et al.* hypothesised that the lower macular expression of BEST1 relative to the periphery(Skeie & Mahajan 2014; Mullins et al. 2007) allows for a smaller margin of error when one chromosomal copy of *BEST1* is mutated, as in Best Disease, explaining the central Vitelliform lesion(Mullins et al. 2007). It has also been hypothesised by Davidson *et al.* that in ARB the visible flecks are only seen in the periphery because *BEST1* is normally expressed at higher levels there and thus it is more sensitive to complete loss(Davidson et al. 2010). It is difficult to see these two hypotheses as anything other than contradictory.

4.1.6.3 Mechanisms of ADVIRC pathology

As a relatively newly described, relatively rare form of a relatively rare class of retinal disease, the number of known ADVIRC patients and mutations is currently quite low. Results that have been published on the effects of ADVIRC mutations on BEST1 properties and function suggest a role for alternative splicing. However the question has been raised as to what extent the cell lines used for these assays are representing native RPE.

Yardley *et al.* 2004 studied individuals in five families heterozygous for ADVIRC-causing mutation. All three mutations (V86M, Y236C, V239M) led to a missense substitution (as in BVMD and AVMD), but also in-frame deletions due to altered splicing, as assayed using a minigene expression system in a lens cell line (CRL-11421) and human embryological kidney cell line (CRL-1573). The authors hypothesised that the severity of the disease may be related to the ratio of the wild-type, missense and truncated isoforms(Yardley et al. 2004).

In 2009, Burgess *et al.* replicated the exon-skipping effect of Y236C using a splice assay in HEK293 cells. They also presented results suggesting an in-frame duplication of exon 6 in the ADVIRC mutant V235A, and altered binding of splicing-associated SR protein to both mutant sequences due to alteration of an exonic splice enhancer (ESE) site(Burgess et al. 2009). The authors suggest that the duplication itself is likely an artefact of the minigene assay, but that the mutation would produce some kind of splice variant *in vivo*.

In 2016, Chen *et al.* presented computational predictions that the ADVIRC G83D mutation would show altered binding of splicing-associated SR proteins. However, using the minigene splice assay in HEK293 cells they found no evidence of altered splicing for this mutant(Chen et al. 2016). This suggested that disrupted splicing might not be a universal feature of ADVIRC mutants.

The picture was further confused by findings published by Carter *et al.* in 2016. The authors examined induced pluripotent stem cell-derived RPE (iPS-RPE) derived from two sibling ADVIRC patients with the V235A mutation. Using PCR and western blot they found no evidence of alternative splicing. Further to this, they found that the V235A BEST1 protein localised to the apical membrane as well as the usual basolateral membrane localisation seen for wild-type BEST1. V235A BEST1 was previously reported to be appropriately basolaterally localised when overexpressed in MDCK cells, as were V86M, Y236C and V239M(Johnson et al. 2014). This suggests that the alternative splicing seen for V235A by Burgess *et al.* could be particular to the HEK293 line and/or an artefact of the minigene assay, while the normal localisation seen in MDCK cells could be particular to MDCK cells.

RPE-specific splicing effects have been shown previously in mouse models of retinitis pigmentosa (RP)(Graziotto et al. 2011). Here mutations in the mRNA processing factors PRPF3, 8 and 31, which are expressed ubiquitously, appear to only cause degenerative changes in the RPE. This suggests that RPE cells may be a unique environment for transcript processing, or at least unique enough that results from other epithelial cell lines cannot be used to generalise transcript behaviour in retinal cell types. RNA sequencing of the neural retina suggests high levels of retina-specific alternative splicing(Farkas et al. 2013).

As for the cellular localisation of ADVIRC BEST1, RPE cells are polarised as is typical of epithelial cells. Many RPE proteins have been found to be polarised in localisation, including those related to vital functions of RPE(Marmorstein 2001). Examples include proteins associated with the release of 11-*cis*-retinal or uptake of all-*trans*-retinal in the visual cycle, such as Ezrin and EBP50/NHERF1, which are found apically in association with the apical microvilli(Huang et al. 2009), and the phagocytosis-associated receptor MERTK which is also located apically(Subrizi et

al. 2012). However, the localisation of some proteins in RPE is atypical of epithelial cells in general. An example is sodium/potassium triphosphatase (Na^+/K^+-ATPase), which is localised apically in RPE(Hu et al. 1994; Vugler et al. 2008) rather than basally such as is found in kidney epithelium cell line MDCK(Caplan et al. 1986; Hammerton et al. 1991). This is not a general reversal of polarity: for example aminopeptidase, found apically in kidney epithelia, is also apical in RPE cells(Gundersen et al. 1991).

The question of whether the alternate-spicing seen in ADVIRC mutations is an artefact of non-RPE cells used for the expression assay or whether the ADVIRC BEST1 mis-localises will form the basis of the next experimental chapter. First the cell lines used to study *BEST1* will be examined.

4.1.7 RPE model cell lines for investigating ADVIRC

If localisation and splicing of BEST1 protein can vary between model cell lines as described above, this raises the question as to the validity of using non-RPE cell lines to model BEST1 function and disruption in Bestrophinopathies, and suggests that this could be one reason for a difference of opinion on the true roles of BEST1 in RPE cells. This is not an entirely new issue. Overexpressed *BEST1* in HEK293 cells is the standard model to compare channel activity and localisation of wild-type and BEST1 mutants. However, in HEK293 cells most BEST1 is retained intracellularly rather than localising to the membrane(Davidson et al. 2009; Davidson et al. 2011). MDCK cells are better in this regard, showing basolateral location that is visibly similar to RPE. However comparisons between BEST1 localisation between MDCK cells and mouse RPE suggests that the effect of mutations on BEST1 localisation can differ between these two cell lines(Johnson et al. 2013). The cell-type differences also raise questions about whether other aspects of BEST1 function could also differ between cell types.

As well as the kidney epithelial cell lines HEK293 and MDCK there also exist cell lines derived from primary RPE. However, while recapitulating some features of RPE, they have been shown to differ in some respects. For example, the RPE-J cell line was derived through infection of rat primary RPE cultures with a temperature-sensitive SV40 virus followed by clonal expansion, and shows many features of differentiated RPE such as apical microvilli, tight junctions, and melanosome synthesis. However they do not show the apical localisation of Na^+/K^+-ATPase or N-CAM(Nabi et al. 1993), suggesting some changes in polarisation. RPE-J cells also do not naturally express *BEST1*, a feature they share with two human-derived RPE model lines D407 and ARPE-19(Marmorstein et al. 2000). RPE cells *in vitro* lose their cobblestone appearance, undergo epithelial to mesenchymal transition (EMT), and appear to show altered ion channel expression over time, possibly reflected an identity shift towards a more neuronal phenotype(Reichhart & Strauß 2014).

4.1.7.1 Stem-cell derived RPE

A promising development in the study of *BEST1* and RPE is the use of stem-cell derived RPE. Within the early blastocyst the cells are pluripotent, capable of producing any of the three germ layers of the embryo, though not the extraembryonic tissues. These embryonic stem (ES) cells were isolated from first mouse(Evans & Kaufman 1981; Martin 1981) and then human embryos(Thomson et al. 1998).

Following the isolation of pluripotent stem cells from embryos it was discovered that a pluripotent state could be induced in adult cells through the expression of a few as four reprogramming factors(Takahashi & Yamanaka 2006). This not only meant that pluripotent stems cells could be produced without the use of human embryos, but importantly for the study of human disease these induced pluripotent stem (iPS) cells could be produced from individual patients with known genetic diseases from only a skin sample.

In 2004 RPE cells were produced from ES cells and shown to express the RPE makers CRALBP, PEDF and BEST1(Klimanskaya et al. 2004). ES-derived RPE (ES-RPE) were also shown to express OTX1/2, Pax6, PMEL17, RPE65, and MERTK, to be able to phagocytose porcine outer segments and were shown to survive after transplantation under rat retinas(Carr, A. Vugler, et al. 2009; Vugler et al. 2008). ES lines show variable tendency to differentiate into specific lineages such as pancreatic cells or cardiac cells(Osafune et al. 2008). This cell-line specific variability also applies to generation of RPE. For example, treatment with the small molecule BMP inhibitor dorsomorphin was found to increase efficiency in one line and decrease in another(Lane et al. 2014).

Production of RPE from iPS cells also proved relatively simple as they appear to spontaneously tend to differentiate along this fate, producing morphologically distinct RPE that can be grown as monolayers(Buchholz et al. 2009). The efficiency could be improved using Wnt and Nodal antagonists(Hirami et al. 2009), or small-molecule induction(Osakada et al. 2009). iPS-RPE have been shown to express the visual cycle genes LRAT, CRALBP, and RPE65(Muñiz et al. 2014), shown to phagocytose photoreceptor material both *in vitro* and *in vivo*, and stabilise vision loss when transplanted sub-retinally into the RCS rat (an animal model of RP, which shows RPE phagocytosis defects)(Carr, A. A. Vugler, et al. 2009).

ES- and iPS-derived RPE show similar morphology, transcriptional profiles, protein expression, and phagocytic function when compared to foetal RPE (fRPE), though global gene expression profiling suggest hESC-derived RPE are more similar to fRPE(Liao et al. 2010).

Much of the research on the production and function of stem cell-derived RPE is conducted to progress towards developing transplantation procedures as treatments for degenerative retinal

diseases. The retina is relatively immuno-privileged due to the blood-retinal barrier, the eye is very accessible for surgery and monitoring, and a monolayer of RPE cells is a relatively simple tissue to produce and transplant. In fact a phase-1 clinical transplantation of ES-RPE patches sub-retinally has shown improvement of vision in two AMD patients 12 months after surgery(Da Cruz et al. 2018).

Stem cell-derived RPE also show promise for investigating many diseases of the retina(Yvon et al. 2015), including Bestrophinopathies. iPS-RPE from BVMD patients showed disrupted fluid flux, build-up of autofluorescent waste material after long-term feeding with outer segments, delay in rhodopsin degradation and changes in calcium response relative to iPS-RPE from unaffected siblings(Singh et al. 2013). Use of patient-derived iPS-RPE has suggested BVMD mutations can affect the Ca^{2+}-activated Cl^- function in RPE, supporting similar results from overexpression studies in HEK293 cells(Moshfegh et al. 2016). iPS-RPE also show chloride currents with characteristic properties of VRACs that is greatly reduced when the iPS-RPE are produced from BMD patients, supporting the idea that BEST1 functions as a VRAC(Milenkovic et al. 2015).

4.2 Project aims

If stem cell-derived RPE are a much more faithful model of native RPE than kidney epithelial cell lines or immortalised RPE-derived cell lines then why not use them for all *BEST1* research from now on? Production of iPS cells is still an inefficient, expensive and time-consuming process, as is then differentiating them into useable quantities of RPE cells. This process also requires a (small) sample of each patient of interest to be reprogrammed, which may not always be possible. In addition transfection of iPS or iPS-RPE is much less efficient than model cells lines and so one is limited to whichever two copies of *BEST1* the patient has, which makes studying mutations in isolation difficult as there is not an appropriate isogenic control. Recent development of new gene editing technologies such as CRISPR mean that introducing patient mutations into iPS-RPE cells may soon be possible(Adli 2018), but for now transfection-overexpression studies using model cells lines represent a valid experimental approach, with the added advantage that the transfected cells are otherwise genetically identical.

Therefore the ARPE-19 cell line was chosen to assay the effects of ADVIRC mutations on BEST1 localisation and compare this to the localisation of the same mutant BEST1 proteins in HEK293 and MDCK cells. Below the ARPE-19 cell line will be described in terms of its appropriateness as a model for native RPE. Following that the research aims will be stated and background information on the *BEST1* mutations investigated will be given.

4.2.1 The ARPE-19 cell line

Since their isolation ARPE-19 cells have been used in a large number of studies as RPE and phagocytic models specifically and epithelial models generally. The ARPE-19 cell line was created from human retinal explants taken from a 19-year-old male(Dunn et al. 1996). After purification it was found to be rapidly growing, with a doubling time of approximately 24 hours, and despite the tendency of some of the lines to senesce, appeared to be spontaneously immortalised. During early culture and at confluency the cells showed cuboidal/columnar shape with the 'cobblestone' morphology typical of RPE cells *in vivo*, as well as pigmentation that increased over several weeks in static culture. The cells also were able to form domes, indicating vertical ion pumping. Unlike many other immortalised RPE lines, which show frequent aneuploidy, ARPE-19 cells appeared karyotypically normal other than a possible small deletion on the long arm of chromosome 8 and small addition to the long arm of chromosome 19. That said, analysis of more highly passaged cells identified heterogeneous chromosomal alterations(Fasler-Kan et al. 2018). The cells were also found to express cellular retinaldehyde-binding protein (CRALBP) and the RPE-specific RPE65, which are both found in RPE cells *in vivo*(Hamel et al. 1993; Bunt-Milam & Saari 1983). Transmission electron microscopy showed the presence of apical microvilli, junctional complexes between cells, and polarised organelle distribution, though pigment

granule distribution was not found to be polarised. Transplantation of ARPE-19 cells into the subretinal space of RCS rats was shown to improve vision as assayed head-tracking relative to sham operation(Lund et al. 2001), suggesting they are able to perform at least some RPE functions *in vivo*. However, comparisons with foetal RPE suggest that ARPE-19 are less uniform in size and shape, fail to metabolise all-*trans* retinal, have a lower trans-epithelial resistance, secrete vastly less PEDF, secrete less VEGF and do so apically instead of basally(Ablonczy et al. 2011).

Over multiple passages in subculture ARPE-19 cells transition from an epithelial to a more mesenchymal morphology, losing their cobblestone morphology and pigmentation and becoming more elongate and/or polygonal, and losing the integrity of their barrier function(Luo et al. 2006). It appears that the nature of the culture medium has a large influence on this process of 'de-differentiation', and typically a condition of low serum is used during RPE line culture in general. A condition of high glucose and high pyruvate has been shown to improve pigmentation and RPE-like gene expression(Ahmado et al. 2011). However, there is not consensus as to which basal mediums or supplements best support RPE-like identity in ARPE19 cells or indeed other RPE model lines(Kuznetsova et al. 2014). Work with chick RPE suggests that exposure of the apical or basal surface of an RPE monolayer to different culture medium can have differential effects(Peng et al. 2003).

Figure 4.3 shows unpublished RNA-sequencing data provided by Amanda Carr (Institute of Ophthalmology, UCL) and Monte Radeke, UCSB). Here ARPE-19 cells grown in DMEM medium, Miller medium, and X-VIVO 10 medium are compared to newly isolated human foetal RPE (fRPE) and fRPE after five passages in culture. It can be seen that over six weeks in X-VIVO 10 medium ARPE-19 show changes in the expression of many RPE-associated genes towards the profile seen in newly-isolated fRPE. C1QTNF5 is secreted by RPE and has been associated with Late-Onset Retinal Degeneration (L-ORD), a disease similar to AMD(Stanton et al. 2017). DOPAchrome tautomerase (DCT) expression is promoted by OTX2 and is involved in melanin biosynthesis(Takeda et al. 2003). Keratin 8 (KRT8) is a common epithelial marker gene may be involved in the regulation of response to oxidative stress(Baek et al. 2017). MERTK is a phagocytosis-associated receptor protein(D'Cruz et al. 2000). MITF is a transcription factor involved in RPE development and that appears to be related to prevention of oxidative stress(Hua et al. 2018). Its targets include TRP-1 and TYR. OCA2 (formerly called the P gene) is involved in melanin synthesis(Gardner et al. 1992; Rinchik et al. 1993). OTX2 is a transcription factor involved in RPE development and pigmentation(Esumi et al. 2009; Martínez-Morales et al. 2003). RLBP1 encodes the protein cellular retinaldehyde-binding protein (CRALPB), which is involved in the visual cycle and can cause RP when mutated(Maw et al. 1997). SERPINF1 encodes

the neuroprotective Pigment Epithelium-Derived Factor (PEDF)(Aymerich et al. 2001). TRPM1 and TRMP3 encode Transient Receptor Potential (TRP) channels, localised to the apical membrane in RPE(Zhao et al. 2015). TYR encodes Tyrosinase, a membrane protein involved in synthesis of melanin. TYRP1, or TYR-related protein 1, shows significant homology with TYR and is believed to have a similar function, though a recent study failed to find presence of the TYRP1 protein in RPE cells(Qiu et al. 2016). Note that RPE65 is only expressed in the freshly isolated fRPE and in no other line.

	ARPE-19 cells															Foetal RPE cells								
	Miller medium (days)			DMEM medium (weeks)						X-VIVO 10 medium (weeks)						Miller medium (passage number)								
	32	32	32	1	2	3	4	5	6	1	2	3	4	5	6	0	0	0	0	0	0	5	5	5
BEST1	0	0	0	0	0	0	0	0	0	0	0	1	2	3	1	100	65	85	73	47	81	0	0	0
C1QTNF5	2	3	2	4	7	3	6	5	5	24	31	55	64	81	100	27	30	27	27	11	23	1	1	1
CDH1	0	0	0	2	3	4	5	6	9	7	18	13	12	13	9	23	44	100	29	40	20	1	5	0
CLDN19	0	0	0	0	0	0	0	0	0	0	0	0	0	0	0	64	87	51	100	32	92	0	0	0
DCT	3	6	3	0	0	0	0	0	0	1	2	8	20	40	37	82	65	54	71	91	100	0	0	0
EYA2	25	7	10	4	4	9	6	4	10	4	4	4	4	7	4	27	36	100	5	11	42	46	7	12
EYA2	25	7	10	4	4	9	6	4	10	4	4	4	4	7	4	27	36	100	5	11	42	46	7	12
ITGB8	6	9	5	2	0	4	1	3	4	7	8	6	11	16	16	44	50	52	45	100	68	1	1	1
KRT8	6	5	6	57	100	48	94	38	39	25	17	13	8	8	7	3	3	3	3	3	3	25	16	27
LHX2	36	34	53	64	100	49	82	55	53	77	77	76	66	96	88	73	79	99	75	44	51	18	23	25
LRAT	0	0	0	0	0	0	0	0	0	0	0	0	0	1	1	26	17	100	14	58	49	0	0	0
MERTK	7	11	17	3	3	4	4	5	7	2	5	11	23	24	30	84	65	100	75	70	70	4	11	7
MITF	34	46	28	26	6	34	14	36	29	48	56	56	97	81	75	70	80	76	84	100	95	13	16	14
MYCN	100	62	85	0	0	0	0	0	0	0	0	0	0	0	0	0	0	0	0	0	0	0	0	0
MYO7A	12	9	10	23	41	22	34	22	26	41	46	79	71	82	100	32	24	22	18	16	18	0	0	0
OCA2	0	0	0	0	0	0	0	0	0	0	2	14	25	35	33	89	71	62	100	71	78	8	5	4
OTX2	19	21	19	16	8	14	8	15	15	36	42	48	66	67	59	100	83	94	98	85	79	5	6	7
PAX6	16	19	21	51	21	73	38	65	63	60	55	77	54	57	75	8	7	15	7	9	7	55	100	59
PMEL	0	0	0	0	0	0	0	0	0	4	9	18	18	15	11	75	83	66	100	55	75	0	0	0
PTGDS	0	0	0	0	1	0	0	0	0	3	4	18	27	53	71	84	100	68	80	33	56	0	0	0
RAX	26	13	26	18	28	14	8	11	11	21	27	54	60	83	100	13	22	26	18	6	10	0	1	0
RBP1	2	4	3	14	21	9	28	13	14	8	9	17	22	25	31	56	70	100	46	69	68	7	20	16
RLBP1	0	0	0	1	2	1	2	1	1	3	12	26	39	41	42	79	61	100	89	38	74	0	0	0
RPE65	0	0	0	0	0	0	0	0	0	0	0	0	2	2	1	53	50	100	37	67	82	0	0	0
SERPINF1	2	2	2	0	0	0	0	0	0	2	6	25	36	48	56	67	100	54	70	35	50	0	0	0
SIX3	36	57	60	46	73	46	47	34	40	28	34	45	51	73	83	35	45	100	41	29	33	16	20	21
SOX11	1	1	1	1	1	1	1	1	1	1	1	1	1	1	1	21	16	13	18	32	17	58	100	56
TJP1	12	13	12	21	4	31	8	20	24	41	37	22	25	23	21	74	58	46	73	100	69	32	40	41
TRPM1	1	1	0	0	0	0	0	0	0	6	10	11	17	19	18	69	34	100	95	83	69	0	0	0
TRPM3	0	1	0	0	0	2	1	3	3	14	32	52	100	92	84	66	65	84	61	81	72	12	10	8
TYR	1	2	0	1	1	2	3	4	5	40	65	86	100	66	63	29	31	47	37	24	42	1	1	1
TYRP1	0	1	0	0	0	0	0	1	1	10	35	73	94	79	77	45	86	46	100	61	75	0	0	0

Figure 4.3 Heat-map of RNA-seq expression data comparing ARPE19 cells maintained in three different culture media and foetal RPE before and after passage. Rows indicate genes assayed and columns indicate the biological sample measured and the culture medium. Values indicate relative expression levels relative to the highest measured level in that row (which is given the value of 100), and are rounded to the nearest integer. A heatmap overlay has been applied, blue=low to red=high. Data courtesy of Amanda Carr, UCL, and Monte Radeke, UCSB.

This supports previous findings that culture medium can significantly affect RPE-derived cell identity and suggests that there may be significant differences between ARPE-19 cells incubated in DMEM and those incubated in X-VIVO 10.

4.2.2 Experimental questions

As already stated, minigene splice assays of ADVIRC mutants in kidney cells has suggested that deletions or duplications within the BEST1 protein are causing the pathology. However analysis of BEST1 in iPS-RPE cells derived from two ADVIRC siblings suggests that the V235A mutation causes mis-localisation and not mis-splicing, implying that *BEST1* expression in kidney epithelial cells is not a good model for expression in RPE. With that in mind the following aims formed the basis for the experimental data presented in this chapter.

Does wild-type BEST1 localise to the basolateral membrane in ARPE-19 cells as it does in iPS-RPE? Does the V235A mutation show mis-localisation in ARPE-19 cells relative to the wild-type, as is seen in iPS-RPE cells?

The use of ARPE-19 cells as a model for native RPE is dependent on the assumption that BEST1 is trafficked the same as in iPS-RPE cells so first they must be compared for both the wild-type and the V235A of known location in iPS-RPE.

Does localisation of wild-type or V235A mutant BEST1 depend on the model cell type in which they are expressed?

Any differences seen in localisation between transfected MDCK, HEK293, and ARPE-19 cells would suggest that BEST1 localisation is cell-type dependent.

Do any of the other four ADVIRC mutations show mis-localisation in ARPE19 cells relative to the wild-type?

No localisation analysis has yet been published for any of the other four ADVIRC mutations shown below. If mis-splicing is not found to be a common factor then mis-localisation might be.

4.2.3 *BEST1* mutants used in this study

Table 4.2 shows the 5 ADVIRC mutations used in this study, as well as 2 ARB mutations that have previously been shown to mis-localise in MDCK cells. The location of these mutations is also shown in **Figure 4.4**, adapted from Boon *et al.,* 2009(Boon et al. 2009). According to this structure all five ADVIRC mutations lie in putative transmembrane domains, while both ARB mutants lie in intracellular domains. The locations of the mutations are also shown in **Figure 4.5** and **Figure 4.6**, adapted from more recent work by Dickson *et al.*, 2014(Dickson et al. 2014). Here their crystallography-based model places all five ADVIRC mutants just intracellularly of the transmembrane domains.

Genetic mutation	Protein substitution	Disease phenotype	References and findings	
248 G>A	G83D	ADVIRC	**Chen *et al.*, 2016** (Missense substitution, but despite computational predictions no alterations in splicing seen in HEK293 cells)	
256 G>A	V86M	ADVIRC	**Vincent *et al.*, 2011** (for phenotype)	**Yardley *et al.*, 2004** (Missense substitution and in-frame deletion seen in lens cells (CRL-11421) and human embryological kidney cells (CRL-1573)
704 T>C	V235A	ADVIRC	**Burgess *et al.*, 2009** (Missense substitution and exon duplication seen in HEK293 cells)	**Carter *et al.*, 2016** (Mislocalisation in iPS-RPE cells
707 A>G	Y236C	ADVIRC	**Burgess *et al.*, 2009** (Missense substitution and in-frame deletion seen in HEK293 cells)	**Yardley *et al.*, 2004** (Missense substitution and in-frame deletion seen in lens cells (CRL-11421) and human embryological kidney cells (CRL-1573)
715 G>A	V239M	ADVIRC		**Yardley *et al.*, 2004** (Missense substitution and in-frame deletion seen in lens cells (CRL-11421) and human embryological kidney cells (CRL-1573)
598 C>T	R200X	ARB	**Burgess *et al.*, 2008** (Non-sense mutation)	**Johnson *et al.*, 2014** (Mislocalised to intracellular compartments in MDCK cells)
974 T>C	M325T	ARB	**Davidson *et al.*, 2011** (Mislocalised and degraded in MDCK cells)	**Johnson *et al.*, 2014** (Mislocalised to intracellular compartments in MDCK cells)

Table 4.2 Details of the 5 ADVIRC and 2 ARB mutations used in this study. The genetic nucleotide substitution and protein residue substitution are given, along with relevant references for the effects on the BEST1 protein.

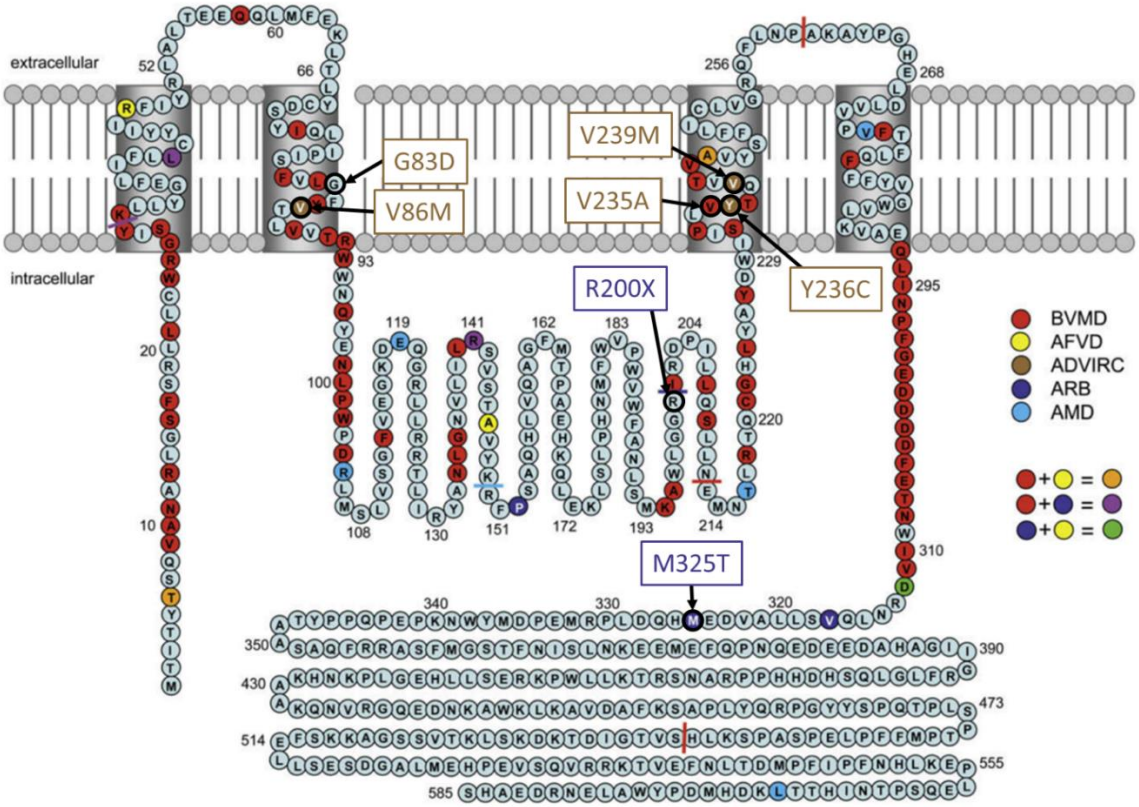

Figure 4.4 Locations of the 5 ADVIRC and 2 ARB mutations used in this study within the BEST1 protein sequence, adapted from Boon *et al.*, 2009. Locations of mutations known to cause retinal dystrophy are shown according to the colour-coding on the right. locations of mutations used in this study are labelled.

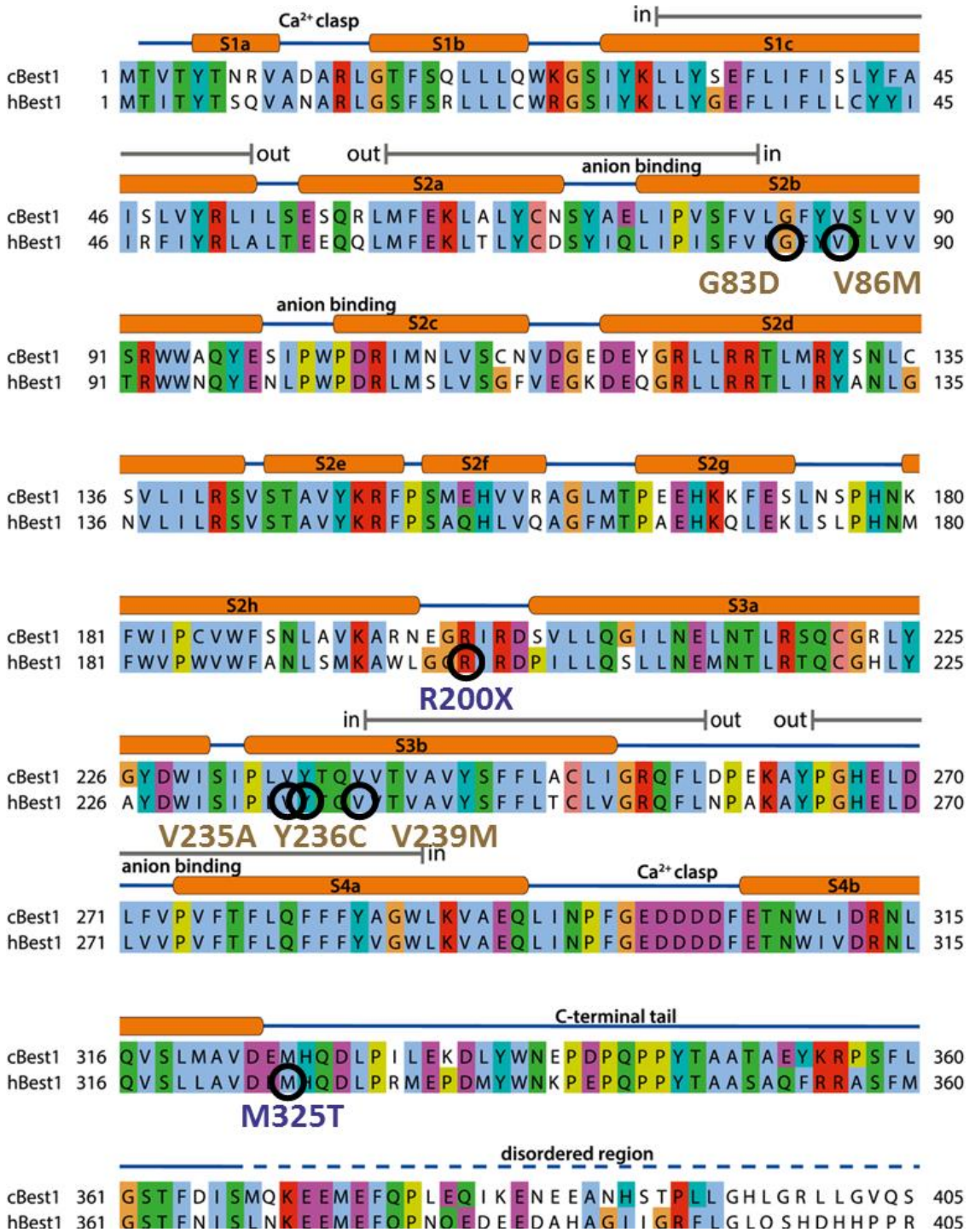

Figure 4.5 Locations of the 5 ADVIRC and 2 ARB mutations used in this study within the BEST1 protein sequence, adapted from Dickson *et al.,* 2014. Mutations are colour coded, ADVIRC in brown, ARB in purple.

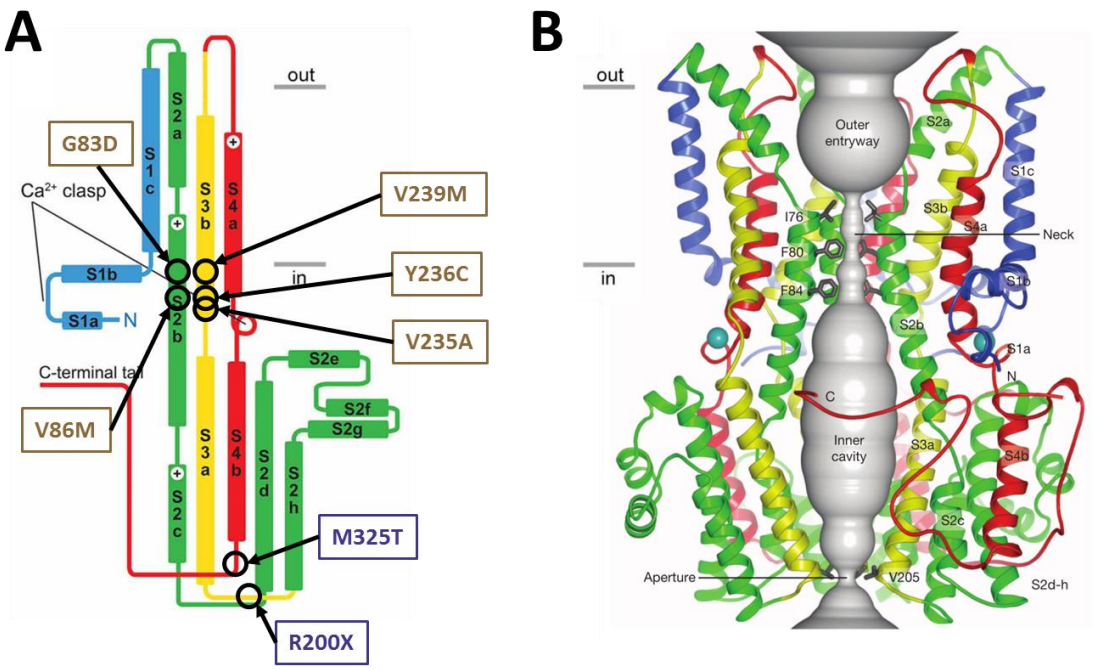

Figure 4.6 Locations of the 5 ADVIRC and 2 ARB mutations used in this study within the BEST1 protein structure, adapted from Dickson *et al.*, 2014. A) Schematic of the transmembrane structure of monomeric BEST1 with the approximate locations of mutations used in this study marked. Mutations are colour coded, ADVIRC in brown, ARB in purple. B) Pore structure of BEST1 pentamer.

4.3 Materials and methods

4.3.1 Cell culture

4.3.1.1 Culture media

All cells were cultured at 37°C, 5% CO_2. Two different base media were used to culture the human cells in this section. In almost all cases high glucose Dulbecco's Modified Eagle Medium (DMEM) with pyruvate (41966029, Thermofisher) with 10% Foetal Bovine Serum (FBS, 16000044, Thermofisher) and Pen/Step (15140-122, Gibco) was used. In following chapters it will be referred to as "DMEM" or "standard culture medium."

For differentiation experiments X-VIVO 10 (LZBE 04-743Q, Lonza) medium with 50µg.ml^{-1} Gentamicin (15750-037, Thermofisher) was used.

For culture of ARPE19 prior to RNA sequencing DMEM with 1% FBS and Pen/Step was used. Another medium used prior to RNA sequencing was Miller medium(Maminishkis et al. 2006), the formulation of which is given below:

For 500ml Miller medium:

α-MEM (Sigma #M4526)	450ml
5% Foetal Bovine Serum (FBS) (heat-inactivated,Hyclone #SH30088.03 HI)	25ml
1x N1 Supplement (Sigma #N6530)	5ml of 100x stock
1x NEAA (Invitrogen #11140-050)	5ml of 100x stock
2mM L-glutamine or GlutaMAX I (Invitrogen #35050-061)	5ml of 100x stock
125mg Taurine (Sigma #T-0625)	
125mg → add solid to 10ml α-MEM to solubilize	
10µg Hydrocortisone (Sigma #H-0396)	
4µl of 2500µg.ml^{-1} stock (Stock = 0.05g into 20ml PBS; sterile filter)	
0.0065µgTriiodoThyronin (Sigma #T-5516)	13µl of 0.5µg/ml stock
1x Normocin (optional antibiotic, Invivogen #ant-nr-2)	1mL of 500x stock

Prepare supplemented media and filter through a 0.22µm bottle top filter before use.

4.3.1.2 Culture dishes and coating

ARPE19, MDCK, HEK293 and GP2-293 cells were all cultured in DMEM medium on standard uncoated plastic cell culture dishes and flasks (178883, 136196, 140675, 142475, Thermofisher). When confluent cells were rinsed with Dulbecco's Phosphate Buffered Saline (DPBS) without Ca^{2+} and Mg^{2+} (DPBS, H15-002, PAA) and incubated with TrypLE™ cell dissociation enzyme (12604-013, Thermofisher) for 5-10 minutes to detach the cells for replating. In the case of GP2-293 cells they were split 1:10 when confluent, which was around every 3 days. Care was taken when aspirating as GP2-293 cells detach easily from the culture plastic.

For long-term differentiation culture of ARPE19 cells, 8-well chamber slides (C7182-1PAK, Nunc) were coated with Matrigel 9354277, BD Biosicencess) at 37^{O}C for at least one hour before plating cells.

4.3.1.3 Freezing and thawing cells

APRE19, MDCK, HEK293, and GP2-293 cells were frozen and thawed according to the same protocol. For freezing, cells were rinsed with Dulbecco's Phosphate Buffered Saline without Ca^{2+} and Mg^{2+} (DPBS, H15-002, PAA) and incubated with TrypLE™ cell dissociation enzyme (12604-013, Thermofisher) for 5-10 minutes to detach the cells. DMEM medium was added and the cells were transferred to a 15ml falcon tube (E1415-0200, StarLab), and centrifuged at 200G for 5 minutes. The medium was aspirated off and the cells were resuspended in 1ml of freezing medium (60% high glucose Dulbecco's Modified Eagle Medium with pyruvate (41966029, Thermofisher), 30% Foetal Bovine Serum (FBS, 16000044, Thermofisher), and 10% DMSO (D12345, Invitrogen). This was transferred to a standard 1.5ml cryovial. The cryovial was placed inside a small polystyrene box to buffer temperature changes and placed at -80^{o}C overnight. The next day the vial was transferred to liquid nitrogen storage.

For defrosting, cryovials were incubated at 37^{o}C to defrost and then mixed with pre-warmed standard culture medium in a 15ml falcon tube. This was then centrifuged at 200G for 5 minutes and the freezing medium/standard culture medium mix aspirated off. The cells were re-suspended in pre-warmed standard culture medium and transferred to the culture flask or plate to attach.

4.3.2 RNA sequencing of foetal RPE and ARPE19 cells

Experiments were performed and ARPE-19 samples were prepared by Amanda Carr (UCL, London, UK) and sent to Monte Radeke (UCLA, California, USA) according to the protocol provided by Amanda Carr as follows:

For the DMEM and XVIVO medium expression time-courses ARPE19 cells were used at passage 25. Foetal RPE cells were acquired from Professor Dean Bok (UCLA, USA) and kept in Miller medium before harvesting. X-VIVO 10 medium (Lonza) was used without serum or antibiotics added. DMEM medium (Thermofisher) was used with 1% foetal bovine serum (FBS) and Pen/Strep antibiotics added.

On the day of RNA collection the cells were washed with DPBS prior to adding Tri-reagent to the cells. This was followed by vigorous scraping of the cells and placing the samples in 1.5ml RNase/DNase free centrifuge tubes. The samples were sent to Dr Monte Radeke (UCLA, California, US), who performed the sequencing. Total RNA was purified according to manufacturer's instructions using a miRNeasy Mini Kit (QIAGEN). Poly(A)+ RNA was purified

from 1mg of total RNA according to manufacturer's instructions using the Magnetic mRNA Isolation Kit (New England BioLabs Inc.) and used to generate RNA-Seq libraries using the Ion Total RNA-Seq Kit V2 (Life Technologies). The resulting libraries were sequenced on Ion PGMTM (Life Technologies) or Ion ProtonTM (Life Technologies) next generation sequencers using Ion PITM Sequencing 200 Kit v3 (Life Technologies). Base calling was carried out using the default parameters in Torrent SuiteTM software 4.4 (Life Technologies). Sequence results were aligned to the human transcriptome and genome (hg38) using a 2-stage pipeline employing TopHat2(Kim et al. 2013) and Torrent Mapping Alignment Program (TMAP, Life Technologies) read aligners. The ten 5-prime bases from each sequence were trimmed using FASTX Trimmer 0.0.14 Toolkit. Sequences with a remaining length greater than 49 bases were then aligned to the human genome (hg38 +45S-RNA and 5S-RNA bait sequences) using TopHat 2.0.12 and Bowtie2 2.2.3 softwares. Settings were optimised for variable read-length Ion Torrent sequences: read-mismatches = 4, read-gap-length = 4, read-edit-dist = 8, max-multihits = 1, b2-1 =S,1,1.15, b2-rdg =5.2. Unmapped sequences were aligned using TMAP 3.4.1 using 5-prime and 3-prime soft-clipping (g = 0). The resulting TopHat and TMAP alignments were merged into a single alignment file and any sequences mapping to the 45S or 5S RNA bait were deleted. The number of reads per mRNA coding gene was determined using Partek Genomics Suite® software 6.6 (Partek®, USA) and the hg38 RefSeq Transcript annotation (17-10-2014). Only reads aligned to exons were considered in the determination of the number of reads per gene. In case there were two sequencing runs for the same condition the alignment results were combined prior to quantification. Any fractional read count values were rounded to the nearest integer. The data set for all samples was normalised using the TMM normalisation method(Oshlack et al. 2010). Differential expression analysis was carried out using edgeR(Robinson et al. 2009; McCarthy et al. 2012). Messenger RNA gene level results for the iPSC-derived RPE data were normalised using the TMM method(Robinson et al. 2009) as implemented by "edgeR". Using the raw integer read counts for genes with a RefSeq accession of "NM_" as input, the normalisation factor and number of aligned mRNAs for each sample was determined. The final processed normalised data was expressed as reads per million aligned reads (RPM) where RPM = raw read count x 1x106/norm.factor x lib.size. All identified genes with false discovery corrected p-value (FDR) 0.005 and 1.5-fold change for pR200X:control fibroblast, iPSC and iPSC-derived RPE data were used for online David Bioinformatics Database to perform gene functional categories enrichment analysis.

4.3.3 Retroviral transfection

Retroviral transfections were performed based on the manufacturer's protocol, which can be found here: https://www.biomol.de/dateien/RetroMaxManual.pdf

Day1: 10cm^2 plastic cell culture dishes (150350, ThermoFisher) were coated with 5ml of 0.1% gelatin (8153066, ThermoScientific) and incubated for 10-30 minutes at 37^{o}C. The gelatin was aspirated off. GP2-293 cells were split 1:5 onto the plates in standard culture medium.

Day 2, morning: In a 15ml falcon tube (E1415-0200, StarLab) was added 7.5ul of 100x PO_4 and 375ul 2xHBS. In a 1.5ml Eppendorf was added 15ug of PCLNC plasmid construct, 5ug of envelope plasmid (pMD.G), 10 ug of the carrier plasmid pBluescriptSK (pBSK), ddH_2O to 372.5ul, then 45ul of 2M $CaCl_2$. The mix from the Eppendorf was added dropwise to the mix in the flacon tube while using a pipetteboy and 2ml stripette to bubble air through the mix in the falcon tube. The combined mix including precipitate was collected using a Pasteur pipette and added dropwise to the GP2-293 cells. The plate was then gently swirled to mix and incubated at 37^{o}C for 6 hours. The medium was replaced with fresh standard DMEM and incubated overnight at 37^{o}C.

Day 3, morning: The medium was replaced with fresh standard medium.

Day 4: Cells for transfection (ARPE19, HEK293, or MDCK) were split into T25 flasks with 3.5x10^5 cells per flask in standard medium.

Day 5, morning: In a 15ml falcon tube was added 1ul polybrene (40mg.ml^{-1} stock) and 1ml FBS. The viral medium was removed from the GP2-293 cells and added to the falcon tube. This was mixed gently and then filtered through a 0.45 micron filter using a syringe into a 50ml falcon tube. 10ml of standard medium was added to bring the volume total to around 20ml. Three 5ml aliquots were removed and stored at 4^{o}C. The remaining 5ml was added to the target cells after the previous medium had been aspirate off. This was incubated at 37^{o}C. In the evening one of the 5ml aliquots was warmed to 37^{o}C and the transfection medium on the cells was replaced.

Day 6: In the morning and again in the evening the viral medium was replaced with pre-warmed 4^{o}C aliquots.

Day 7, 8, 9: The viral medium was replaced with standard medium and then the cells were fed once per day. Control pCLNC-GFP transfected cells were checked for GFP expression from day 9.

4.3.3.1 Buffers

2xHBS (500ml)

HEPES 5g

NaCl 8g

Dissolve in 400ml H_2O

Adjust to pH 7.1 with 10M NaOH

Bring to 500ml with H_2O

Autoclave, store at room temperature.

100xPO_4

Na_2HPO_4 (Mw 142) 4.97g

NaH_2PO_4 (Mw 120) 4.2g

Dissolve in 400ml H_2O

Bring to 500ml with H_2O

Autoclave, store at room temperature.

2M $CaCl_2$

73.5g

Dissolve in 250ml H_2O.

Autoclave, store at room temperature.

4.3.4 Immunocytochemistry

A list of primary and secondary antibodies used are shown in **Table 4.3**.

Target	Antibody	Species	Dilution for immunocyto chemistry	Dilution for western blotting	Company	Catalogue number
Mouse monoclonal to BESTROPHIN1	Primary	Mouse	1:500	1:1000	Abcam	ab2128
Rabbit oligoclonal to FLAG (DYKDDDDK)	Primary	Rabbit	1:500	1:500	Invitrogen	710662
(DYKDDDDK)-Alexa Fluor 488 conjugate	Primary	Rabbit	1:100	1:500	Invitrogen	MA1-142-A488
Goat polyclonal to GAPDH	Primary	Goat		1:1000	Everest	EB07069
Rabbit monoclonal to MERTK	Primary	Rabbit	1:100		Abcam	ab52968
Mouse monoclonal to EZRIN	Primary	Mouse	1:100		Santa Cruz Biotechnology	sc-58758
Polyclonal goat anti-rabbit immunoglobulins/HRP	Secondary	Goat		1:2000	Dako	P0448
Polyclonal goat anti-mouse immunoglobulins/HRP	Secondary	Goat		1:2000	Dako	P0447
Polyclonal rabbit anti-goat immunoglobulins/HRP	Secondary	Rabbit		1:2000	Dako	P0449
Donkey Anti-Mouse IgG H&L (Alexa Fluor® 555) (ab150106)	Secondary	Donkey	1:500		Alexa	ab150106
Donkey Anti-Rabbit IgG H&L (Alexa Fluor® 488) (ab150073)	Secondary	Donkey	1:500		Alexa	ab150073
Donkey Anti-Mouse IgG H&L (Alexa Fluor® 488) (ab150105)	Secondary	Donkey	1:500		Alexa	ab150105
Donkey Anti-Rabbit IgG H&L (Alexa Fluor® 555) (ab150074)	Secondary	Donkey	1:500		Alexa	ab150074

Table 4.3 List of antibodies used in this chapter for Western blotting and immunocytochemistry

Cells were fixed *in vitro* in 4% paraformaldehyde (PFA) for 30 minutes at 4°C. The cells were washed 3 times with phosphate buffered saline (PBS) and stored at 4°C in PBS before staining. Staining was performed as soon afterwards as possible, within 48 hours.

Cells were permeablised in 0.3% Triton-X-100™ (341973r, BDH) detergent for 10 minutes. The cells were then washed 3 times in PBS.

The PBS was poured off and the cells were blocked in blocking solution made from 5% normal donkey serum (017-00-121, Jackson Immunoresearch) and 3% bovine serum albumen (BSA) (A9418, Sigma) in PBS. They were incubated at 4°C for 30-60 minutes.

The blocking solution was poured off and the primary antibody added in the same blocking solution. This was incubated at 4°C overnight (around 16 hours).

The cells were washed 5 times with PBS and the secondary antibody was added in blocking solution. This was incubated for 30-60 minutes. The secondary antibody was poured off and the cell were washed 5 times with PBS.

Excess PBS was drawn off with tissue and a few drops of Vectorshield with DAPI nuclear stain (H-1200, VECTOR laboratories) were added. A glass coverslip was placed on top with tweezers. Excess Vectorshield was drawn off with tissue. Nail polish was used to seal the edges of the coverslip and left to dry in darkness for at least 120 minutes before storage and imaging.

4.3.5 Western blot

A list of primary and secondary antibodies used can be found in **Table 4.3**.

4.3.5.1 Preparing protein samples

The live cells were transferred in their culture dish or flask onto ice. Here they were washed 2x in ice-cold PBS and aspirated. 1ml of lysis buffer was added per plate well or flask and the cells were scraped from the culture plastic with a plastic cell scraper. The cell suspension in lysis buffer was then transferred to a 1.5ml Eppendorf tube. This was then incubated at 11°C on a rotator for 30 minutes, and then spun at 13,000RPM on a tabletop centrifuge at 4°C for 30 minutes. The supernatant was transferred to a fresh 1.5ml Eppendorf tube and the pellet was frozen down.

Protein concentrations were estimated using the BioRad assay kit. 795ul of H_2O was added to 5ul of the sample and 200ul of the 5x Biorad protein assay dye (500-0006) inside the light-path cuvette. This was mixed and incubated at room temperature for 10 minutes. The absorbance was read at 595nm wavelength.

The rest of the protein solution was split in half and reducing or non-reducing running buffer was added to each. The reducing samples were boiled at 95°C for 5 minutes before freezing at -18°C. The non-reducing samples were stored at -18°C and boiled before running.

4.3.5.2 *Running western blot*

Western blots were running using a BioRad electrophoresis tank (Mini-PROTEAN® Tetra Vertical Electrophoresis Cell), precast gels (4–20% Mini-PROTEAN® TGX™ Precast Protein Gels, 10-well, 50 µl #4561094), transfer packs (Trans-Blot® Turbo™ Mini PVDF Transfer Packs #1704156), transfer system (Trans-Blot® Turbo™ Transfer System #1704150) and Lumi-Light detection solutions (12015200001, Roche Life Science, UK). This was performed according to a protocol based on the manufacturer's instructions, which can be found here: (http://www.bio-rad.com/webroot/web/pdf/lsr/literature/10007296D.pdf).

4.3.5.3 *Running the electrophoresis*

The precast gel was removed from its packaging and the comb and basal green strip were removed. The gel was placed into the electrode assembly with the wells facing inwards. If only one gel was being run then the plastic buffer dam was placed opposite, otherwise the two gels were inserted facing each other. Fresh 1x running buffer made up with distilled water from the 10x Tris/Glycine/SDS stock was added inside the dam to above the wells and outside to the mark indicated on the electrophoresis tank. The protein samples in running buffer were added using long pipette tips to the wells, being careful to avoid overspill. Standard protein ladders were used at either end (Precision Plus Protein™ Dual Color Standards, 500 µl #1610374). The lid was placed on the tank and the electrophoresis was run at 100 volts for 10 minutes and then 250 volts until the dye began to run off the gel.

4.3.5.4 *Transferring the proteins*

The gel was carefully removed and placed on the anode stack from the transfer pack, keeping the gel moist with running buffer from the tank. The anode stack was placed in the transfer cassette just before this. Bubbles were removed using the roller and the top ion stack was placed on top, again removing bubbles with the roller. The cassette was closed and placed into the blot transfer system. The gel type was selected and the program run. Once the protein transfer had been completed the cassette was removed and opened.

4.3.5.5 *Blocking the membrane*

The blotting stack and gel were discarded and the transfer membrane was transferred to 0.05% PBS-Tween, keeping it moist at all times. The PBS-Tween was poured off and 10ml blocking solution added (10% milk, 5g milk powder in 50ml 0.05% PBS-Tween(P1379, Sigma-Aldrich) inside a 50ml falcon (the blot was rolled up to fit). This was incubated on a rolling mixer for 2 hours.

4.3.5.6 *Primary antibodies*

Primary antibodies were added directly to the blocking solution in the 50ml falcon. And incubated overnight at room temperature.

4.3.5.7 Secondary antibodies

The blot was transferred to a plastic dish and washed three times with PBS-Tween, incubating on a rocking mixer for 15 minutes between washes. Secondary antibodies were added in 10% block again and incubated on the rocking mixer for 45-120 minutes. The secondary antibody was then poured off and the membrane was washed two times in PBS-Tween for 15 minutes each.

4.3.5.8 Imaging

The wash buffer was poured off a d 3ml of the lumi light enhancer solution was added, followed by 3ml of the lumi light perioxide solution. This was incubated on the shaker for 5 minutes.

The blot was then transferred to a ChemiDoc™ XRS+ System for imaging using ImageLab software (BioRad). The blot was sprinkled with excess solution to keep it moist during imaging.

4.3.5.9 Buffers

Lysis buffer

Per 1ml:

10 µl 0.5mM HEPES

200 µl 5% Triton-X

150 µl 1M KCl

10 µl PMSF (100mM)

1 µl Leupeptin (10ug/ml)

1 µl DTT (1M)

5 µl Aprotonin (10mg/ml)

10 µl NaF (1M)

0.5 µl Sodium Vanadate (200mM)

612.5 µl H_20

2x loading buffer (Shalini)

1.25ml Tris pH8.6 (Final 18.75mM)

2ml 20% SDS (final 4%)

4ml 50% glycerol (final 20%)

2.5ml H_2O

0.1% bromophenol blue (0.01g)

For reducing buffer only add 40 µl β-mercaptoethanol per 2ml buffer.

4.3.5.10 Stock solutions – store at -20°C

Aprotonin: reconstitute in H_2O to 10ug.ml^{-1}.

DDT: reconstitute in H_2O to 1M solution.

Leupeptin: dilute in H_2O to 10ug/ml.

PMSF: Reconstitute in 100% ethanol to 100mM.

NaF: reconstitute in H_2O to 200mM.

Sodium orthovanadate: prepare in a fume hood. Make a 100nM solution in ddH_2O. Add HCl to pH9.0. Boil until colourless, covering loosely. Cool to room temperature. Add HCl to pH9.0 again. Boiling again until colourless. Repeat until pH remains at pH9.0 after boiling and cooling. Add ddH_2O back to initial volume. Store at -20^oC. Discard if solution turns yellow.

4.3.6 Genomic DNA extraction

This was performed using the GenElute™ Mammalian Genomic DNA Miniprep Kit (G1N70, Sigma) according to the manufacturer's instructions. 25cm^2 of confluent cell monolayer was used for each extraction. This was dissociated using TrypLE™ and centrifuged at 300G for 5 minutes to collect the cells, which were then resuspended in 200µl resuspension solution (without RNase A treatment). 20µl of proteinase K (20$mg.ml^{-1}$) was added and then 200µl of lysis solution C was added. This was vortexed for 15 seconds. This was then incubated at 70^oC for 10 minutes. 500µl of column prep solution was added to each column. This was centrifuged at 12,000G for 1 minute and the flow-through was discarded. 200µl of ethanol was added to the cell lysate. This was vortexed for 10 seconds and the solution was transferred to the column. This was centrifuged at 6,500G for 1 minutes. The flow-through was discarded. The column was placed in a fresh tube, 500µl of wash solution was added and was centrifuged at 6,500G for 1 minute. The column was placed in a fresh tube, 500µl of wash solution was added and was centrifuged at 6,500G for 1 minute. The flow-through was discarded and the column was centrifuged for a further 2 minutes. The column was placed in a collection tube. 200µl of elution solution was added and incubated for 5 minutes. The column was centrifuged at 6,500G for 1minute and the flow-through used for downstream application.

4.3.7 Microscopy

Images presented were all acquired using either an EVOS FL Cell Imaging System (Invitrogen) or using a Zeiss LSM 700 upright confocal microscope.

4.3.8 PCR amplification

PCR amplification protocols were conducted using GoTaq DNA Polymerase (M3171, Promega) or Platinum Blue PCR SuperMix (12580015, Invitrogen) according to the manufacturer's instructions. For cloning protocols including Site-Directed Mutagenesis protocols Phusion® High-Fidelity DNA Polymerase (M0530S, NEB) or Phusion High-Fidelity PCR Master Mix with HF Buffer (F531S, Thermo Scientific) was used due to its higher amplification fidelity.

4.3.9 DNA sequencing

In a standard PCR tube was added 4µl BigDye™ (4458687, Applied Biosystems), 1µ BigDye sequencing buffer, 1µl sequencing primer, around 100µg target DNA, and ddH_2O to a total of 10µl. This was incubated at 96°C for 60 seconds, then subjected to 40 cycles of: 96°C for 10 seconds, 50°C for 5 seconds, 60°C for 240 seconds. It was then stored at 4°C until the next step. The DNA was precipitated by adding 0.5µl 0.5M EDTA, then 2µl 3M NaOAc, then 50µl ethanol. The solution was transferred to a 0.5ml Eppendorf tube and incubated at room temperature for 15 minutes. The tube was spun at 13,000RPM using a tabletop centrifuge for 40 minutes. The supernatant was removed and 50µl of 70% ethanol was added. This was spun at 13,000RPM for 10 minutes then the supernatant was removed and the pellet dried in a 95°C heatblock for 30 seconds. The pellet was dissolved in 12µl of Hi-Di Formamide (4311320, Applied Biosystems) and the DNA denatured at 95°C for 5 minutes. The solution was placed on ice for at least 2 minutes before storage at 4°C or immediate loading for sequencing. Sanger sequencing was performed by Naushin Waseem and Beverley Scott.

4.3.10 Cloning

4.3.10.1 Site-directed mutagenesis

Site-directed mutagenesis reactions were performed using the GeneArt™ Site-Directed Mutagenesis System (A13282, Invitrogen).

4.3.10.1.1 Methylation and mutagenesis reactions – to amplify the plasmid with the base substitution

The following components from the Geneart kit and Phusion polymerase kit were combined in a PCR tube on ice. 1µl of dNTPs, 10µl 10x phusion HF buffer, 0.5µl phusion polymerase, 5µl 10x enhancer, 1.5µl primer mix, 1µl 20ng/µl DNA template, 1µl DNA methylase, 2µl SAM, 28µl ddH_2O.

A PCR was performed on this mixture as follows. 37°C for 20 minutes, 98°C for 1 minute, 18x(98°C for 20 seconds, 60°C for 30 seconds, 72°C for 150 seconds), 72°C for 5 minutes, hold at 4°C.

5µl of the product of this reaction was run on a 0.8% agarose gel. A successful reaction produced a band at the length of the original plasmid.

4.3.10.1.2 Recombination reaction – to recombine the linear plasmid into a circular one

The following were combined in a PCR tube. 4µl of 5X reaction buffer, 10µl of PCR water, 4µl of PCR product from the previous step, 2µl of 10X enzyme mix. They were mixed well and incubated at room temperature for 10 minutes. The reaction was stopped by adding 1µl of 0.5M EDTA. The solution was mixed and placed on ice before proceeding to bacterial transformation.

4.3.10.1.3 Transformation of mutated plasmids into bacteria

For transformation One Shot™ MAX Efficiency™ DH5α™-T1R Competent Cells (12297016, Invitrogen) were used. All actions were performed under aseptic conditions, with a Bunsen flame nearby on the bench. On ice a 50µl vial of cells was thawed. 2µl of the recombination reaction was transferred to the cells and mixed by gentle tapping. The cell vial was then covered with ice for 12 minutes. The vial was then incubated at 42^{o}C for exactly 30 seconds and returned to the ice for 2 minutes. 250µl of room temperature SOC medium (15544034, Invitrogen) was added and the vial was placed in a 37^{o}C shaker incubator for exactly 1 hour at 225 RPM. During this time LB agar (L2897-1KG, Sigma) plates containing 50µg.ml^{-1} kanamycin were prewarmed in a 37^{o}C incubator. These had been made by adding 100µl of 50mg.ml^{-1} kanamycin to 100ml of LB agar as it cooled, just before the plates were poured.

7µl of the transformation reaction was taken and diluted in 93µl of SOC medium. This 100µl was transferred to the LB agar kanamycin plate and spread using sterile glass beads and shaking in a circular motion. The beads were then removed by tipping. The remaining transformation reaction was stored at 4^{o}C and the plates were inverted and incubated at 37^{o}C overnight (around 16 hours). Resulting colonies were assayed for the presence of the plasmid through a PCR reaction using primers specific to the plasmid and DNA sampled by touching a 10µl pipette tip to the colony and then swirling it in the PCR mixture. Positive colonies were then picked into 5ml of LB broth (L3022-1KG, Sigma) with 50µg.ml^{-1} kanamycin and grown overnight. Samples of this were then frozen down by mixing 1:1 with 70% glycerol and storing at -80^{o}C or used to grow up more bacteria for plasmid prepping.

4.3.10.2 Gel DNA extraction and PCR plasmid purification

Purification of plasmid DNA from PCR products or agarose gels was performed using QIAprep Spin Miniprep Kit (27104, Qiagen) according to the manufacturer's instructions. Gels were cut using an ultraviolet trans-illuminator and a sterile razor blade.

4.3.10.3 Plasmid amplification and purification from bacterial host strains

Bacterial culture stocks containing desired plasmids were kept at -80^{o}C. A sterile pipette tip was used to scrap a small amount of the frozen culture. This was placed in a 15ml falcon tube (E1415-0200, StarLab) and 5ml of LB broth (L3022-1KG, Sigma) was added contain the appropriate antibiotic (typically Ampicillin or Kanamycin). This was incubated at 37^{o}C in a shaker-incubator overnight. 1-5 ml of this could be then used for the miniprep protocol. For the maxiprep protocol 1ml of the turbid culture was transferred to a sterile culture conical flask and 200-500ml of LB broth was added. This was incubated for 10-16 hours until opaque and turbid before proceeding to the maxiprep protocol.

For isolating large quantities of plasmid for transfection the PureLink™ HiPure Plasmid Filter Maxiprep Kit (K210016, Invitrogen) was used according to the manufacturer's instructions, using either the PureLink™ HiPure Precipitator Module (K210021, Invitrogen) or the centrifugation protocol detailed in the manufacturer's instructions.

For isolating small quantities of plasmid for sequencing or cloning the QIAprep Spin Miniprep Kit (27104, QIAGEN) was used according to the manufacturer's instructions.

4.3.10.4 Phosphorylation and Annealing overlapping oligonucleotides

Double-stranded oligonucleotides for plasmid cloning were produced through annealing of complementary single-stranded oligonucleotides. To allow ligation of these double-stranded oligonucleotides into plasmid backbones a polynucleotide kinase was used to transfer the γ-phosphate from ATP to the 5' end of both single-stranded oligonucleotides prior to annealing together. Phosphorylation and annealing were combined into a single reaction. In a PCR tube were combined 1µ of each oligonucleotide at 100µM, 1µl of 10x PnK buffer (M4101, Promega), 6.5µl ddH_2O, and 0.5µl of T4 PnK kinase (M4101, Promega). This was incubated at 37^oC for 30 minutes, 95^oC for 5 minutes, and then cooled at a rate of 5$^oC.min^{-1}$ to 25^oC.

4.3.10.5 Restriction digests

All restriction enzymes and 10x buffers were acquired from Promega and kept at -20^oC.

35µl of purified plasmid from bacterial preps or insert from PCR was placed in a PCR tube. To this was added 5µl of each restriction enzyme used (for example NotI and MluI). To this was added 5µl of the appropriate buffer (for example buffer D for NotI and MluI). This was made up to 50µl with ddH_2O. This was incubated at 37^oC for 2-16 hours. Products were separated on an agarose electrophoresis gel and gel-extracted and purified prior to use in ligation reactions.

4.3.10.6 Ligations

Restriction-digested plasmids and inserts were run on agarose gels and gel-extracted prior to ligation reactions. For ligation 1, 3, or 7µl of digested insert was combined with 1µl of plasmid, to which was added 1µl of 10x T4 buffer and 1µl T4 ligase (M1801, Promega), and made up to 10ul with ddH_2O. This was then stored at 4^oC overnight to allow the ligation reaction to proceed. This was then used directly for bacterial transformations.

4.3.10.7 Transformations

Plasmid transformations were performed into Subcloning Efficiency™ DH5α™ Competent Cells (18265017, Thermofisher Scientific) for subcloning or One Shot® MAX Efficiency® DH5α™-T1R cells (12297016, Invitrogen) for site-directed mutagenesis reactions. Details of the transformation protocol for One Shot® MAX Efficiency® DH5α™-T1R cells can be found in the Site-directed mutagenesis section. Transformation into Subcloning Efficiency™ DH5α™

Competent Cells was performed as follows. 50µl aliquots of bacteria were defrosted from -80°C storage on ice. 1-10µl of purified plasmid prep was added and stirred using a pipette tip. The cells were incubated on ice for 30 minutes, heat-shocked at 42°C for 20 seconds, and then returned to ice for 2 minutes. 950µl SOC medium (15544034, Invitrogen) was added and the cells were incubated at 37°C in a shaker incubator at 225RPM for 1 hour.

4.3.10.8 Plating, Antibiotic selection

200µl of the transformation culture was transferred to a pre-warmed LB agar plate and spread using sterile glass beads and shaking in a circular motion. The beads were then removed by tipping. The remaining transformation reaction was stored at 4°C and the plates were inverted and incubated at 37°C overnight (around 16 hours).

LB Agar plates containing antibiotics were made by adding and mixing the antibiotic into the LB agar as it cooled, just before the plates were poured. 100µl of 50mg.ml^{-1} kanamycin or 200µl of 50mg.ml^{-1} Ampicillin were used per 100ml of LB agar.

4.3.10.9 Picking colonies

Resulting colonies were assayed for the presence of the plasmid through a PCR reaction using primers specific to the plasmid and DNA sampled by touching a 10µl pipette tip to the colony and then swirling it in the PCR mixture.

4.3.10.10 Culturing

Resulting colonies were assayed for the presence of the plasmid through a PCR reaction using primers specific to the plasmid and DNA sampled by touching a 10µl pipette tip to the colony and then swirling it in the PCR mixture. Positive colonies were then picked into 5ml of LB broth (L3022-1KG, Sigma) with 50µg.ml^{-1} and grown overnight.

4.3.10.11 Freezing bacteria

For freezing stocks of transformed bacteria, samples of culture were mixed 1:1 with 70% glycerol and then placed at -80°C.

4.3.11 LysoTracker and CellLight staining for lysosomes and acidic cellular compartments

For this protocol two kits were used: LysoTracker™ Deep Red (L12492, Invitrogen) and CellLight™ Lysosomes-GFP, BacMam 2.0 (C10507, Invitrogen). The staining was performed according to the manufacturer's instructions as follows.

Cells were plated into 8-well chamber slides (C7182-1PAK, Nunc) at approximately 32,000 cells per well (as determined by counting cells using a haemocytometer) in standard culture medium. They were allowed to settle and attach to the plastic for several hours. The medium was then aspirated and 9.6µl of CellLight reagent in 200µl of standard medium was added to each well. The cells were incubated overnight for around 16 hours. In the morning the medium was

aspirated and Lysotracker stain at 75nM in 300µl standard medium was added. This was left for 2 hours and then the medium was aspirated. The cells were washed twice with PBS and 200µl standard culture medium was added. The cells were then immediately imaged using the EVOS microscope.

Alternatively after the 2-hour incubation in Lysotracker medium the cells were washed and fixed in 4% paraformaldehyde (PFA) in PBS for 30 minutes at 4^{o}C. The cells were washed 3 times with phosphate buffered saline (PBS). Excess PBS was drawn off with tissue and a few drops of Vectorshield with DAPI stain were added. A glass coverslip was placed on top with tweezers. Excess Vectorshield was drawn off with tissue. Nail polish was used to seal the edges of the coverslip and left to dry in darkness for at least 120 minutes before storage and confocal imaging.

4.4 Results

4.4.1 Expressing *BEST1* Bestrophinopathy mutations in a human RPE cell line, ARPE-19

To investigate the localisation of mutations associated with Bestrophinopathies a retroviral transfection protocol was used to integrate the mutant forms of the *BEST1* gene into ARPE-19 cells. This would allow direct comparison between otherwise genetically identical lines. These lines could then also be compared after maintenance in standard DMEM medium and the differentiation-inducing X-VIVO 10 medium to see if BEST1 protein localisation changed during RPE cell maturation.

These results could then be compared to the same constructs transfected into the commonly-used epithelial cell lines, HEK293 and MDCK, to cells to see if the localisation in these common model lines is consistent.

Finally, using a FLAG epitope tag conjugated to the BEST1 protein expressing the R200X mutation it was assessed whether a truncated translated product was produced in the case of the pR200X ARB mutant.

4.4.1.1 Choice of best1 mutants

For the cloning and expression experiments described below seven Bestrophinopathy-associated point mutations were used. The first five are ADVIRC mutations that have previously been assayed for alternate splicing in cell lines, with mixed results. The last two are BEST1 mutations that cause ARB. These mutants are shown in the table below.

Genetic mutation	**Protein substitution**	**Disease**	**Reference**
248 G>A	pGly83Asp	ADVIRC	Chen *et al.*, 2016
256 G>A	pV86M	ADVIRC	Yardley *et al.*, 2004
704 T>C	pV235A	ADVIRC	Burgess *et al.*, 2009; Carter *et al.*, 2016
707 A>G	pY236C	ADVIRC	Burgess *et al.*, 2009; Yardley *et al.*, 2004
715 G>A	pV239M	ADVIRC	Yardley *et al.*, 2004
598 C>T	pR200X	ARB	Burgess *et al.*, 2008; Johnson *et al.*, 2014
974 T>C	pM325T	ARB	Burgess *et al.*, 2011; Johnson *et al.*, 2014

4.4.1.2 Cloning program

The aim was to produce a construct that could be retrovirally inserted into the genome resulting in the expression of BEST1 mutant proteins under the control of a constitutive promoter. For this the pCLNCX cloning vector, which produces proteins under control of the CMV promoter, was used within the Retromax system (Novus Biologicals).

4.4.2 Cloning the BEST1 coding sequence

The double-stranded BEST1 coding sequence was synthesised by Eurofins MWG/operon and cloned into the pEX-K vector inside a packaging plasmid. This plasmid is referred to as pEX.*BEST1*. The plasmid was transformed into Subcloning Efficiency™ DH5α™ Competent bacterial cells were using a heat-shock protocol. Cells were plated onto an LB agar bacterial plate, a single colony was isolated and cultured in LB broth, and plasmid isolated using a maxi prep protocol. The plasmid was then sequenced to confirm the insert sequence was correct. Information for this plasmid, as well as the primer sequences used during cloning can be found in the Appendix.

4.4.2.1.1 Site-directed mutagenesis

The pEX-K4.*BEST1* plasmid was used as the template for the site-directed mutagenesis reactions. This method was used to introduce targeted mutations into the *BEST1* sequence, recapitulating the patient mutations described in the Introduction of this chapter. Briefly, long primers of 45 bases were designed to anneal to the *BEST1* sequence with the mutations site being introduced located in the middle of each primer. The primers were exactly complementary to the 5' and 3' strands of the plasmid except for the base to be mutated. A PCR amplification of the pEK.BEST1 plasmid using these primers yielded linear copies of the plasmid with the altered base and overlapping ends. A recombination reaction reproduced the circular plasmid, now with the mutated base. The reaction, containing the original template and the site-directed mutation copy were then transformed into DH5α competent cells. The template plasmid was methylated prior to the PCR amplification step, resulting in the degradation of the original template plasmid in the host bacteria upon transformation.

This reaction was performed for the seven *BEST1* variants (five ADVIRC mutations, two ARB mutations, and a silent control mutation, 699A>T, P233P). The presence of the desired mutated base and the absence of off-target mutations was confirmed through plasmid sequencing. These plasmids were then used as templates for cloning into the pCLNCx retroviral expression vector. A schematic of this cloning protocol can be found in **Figure 4.7** and is described briefly below.

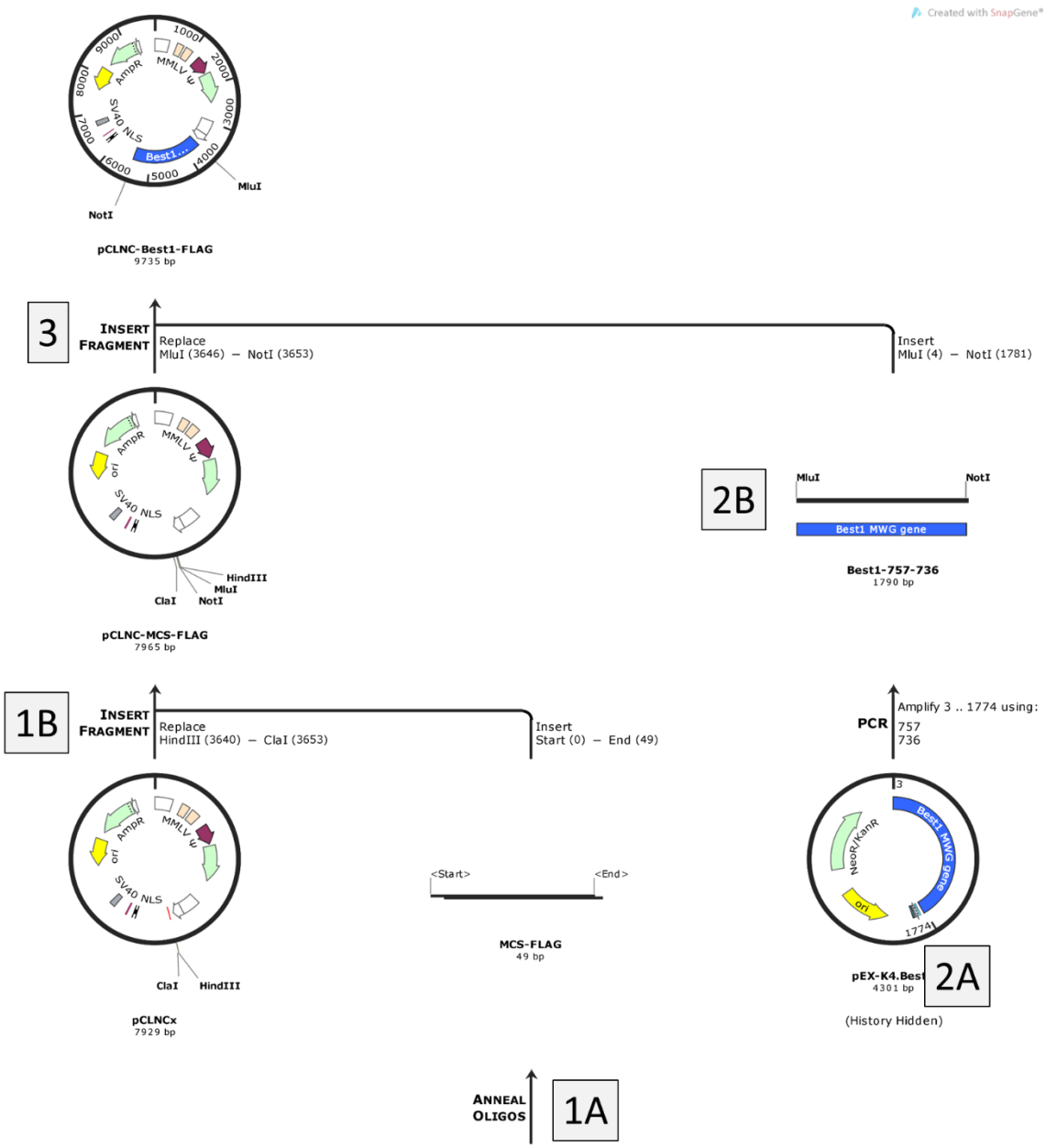

Figure 4.7 Schematic cloning scheme for the pCLNC-Best1-FLAG retroviral expression vector. This diagram was produced using Snapgene software. 1A) An oligonucleotide pair were ordered and annealed to create the multiple cloning site (MCS) and FLAG coding sequence. When annealed these oligonucleotides left a HindIII digest-compatible overhang at one end and a ClaI digest-compatible overhang at the other. 1B) The pCLNCx template plasmid was digested with HindIII and ClaI and the annealed oligos from step 1A were ligated into the gap to produce pCLNC-MCS-FLAG. 2A) Once site-directed mutagenesis (SDM) had been used to produce the pEX-K4 Best1 plasmid with each of the disease-causing mutations in it, the Best1 sequence of each of these plasmids was amplified using a pair of primers that also added an MluI or NotI digestion sites at each end. 2B) These PCR products were then digested with MluI and NotI to produce overhangs. 3) the pCLNC-MCS-FLAG plasmid was also digested with MluI and NotI and then the mutant Best1 fragment from step 2B was ligated into the MCS to produce the final plasmid pCLNC-Best1-FLAG.

4.4.2.1.2 Cloning of *BEST1* sequences into the retroviral vector

The pCLNCX Retrovirus Expression Vector was used for retroviral cloning. The vector was first modified to include a multiple-cloning site and FLAG tag peptide coding sequence. This was acheived by annealing two complementary oligonucleotides containing a new multiple cloning site sequence and ClaI and HindII restriction digest overhangs. This allowed the annealed oligonucleotides to ligate into HindIII and ClaI digested pCLNCX to produce pCLNC-MCS-FLAG. This pCLNC-MCS-FLAG plasmid was sequenced with primers flanking the modified site to confirm that the MCS-FLAG site was inserted as expected.

The pCLNC-MCS-FLAG plasmid and each of the variants of the pEX-K4.*BEST1* plasmid were then digested with MluI and NotI (two restriction digest sites introduced in the MCS of pCLNCx) and ligated together to make pCLNC-*BEST1*-FLAG plasmids, each identical except for the *BEST1* mutated base. Again these plasmids were sequenced to confirm the presence of the desired mutation and the absence of off-target mutations.

4.4.2.1.3 The structure of the construct

A schematic of the resulting pCLNC-*BEST1*-FLAG plasmid is shown in **Figure 4.8**. Important features are labelled. **Figure 4.9** shows a closer view of the *BEST1* coding sequence, with labels to indicate where the point-mutations were introduced into each version.

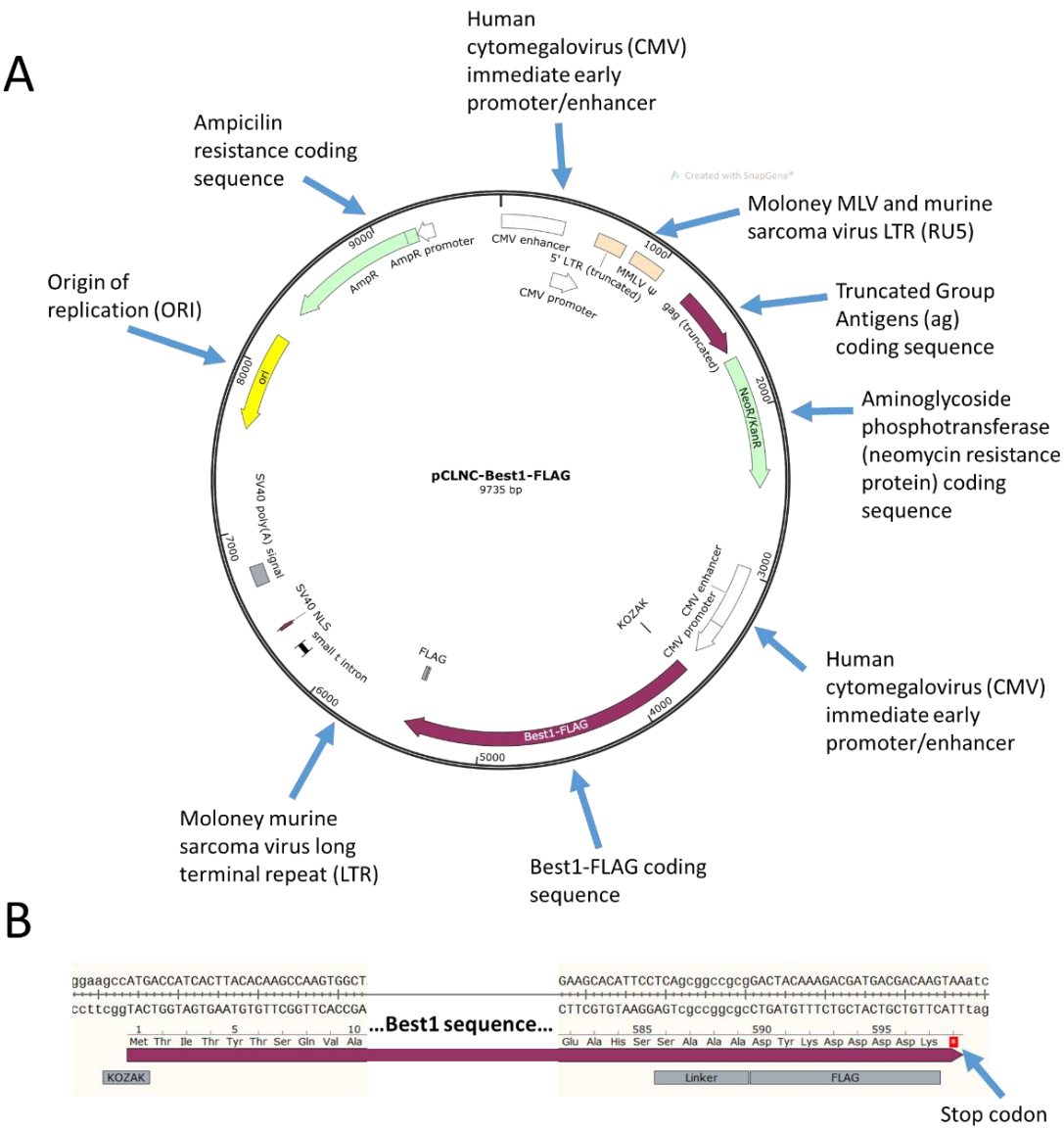

Figure 4.8 Schematic showing the basic structure of the pCLNC-Best1-FLAG retroviral plasmid. A) A circular diagram of the 9735bp plasmid with labels showing the main features. B) A linear section of the plasmid showing the start and end of the Best1-FLAG coding sequence including the KOZAK sequence, Best1 sequence, linker sequence, FLAG sequence, and stop codon.

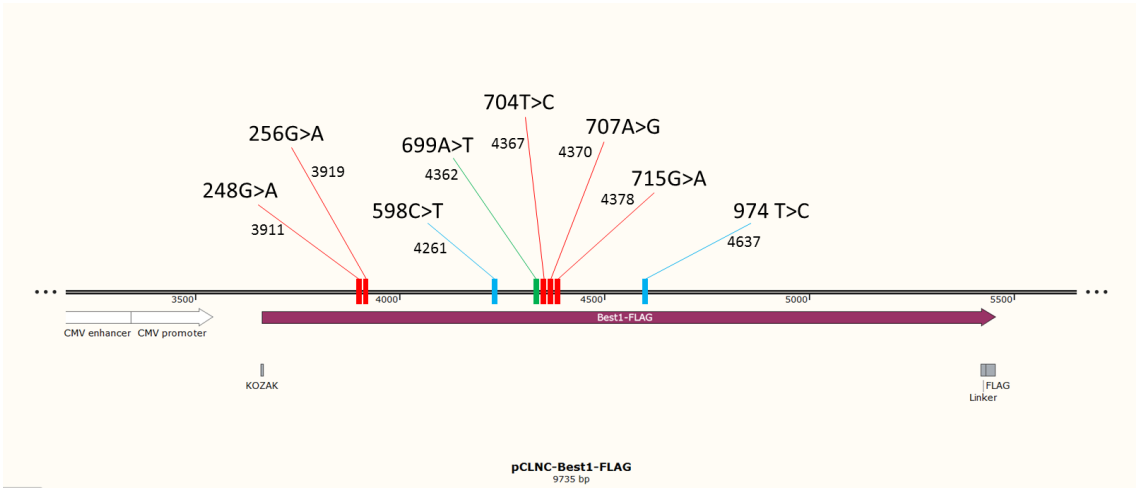

Figure 4.9 Diagram showing the localisation of the 8 mutagenesis sites within the Best1 gene. Red bars represent ADVIRC mutations. Blue Bars represent ARB mutants. The Green bar represents the control silent mutation site. The base substitution is shown in the label for each bar and the base position of the point mutation within the pCLNC-Best1-FLAG plasmid is shown alongside. Bar positions are approximate.

The Cytomegalovirus (CMV) Immediate-Early (IE) enhancer-promoter drives high levels of transcription in the packaging GP2-293 cell line, but is lost during viral replication so the Moloney MLV and murine sarcoma virus LTR (RU5) drives expression of the aminoglycoside phosphotransferase (Neo^R) antibiotic resistance gene for selection purposes.

A second CMV promoter drives transcription of the gene of interest cloned into the MCS. This starts with an 'adequate' KOZAK sequence(Kozak 1987), designed to have the same three upstream bases as in the genomic *BEST1* sequence (GGC). This is followed by the 1758bp *BEST1* coding sequence, with the stop codon modified into the serine of the following 4-amino acid linker sequence (Ser-Ala-Ala-Ala). This is followed by the FLAG coding sequence and then by a stop codon. Thus the *BEST1* protein is conjugated via the linker sequence to the FLAG tag.

A linker sequence was included between the *BEST1* sequence and the FLAG sequence to improve accessibility of the translated FLAG sequence to FLAG-specific antibodies.

The linker amino acid sequence was chosen as the stop codon of the original *BEST1* transcript could be modified to code for Serine instead (TAA>TCA), while the code for the string of three alanines (GCG-GCC-GCG) could be conveniently made from the NotI restriction site (GCGGCCGC). Both serine and alanine have been found to be enriched in natural linker sequences(Argos 1990).

The RNA-sequencing data from Amanda Carr presented in the introduction suggests that even highly differentiated ARPE-19 do not express *BEST1*, even as other genes show upregulation over time. However, it was considered possible that forced expression of the retroviral *BEST1*

constructs could lead to an increase in endogenous *BEST1* expression through positive feedback. The FLAG tag (DYKDDDDK) was included in the retroviral construct so that the retrovirally introduced mutant *BEST1* protein could be distinguished from any endogenous *BEST1* that might be expressed. The FLAG tag was placed at the cytoplasmic C-terminal end of the *BEST1* protein as this end is considered to be more functionally redundant than the N-terminus and has been shown to tolerate conjugation of YPF(Johnson et al. 2014).

The 598C>T mutation introduces a premature stop codon into the *BEST1* sequence which truncates the mRNA transcript. It appears that this transcript is translated into a truncated protein(Johnson et al. 2014). The BEST1 antibody used in this study recognises the protein at positions 568-585, which further towards the C-prime end than would exist in such a truncated protein. Details of this antibody can be found here: https://www.abcam.com/bestrophin-antibody-e6-6-ab2182.html

Therefore a second set of cloning was performed to create an identical retroviral plasmid as described above, only with the FLAG tag at the N-terminal end of the *BEST1* protein. Here instead of the transcript reading KOZAK-*BEST1*-linker-FLAG the construct read KOZAK-FLAG-linker-*BEST1*. The cloning plan for this plasmid is shown in **Figure 4.10** and a schematic of the resulting plasmid is shown in **Figure 4.11**. The construct started with the same 3bp upstream KOZAK sequence as in the pCLNC-*BEST1*-FLAG cloning, followed by a methionine, followed the FLAG, followed by the same linker sequence, followed by the *BEST1* sequence with it's wild-type stop sequence. This plasmid was made for both the wild-type *BEST1* sequence and the 598C>T sequence. A list of primers used can be found in the Appendix.

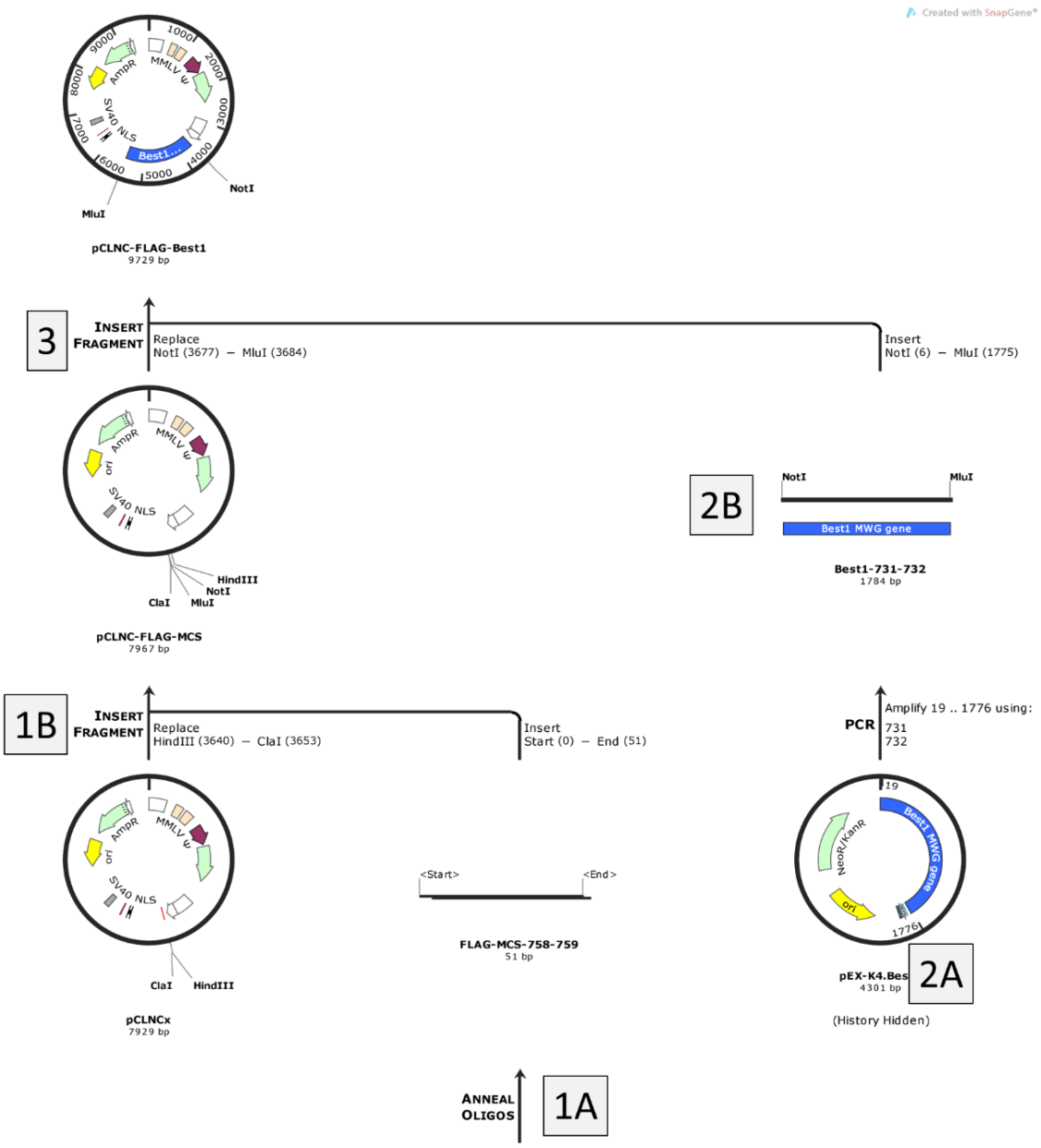

Figure 4.10 Schematic cloning scheme for the pCLNC-FLAG-Best1 retroviral expression vector. This diagram was produced using Snapgene software. 1A) An oligonucleotide pair were ordered and annealed to create the FLAG coding sequence and multiple cloning site. When annealed these oligonucleotides left a HindIII digest-compitable overhang at one end and a ClaI digest-compitable overhang at the other. 1B) The pCLNCx template plasmid was digested with HindIII and ClaI and the annealed oligos from step 1A were ligated into the gap to produce pCLNC-FLAG-MCS. 2A) Once site-directed mutagenesis (SDM) had been used to produce the pEX-K4 Best1 plasmid with each of the disease-causing mutations in it, the Best1 sequence of each target plasmid was amplified using a pair of primers that also added an MluI or NotI digestion sites at each end. 2B) These PCR products were then digested with MluI and NotI to produce overhangs. 3) the pCLNC-FLAG-MCS plasmid was also digested with MluI and NotI and then the mutant Best1 fragment from step 2B was ligated into the MCS to produce the final plasmid pCLNC—FLAG-Best1.

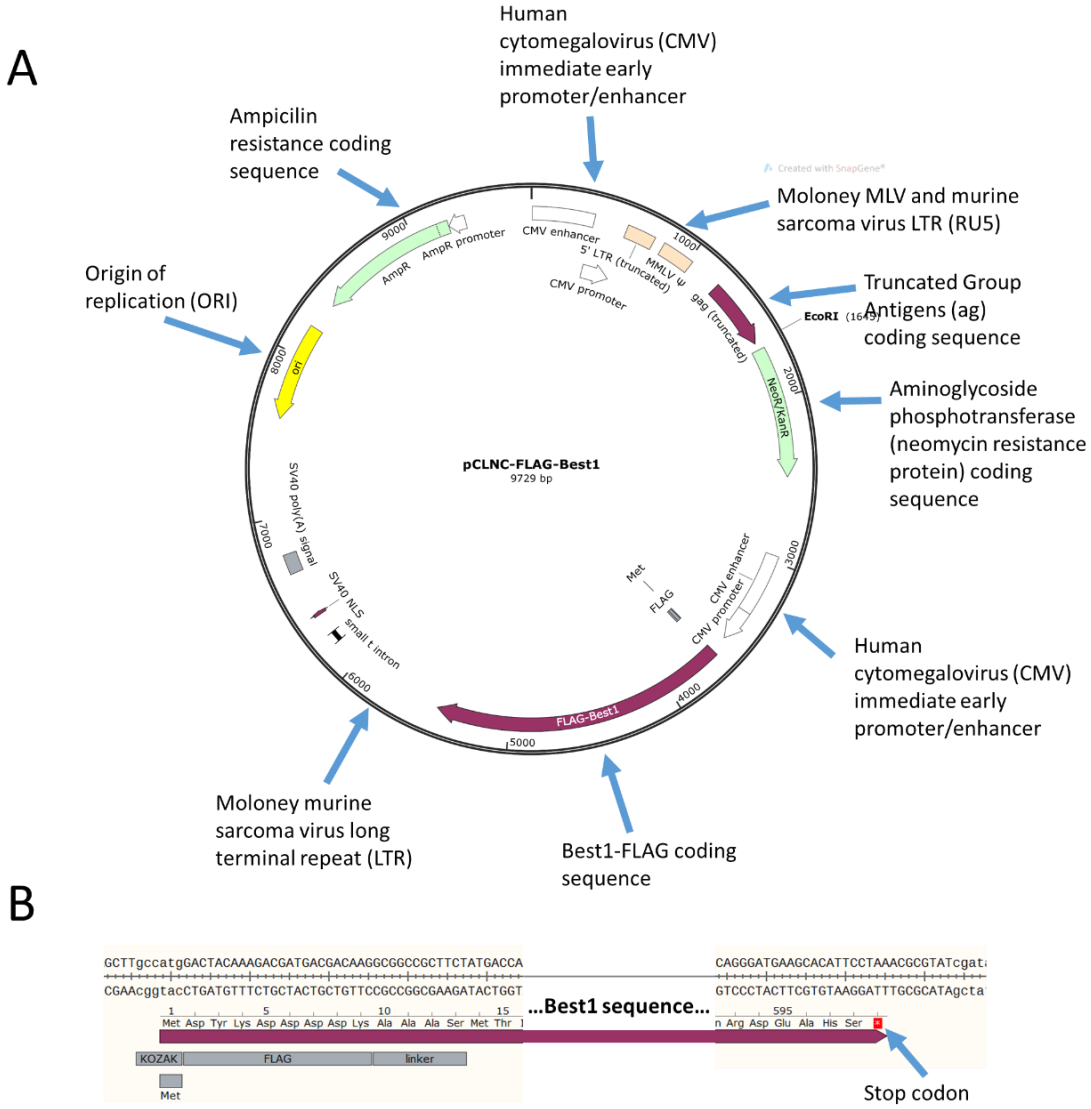

Figure 4.11 Schematic showing the basic structure of the pCLNC-FLAG-Best1 retroviral plasmid. A) A circular diagram of the 9729bp plasmid with labels showing the main features. B) A section of the plasmid showing the start and end of the FLAG-Best1 coding sequence including the KOZAK sequence, FLAG sequence, linker sequence, Best1 sequence, and stop codon.

The table below shows the list of plasmids generated for transfections. Also shown is the pCLNC-GFP plasmid that was used as a control plasmid for transfections. In this plasmid the second CMV drives expression of a GFP transcript which, once translated, causes the cells to fluoresce green.

plasmid ID	plasmid structure	Genetic mutation	Protein substitution	FLAG tag terminus	Disease
0C	pCLNC-*BEST1*-FLAG	wild type	-	C	-
1C	pCLNC-*BEST1*-FLAG	248 G>A	pGly83Asp	C	ADVIRC
2C	pCLNC-*BEST1*-FLAG	256 G>A	pV86M	C	ADVIRC
3C	pCLNC-*BEST1*-FLAG	704 T>C	pV235A	C	ADVIRC
4C	pCLNC-*BEST1*-FLAG	707 A>G	pY236C	C	ADVIRC
5C	pCLNC-*BEST1*-FLAG	715 G>A	pV239M	C	ADVIRC
6C	pCLNC-*BEST1*-FLAG	598 C>T	pR200X	C	ARB
7C	pCLNC-*BEST1*-FLAG	974 T>C	pM325T	C	ARB
8C	pCLNC-*BEST1*-FLAG	699 A>T	pP233P	C	-
0N	pCLNC-FLAG-*BEST1*	wild type	-	N	-
6N	pCLNC-FLAG-*BEST1*	598 C>T	pR200X	N	ARB
GFP	pCLNC-GFP	-	-	-	-

4.4.3 Test retroviral transfection

The wild-type pCLNC-*BEST1*-FLAG plasmid with no mutations and the pCLNC-GFP plasmid were used to perform a test retroviral transfection in ARPE-19 cells. Details of the retroviral transfection protocol are given in the Materials and Methods and the plasmid details are shown in the table below. After day 9 of the retroviral transfection protocol GFP expression was seen in the pCLNC-GFP transfected cells, suggesting that the transfection had worked. Details of the two plasmids used for this test transfection are shown below.

plasmid ID	plasmid structure	Genetic mutation	Protein substitution	FLAG tag terminus	Disease
0C	pCLNC-*BEST1*-FLAG	wild type	-	C	-
GFP	pCLNC-GFP	-	-	-	-

4.4.3.1 Western blot

Protein expression in ARPE-19 cells transfected with wild-type pCLNC-*BEST1*-FLAG or pCLNC-GFP were examined by western blotting, according to the protocol in the Materials and Methods. The results are shown in **Figure 4.12**. In the case of the cells transfected with pCLNC-*BEST1*-FLAG bands were detected for both the *BEST1* antibody and the FLAG antibody when lysates were prepared in reducing buffer. The sizes of these bands had a molecular weight of approximately 60-65 kiloDaltons (kDa), which is what would be expected from monomeric *BEST1*, which has a molecular weight of 66.7 kiloDaltons (plus approximately 1.32kDa for the extra amino acids contained in the linker sequence, assuming 12 additional amino at 0.11kDa each). In the case of the lysates prepared in non-reducing buffer the band is more prominent and a second fainter band is present at around 130-140 kDa, which could correspond to a dimerised form of the BEST1 protein under non-reducing conditions.

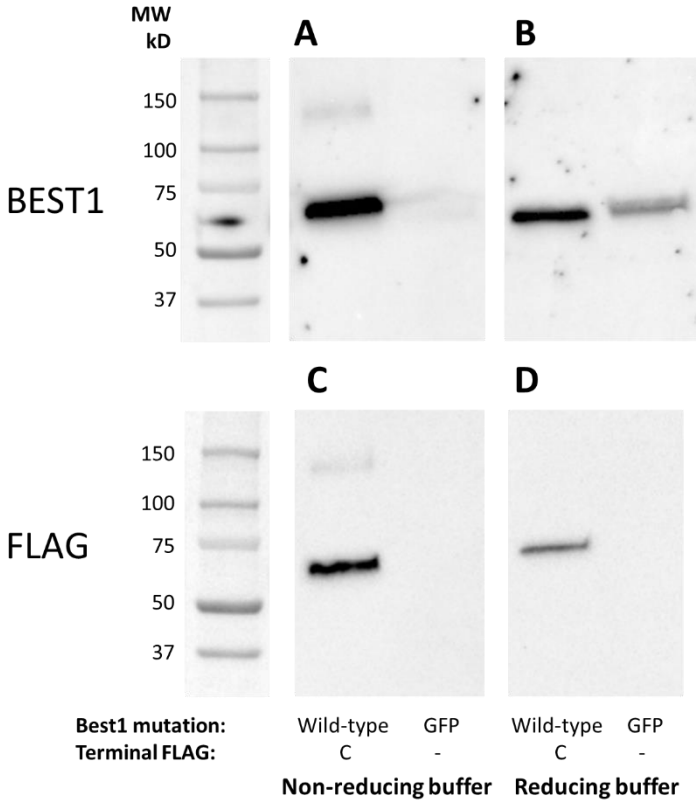

Figure 4.12 Western blot staining of cell lysates from retrovirally transfected ARPE19 cells using BEST1 and FLAG antibodies. A) Staining using the BEST1 antibody of cells transfected with the wild-type pCLNC-Best1-FLAG construct or the control pCLNC-GFP construct, with the cell lysates in non-reducing running buffer or B) in reducing running buffer. C) Staining using the FLAG antibody and with non-reducing buffer or D) the staining with the FLAG antibody and reducing buffer. Molecular weights according to the protein ladder standard are shown on the left of each panel.

The pCLNC-GFP samples show no bands for the FLAG antibody, as would be expected. The *BEST1* antibody appears to give a weak band in the reducing buffer. However, this was considered to likely be due to a small overflow between wells coupled with the high exposure of the blot. This band did not occur in the non-reducing condition.

4.4.3.2 Immunocytochemistry

The ARPE-19 cells transfected with pCLNC-*BEST1*-FLAG or pCLNC-GFP were immuno-stained according to the protocol in the Materials and Methods. These cells were then imaged using the EVOS. These images are shown in **Figure 4.13** and **Figure 4.14**. Row 1 show shows that the pCLNC-*BEST1*-FLAG cells stain positively with the BEST1 antibody (red), but not the FLAG antibody (green). Row 2 shows again BEST1 antibody staining (red), but not FLAG-GFP conjugate antibody staining. Rows 3 and 4 show no staining when the secondary antibodies are used alone.

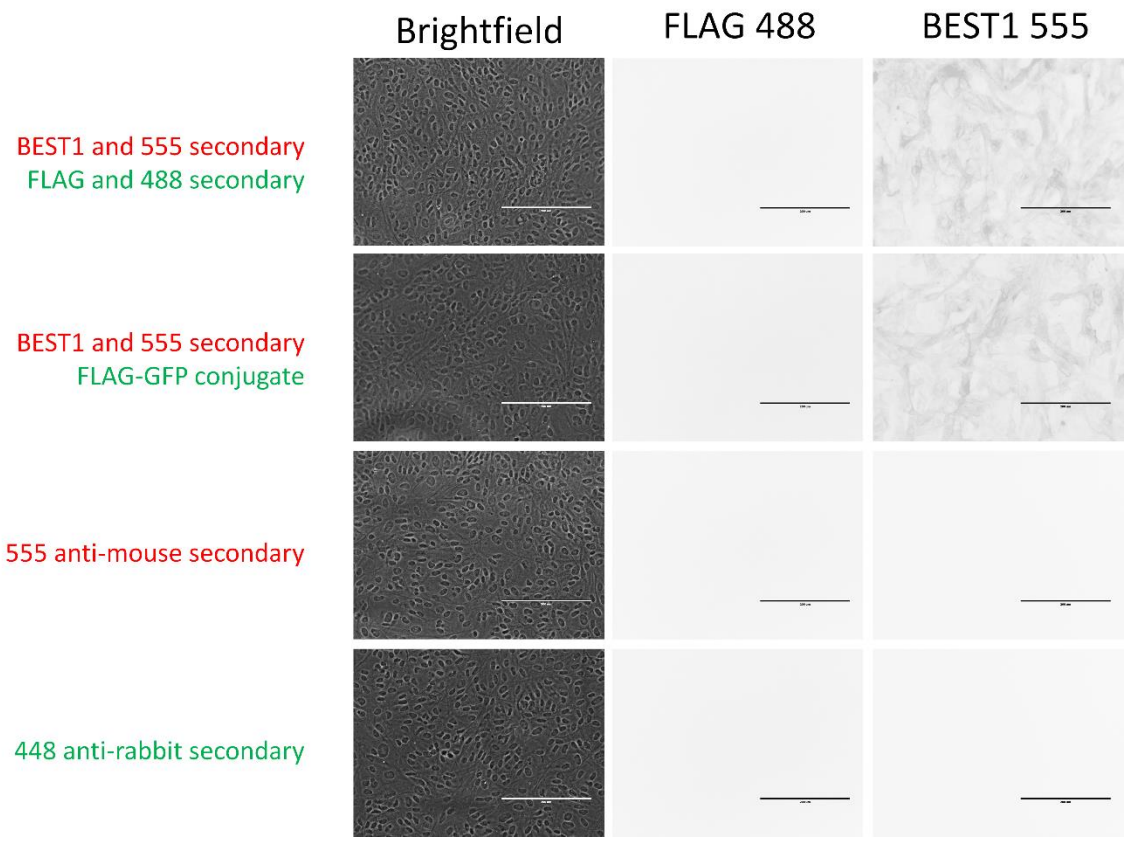

Figure 4.13 Immunocytochemistry staining using the BEST1 and FLAG antibodies of cell monolayers from ARPE19 cells transfected with the wild-type pCLNC-Best1-FLAG plasmid. To the left of each row is indicated the staining applied to the cells, colour-coded according to the expected fluorescence. Along the top of the panels is shown the brightfield or fluorescence channel of that column. The images for the FLAG 488 and BEST1 555 columns have been colour-inverted, showing positive staining in black. All images were taken using an EVOS FL Cell Imaging System. Scale bars indicate 200µm.

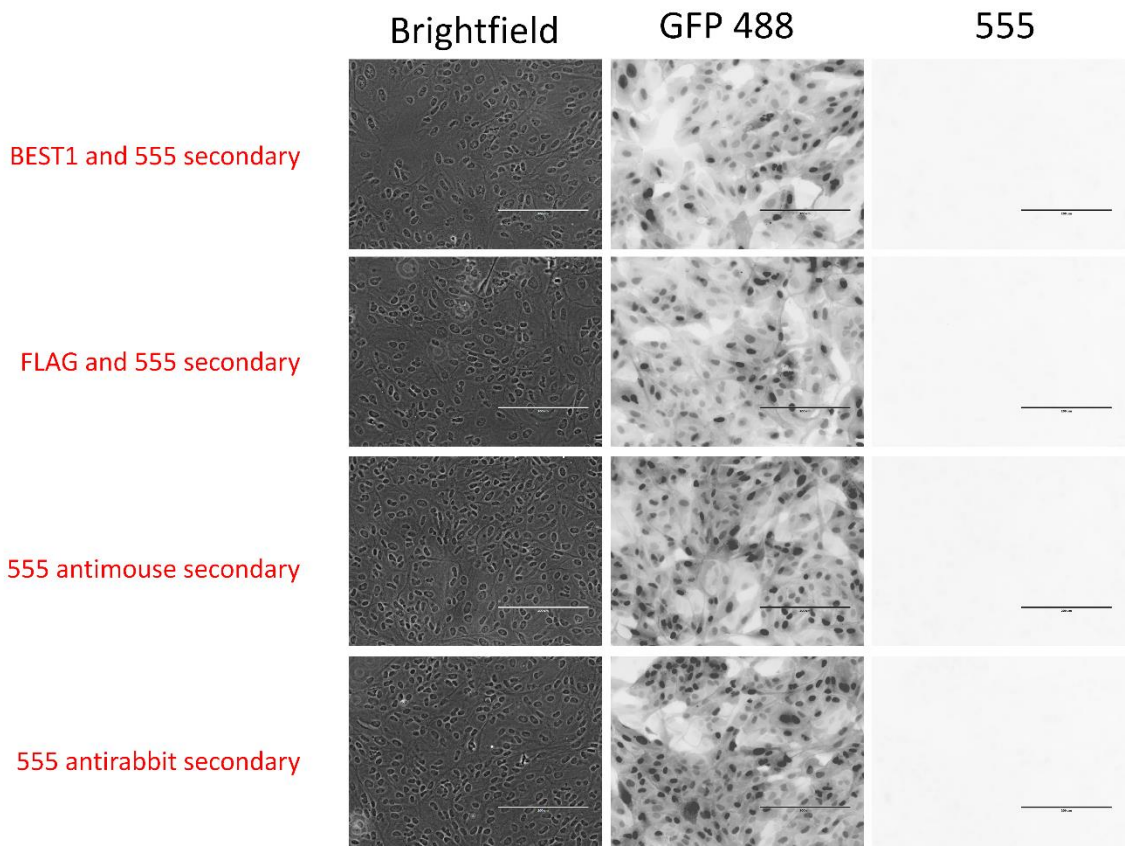

Figure 4.14 Immunocytochemistry staining using the BEST1 and FLAG antibodies of cell monolayers from ARPE19 cells transfected with the control pCLNC-GFP plasmid. To the left of each row is indicated the staining applied to the cells, colour-coded according to the expected fluorescence. Along the top of the panels is shown the brightfield or fluorescence channel of that column. All images were taken using an EVOS FL Cell Imaging System. The GFP488 and 555 columns show positive staining as dark areas. Scale bars indicate 200 µm.

Row 5, 6, 7, and 8 show that the pCLNC-GFP construct is producing GFP protein. Co-staining these cells with antibodies directed to BEST1 or the FLAG sequence (FLAG/FLAG488conjugate – antibodies) shows that BEST1 is not produced in these cells. Absence of FLAG staining suggests that, although these antibodies recognise the correct epitope using Western blot, these antibodies do not recognise or cannot bind to the epitope in fixed cells. A small amount of bleed-through from the extremely bright GFP can be seen in the red channels of rows 5,6,7, and 8.

Taken as a whole the data in this figure confirms *BEST1* expression in the pCLNC-*BEST1*-FLAG line only and GFP expression in the pCLNC-GFP line only. It also suggested that neither the FLAG primary antibody nor the FLAG-GFP conjugate antibody stains for best in the pCLNC-*BEST1*-FLAG line. This could be due to the C-terminal FLAG tag being inaccessible to the antibodies, a theory supported by the positive staining seen using the same FLAG antibody in the case of the western blot. The fact that there is no visible staining of the pCLNC-GFP cells with the BEST1 antibody

suggests that the band seen in the corresponding western blot **Figure 4.12B** was due to lane overspill.

4.4.4 Can ARPE-19 be used to express mutant *BEST1* retrovirally?

4.4.5 Retroviral transfection of the remaining constructs into ARPE-19 cells

Having confirmed that the pCLNC-GFP control construct produced green fluorescence and that the wild-type pCLNC-*BEST1*-FLAG produced BEST1 protein (detectable using antibodies to both BEST1 and the FLAG epitope tag in western blots, and the antibody to BEST1 in immunocytochemistry), transfections were now repeated using all of the BEST1 mutation pCLNC constructs in ARPE-19 cells.

4.4.5.1 Selection

Retroviral transfection was performed as previously described. These lines were then placed into G418 selection, starting at 200µg.ml^{-1} and gradually increasing over the next several weeks in culture. The pCLNC-GFP construct fluorescent output could be easily seen in the live cells using the EVOS microscope, and so this was used as an indicator that the selection was working.

ARPE-19 cells were split once a week at a 1:2 ratio during selection.

4.4.5.2 Western blot – BEST1 antibody

Protein samples were taken from the ARPE-19 cell lines 22 days after transfection, which was after 18 days of G418 selection. Western blots were performed to assay for *BEST1* expression. The results are shown in **Figure 4.15**. Here it can be seen in (A) that only the 248G>A C-terminal FLAG sample shows any trace of the BEST1 band, even after prolonged exposure of the blots. As a positive control (B) the test pCLNC-*BEST1*-FLAG sample used in **Figure 4.12** was included, and showed the same strong signal as before.

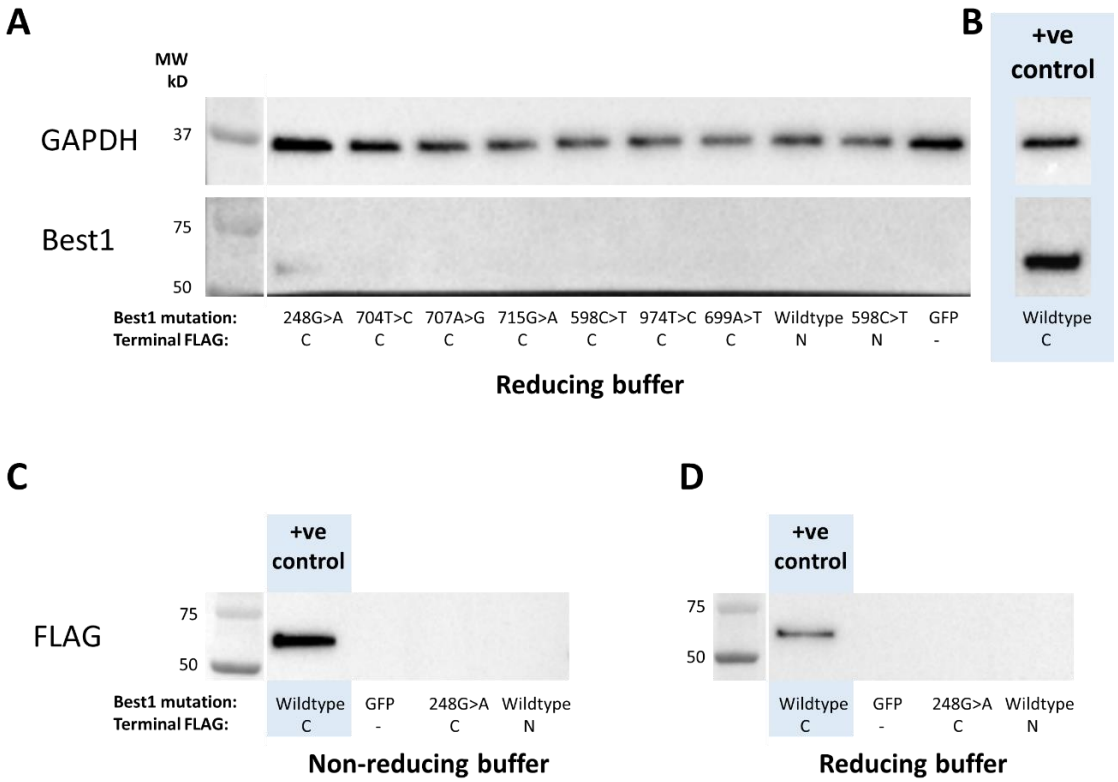

Figure 4.15 Western blot staining of cell lysates from retrovirally transfected ARPE19 cells using GAPDH, BEST1 and FLAG antibodies. A) GAPDH and BEST staining of cell lysates from retrovirally transfected cells after 18 days in strong G418 selection. B) a positive control wild-type sample that was harvested immediately after transfection, without selection. C) FLAG antibody staining of three of the same samples, both in non-reducing buffer and D) in reducing buffer.

The bottom panel (C) shows three of the same samples (GFP, 248G>A C-terminal FLAG, and Wild-type N-terminal FLAG) alongside the same control sample stained for FLAG. Here it can be seen that again the samples that have been through selection show no band, while the positive control shows the BEST1 band in both reducing and non-reducing buffer.

It was hypothesised that the important difference was that the second set of transfected lines had been maintained in culture under selection for several weeks before samples were taken, while the test samples had been taken within days of transfection. If the forced expression of *BEST1* leads to cell death, detachment, or a significant growth disadvantage then it could be expected that after some time in culture the number of cells expressing the construct would drop dramatically.

4.4.5.3 Immunocytochemistry

Immunocytochemistry was performed on each of the transfected ARPE-19 cell lines to stain for BEST1. The results are shown in **Figure 4.16**, **Figure 4.17** and **Figure 4.18**. Here it can be seen that although the BEST1 staining is clear and bright in the case of the wild-type *BEST1* cells

without selection (A), the selected lines show much dimmer and less consistent staining. Of the C-terminal FLAG lines only the wild-type, 707A>G, and 699A>T show some visible staining, and of the N-terminal lines only the wildtype appears to show a small amount of staining. Both the C-terminal and the N-terminal 598C>T lines show bright punctate staining. However, as the BEST1 antibody should be unable to bind to any truncated product of this mutant form of *BEST1* this suggests that this punctate staining is an artefact of staining. Why though it seems to occur in both of these lines to a much greater extent than the others is unclear.

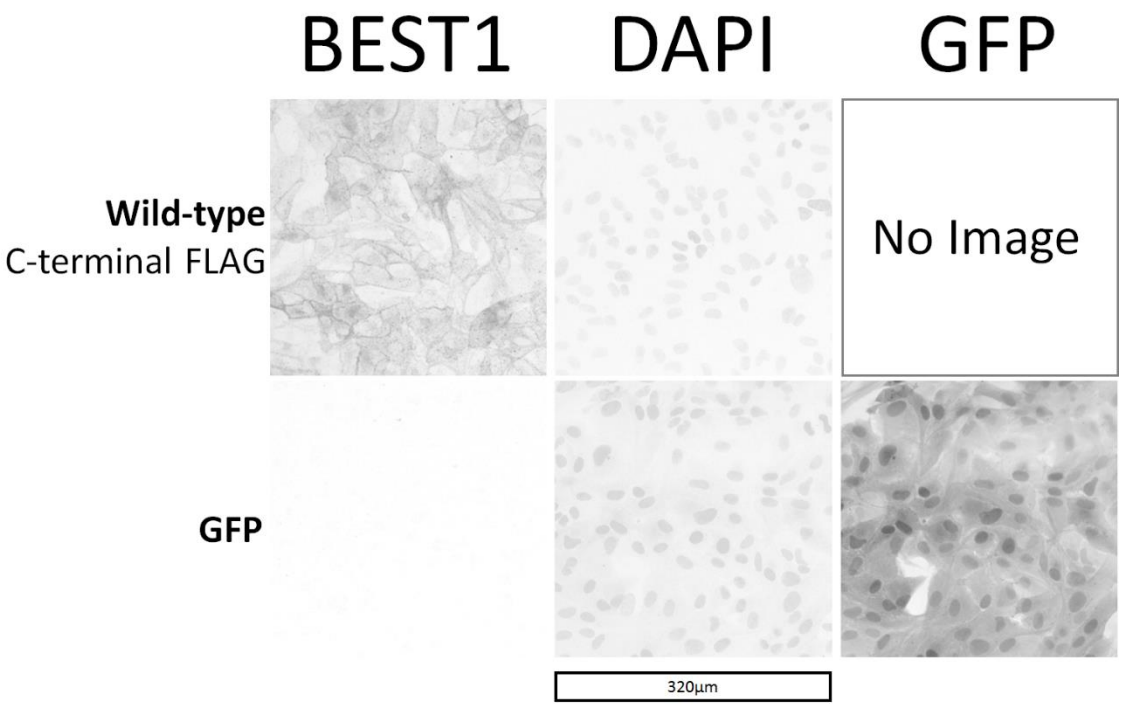

Figure 4.16 Confocal images of the wild-type BEST1 and GFP control ARPE19 cells from the first transfection and stained with the BEST1 antibody and 555 secondary antibody. The genotypes of the pCLNC plasmids is indicated to the left of the confocal images, mutation on top and terminal FLAG below. All images of each channel were taken using identical settings. All images were taken at 20x. Dark areas indicate positive staining. Each image is 320µm by 320µm, as indicated by the sale bar.

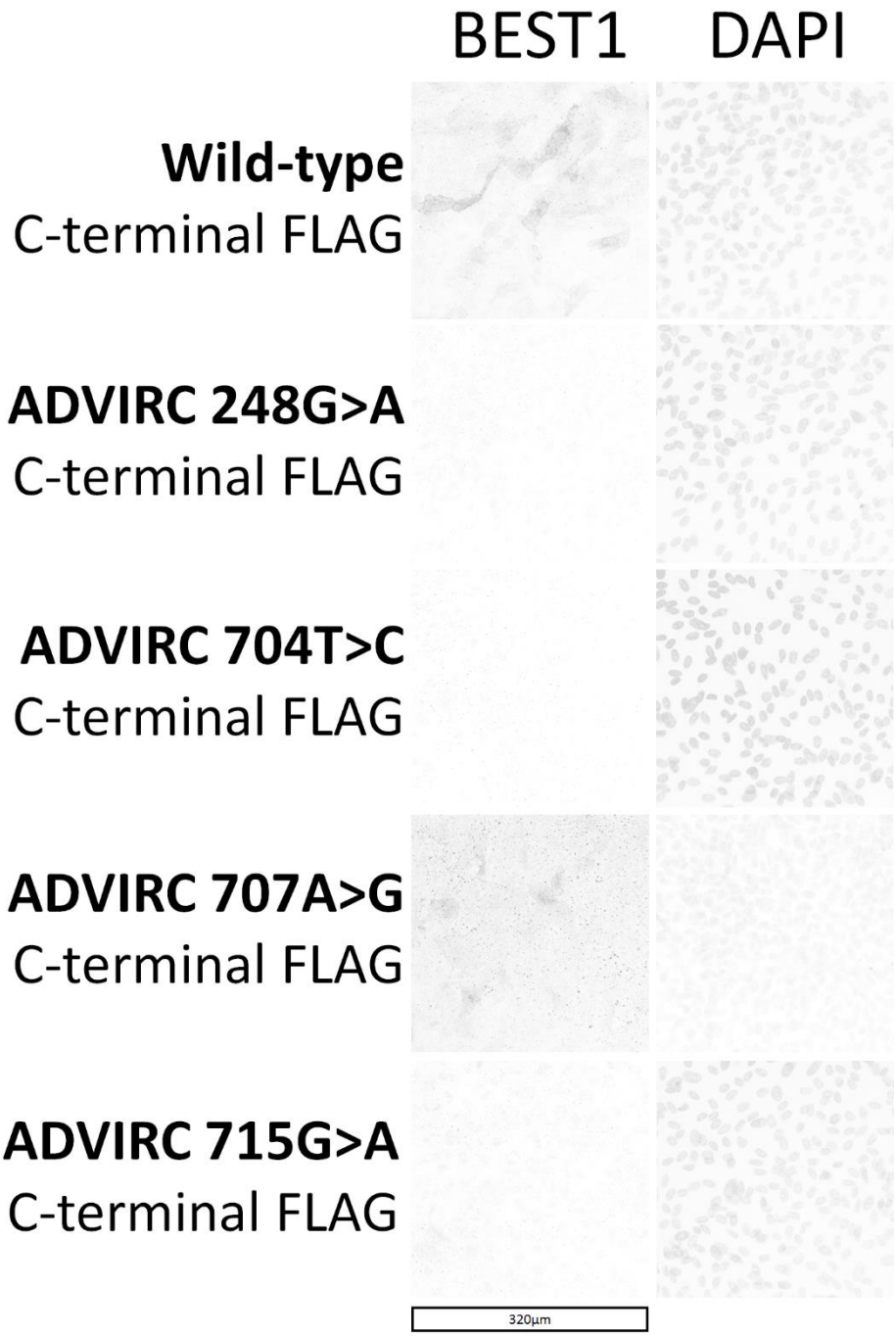

Figure 4.17 Confocal images of the wild-type BEST1 and GFP control ARPE19 cells from the first transfection and stained with the BEST1 antibody and 555 secondary antibody. The genotypes of the pCLNC plasmids is indicated to the left of the confocal images, mutation on top and terminal FLAG below. All images of each channel were taken using identical settings. All images were taken at 20x. Dark areas indicate positive staining. Each image is 320µm by 320µm, as indicated by the sale bar.

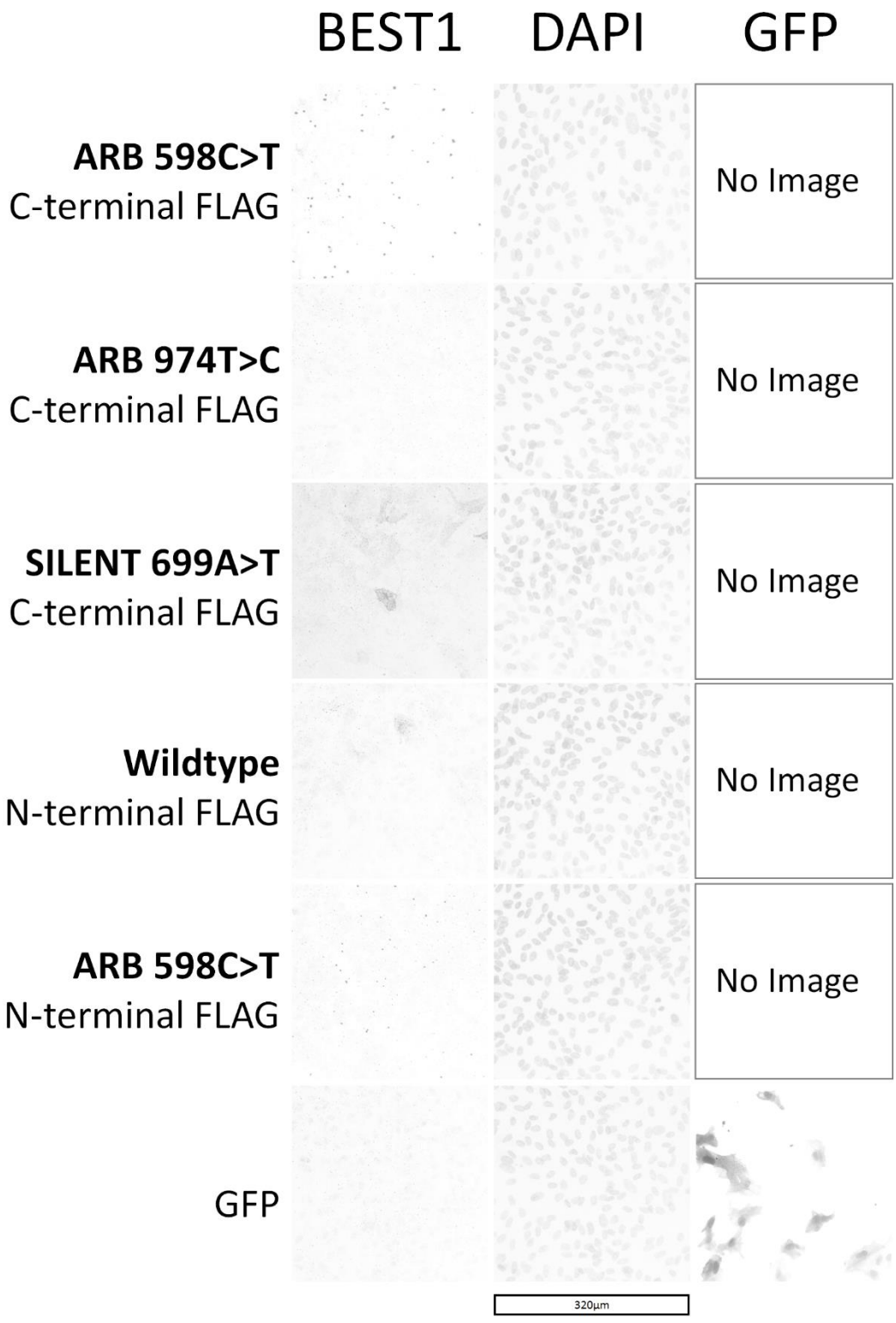

Figure 4.18 Confocal images of the wild-type BEST1 and GFP control ARPE19 cells from the first transfection and stained with the BEST1 antibody and 555 secondary antibody. The genotypes of the pCLNC plasmids is indicated to the left of the confocal images, mutation on top and terminal FLAG below. All images of each channel were taken using identical settings. All images were taken at 20x. Dark areas indicate positive staining. Each image is 320µm by 320µm, as indicated by the sale bar.

It is also of note that the GFP expression appears much brighter in the case of the test transfection line than the selected line. This could suggest that transfection efficiency was lower in the second transfection, although this would not explain why GFP positive cells were not more enriched by the selection.

The 256 G>A (C-terminal FLAG) line is not shown as the cells in this line died soon after transfection. The wild-type and 248G>A (C-terminal FLAG) lines also died off after the samples were taken for the western and immunocytochemistry assays.

4.4.5.4 Repeated transfections using ARPE-19 cells

Additional retroviral transfections of ARPE-19 cells with the constructs were performed. It was noted that lines transfected with wild-type, 248G>A and 256 G>A tended to die off within a week of transfection, whether or not they were in G418 selection. It was also noted that vesicle-like structures similar in appearance to bubbles appeared in some of the lines soon after transfection and were gradually lost over the next few weeks. Further investigation into the vesicle-like structures are described later in this chapter.

4.4.6 Can HEK293 and MDCK cells be used to express *BEST1* retrovirally?

While attempting to successfully retrovirally transfect the ARPE-19 cells with the mutant *BEST1* constructs the constructions containing wild-type and 704T>C *BEST1* were also transfected into MDCK and HEK293 cells.

4.4.6.1 Additional western blotting

Following repeat transfections and selection of more ARPE-19 cells alongside MDCK cells additional western blotting was performed. This is shown in **Figure 4.19**, where it can be seen that clear BEST1 staining is once again not observed in the selected ARPE-19 lines, though bands are seen at high exposures in the wild-type and 704T>C lines in MDCK cells. These MDCK cells had been exposed to G418 selection, though at lower concentrations and for shorter time than the ARPE-19 cells.

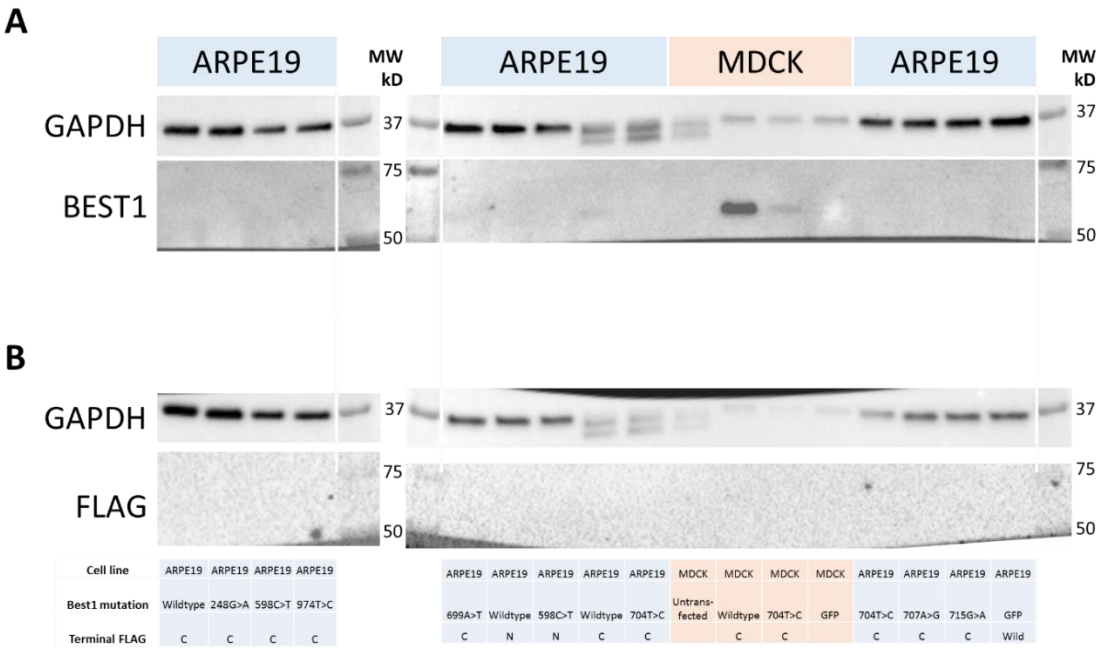

Figure 4.19 Western blot staining of cell lysates from retrovirally transfected ARPE19 and MDCK cells using GAPDH, BEST1 and FLAG antibodies. A) samples stained with GAPDH and BEST1 antibodies. B) samples stained with GAPDH and FLAG antibodies. ARPE19 sample labels are shown in grey, MDCK sample labels are shown in orange. All samples were loaded in non-reducing buffer.

The data presented above suggests that even after strong G418 selection that was sufficient to kill untransfected ARPE-19 cells, these retrovirally transfected lines show extremely low or apparently absent detectable BEST1 protein. In some cases this is expected: the 598C>T mutation generates a premature stop codon and one would therefore not expect any product to be detected using a BEST1 antibody that recognises the C-terminal end of the protein. The others require a different explanation.

To assay for retroviral integration in to the genome gDNA samples were prepared from 26 cell lines that had been transfected with pCLNC constructs containing either *BEST1* or GFP. These included ARPE-19 cells, HEK293 cells, and MDCK cells. These samples were then assayed for the presences of the NEO^R gene through semi-quantitative PCR. The results are shown in **Figure 4.20**. As expected the untransfected ARPE-19 line and the untransfected MDCK line on the far right of the figure showed no amplification for the NEO^R gene, which does not occur naturally in the human genome. All the other lines show amplification of the NEO^R gene, confirming retroviral integration. The fact that the MDCK 704T>C (C-terminal FLAG) line shows only a very faint band for NEO^R gene amplification is particularly odd, as this line does shows visible band for BEST1 staining in the western blot in **Figure 4.19**. In any case it is clear in the case of the

ARPE-19 lines that retroviral insertion can be detected by PCR in the absence of any detectable BEST1 protein assayed by western blotting.

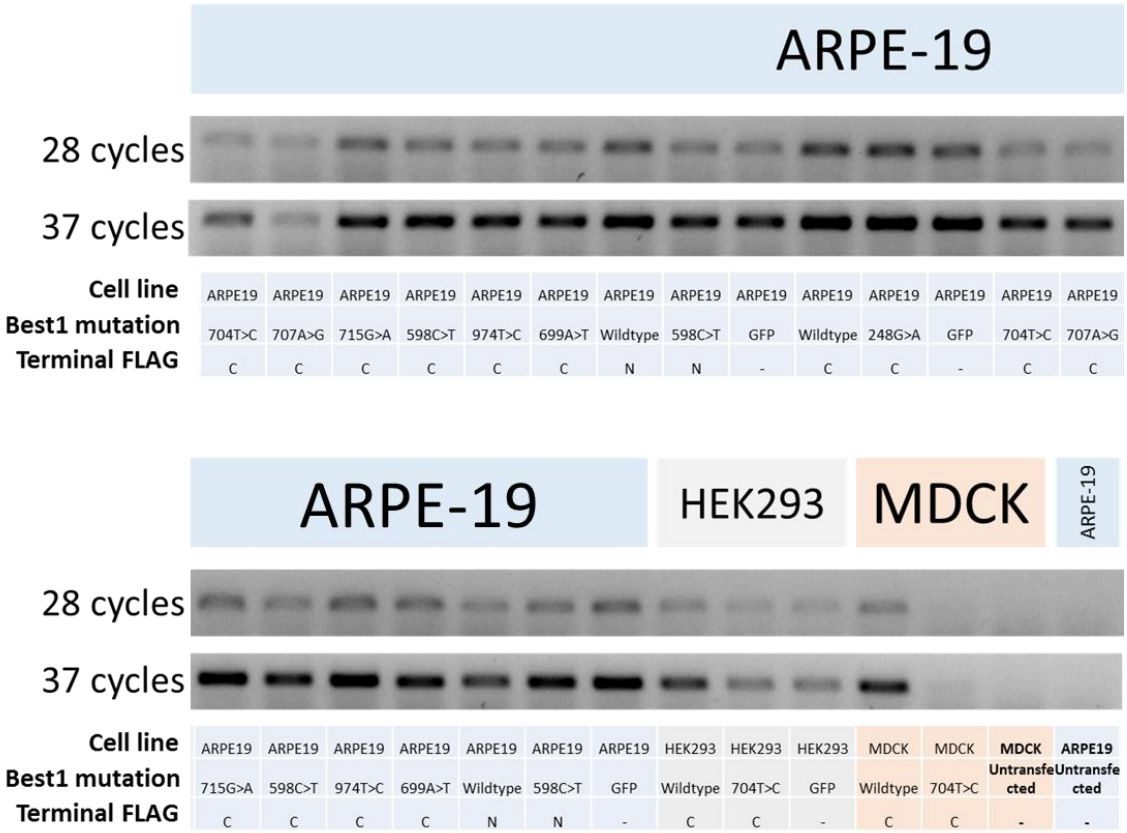

Figure 4.20 PCR assay for the presence of the retrovirally introduced NEO^R gene in genomic DNA extracted from 26 retrovirally transfected cell lines and 2 untransfected control lines. The samples have been split into two panels for this figure, but were run and imaged as a single agarose gel. In each case the panel shows band intensity after 28 cycles and after 37 cycles. The two untransfected cells lines at the far right of the lower panel served as negative control samples. ARPE19 sample labels are shown in grey, MDCK sample labels are shown in orange.

This suggests an explanation for the lack of BEST1 detection using western blotting and immunocytochemistry. Expression of the Neo^R gene is driven by driven by a Moloney MLV and murine sarcoma virus LTR (RU5), while expression of the *BEST1* gene is driven by a human cytomegalovirus (CMV) immediate early promoter/enhancer. It is therefore possible that the CMV promoter/enhancer is being epigenetically silenced while the RU5 is not. If the level of *BEST1* expression produced from these constructs reduces their fitness relative to untransfected cells then over time in culture the proportion of transfected cells will decrease. Under the condition of selection with G418 the fitness of transfected cells should be much higher than untransfected cells. However, the fitness of transfected cells with active NEO^R expression but silenced *BEST1* expression would be highest of all.

This argument is supported by the fact that GFP expression in the G418-selected lines did increase over time, images of which can be found in the Appendix.

4.4.7 What is the nature of the vesicle-like structures seen after transfection?

4.4.7.1 Staining for acidic compartments and for lysosomes

If expression of the *BEST1* constructs in ARPE-19 cells is causing a fitness reduction then this could be linked to the vesicle-like structures mentioned previously that were seen in some lines following transfection. To investigate this a new set of tranfections of ARPE-19 cells was performed and examined for the presence of the vesicle-like structures.

These structures are shown in **Figure 4.21** and **Figure 4.22**, and examples of two lines with and with the structures are shown at higher magnification in **Figure 4.23**. The vesicle-like structures were prominent in lines, 256G>A, 704T>C, and 715G>A, though some were observed in lines 248G>A and 707A>G. This is described in **Table 4.4.** After replating the number and size of the vesicle-like structures had decreased. After several weeks in culture vesicles were absent.

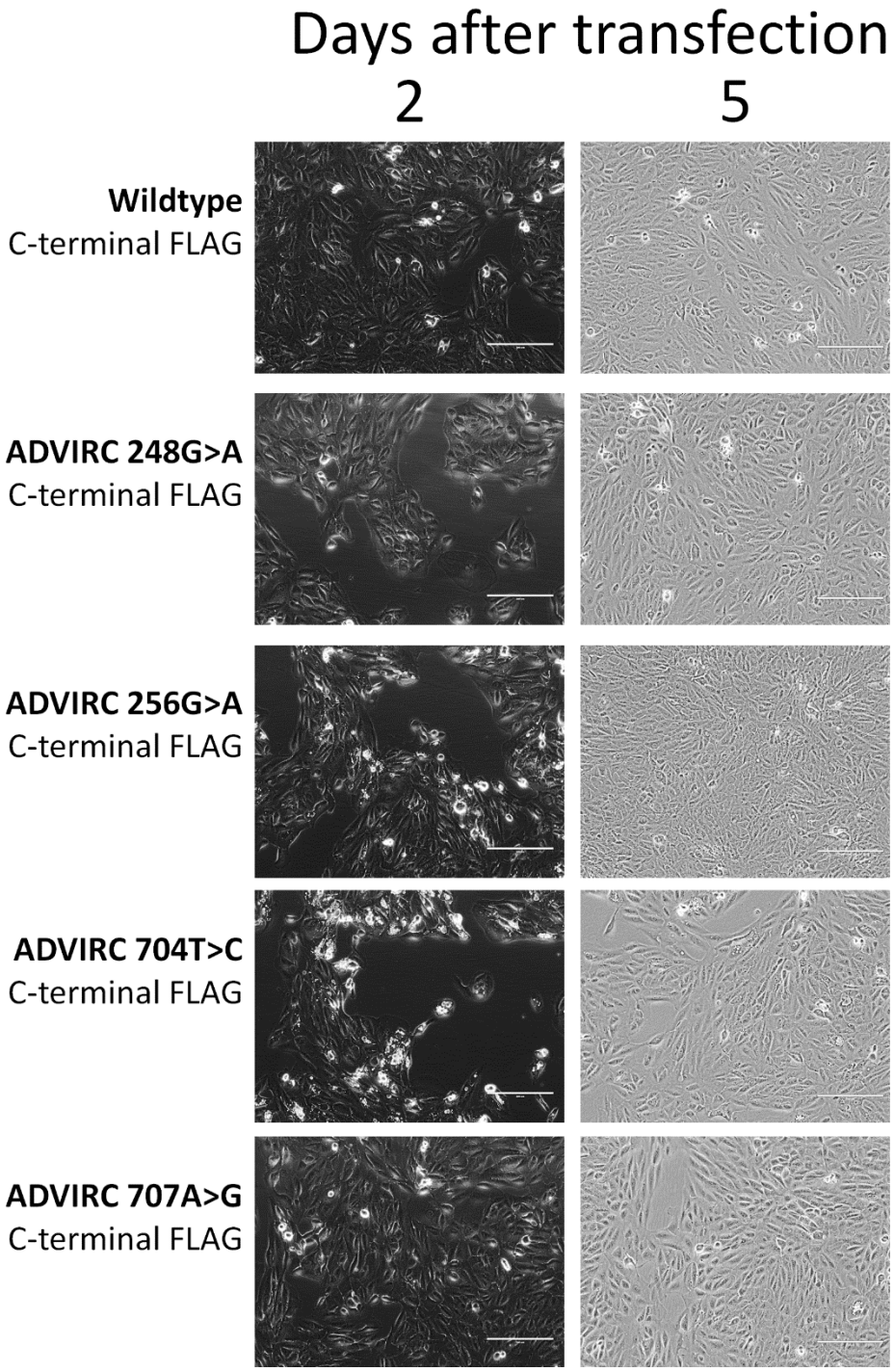

Figure 4.21 Phase-contrast EVOS images of ARPE19 cells transfected with pCLNC retroviral plasmids and imaged 2 days after transfection and then again 5 days after transfection, which was also after replating. To the left of each pair of images is the given the Best1 mutation and terminal FLAG of the pCLNC plasmid in each case. The no-plasmid transfection used the same protocol, but no pCLNC plasmid was included. All images were taken at 20x. Scale bars indicate 200 µm.

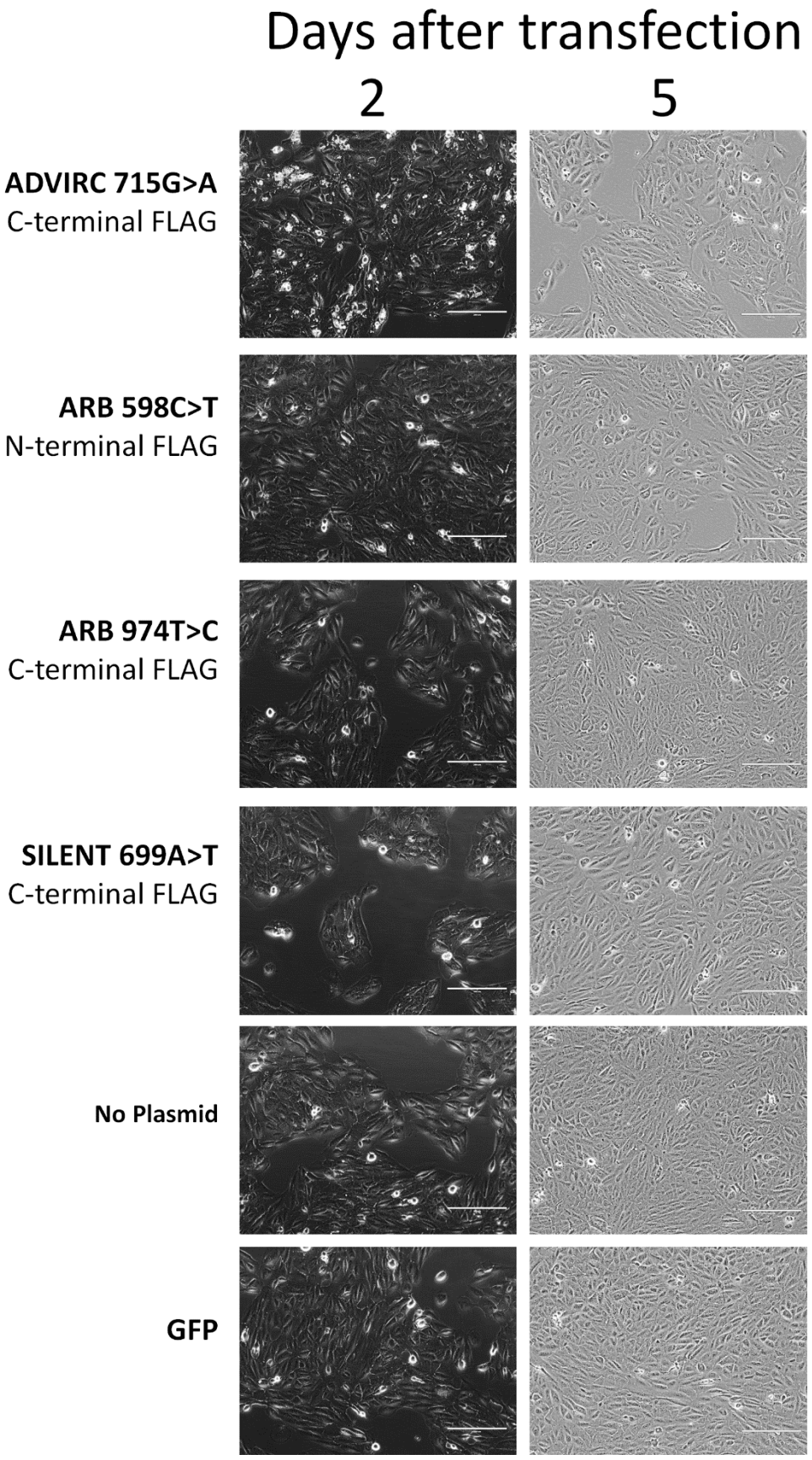

Figure 4.22 Phase-contrast EVOS images of ARPE19 cells transfected with pCLNC retroviral plasmids and imaged 2 days after transfection and then again 5 days after transfection, which was also after replating. To the left of each pair of images is the given the Best1 mutation and terminal FLAG of the pCLNC plasmid

in each case. The no-plasmid transfection used the same protocol, but no pCLNC plasmid was included. All images were taken at 20x. Scale bars indicate 200 µm.

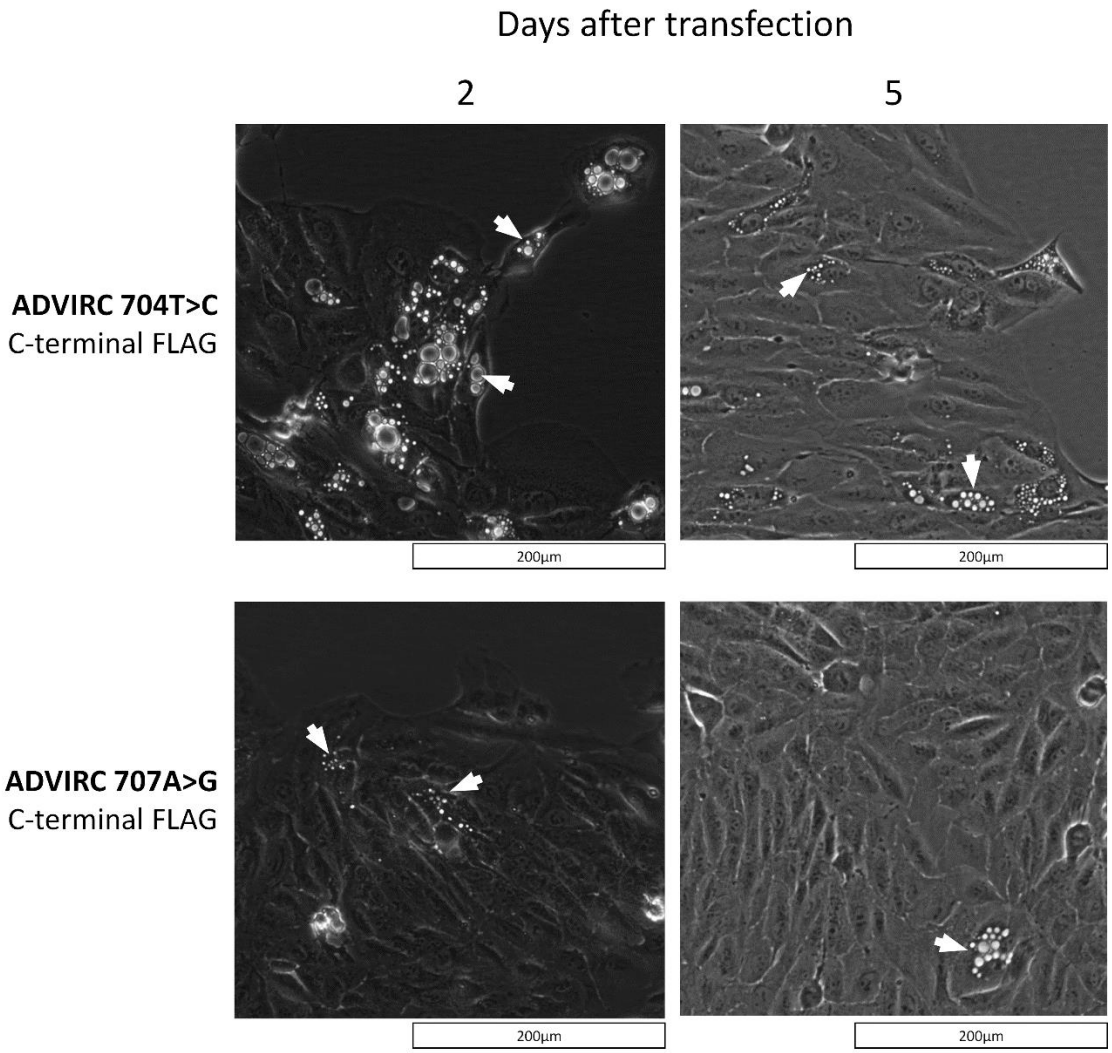

Figure 4.23 Magnified example EVOS images of ARPE19 cells transfected with pCLNC retroviral plasmids and imaged 2 days after transfection and then again 5 days after transfection, which was also after replating. To the left of each pair of images is the given the Best1 mutation and terminal FLAG of the pCLNC plasmid in each case. Images have been magnified and cropped to show the appearance of the vesicle structures, examples of which have been marked with white arrows. Scale bars indicate 200µm.

			Appearance of vesicular structures after transfection			
Best1 mutation	**FLAG tag**	**Disease**	**Day 2**	**Day 3**	**Day4 (after replating)**	**Day 5**
Wild-type	C	-				
248 G>A	C	ADVIRC		**very little**	**very little**	**almost none**
256 G>A	C	ADVIRC	**many**	**many**	**many**	**some**
704 T>C	C	ADVIRC	**many**	**many**	**many**	**many**
707 A>G	C	ADVIRC	**some**	**some**	**very little**	**one cell**
715 G>A	C	ADVIRC	**many**	**many**	**many**	**many**
598 C>T	N	ARB				
974 T>C	C	ARB				
699 A>T	C	-				
No plasmid	-	-				
GFP control	-	-				

Table 4.4 Visual analysis of vesicle presence in ARPE19 lines following retroviral transfection. In the leftmost column the Best1 point mutation of the transfected construct is shown, including the no-plasmid control and the GFP control plasmid. Next the location of the terminal FLAG tag is shown (N or C). Next a qualitative description of the presence of the presence of vesicular structures on each day is shown in terms of the proportion of cells containing visible structures. Note that the cells were replated between days 3 and 4. Images used for analysis were taken at 20x at 4 random locations within each well of cells (broadly top-left, top-right, bottom-left, bottom-right). Empty cells indicate a lack of visible vesicular structures.

It was hypothesised that the vesicle-like structures seen in some transfected lines could be lysosomes or autophagosomes, hydrolysing and degrading excess BEST1 product. Therefore the cells were stained using two intracellular stains. LysoTracker™ Deep Red is a fluorescent dye for labelling acidic organelles consisting of a fluorophore conjugated to a weak base. This can freely permeate cell membranes and builds up in intracellular compartments with low pH. CellLight™ Lysosomes-GFP is a plasmid expression construct of a GFP fluorophore fused to lysosomal associated protein 1 (Lamp1) which localises to lysosomes on expression. The results of this staining are shown in **Figure 4.24** and **Figure 4.25**. A subset of cells in each case stain for CellLight and in some cases cells are positive for Lysotracker. This could be due to some cells not containing lysosomes or acidic compartments, but more likely reflects heterogeneous efficiency of staining on a cell to cell basis. However, the important detail is that in the cases that clear vesicle-like structures are observed (256G>A, 704T>C, and 715G>A, all C-terminal FLAG) CellLight or Lysotracker staining does not localise to the vesicle-like structures. These three lines are shown again as composite images in **Figure 4.26**, alongside composite confocal images of fixed 704T>C (C-terminal FLAG) cells from a different transfection that show the same pattern.

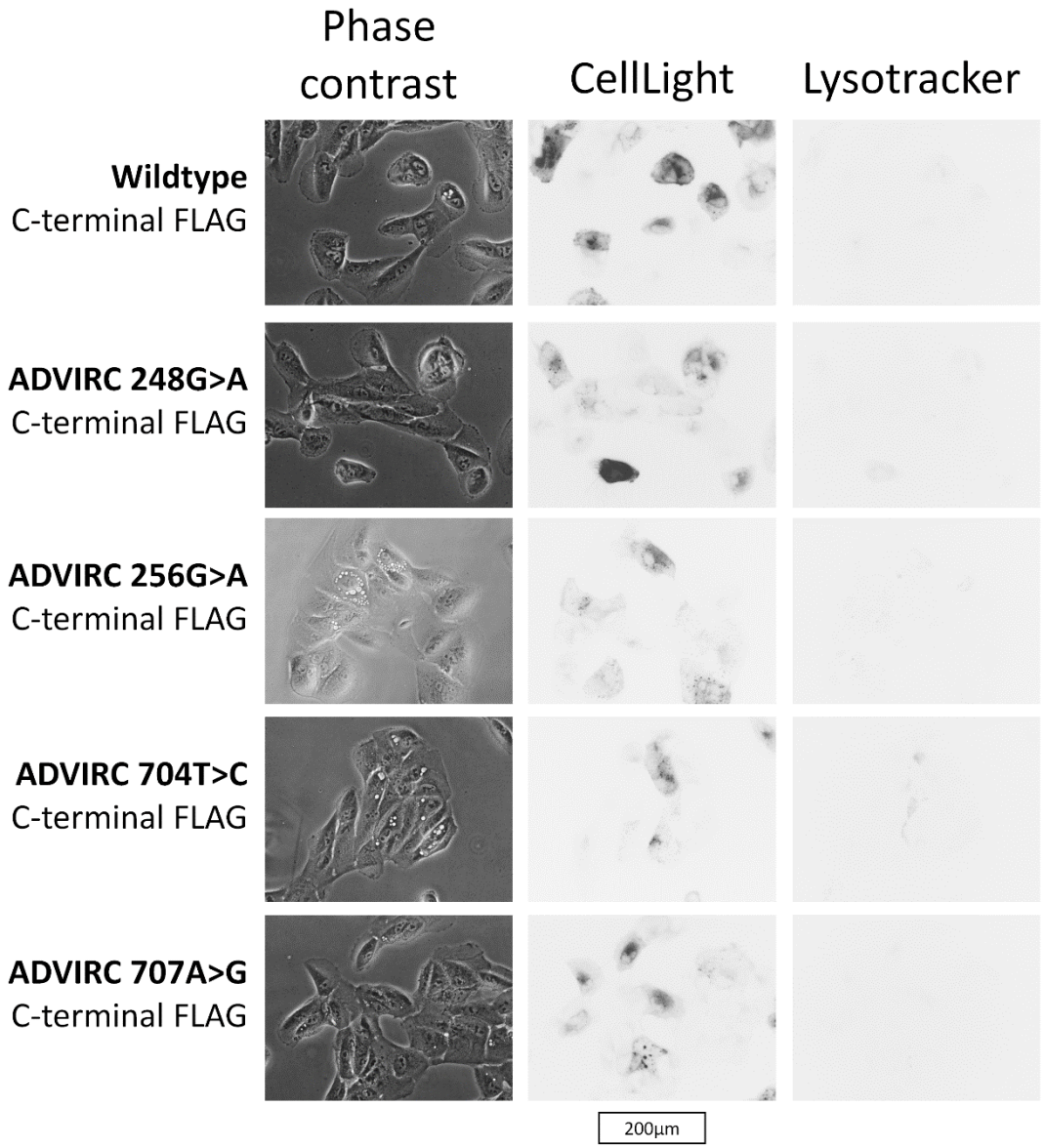

Figure 4.24 EVOS images of live ARPE19 cells transfected with pCLNC retroviral plasmids and imaged after staining with CellLight and Lysotracker reagents. To the left of each pair of images is the given the Best1 mutation and terminal FLAG of the pCLNC plasmid in each case. The no-plasmid transfection used the same protocol, but no pCLNC plasmid was included. In the CellLight and Lysotracker columns black indicates positive staining. All images were taken at 40x. The scale bar at the base shows 200µm.

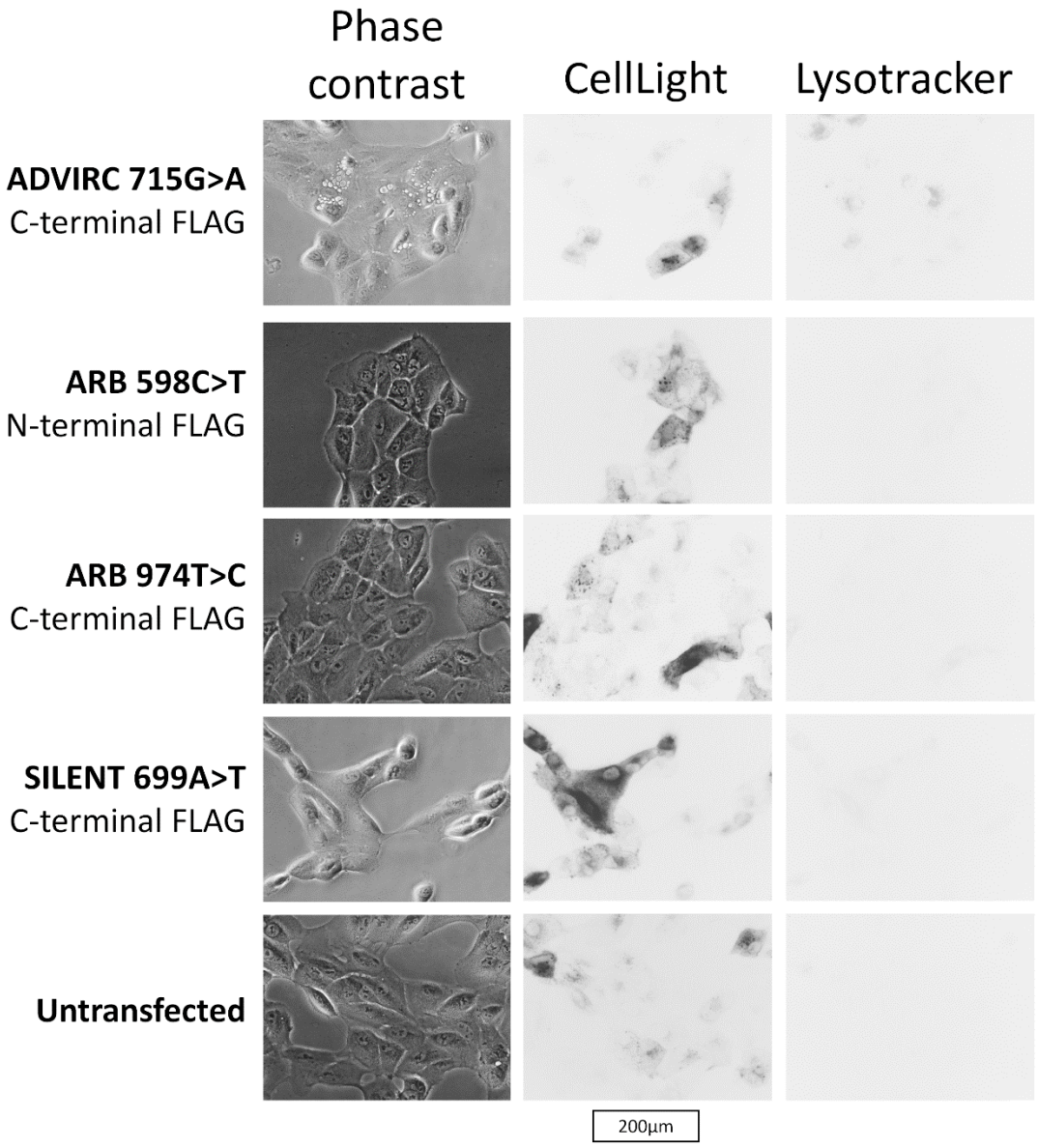

Figure 4.25 EVOS images of live ARPE19 cells transfected with pCLNC retroviral plasmids and imaged after staining with CellLight and Lysotracker reagents. To the left of each pair of images is the given the Best1 mutation and terminal FLAG of the pCLNC plasmid in each case. The no-plasmid transfection used the same protocol, but no pCLNC plasmid was included. In the CellLight and Lysotracker columns black indicates positive staining. All images were taken at 40x. The scale bar at the base shows 200µm.

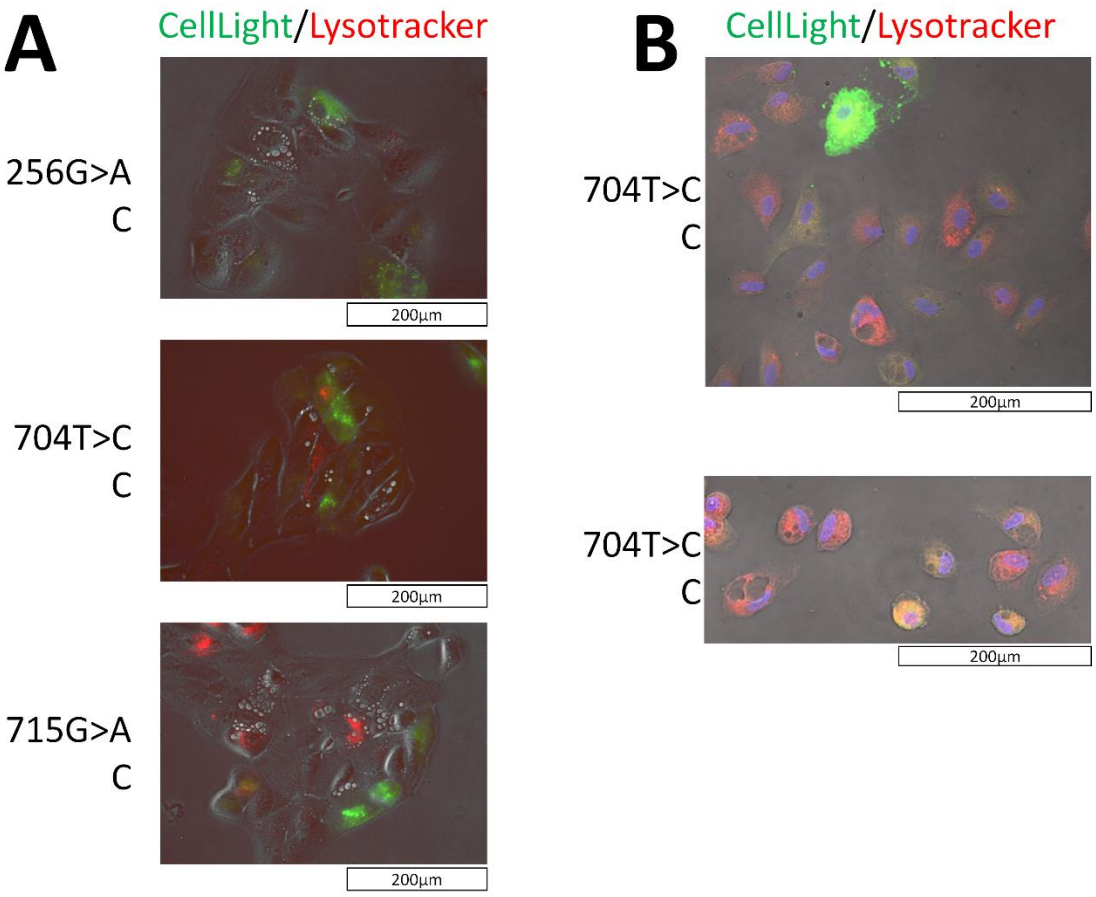

Figure 4.26 Composite images of ARPE19 cells transfected with pCLNC retroviral plasmids and imaged after staining with CellLight and Lysotracker reagents. A) EVOS images of live ARPE19 cells. The three lines with clear vesicular structures are shown as composite images. To the left of each pair of images is the given the Best1 mutation and terminal FLAG of the pCLNC plasmid in each case. Images were taken at 40x. B) Confocal composite images of fixed 704T>C (C-terminal FLAG) cells from a line created in a different transfection event. Images were taken at 20x and have been cropped to show detail.

4.4.7.2 Staining for BEST1 localisation

Staining was also performed on the transfected lines above for BEST1 to assess whether BEST1 protein localised to the vesicle-like structures. The results are shown in **Figure 4.27**, where it can be seen that BEST1 staining in the 704T>C and 715G>A (C-terminal FLAG) lines did not localise to the vesicle-like structures. After fixation no vesicle-like structures could be found in other lines, including 256G>A (C-terminal FLAG) and the number of vesicle-like structures in the two lines shown was greatly reduced, although they were perhaps larger. This suggests that the vesicle-like structures collapse during fixation. One possibility is that they are not in fact intracellular, but subcellular. As BEST1 operates as an ion pump it is conceivable that overexpression of *BEST1* transgenes could affect ion flow and cause pockets of fluid to form between the cell and the plastic culture surface.

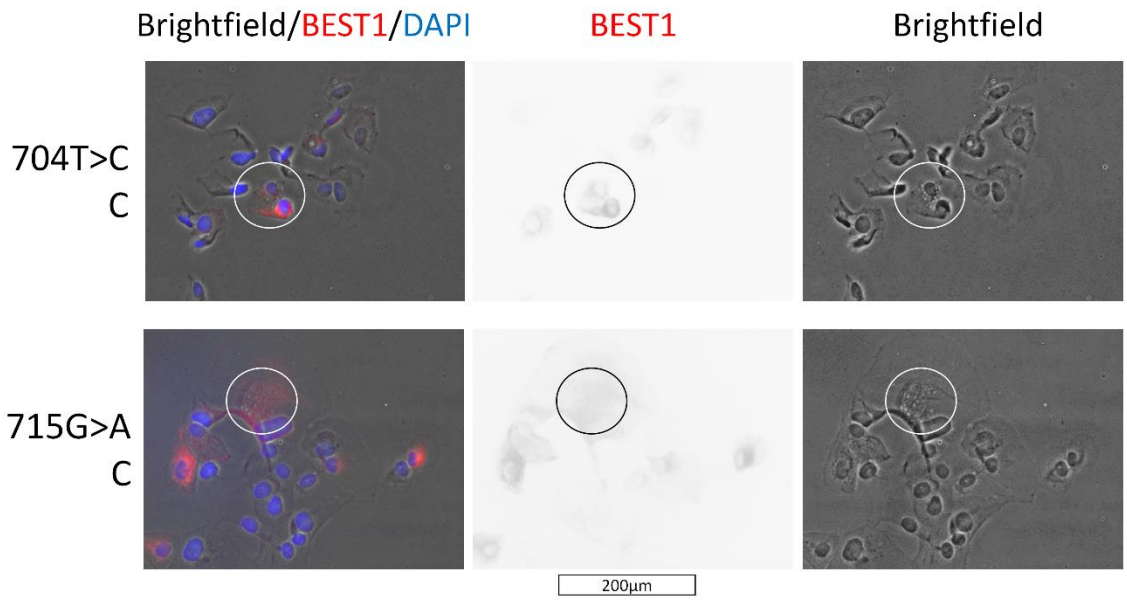

Figure 4.27 Composite EVOS images of fixed ARPE19 cells transfected with pCLNC retroviral plasmids and imaged after staining with BEST1 antibody and DAPI. After fixation only two lines showed visible vesicles, which are shown above. White circles have been added to indicate cells with both BEST1 staining and vesicles. BEST1 only images are shown in the middle to clarify which cells show BEST1 staining, with black representing positive staining. Brightfield only images are shown on the right to clarify which cells have vesicular structures. The scale bar shows 200µm.

Figure 4.28 and **Figure 4.29** show BEST1 staining on all the lines assayed for vesicle-like structures, demonstrating that BEST1 staining is seen in all lines in which it would be expected (excluding the no-plasmid control, the GFP control, and the 598C>T premature stop codon), and therefore the presence of vesicle-like structures is not simply due to the presence or absence of BEST1 protein in general.

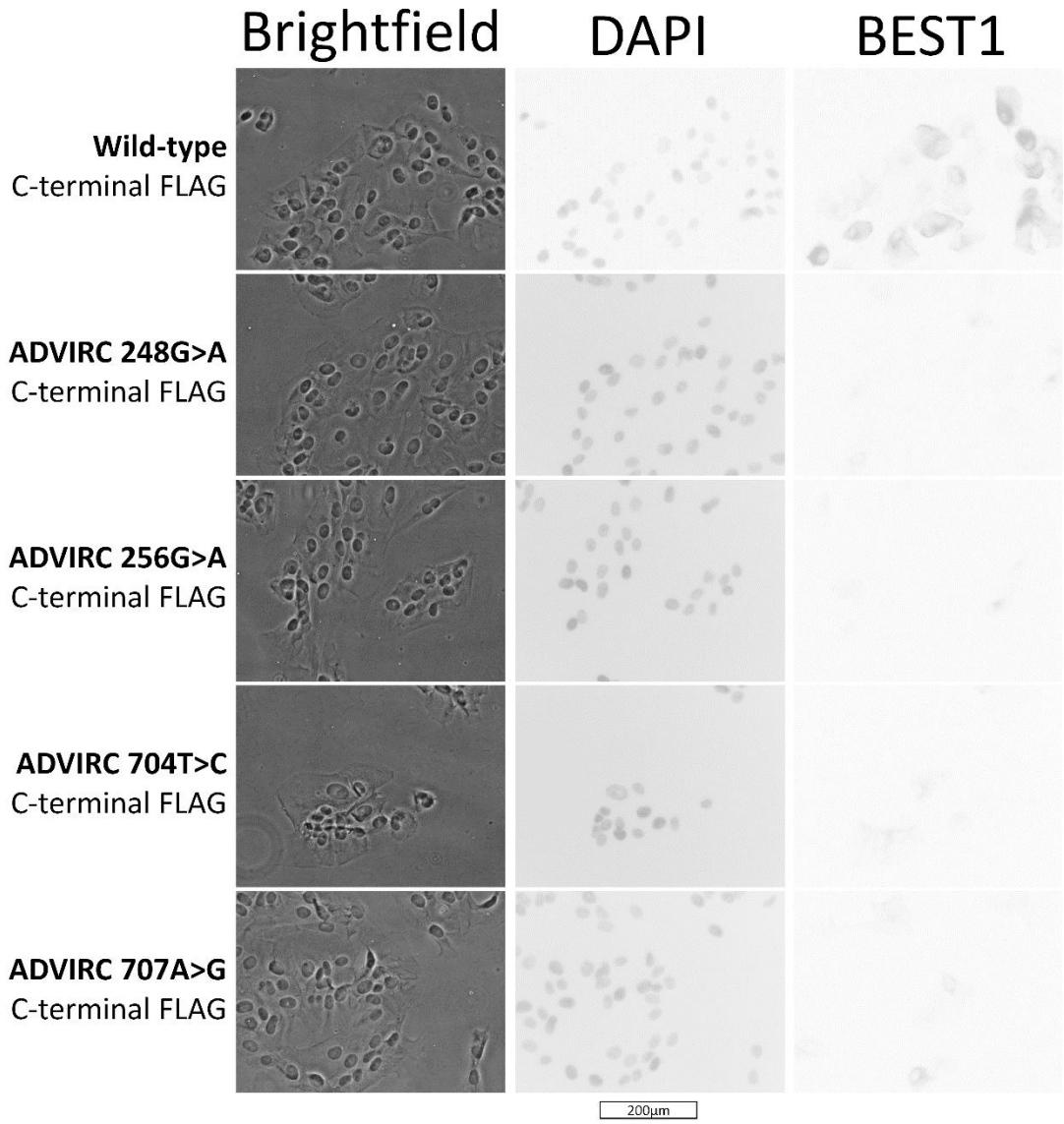

Figure 4.28 EVOS images of ARPE19 cells transfected with pCLNC retroviral plasmids and stained with the BEST1 primary antibody and 555 secondary antibody. The genotypes of the pCLNC plasmid with which the cells were transfected is indicated to the left of the images, mutation on top and terminal FLAG below. The DAPI and BEST1 columns show black as positive staining. All images of each channel were taken using identical settings. All images were taken at 40x, with the scale bar showing 200µm.

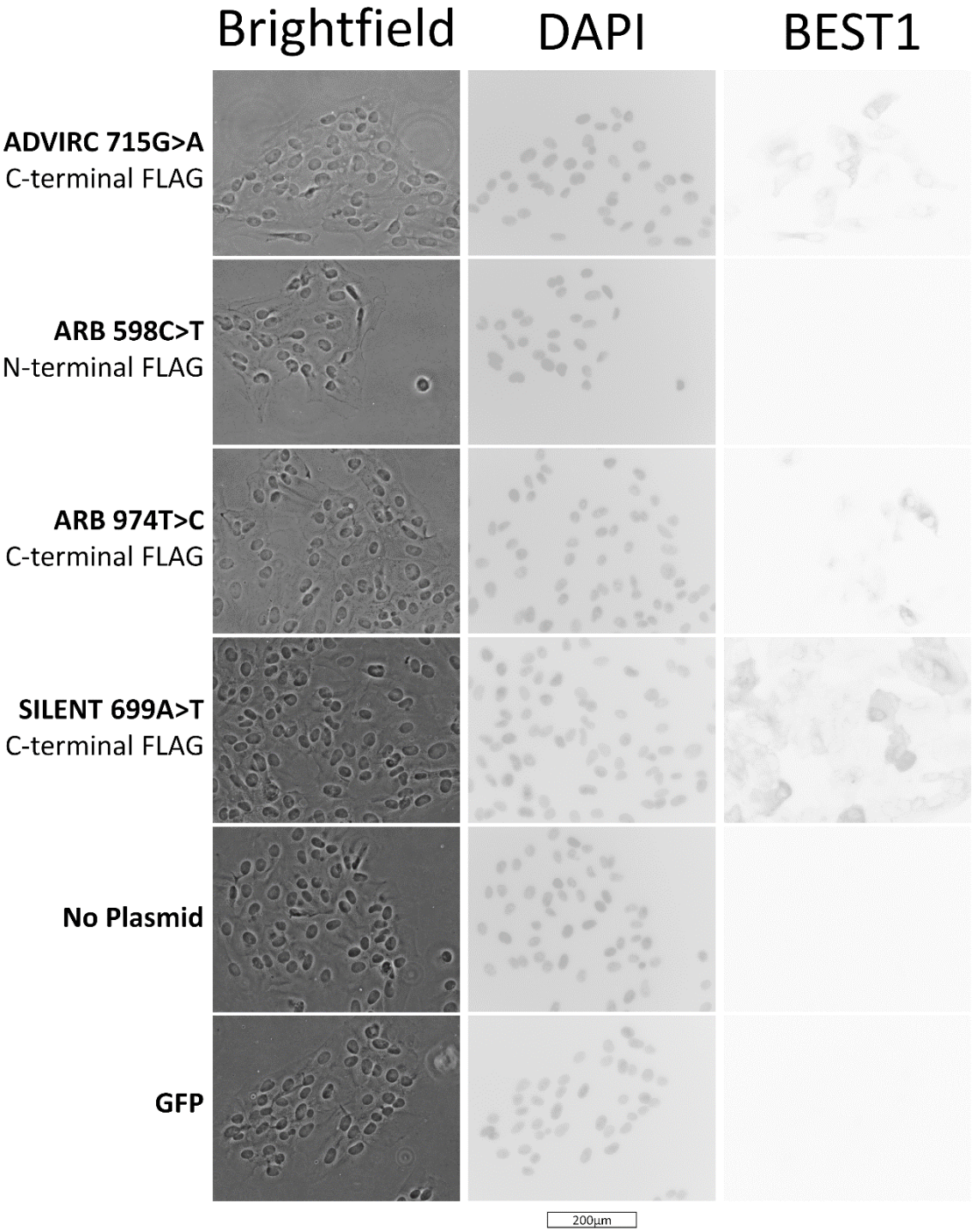

Figure 4.29 EVOS images of ARPE19 cells transfected with pCLNC retroviral plasmids and stained with the BEST1 primary antibody and 555 secondary antibody. The genotypes of the pCLNC plasmid with which the cells were transfected is indicated to the left of the images, mutation on top and terminal FLAG below. The DAPI and BEST1 columns show black as positive staining. All images of each channel were taken using identical settings. All images were taken at 40x, with the scale bar showing 200µm.

4.4.7.3 Are these vesicle-like structures seen in MDCK and HEK293 cells after transfection?

Although these vesicle-like structures were not noted in either MDCK or HEK293 cells following transfection, these cell lines grow to a higher confluent cell density than ARPE-19 cells and so any that were present may have simply not been seen.

4.4.8 Can confocal imaging be used to localise retrovirally expressed BEST1 protein?

With the nature of the vesicle-like structures still largely a mystery it was decided to return to the question of whether BEST1 protein localisation could be assayed using the transfected ARPE-19, MDCK and HEK293 cell lines that had been generated. Although transfection and selection protocols were performed with the aim of maximum expression efficiency of the *BEST1* constructs, for the purposes of analysing protein localisation it would not be necessary for all cells to be expressing the construct at high levels. A low level of *BEST1* transgene within each cell could actually be advantageous as the cells would be less likely to show aberrant protein trafficking due to extremely high levels of expression. A low number of cells expressing the *BEST1* transgenes could be advantageous for distinguishing cell boundaries.

4.4.8.1 Early imaging

Therefore the 25 surviving ARPE-19, HEK293, and MDCK lines that had been generated through retroviral transfection were plated onto 8-well chamber slides coated with Matrigel. This coating was used because ARPE-19 cells had been found to detach from non-coated chamber slides after several weeks in culture. The cells were grown to confluency, fixed, and stained using the BEST1 antibody and the FLAG antibody in separate slides. This BEST1 and FLAG antibody staining was compared using the EVOS and was found to be identical between identical lines for those transfected with C-terminal FLAG constructs, the only difference being that the FLAG antibody staining was less bright than the BEST1 antibody staining. In all cases the ARPE-19 lines transfected with N-terminal FLAG constructs showed no staining with the FLAG antibody. The premature stop codon mutation 598C>T showed no staining with the BEST1 antibody either, as would be expected. Together this all suggested that the C-terminal FLAG tag was accessible to the FLAG antibody, but that the N-terminal FLAG tag was not. From then on only the BEST1 antibody was used for staining.

Cells stained for BEST1 cells were then imaged using the confocal microscope and assessed for BEST1 localisation by taking z-stacks through the cell layer. Z-projections through these stacks, as well as X-Z or Y-Z scans through these same stacks are shown in **Figure 4.30**, **Figure 4.31**, **Figure 4.32**, and **Figure 4.33**. To improve visual clarity the images are present as red (BEST1) and blue (DAPI) on a white background. This was done by inverting the colour of the image so that black became white, red became green, and blue became yellow, and then adjusting the hue so that the BEST1 staining was red again and the DAPI blue.

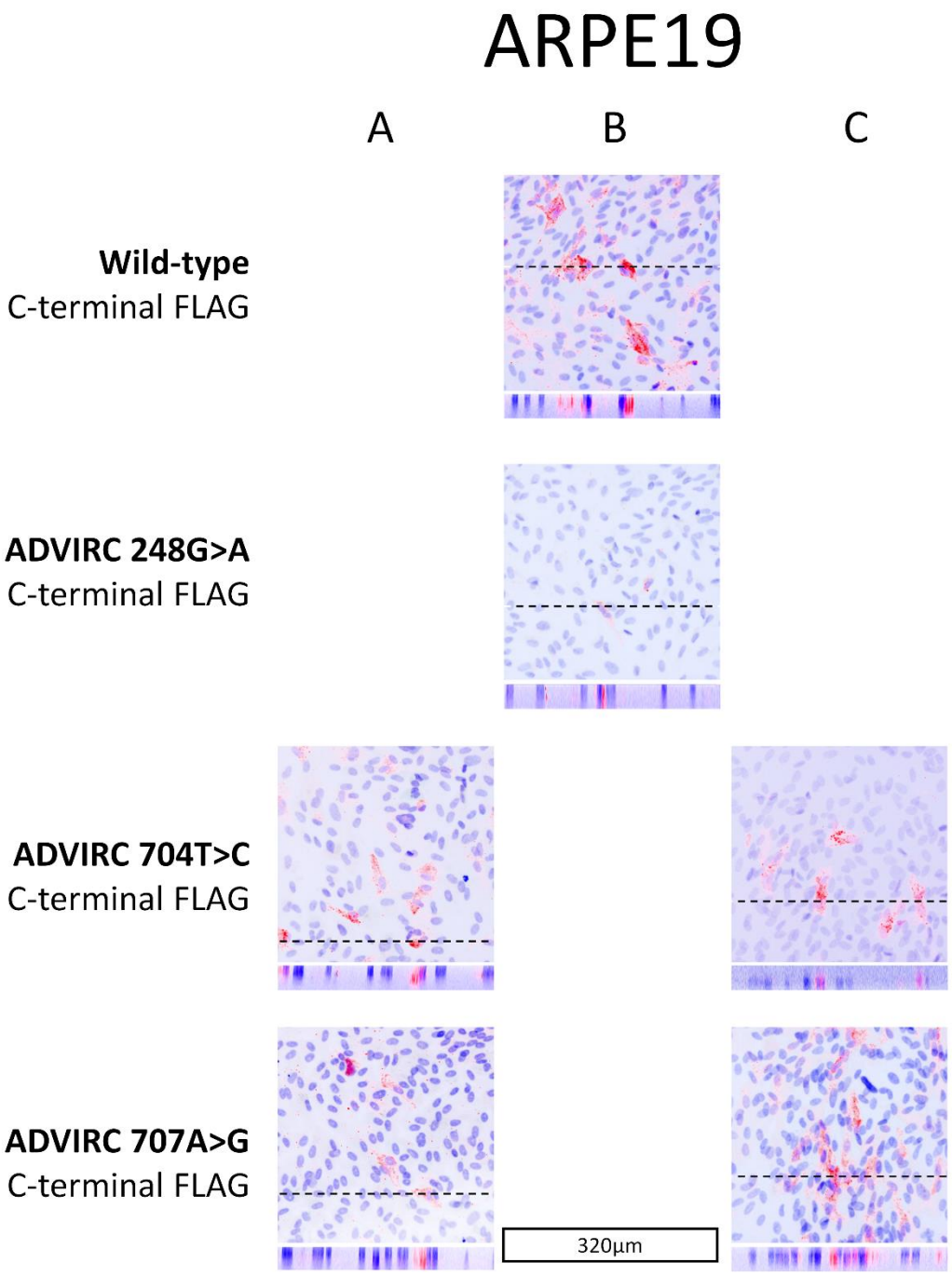

Figure 4.30 BEST1 and DAPI staining in retrovirally transfected ARPE19 cell lines. Shown are average intensity z-projections through 20x image stacks with brightness and contrast altered to show the cellular location of BEST1. Below each image is shown a representative X-Z scan through the same image stacks with brightness and contrast altered and cropping and resizing to show the cellular location of BEST1. The location of the X-Z scan is shown by the black dotted line. BEST1 staining is shown in red and DAPI in blue. The rows labelled A, B, and C indicate three independent retroviral transfections of the ARPE19 line. Along the left of the figure is indicated the plasmid with which the cells were transfected. The upper line gives the position of the genetic substitution and the nature of the substitution. The lower "C" or "N" indicates a C or N-terminal FLAG tag within the construct. Each image is 320µm by 320µm, as indicated by the sale bar.

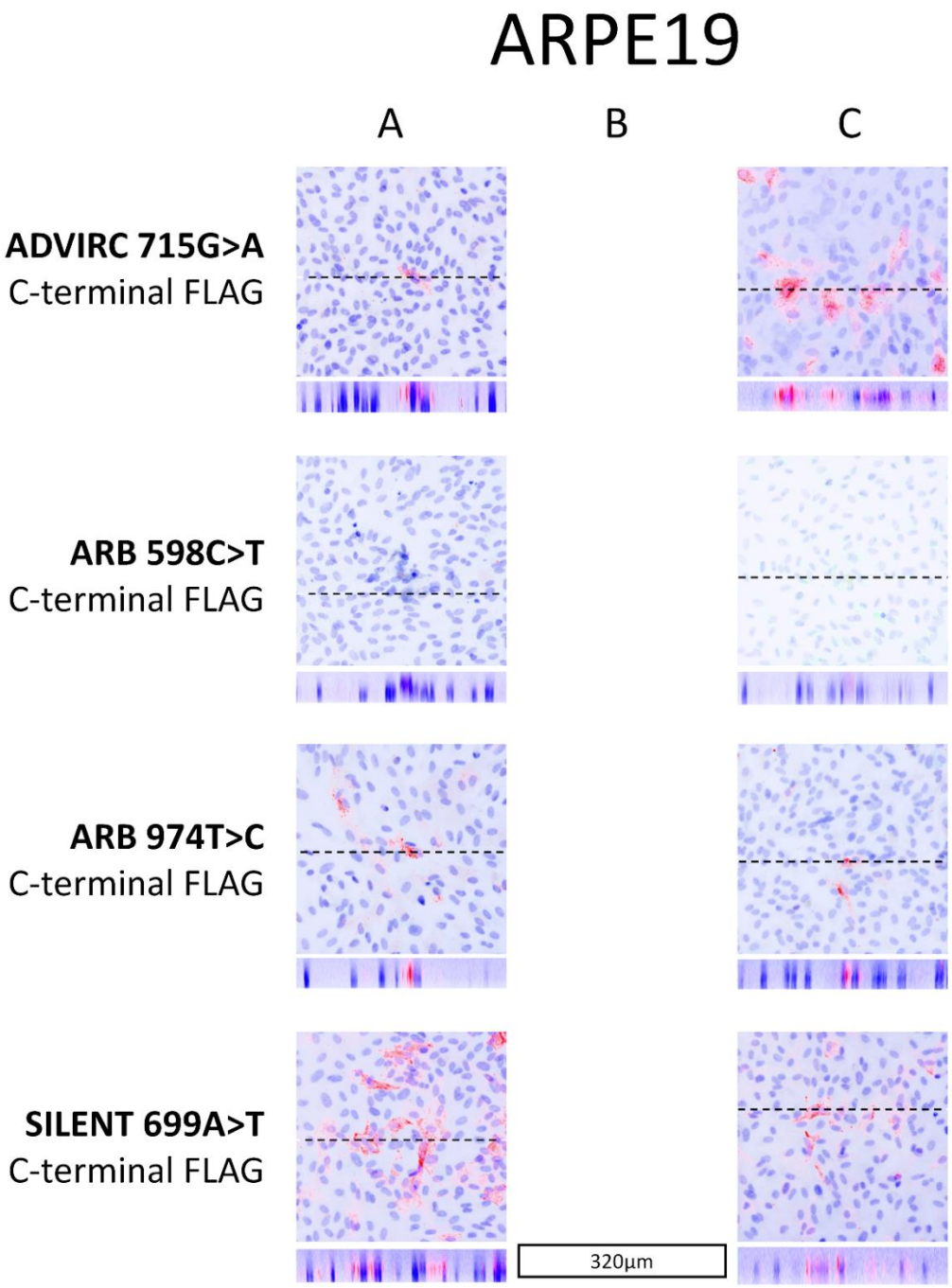

Figure 4.31 BEST1 and DAPI staining in retrovirally transfected ARPE19 cell lines. Shown are average intensity z-projections through 20x image stacks with brightness and contrast altered to show the cellular location of BEST1. Below each image is shown a representative X-Z scan through the same image stacks with brightness and contrast altered and cropping and resizing to show the cellular location of BEST1. The location of the X-Z scan is shown by the black dotted line. BEST1 staining is shown in red and DAPI in blue. The rows labelled A, B, and C indicate three independent retroviral transfections of the ARPE19 line. Along the left of the figure is indicated the plasmid with which the cells were transfected. The upper line gives the position of the genetic substitution and the nature of the substitution. The lower "C" or "N" indicates a C or N-terminal FLAG tag within the construct. Each image is 320µm by 320µm, as indicated by the sale bar.

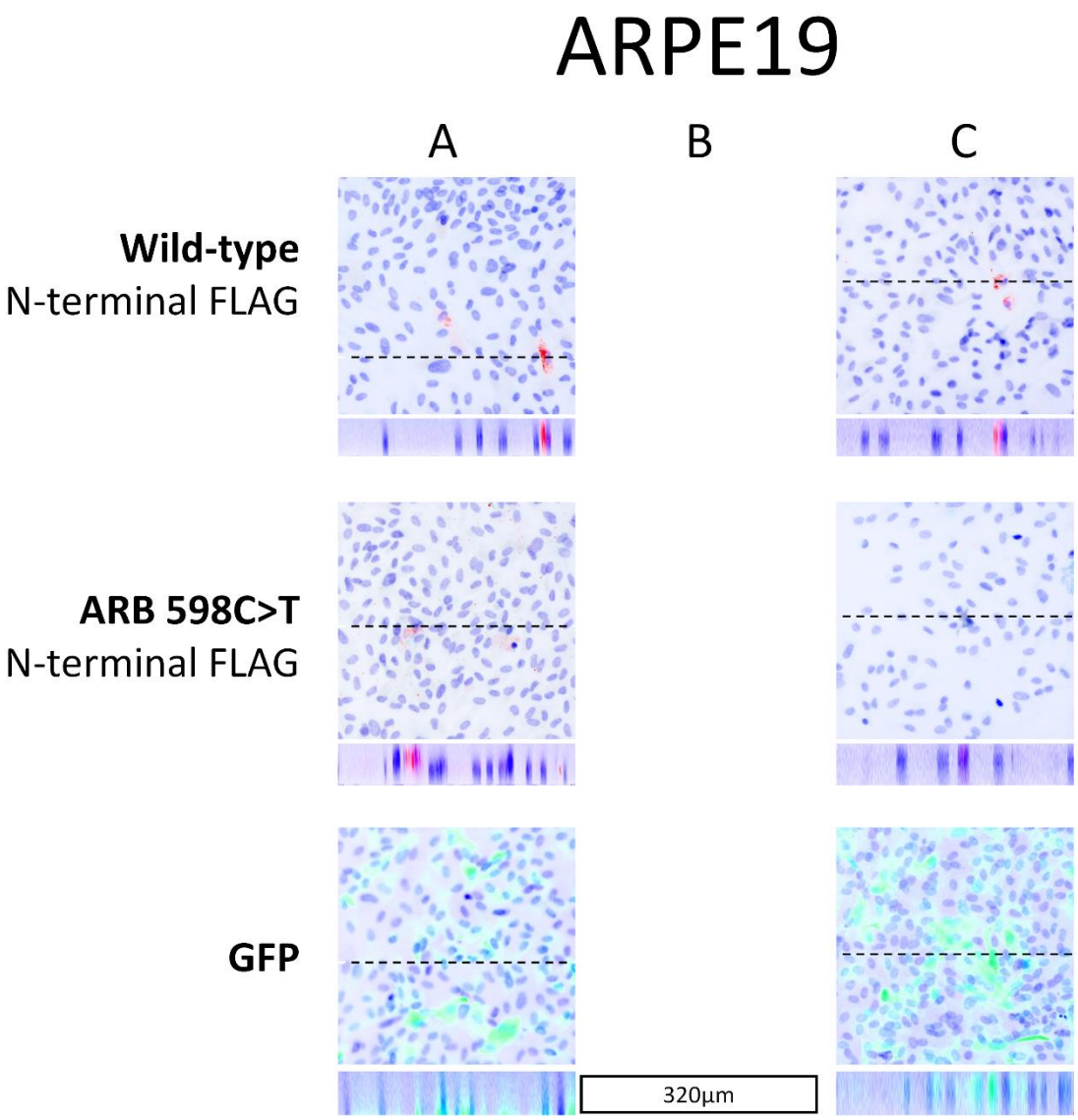

Figure 4.32 BEST1 and DAPI staining in retrovirally transfected ARPE19 cell lines. Shown are average intensity z-projections through 20x image stacks with brightness and contrast altered to show the cellular location of BEST1. Below each image is shown a representative X-Z scan through the same image stacks with brightness and contrast altered and cropping and resizing to show the cellular location of BEST1. The location of the X-Z scan is shown by the black dotted line. BEST1 staining is shown in red and DAPI in blue. The rows labelled A, B, and C indicate three independent retroviral transfections of the ARPE19 line. Along the left of the figure is indicated the plasmid with which the cells were transfected. The upper line gives the position of the genetic substitution and the nature of the substitution. The lower "C" or "N" indicates a C or N-terminal FLAG tag within the construct. Each image is 320µm by 320µm, as indicated by the sale bar.

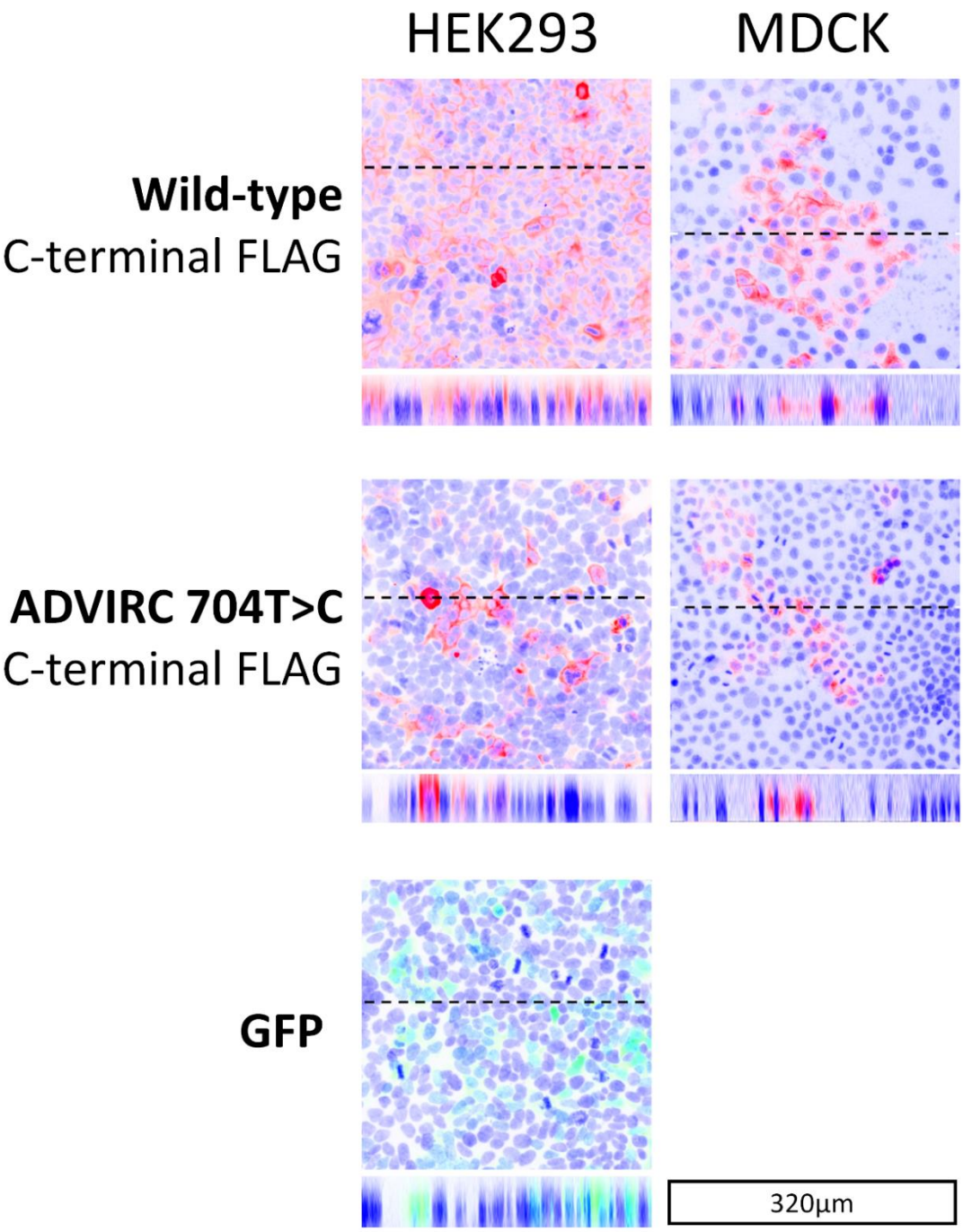

Figure 4.33 BEST1 and DAPI staining in retrovirally transfected MDCK and HEK293 cell lines. Shown are average intensity z-projections through 20x image stacks with brightness and contrast altered to show the cellular location of BEST1. Below each image is shown a representative X-Z scan through the same image stacks with brightness and contrast altered and cropping and resizing to show the cellular location of BEST1. The location of the X-Z scan is shown by the black dotted line. BEST1 staining is shown in red and DAPI in blue. The rows labelled A, B, and C indicate three independent retroviral transfections of the ARPE19 line. Along the left of the figure is indicated the plasmid with which the cells were transfected. The upper line gives the position of the genetic substitution and the nature of the substitution. The lower "C" or "N" indicates a C or N-terminal FLAG tag within the construct. Each image is 320µm by 320µm, as indicated by the sale bar.

4.4.8.2 Localisation of the BEST1 protein analysis

4.4.8.3 Lateral localisation

All four of the BEST1 MDCK and HEK293 cell lines (wild-type and 704T>C for each) are shown in **Figure 4.33**, and show bright BEST1 staining in the majority or a significant minority of cells. It can be seen that for both MDCK and HEK293 cells the wild-type (C-terminal FLAG) BEST1 staining localises somewhat laterally in the cell, clearly marking cell borders. In the case of the 704T>C (C-terminal FLAG) lines the HEK293 cells show lateral BEST1 staining while the MDCK cells do not.

4.4.8.4 Apical-basal localisation

However, when stacks were taken through the cells it was difficult to determine visually whether the medial staining seen in the cells was apical or basal, although in **Figure 4.33**, the localisation in HEK293 cells appears mostly apical. This was true at both 20x and 40x magnification. However, by collapsing the 3-dimensional stack into a 1-dimentional stack it was possible to compare the average DAPI and BEST1 staining intensities in the z-axis, apical to basal. This was done by opening each stack in ImageJ and then using the Analyse>Measure function for each slice of each channel. This gave a value for the mean pixel intensity for each slice between 0 and 255 (saturation). Using the Conditional Formatting>Colour Scales function in Microsoft Excel these values were then converted to a colour scale for each channel. An example of this analysis is shown in **Figure 4.34** for MDCK cells transfected with the wildtype (C-terminal FLAG) *BEST1*. Here it can be seen that the brightest bars are in the 6th slice for both DAPI and BEST1 staining, suggesting that BEST1 protein is not localised predominately to the apical or basolateral cell membrane.

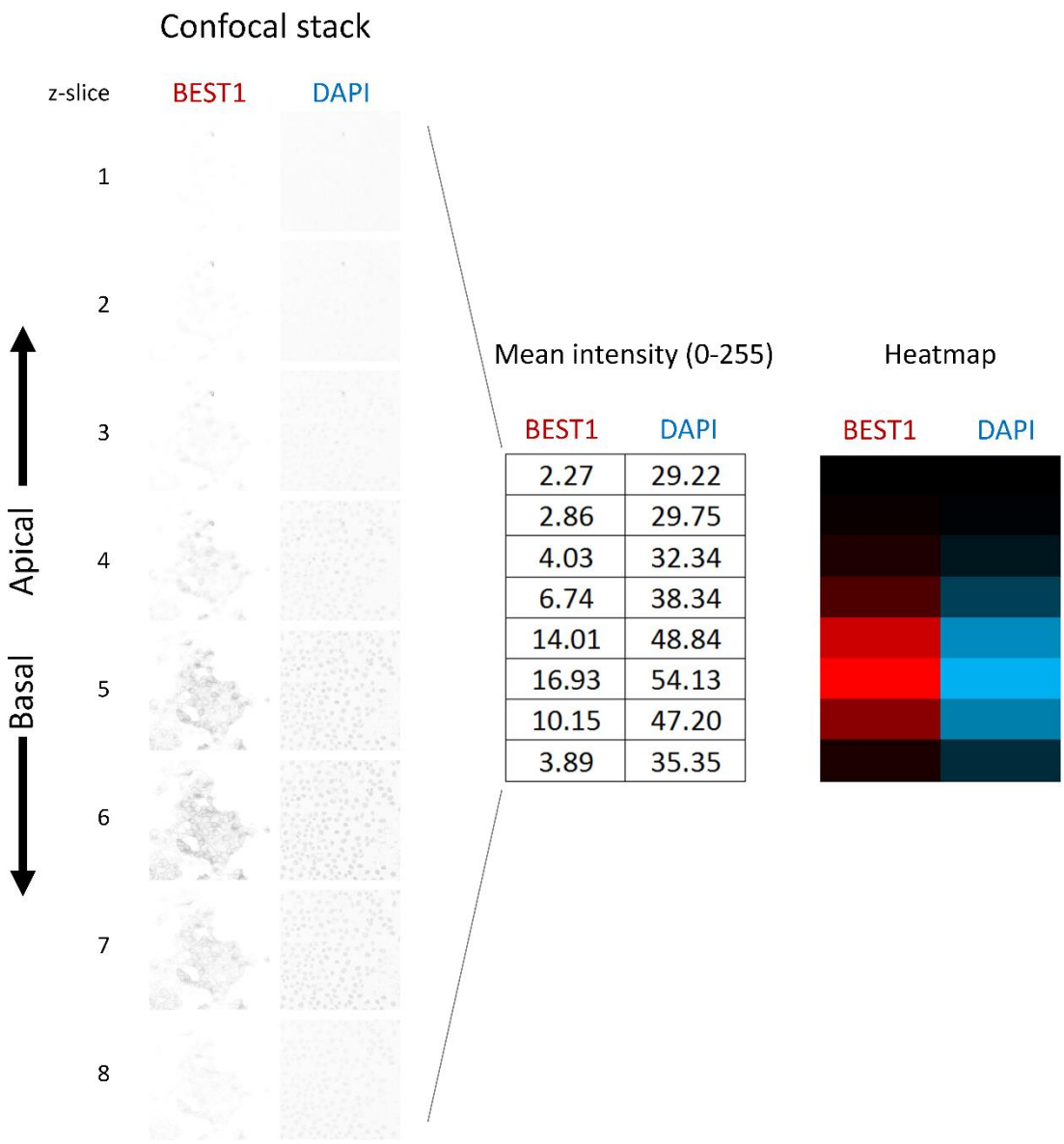

Figure 4.34 Producing 1-dimensional heatmaps of BEST1 and DAPI staining localisation using mean intensity readings from z-slice intervals using ImageJ. On the left are shown 20x confocal microscope z-stacks through MDCK cells transfected with the wild-type Best1 construct with the C-terminal FLAG tag. Red staining was produced from using the BEST1 primary antibody with an anti-mouse 555 secondary antibody. Blue DAPI stain was included in the mounting fluid. The DAPI and BEST1 columns show positive staining as black. The mean intensity of each image was measured using ImageJ, and are shown in the centre. Using these values Microsoft Excel was used to produce the heatmaps on the right, black showing the lowest intensity and red/blue colour showing the highest. The interval between z-stacks was 2.643µm.

In **Figure 4.35**, the same analysis has been performed in the same way for HEK293 cells transfected with the 704T>C (C-terminal FLAG) *BEST1* construct. Here the z-slice with the highest mean pixel intensity has been marked with an asterisk for each channel. It can be seen that the brightest bar for BEST1 is more apical than the brightest bar for DAPI when the mean intensity readings are taken for the whole field of view. This suggests that the 1-dimensional analysis is

able to resolve BEST1 localisation in the z-axis relative to the DAPI localisation. The 1-dimensional heat-maps for three individual cells also show apical BEST1 relative to DAPI, supporting the pattern seen for the entire field of view. Also shown in **Figure 4.35** is the distance between peak BEST1 and DAPI staining in the z-axis, calculated using the difference in slices and the slice interval (2.643µm). Of course these values are based on low-resolution z-axis sampling and so shall only be interpreted qualitatively as an indication of apical or basal localisation of BEST1 relative to DAPI. In this cast BEST1 staining occurs predominantly apically to DAPI staining by a few micrometres.

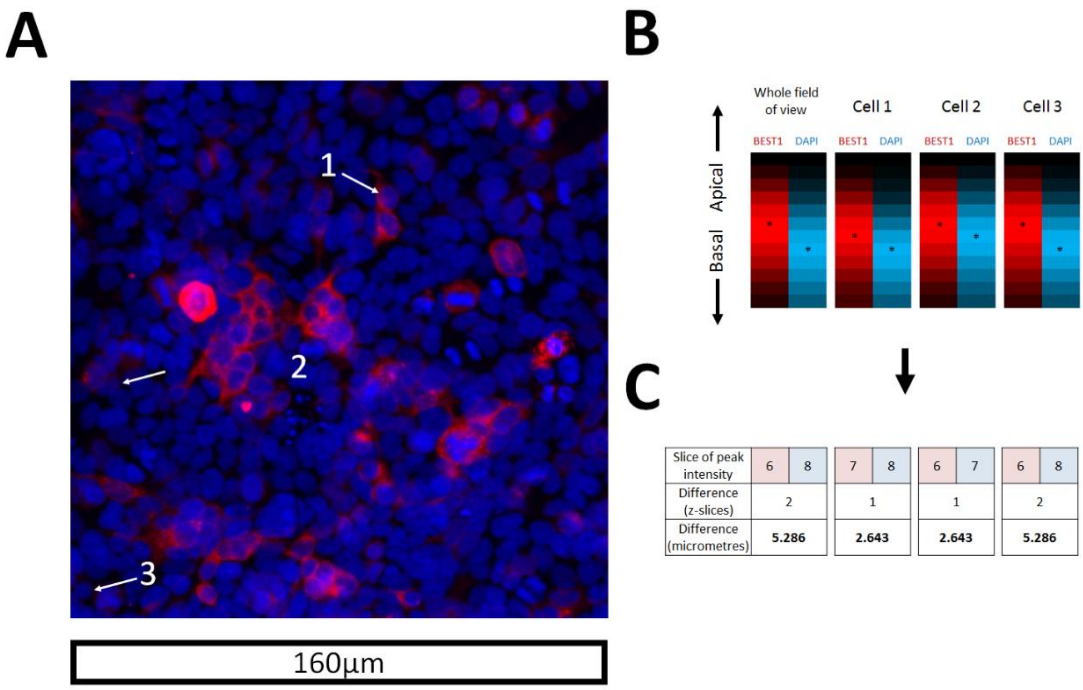

Figure 4.35 Comparing 1-dimensional heatmaps of BEST1 and DAPI staining localisation between individual cells in a field of view. A) Confocal composite image of a field of HEK293 cells that have been retrovirally transfected with the 704T>C Best1 construct with a C-terminal FLAG tag and then stained for BEST1 (red) and DAPI (blue). The 12 stacks have been projected down into a single image and then brightened to show cell locations. B) 1-dimensional distributions of BEST1 and DAPI are given for the whole field of view as shown in A, as well as for the three marked cells. For each channel the stack with the highest mean intensity is marked with an asterisk. C) Using the z-slice of peak mean pixel intensity for each channel and the known distance between z-slices (2.643µm), an estimate of the mean distance that BEST1 staining lies apically to the DAPI staining can be calculated for the whole field of view and each of the three individual cells.

4.4.9 How does BEST1 protein localisation vary between HEK293, MDCK and ARPE-19 cells?

Combining visual assessment of lateral staining and 1-dimensional analysis of apical-basal staining for all of the MDCK, HEK293, and ARPE19 lines produced the results shown in **Table 4.5**.

The 256G>A results are not included as no cell line was produced. The 598C>T line is not included as any truncated protein produced is undetectable using this BEST1 antibody.

Due to the very low levels of BEST1 staining relative to background staining in most lines it was impossible to produce an accurate estimate of the total number of cells in each image. Instead an estimate was produced for the percentage of pixels in each image that showed positive BEST1 staining. This was done in ImageJ by:

1) Performing an average intensity z-projection on each negative control image stack, (which should show only background staining).
2) Measuring the average pixel intensity of each resulting 8-bit image, giving an average pixel intensity of the background signal for the entire stack. These lay between 1.019 and 1.934 and can be found in the appendix.
3) A value of 5x the mean background signal was chosen as a thresholding value for defining a positive pixel (5*1.309= 6.545). Only an integer value can be used for thresholding so 7 was used as the thresholding value.
4) Each experimental image stack was then subjected to an average intensity z-projection followed by a thresholding at intensity value 7. The percentage of pixels that exceeded the threshold is shown on the right in **Table 4.5**, and can also be found in the appendix.
5) The percentage of pixels that exceeded the threshold in the negative controls ranged from 0.004% to 1.909%. Therefore any image stack with a positive pixels percentage less than 1.909% was defined as showing no signal and excluded from the analysis. This applied to three samples: the ARPE19 715 G>A with C-terminal FLAG sample from transfection A, the ARPE19 248G>A with C-terminal FLAG sample from transfection B, and the ARPE19 wildtype N-terminal FLAG sample from transfection C. The rest of the samples are included in **Table 4.5**.

Cell type	Best1 mutation	Terminal flag tag	Disease	BEST1 staining	Lateral staining?	Positive pixels (%)
MDCK	Wild-type	C	-	Neither apical or basal	2	35.1
	704T>C	C	ADVIRC	Apical	0	2.8
HEK293	Wild-type	C	-	Apical	2	91.8
	704T>C	C	ADVIRC	Apical	2	40.0
ARPE-19	Wild-type	C	-	Apical	0	11.9
	704 T>C	C	ADVIRC	Neither apical or basal	0	4.8
				Neither apical or basal	0	4.2
	707 A>G	C	ADVIRC	Apical	0	1.9
				Neither apical or basal	0	32.9
	715 G>A	C	ADVIRC	Neither apical or basal	0	17.6
	974 T>C	C	ARB	Apical	0	7.3
				Apical	0	4.2
	699 A>T	C	-	Apical	1	17.4
				Neither apical or basal	0	17.3
	Wild-type	N	-	Apical	0	2.5

Table 4.5 BEST1 protein localisation in retrovirally transfected MDCK, HEK293, and ARPE-19 cell lines, based on BEST1 and DAPI staining of fixed cells imaged at 20x with a confocal microscope. The table shows (from left to right): the transfected cell line; the Best1 mutation contained in the transfected plasmid; whether the construct had a C or N-terminal FLAG tag; the disease associated with the mutation; whether the 1-dimensional mean pixel intensity analysis indicated BEST1 staining apically or basally to the DAPI staining; whether the BEST1 staining within the cells appears laterally located; the percentage of pixels with positive BEST1 staining, calculated by applying a thresholding value of 7 to the 8-bit average-intensity z-stack projection. Lateral staining was scored from 0-2, with 0 meaning a lack of lateralised BEST1 signal in the cells, 2 meaning clear lateralisation of staining, and 1 meaning an unclear result.

Both the wild-type and 704T>C HEK293 lines appear to show lateral localisation. The wild-type but not the 704T>C MDCK line appears to shows lateral localisation. None of the ARPE-19 lines other than the silent mutation 699AT (C-terminal FLAG) shows any suggestion of lateral localisation. In addition z-localisation of the most intense BEST1 staining is either apical to or level with the z-localisation of the most intense DAPI staining. Undifferentiated ARPE-19 then appear to show none of the basolateral BEST1 localisation associated with mature RPE cells.

4.4.10 How does prolonged incubation of ARPE-19 in XVIVO medium affect BEST1 protein localisation?

The staining and confocal imaging discussed above have demonstrated that at least some of the retrovirally transfected ARPE-19 lines contained cells that expressed detectable BEST1 protein, and that the localisation of this BEST1 could be visually assessed for lateral location and assessed using a 1-dimensional analysis for apical-basal localisation. The question remained as to whether incubation in X-VIVO medium, known to induce pigmentation and 'cobblestone' cell appearance in ARPE-19 cells as well as changes in gene expression that appear to somewhat mimic what is seen in foetal RPE, would affect the patterns of BEST1 localisation seen.

Therefore the ARPE-19 lines above were used to investigate the effects of culturing the cells for extended periods of time in X-VIVO medium. Cells from each line were plated in 8-well chamber slides coated with Matrigel, grown to confluency in standard 10% FBS DMEM medium then

either maintained in DMEM medium or switched to X-VIVO medium. These two sets of cells were incubated in identical conditions for 85 days. On day 84 phase-contrast images were taken of the cells, and are shown in **Figure 4.36**, **Figure 4.37**, **Figure 4.38**, and **Figure 4.39**. It can be seen that the cells in XVIVO are more highly pigmented that those in DMEM, although there is significant variation between lines and between cells. On day 85 the cells were fixed and stained for BEST1 protein and DAPI.

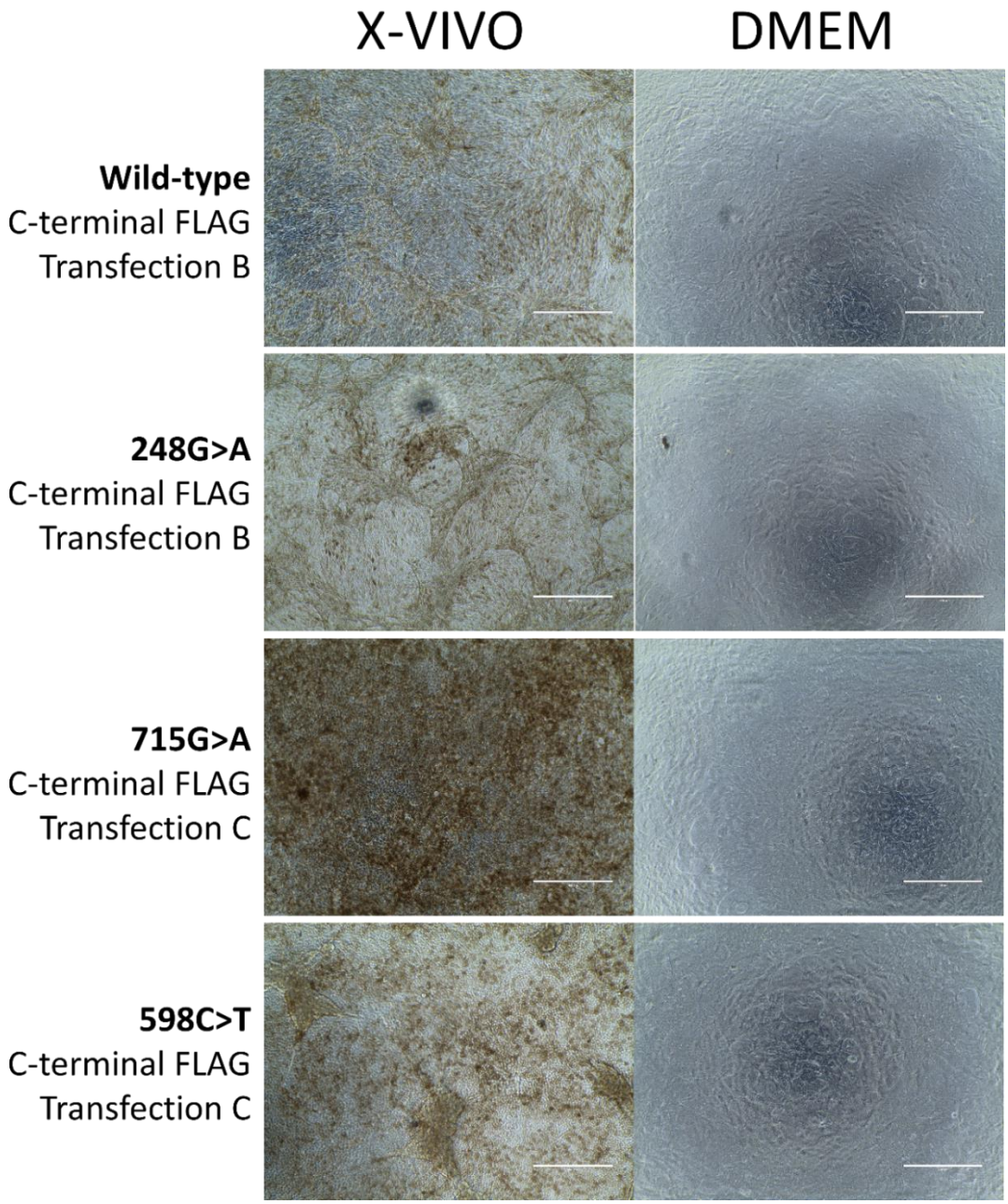

Figure 4.36 Phase contrast images taken at 10x of ARPE19 cell lines, grown in X-VIVO10 or DMEM medium for 85 days. Along the top of the figure is indicated the medium used to feed the cells of each column. Along the left of the figure is indicated the plasmid with which the cells were transfected, the position of the terminal FLAG, and the transfection lot in which the cell line was created. Scale bars indicate 400µm.

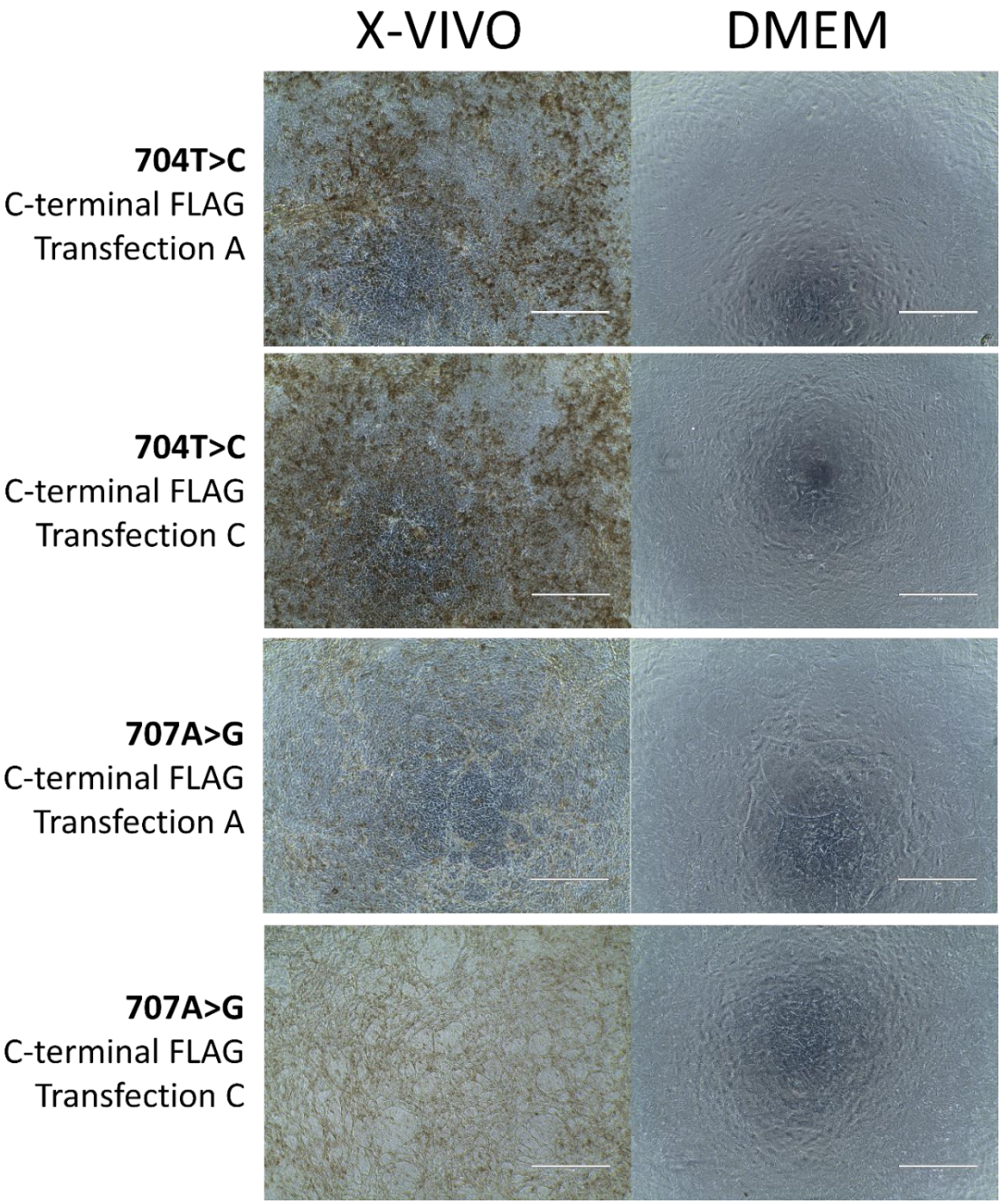

Figure 4.37 Phase contrast images taken at 10x of ARPE19 cell lines, grown in X-VIVO10 or DMEM medium for 85 days. Along the top of the figure is indicated the medium used to feed the cells of each column. Along the left of the figure is indicated the plasmid with which the cells were transfected, the position of the terminal FLAG, and the transfection lot in which the cell line was created. Scale bars indicate 400µm.

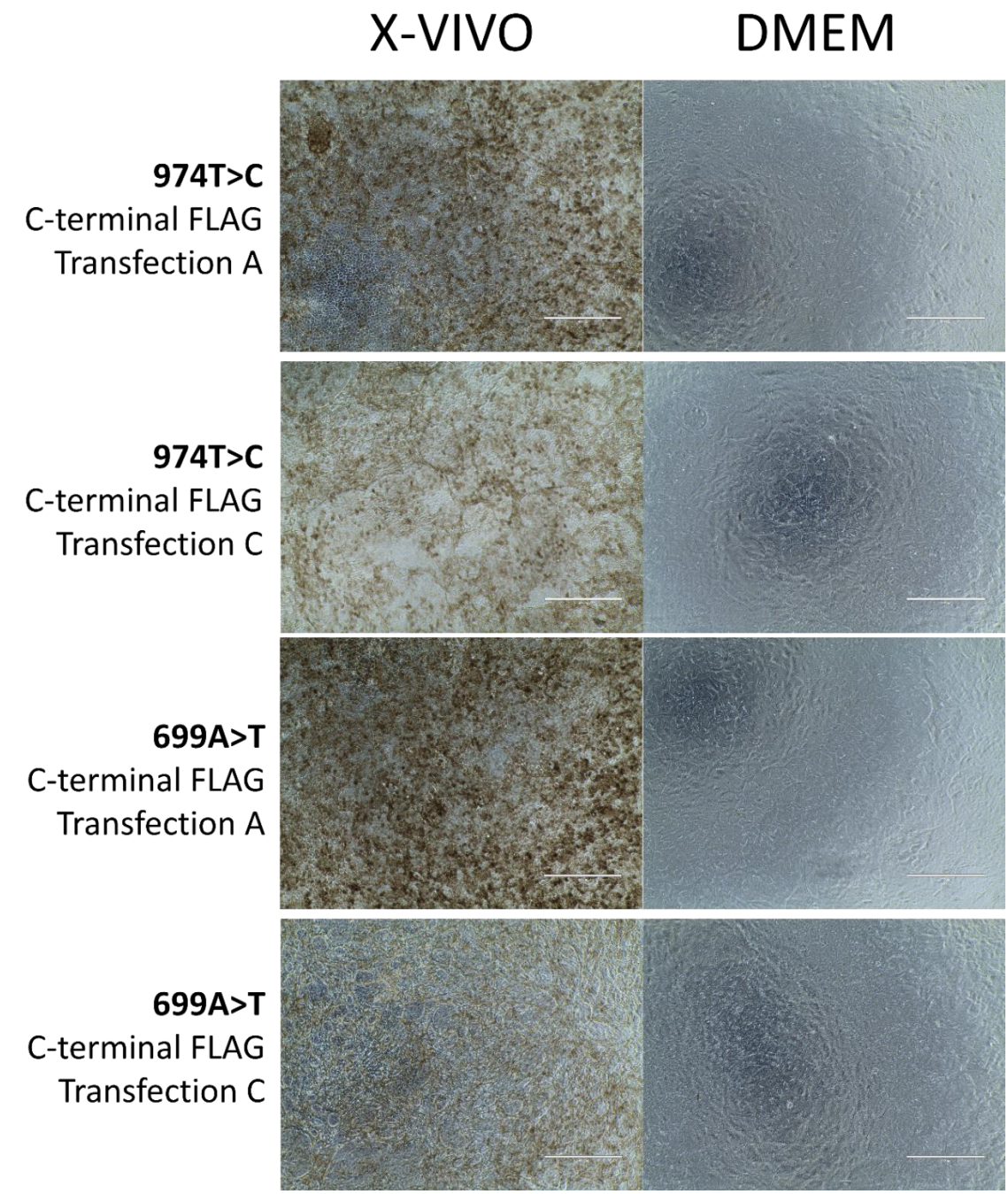

Figure 4.38 Phase contrast images taken at 10x of ARPE19 cell lines, grown in X-VIVO10 or DMEM medium for 85 days. Along the top of the figure is indicated the medium used to feed the cells of each column. Along the left of the figure is indicated the plasmid with which the cells were transfected, the position of the terminal FLAG, and the transfection lot in which the cell line was created. Scale bars indicate 400µm.

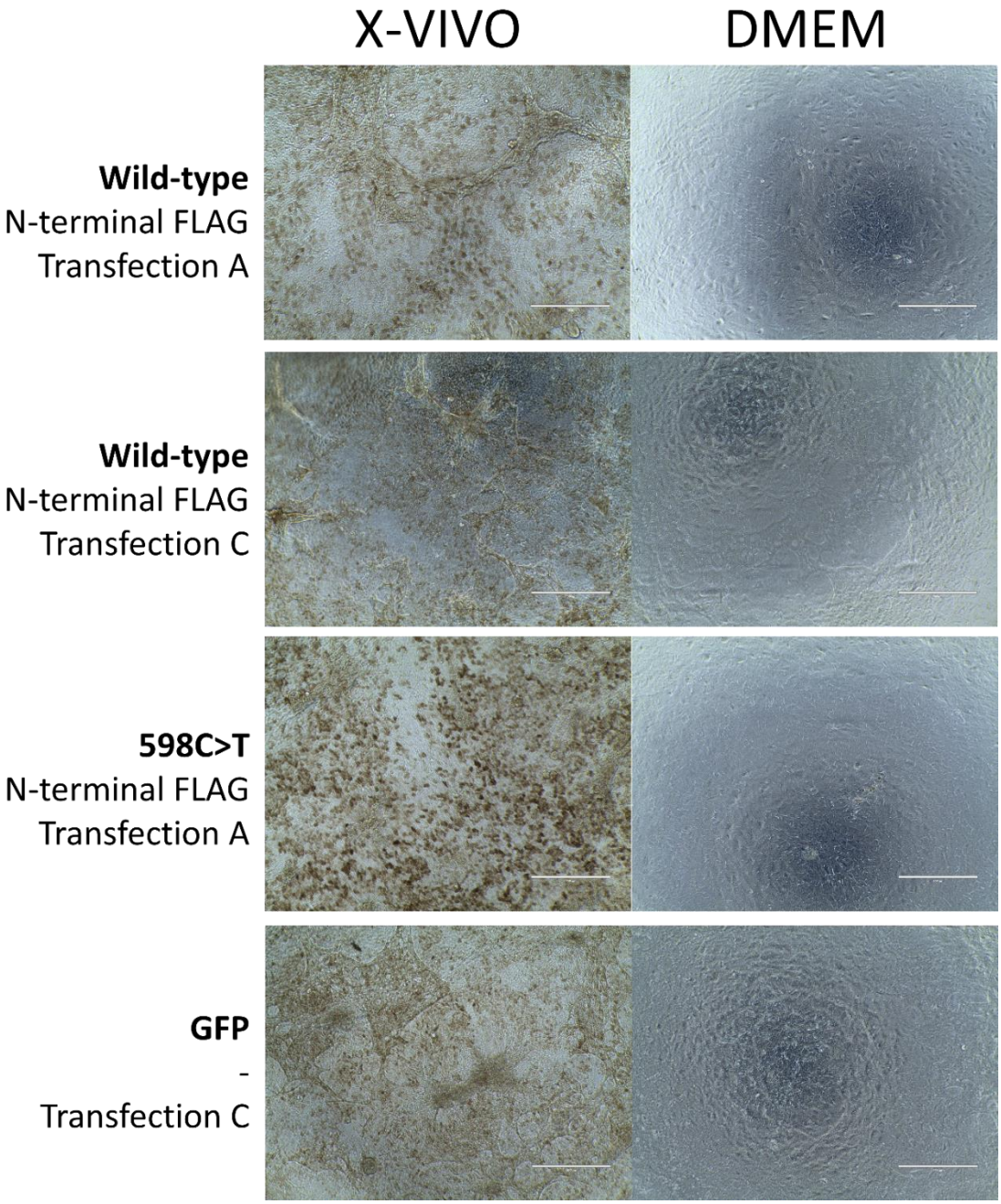

Figure 4.39 Phase contrast images taken at 10x of ARPE19 cell lines, grown in X-VIVO10 or DMEM medium for 85 days. Along the top of the figure is indicated the medium used to feed the cells of each column. Along the left of the figure is indicated the plasmid with which the cells were transfected, the position of the terminal FLAG, and the transfection lot in which the cell line was created. Scale bars indicate 400µm.

Staining was also performed for EZRIN and MERTK, which should both be expressed in mature RPE and both of which should localise to the apical membrane. Neither one produced visible staining, which could indicate a lack of expression of these proteins or a failure of the immunocytochemistry protocol. Without a positive control it was impossible to tell.

The BEST1 and DAPI stained slides were then imaged using a confocal microscope to produce stacked images through the cells. All of the stacks were taken with 2µm intervals between z-slices and using identical laser illumination and digital gain settings.

Below the results of that imaging will be presented in various tables in an attempt to at least partially quantify the differences seen between lines. Discussion of the differences between lines will be had in the next section as to the effects of the *BEST1* mutations and the effects of incubation in the two different culture media.

4.4.11 Can BEST1 protein staining be seen after more than 85 days in culture after transfection?

The retrovirally transfected ARPE-19 cell lines not only spent 85 days in either DMEM or XVIVO medium as part of this experiment, but also between several weeks and several months (depending on whether they were part of transfection A, B or C) in culture and G418 antibiotic selection before that. Therefore it was considered possible, particularly as there appeared to be at least some evidence that retroviral BEST1 overexpression produced a competitive disadvantage in cells, that by the end of the 85-day incubation that no cells at all would still be producing the retroviral BEST1 protein products.

However, as can be seen in **Figure 4.40**, **Figure 4.41**, **Figure 4.42**, and **Figure 4.43**, clear cellular staining can be seen in some of the lines examined in both DMEM and XVIVO medium. It must be pointed out, however, that not only is the number of positively stained cells often low relative to the total number of cells in the field of view (as determined by DAPI nuclear staining), but that often the entire 0.8cm^2 culture area of cells had to be searched to find that number of positive cells in one place. A list of all of the imaged lines and the approximate number of BEST1-positive cells in the field of view can be found in the Appendix. As can be seen several stacks contain only a single positive cell. This fact should be borne in mind when considering following analyses.

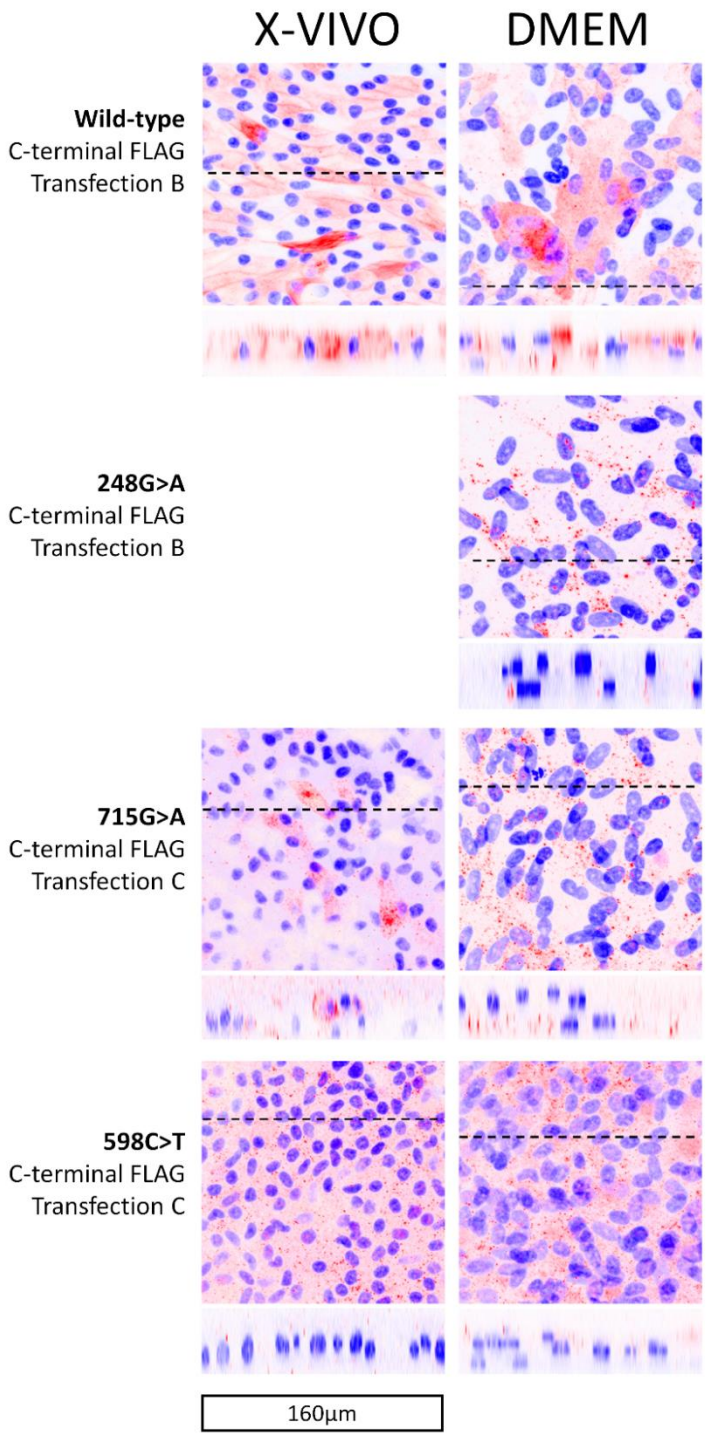

Figure 4.40 BEST1 and DAPI staining in retrovirally transfected ARPE19 cell lines, grown in X-VIVO10 or DMEM medium for 85 days. Shown are average intensity z-projections through 40x image stacks with brightness and contrast altered to show the cellular location of BEST1. Below each image is shown a representative X-Z scan through the same image stacks with brightness and contrast altered to show the cellular location of BEST1. The location of the X-Z scan is indicated by the black dotted line. BEST1 staining is shown in red and DAPI in blue. Along the top of the figure is indicated the medium used to feed the cells of each column. Along the left of the figure is indicated the plasmid with which the cells were transfected, the position of the terminal FLAG, and the transfection lot in which the cell line was created. Each image is 160µm by 160µm, as indicated by the sale bar.

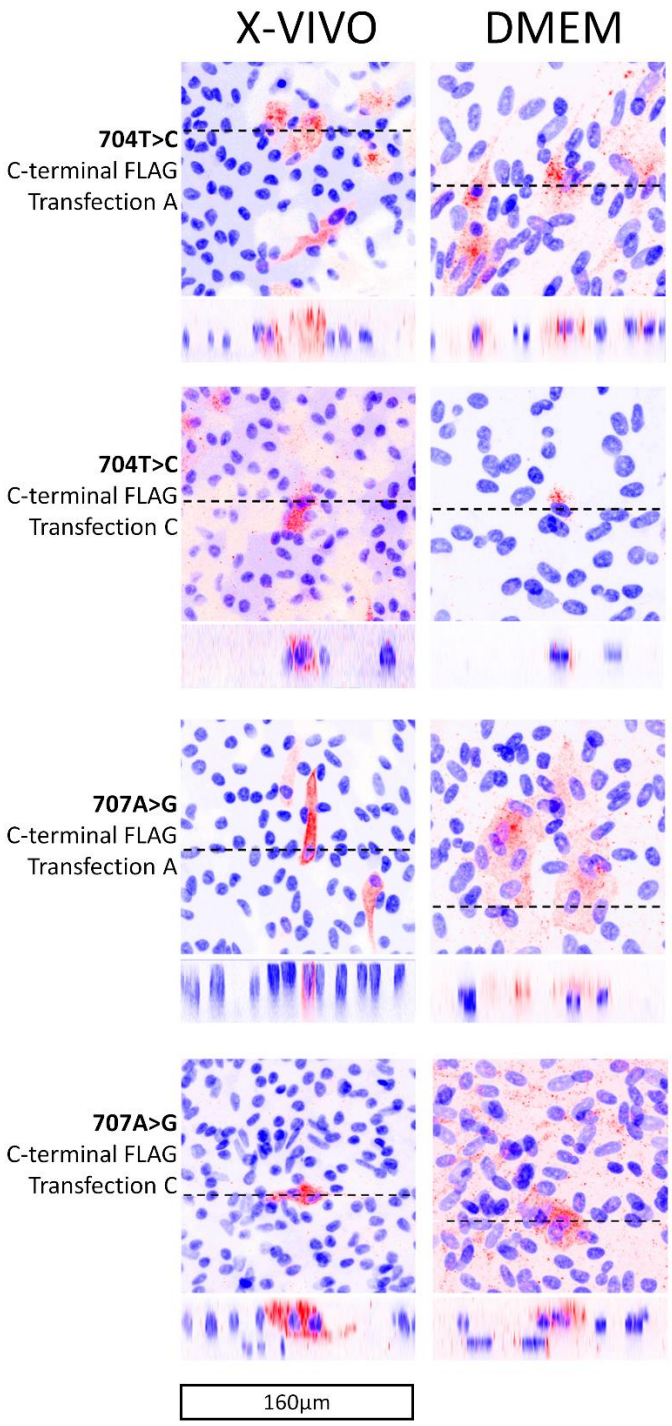

Figure 4.41 BEST1 and DAPI staining in retrovirally transfected ARPE19 cell lines, grown in X-VIVO10 or DMEM medium for 85 days. Shown are average intensity z-projections through 40x image stacks with brightness and contrast altered to show the cellular location of BEST1. Below each image is shown a representative X-Z scan through the same image stacks with brightness and contrast altered to show the cellular location of BEST1. The location of the X-Z scan is indicated by the black dotted line. BEST1 staining is shown in red and DAPI in blue. Along the top of the figure is indicated the medium used to feed the cells of each column. Along the left of the figure is indicated the plasmid with which the cells were transfected, the position of the terminal FLAG, and the transfection lot in which the cell line was created. Each image is 160µm by 160µm, as indicated by the sale bar.

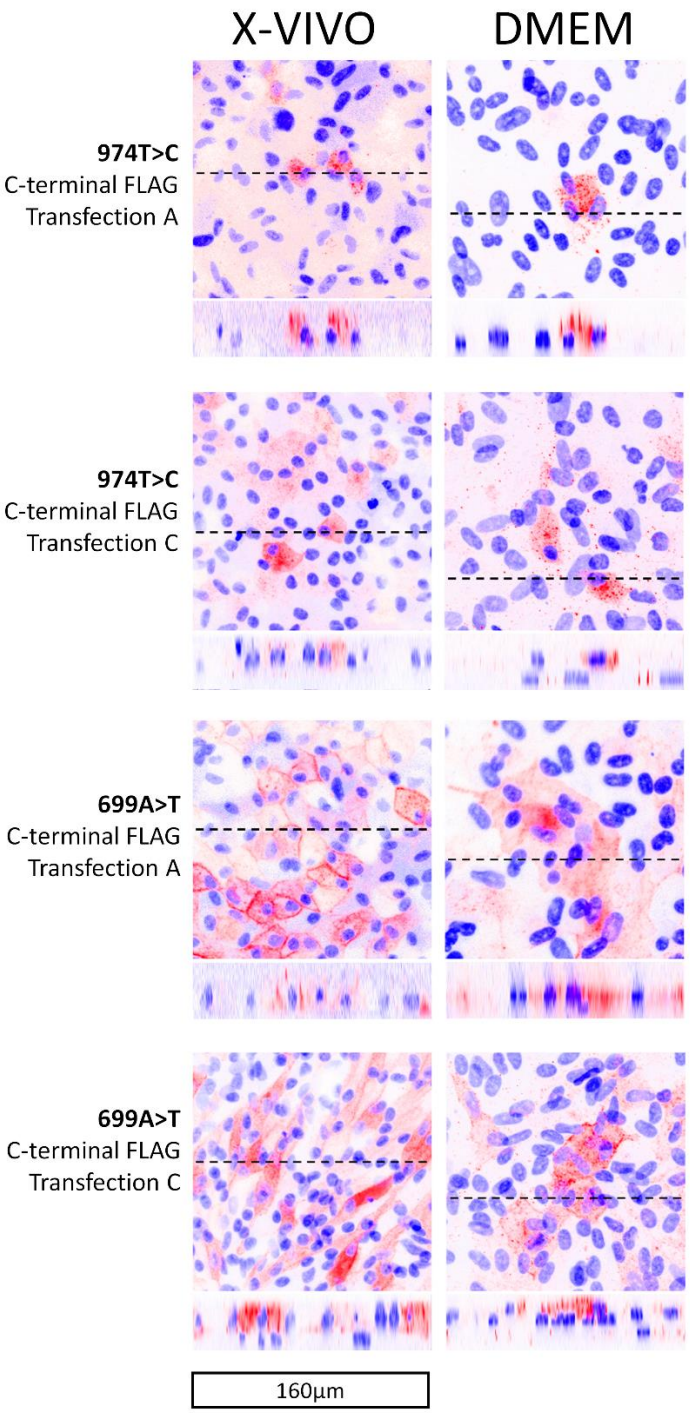

Figure 4.42 BEST1 and DAPI staining in retrovirally transfected ARPE19 cell lines, grown in X-VIVO10 or DMEM medium for 85 days. Shown are average intensity z-projections through 40x image stacks with brightness and contrast altered to show the cellular location of BEST1. Below each image is shown a representative X-Z scan through the same image stacks with brightness and contrast altered to show the cellular location of BEST1. The location of the X-Z scan is indicated by the black dotted line. BEST1 staining is shown in red and DAPI in blue. Along the top of the figure is indicated the medium used to feed the cells of each column. Along the left of the figure is indicated the plasmid with which the cells were transfected, the position of the terminal FLAG, and the transfection lot in which the cell line was created. Each image is 160µm by 160µm, as indicated by the sale bar.

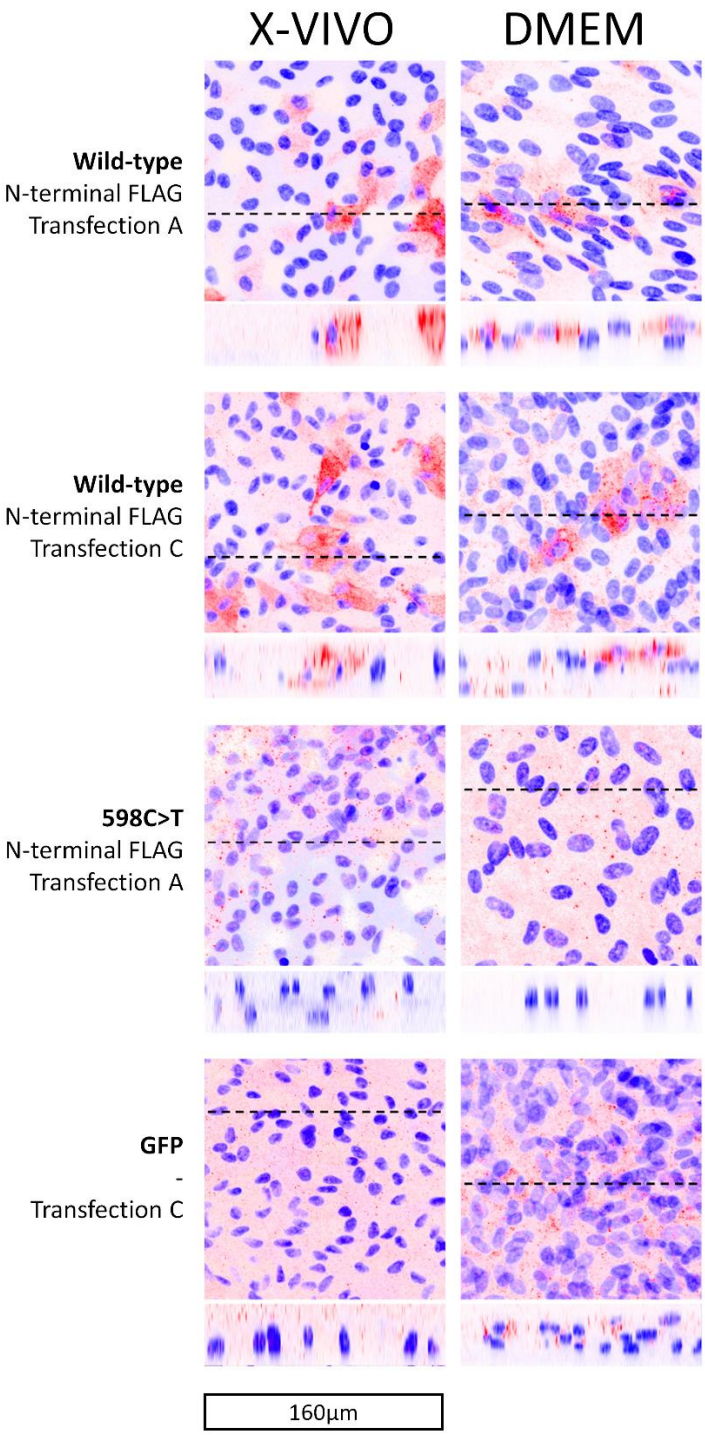

Figure 4.43 BEST1 and DAPI staining in retrovirally transfected ARPE19 cell lines, grown in X-VIVO10 or DMEM medium for 85 days. Shown are average intensity z-projections through 40x image stacks with brightness and contrast altered to show the cellular location of BEST1. Below each image is shown a representative X-Z scan through the same image stacks with brightness and contrast altered to show the cellular location of BEST1. The location of the X-Z scan is indicated by the black dotted line. BEST1 staining is shown in red and DAPI in blue. Along the top of the figure is indicated the medium used to feed the cells of each column. Along the left of the figure is indicated the plasmid with which the cells were transfected, the position of the terminal FLAG, and the transfection lot in which the cell line was created. Each image is 160µm by 160µm, as indicated by the sale bar.

Looking at **Figure 4.43**, the GFP control showed no clear cellular staining of BEST1, as would be expected of a negative control. In addition the 598C>T mutant lines showed no clear cellular staining of BEST1 in either case of a C or N-terminal FLAG tag. This was also expected as the 598C>T mutation produces a premature stop codon, and so the C-terminal end of the protein to which the BEST1 antibody binds would not be expected to be present even if a truncated protein product was produced. The 248G>A line in XVIVO was lost due to medium leaking out from the well and the DMEM cells do not show clear cellular location. The 256G>A line is not shown as a viable cell line was never produced for this plasmid.

Once again, due to the very low levels of BEST1 staining relative to background staining in most lines it was impossible to produce an accurate estimate of the total number of cells in each image. Instead an estimate was produced for the percentage of pixels in each image that showed positive BEST1 staining. This was done in ImageJ by:

1) Performing an average intensity z-projection on each negative control image stack, (which should show only background staining).
2) Measuring the average pixel intensity of each resulting 8-bit image, giving an average pixel intensity of the background signal for the entire stack. These lay between 0.798 and 3.646 and can be found in the appendix.
3) A value of 5x the mean background signal was chosen as a thresholding value for defining a positive pixel (5*2.238= 11.19). Only an integer value can be used for thresholding so 12 was used as the thresholding value.
4) Each experimental image stack was then subjected to an average intensity z-projection followed by a thresholding at intensity value 12. The percentage of pixels that exceeded the threshold is shown on the right in **Table 4.6**, and can also be found in the appendix.
5) The percentage of pixels that exceeded the threshold in the negative controls ranged from 0.010% to 0.481%. Therefore any image stack with a positive pixels percentage less than 0.481% was defined as showing no signal and excluded from the analysis. This applied to seven samples: both 704T>C C-terminal FLAG X-VIVO samples, the 974T>C C-terminal FLAG X-VIVO sample, both 707A>G C-terminal FLAG DMEM samples, the second 704T>C C-terminal FLAG DMEM sample, and the 715G>A C-terminal FLAG DMEM sample. The rest of the samples are included in **Table 4.6**.

4.4.12 How does prolonged incubation in XVIVO medium affect BEST1 protein localisation?

4.4.12.1 -Laterally?

The confocal stacks that had not been excluded using the above analysis were visually assessed for lateral cellular staining of BEST1. Although somewhat subjective, staining could be considered lateral if there appeared to be a clear lateral band of higher intensity staining that clearly marked the boundary of one cell from its neighbours. The images were scored as '2' – clear lateral staining, '1' – unclear or mixed, or '0' – no lateralisation of staining. The results of this analysis are shown in **Table 4.6**. The colour-coding in the table is to aid visual

comprehension. The results shown in this table will be discussed in more detail in the next section, but it is worth noting here that incubation in X-VIVO medium does appear to lead to increased lateral staining in some cases, that lateral staining is never found a DMEM condition and not the corresponding XVIVO condition. It is also worth noting that wild-type BEST1 is not always laterally located even in X-VIVO (although in this case the estimated number of positive pixels is only 0.74%), and that cell lines that have been transfected with identical plasmids do not always show the same degree of lateral staining. Finally it is of note that even lines with visually obvious lateral staining when viewed *en face* as an Z-projection show cytoplasmic BEST1 staining when viewed as an X-Z scan. The only obvious exception to this is the 699A>T (C-terminal FLAG, Transfection A) sample shown in **Figure 4.42**, where clear lateral staining can be seen without cytoplasmic staining. It is also of note that in every case except the first wild-type N-terminal FLAG line the X-VIVO condition showed a higher estimated positive pixel percentage than the corresponding DMEM condition.

				BEST1 staining (lateral localisation)			
Cell type	**Best1 mutation**	**Terminal flag tag**	**Disease**	**X-VIVO**	**Estimated positive pixels (%)**	**DMEM**	**Estimated positive pixels (%)**
ARPE19	Wild-type	C	-	**2**	19.03	**1**	15.43
	704 T>C	C	ADVIRC			**0**	1.29
	707 A>G	C	ADVIRC	**2**	2.62		
				0	1.79		
	715 G>A	C	ADVIRC	**1**	0.82		
	974 T>C	C	ARB			**0**	0.92
				1	27.74	**0**	3.43
	699 A>T	C	-	**2**	15.28	**0**	1.78
				2	58.58	**1**	5.46
	Wild-type	N	-	**0**	0.74	**0**	4.24
				2	10.81	**0**	2.21

Table 4.6 BEST1 lateral localisation in retrovirally transfected AREP19 cell lines, incubated for 85 days in X-VIVO 10 or DMEM medium. The table shows (from left to right) the transfected cell line; the Best1 mutation contained in the transfected plasmid; whether the construct had a C or N-terminal FLAG tag; the disease associated with the mutation; whether the line had lateral staining in cells or not after culture in X-VIVO medium; the estimated positive pixels for these lines; whether the line had lateral staining in cells or not after culture in DMEM medium; and the estimated positive pixels for these lines. Analysis was based on BEST1 and DAPI staining of fixed cells imaged at 40x with a confocal microscope. Lateral staining was scored from 0-2, with 0 meaning a lack of lateralised BEST1 signal in the cells, 2 meaning clear lateralisation of staining, and 1 meaning an unclear result.

4.4.12.2 -Apical/Basal?

One advantage to using identical imaging settings for all cell lines is that the intensity of staining can be compared. Many of the lines show BEST1 staining that is less intense than the background staining in the GFP control line, including in lines that show clear cellular staining. For example both 704T>C and both 707A>G lines show peak BEST1 staining intensity that is lower than the

GFP control, despite all four lines showing clearly visible cellular BEST1 staining. A table of this data can be found in the Appendix. There could be several causes of this: that the level of BEST1 production is very low, that the binding of the primary or secondary antibody is inefficient, that there is some off-target binding of either the primary or secondary antibody, that either the unbound primary or unbound secondary antibody was not efficiently removed during the washing steps, that the cells produced some autofluorescence, or some combination of the above. It is also possible that cells are producing a small amount of endogenous BEST1 protein, though this would be expected to localise to the membrane. In any case it was considered likely that this background or off-target signal in the red 555 channel could affect the analysis of apical-basal BEST1 localisation, particularly if it was not uniformly distributed in the z-axis.

With this in mind the 1-dimensional analysis was performed as described for the previous dataset and the results are shown in **Table 4.7**. The colour-coding is to aid visual comprehension. Here it can be seen that there are some large differences in z-axis location of peak BEST1 signal relative to DAPI signal. For example the second wild-type N-terminal FLAG line shows a BEST1 signal that is approximately 4µm basal to the DAPI in X-VIVO medium, and 4µm apical to it in DMEM medium, a difference of 8µm.

				Apical BEST1 staining (micrometres)			
Cell type	**Best1 mutation**	**Terminal flag tag**	**Disease**	**X-VIVO**	**Estimated positive pixels (%)**	**DMEM**	**Estimated positive pixels (%)**
ARPE19	Wild-type	C	-	**4**	19.03	**4**	15.43
	248 G>A	C	ADVIRC	**Well was lost**		**-6**	0.55
	704 T>C	C	ADVIRC			**0**	1.29
	707 A>G	C	ADVIRC	**-2**	2.62		
				2	1.79		
	715 G>A	C	ADVIRC	**6**	0.82		
	974 T>C	C	ARB			**2**	0.92
				4	27.74	**0**	3.43
	699 A>T	C	-	**-4**	15.28	**0**	1.78
				2	58.58	**2**	5.46
	Wild-type	N	-	**0**	0.74	**2**	4.24
				-4	10.81	**4**	2.21

Table 4.7 BEST1 1-Dimensional apical/basal localisation in retrovirally transfected AREP19 cell lines, based on BEST1 and DAPI staining of fixed cells imaged at 40x with a confocal microscope. The table shows (from left to right) the transfected cell line; the Best1 mutation contained in the transfected plasmid; whether the construct had a C or N-terminal FLAG tag; the disease associated with the mutation; the distance in the z-axis between the peak of BEST1 staining intensity and DAPI staining for the cell lines in X-VIVO medium; the estimated positive pixel percentage; the distance in the z-axis between the peak of BEST1 staining intensity and DAPI staining for the cell lines in DMEM medium; the estimated positive pixel percentage. A positive value for Apical BEST1 staining indicates BEST1 staining apical to DAPI, a negative value indicates basal. Values are colour-coded such that green indicates apical BEST1 and red indicates apical DAPI. Yellow indicates no difference.

4.4.13 Does DMEM vs XVIVO medium affect the amount of layering seen in the cell lines?

Another factor that was observed and that could have a large effect on the analysis of apical-basal localisation was that a significant amount of multilayering was seen in the cell lines during imaging. DAPI-stained nuclei were seen to be laying directly on top of each other, sometimes in well-defined sheets of cells. Four examples of this multilayering are shown as orthogonal visual sections in **Figure 4.44**. A table of the degree of multilayering in each line can also be found in the Appendix. In most cases there were two layers over at least part of the field of view. There were also areas with three layers. For the most part the images consisted of one complete 'main' layer with partial layers above and/or below it. Because the imaging location within the slide was selected based on the presence of clusters of visibly BEST1-positive cells, the extent of layering within each image cannot reasonably be considered strictly representative for that cell line. However, there is a suggestion that lines kept in DMEM show a greater degree of multilayering than those kept in XVIVO.

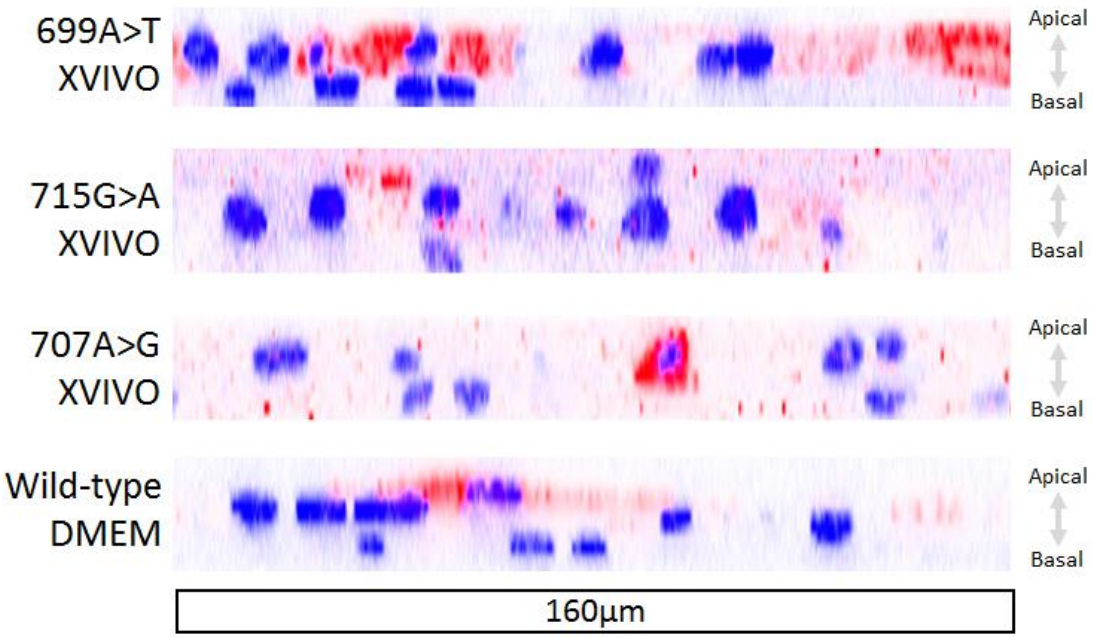

Figure 4.44 Examples of multilayering seen in ARPE-19 cells after 85-day incubation in X-VIV 10 medium or DMEM medium. Four examples are shown, each an orthogonal slice through a confocal stack. The apical-basal axis is shown on the left, as are the mutations of the transfected Best1 plasmid and the medium the cells were incubated in. DAPI staining is shown in BLUE, BEST1 staining in RED.

In any case the fact of the presence of secondary or tertiary layers of cells within most of the confocal stacks suggests that the 1-dimensional analysis is likely significantly affected by the DAPI signal from these additional layers. This will particularly be the case if the BEST1-positive cells are found in only one of the layers present, which will necessarily be the case for those images with only a single BEST1-positive cell.

4.4.14 Do BEST1-positive cells localise to a particular layer?

It was seen that the BEST1-positive cells were not consistently found to localise to the more apical or basal layers. In some cases there appears to be BEST1-positive cells in multiple layers, although with so few cells in most images it is difficult to draw conclusions from this. It is also possible that BEST1-positive cells might localise themselves differently depending on the BEST1 mutation present. However, the amount of data present here is vastly insufficient to draw any conclusions about whether presence of retrovirally transfected BEST1 protein has any effect on the degree of layering of cells or whether BEST1-positive cells preferentially localise to particular cell layers in a mutation-dependent manner. A table of the locations of the BEST1-positive cells within the layers can be found in the Appendix.

It is also possible that cells in different layers could show different cell morphology and BEST1 localisation caused by differential contact to other cells apically or basally as well as the plastic culture material or the Matrigel coating. These effects could also be dependent on the *BEST1* mutation considered. In some cases the basal layer of cells appeared to have larger nuclei than apical cells.

Taken together the presence of background or off-target BEST1 staining and the heterogeneous distribution of BEST1 positive cells in an inconsistent number of cell layers suggests that the 1-dimensional apical-basal analysis cannot be considered reliable.

4.4.15 Summary of results

In this Results section data has been presented demonstrating that retroviral transfection protocols can be used to induce wild-type and mutant BEST1 protein production in ARPE-19 cells, although not with the same reliability and efficiency as in MDCK and HEK293 cells. It has also been shown that transfection of some constructs leads to temporary production of vesicle-like structures in some lines and not others, although the nature of these structures remains unclear. It has been demonstrated that the BEST1 protein produced shows different patterns of lateral localisation between mutant lines, and that incubation in XVIVO medium affects this localisation, but that the 1-dimensional analysis of apical-basal localisation cannot be considered reliable in the case of ARPE-19 cells due to their tendency to form multiple cell layers in long-term culture.

In the Discussion section these results will be discussed further and put into the context of the *in vitro* study of human Bestrophinopathies.

4.5 Discussion

4.5.1 Introduction

In this section the data presented in the Results section will be discussed and placed into context of the study of Bestrophinopathies and other genetic retinal disease.

Based on the published material discussed in the introduction three questions were given as aims for the experimental section of this chapter.

Does wild-type BEST1 localise to the basolateral membrane in ARPE-19 cells as it does in iPS-RPE? Does the V235A mutation show mis-localisation in ARPE-19 cells relative to the wild-type, as is seen in iPS-RPE cells?

Does localisation of wild-type or V235A mutant BEST1 depend on the model cell type in which they are expressed?

Do any of the other four ADVIRC mutations show mis-localisation in ARPE19 cells relative to the wild-type?

All three of these questions were addressed by the experimental work presented in the previous section. The conclusions that can be drawn from this work are discussed below.

4.5.2 The *BEST1* V235A mutation appears to affect BEST1 localisation in a cell line-dependent manner.

In the introduction to this chapter the role of *BEST1* in the Bestrophinopathies was discussed. It is considered likely that the clustering of retinal dystrophic symptoms into discrete disease phenotypes (BVMD, ARB, and ADVIRC, and also possibly AVMD and some cases of RP) represents specific disruptions of BEST1 function. Published work investigating the nature of ADVIRC *BEST1* mutations was discussed. Work by Yardley *et al.* was presented suggesting that the mutations V86M, Y236C, V239M all lead to alterations in splicing(Yardley et al. 2004). This was supported by work by Burgess *et al.* which replicated the exon-skipping effect of Y236C and reported alterations in splicing for V235A(Burgess et al. 2009). Chen *et al.* found no evidence of altered splicing for the ADVIRC mutation G83D, despite computational predictions, suggesting that altered splicing is not a universal feature of ADVIRC mutations(Chen et al. 2016). All three of these papers used human kidney cells for their splice assays.

Carter *et al.* further investigated the V235A mutation using iPS-RPE cells derived from two sibling patients. No evidence of mis-splicing was found, but the BEST1 protein from both patients was found to be mis-localised(Carter et al. 2016). This contradicted both the results from Burgess *et al.* and results from Johnson *et al.*, which found V235A to be appropriately localised in MDCK cells(Johnson et al. 2014).

One possible explanation is that the cellular environment of RPE cells is sufficiently different to the kidney epithelial lines HEK293 and MDCK that both splicing and localisation of BEST1 are different. This is not a trivial question, as the key assumption of any model is that it accurately represents the key features of the real-world system. Therefore the primary aim of the research presented in this chapter was to investigate the localisation of V235A (704T>C) BEST1 compared to the wild-type BEST1 in HEK293 cells, MDCK cells and an RPE-derived line ARPE19. To investigate this, retroviral expression vectors were created for wild-type and V235A (704T>C) *BEST1* (along with several other mutations that will be discussed shortly). These vectors were transfected into HEK293, MDCK and ARPE-19 cells. These lines were stained using a BEST1 antibody and imaged to assay for BEST1 localisation.

The results of this were that in no case was there visibly clear apical or basal staining of BEST1. A 1-dimensional analysis comparing DAPI and BEST1 staining in the z-axis for each stack suggested that if there was a difference in apical-basal localisation then this was generally on the side of apical BEST1 localisation. However, this was a very coarse assay, partially because the HEK293 and MDCK cells in particular formed extremely flat monolayers. In any case the apical-basal localisation analysis should not be considered reliable enough to draw conclusions about localisation, other than that localisation was not clearly only apical or basal or clearly very different between lines.

For examining medial-lateral localisation the data was more useful, although based on subjective appraisal of a small number of cells. The ARPE-19 cells did not appear to show lateral BEST1 localisation for wild-type or V235A (704T>C), the HEK293 cells appeared to show lateral localisation for both wild-type and V235A (704T>C), and MDCK appeared to show lateral localisation of the wild-type but not V235A (704T>C). These results suggest that BEST1 localisation varies according to the cell line, and that the V235A (704T>C) mutation affects localisation at least in the MDCK cell line. An alternative explanation is that a high degree of relative expression is required for lateral localisation – the V235A (704T>C) MDCK line showed an estimated positive pixel percentage of only 2.8% compared to 35.1 for the wild-type MDCK line.

The mis-localisation of V235A (704T>C) BEST1 in the MDCK line is in direct contradiction to the results from Johnson *et al.*, which found strong lateral localisation of V235A (704T>C) BEST1 in MDCK cells(Johnson et al. 2014). At least one region of the C-terminal cytoplasmic region has been associated with BEST1 trafficking(Reichhart et al. 2010), and so it is possible that the presence of the C-terminal FLAG sequence could be affecting localisation. The BEST1 construct used by Johnson *et al.* had an entire YFP molecule conjugated to the C-terminus, which could also explain the difference. However, as the C-terminal FLAG was the same for all of the

constructs used here this still points to a cell-type specific effect. AREP-19 cells transfected with the wild-type construct with an N-terminal FLAG also showed no lateral localisation.

It is also worth noting that the MDCK and HEK293 cells had much larger nuclei relative to the size of the cell than ARPE-19. As BEST1 staining was never present in the nucleus this means that any cytoplasmic staining of HEK293 or MDCK cells will appear more lateral than any cytoplasmic staining in ARPE-19 cells. In future, co-staining with a membrane marker such as ZO-1 or β-CATENIN would allow better discrimination between BEST1 that is located to the membrane and BEST1 that is cytoplasmic but excluded laterally by the cell nucleus(Doumanov et al. 2013) .

4.5.3 BEST1 does not show lateral localisation in ARPE-19 cells incubated in DMEM medium

Along with the wild-type and V235A (704T>C) constructs, ARPE-19 cells were also transfected with constructions containing the other four ADVIRC mutations, two ARB constructs that had been previously shown to mis-localise in MDCK cells, and a control silent mutation construct P233P (699A>T). No BEST1 staining was observed in the R200X (598C>T) line, which has a premature stop codon and so would not be expected to be recognised by the antibody that recognises towards the C-terminal end. In addition no viable V86M (256G>A) line was ever produced after several attempts. In addition, the confocal images for three lines did not show higher levels BEST1 staining than the negative controls and were excluded. These were: ARPE19 715 G>A with C-terminal FLAG sample from transfection A, the ARPE19 248G>A with C-terminal FLAG sample from transfection B, and the ARPE19 wildtype N-terminal FLAG sample from transfection C.

The other images were analysed and in all cases the BEST1 staining was found to not show clear apical or basal localisation, and the 1-dimensional analysis found the peak BEST1 signal to be marginally apical relative to the peak DAPI signal. None of the lines showed lateral BEST1 staining other than the silent mutation, where there was some suggestion of lateral staining. Therefore even the wild-type BEST1 construct did not show the basolateral localisation in ARPE-19 cells that is characteristic in RPE cells.

The RNA-seq data provided by Amanda Carr and presented in the introduction section demonstrated that ARPE-19 cells incubated in X-VIVO 10 medium for six weeks show changes in expression of some RPE-related genes, including the RPE-identity transcription factors MITF and OTX2, becoming more similar to foetal RPE cells. At the same time the cells become increasingly pigmented and adopt the ‘cobblestone’ morphology associated with RPE monolayers. Together this suggests that incubation in X-VIVO 10 medium produces ARPE-19 that are much more RPE-like than those kept in DMEM.

Therefore ARPE-19 cell lines were incubated in DMEM or XVIVO medium for 85 days, and then stained for BEST1. This time in order to more easily assess apical-basal BEST1 localisation the cells were also stained for MERTK or EZRIN, which are both apical markers expressed by mature RPE(Huang et al. 2009; Subrizi et al. 2012). Neither antibody produced visible staining relative to a negative control, but without a positive control it was impossible to know if this is because there was no MERTK or EZRIN expressed or whether the staining did not work for some other reason.

The BEST1 staining marked visible cells in some of the lines, indicating that BEST1 expressing cells survived in culture for the 85-day incubation. The exceptions were the GFP control, the premature stop codon R200X (598C>T) line, the V86M (256G>A) line which was never produced, and the (248G>A) line, one sample of which was also lost during staining. Of the other lines, seven did not show greater staining intensity than the negative controls and were excluded. This included most of the ADVIRC mutation lines, and the ones that remained showed very low levels of expression.

Once again none of the lines showed clear basal or apical localisation of BEST1 staining. In addition it was found that the cells generally did not lie in flat monolayers, but rucked and formed multi-layered sheets. This meant that the apical-basal 1-dimensional analysis provided no useful information. However, once again it was possible to assess the medio-lateral localisation of the BEST1 staining. In the wild-type (C-terminal FLAG) line and one of the silent mutation (C-terminal FLAG) lines there was some hint of lateral localisation, but in all other cases there was none. This suggests that long-term culture in DMEM does not affect medio-lateral BEST1 localisation in ARPE-19 cells.

4.5.4 Incubation in X-VIVO 10 medium induces lateral BEST1 localisation in some lines, but not consistently across repeat transfections

Incubation in X-VIVO 10 medium rather than DMEM medium for 85 days appeared to induce lateral BEST1 localisation in some cases. However, in some cases supposedly identical lines differed. Of the two wild-type lines (N-terminal FLAG), only one showed lateral staining in X-VIVO 10. Of the two Y236C (707A>G) lines (C-terminal FLAG), only one showed lateral staining in X-VIVO 10. The difference between the identical lines were that they were transfected at different times and then maintained in selection for a different number of passages. However it is not the case that lines from one transfection show lateral localisation while those from another do not, so this does not provide an explanation. However, the estimated positive pixels in the line that did not show lateralisation was only 0.74%, compared to 10.81% in the other. This could suggest that levels of expressions influence localisation of BEST1.

4.5.5 ARPE-19 cells grown for 85 days on matrigel-coated chamber slides show mixed morphology and multi-layering, which could explain differences between lines transfected with the same construct

One difficultly when assessing the apical-basal localisation of BEST1 staining in the ARPE-19 lines that had been incubated in X-VIVO 10 or DMEM medium for 85 days was that the cells did not stay in stable monolayers, but rucked up and formed multiple cell layers. This was particularly true for the cells incubated in DMEM. In addition, in the wells that had been incubated in X-VIVO 10 and that had become pigmented and showed a more 'cobblestone' morphology there was still a lot of variation in cell morphology and pigmentation. These kind of variations had been noted previously for ARPE-19 cells(Ablonczy et al. 2011). It was noted that for the confocal image stacks that contained a large number of BEST1-positive cells that the degree of lateral staining varied between cells, particularly when there were cells in more than one layer. This suggests that for the confocal image stacks that contained only a few cells or a single cell that this cell or cells might not be representative. This could particularly be the case as cells in different layers showed difference cell morphology, with the basal cells that lay beneath the main monolayer showing generally larger and more widely spaced nuclei, suggesting cells with a larger surface area. Flattened migratory RPE are seen during RPE wound healing *in vitro* and could represent a response to the disrupted monolayer(Hergott et al. 1994). This multi-layered growth over time could be due to the Matrigel coating that was used prior to plating the cells. MDCK and HEK293 cells were found to detach during the washing and staining process if grown on culture plastic only. Matrigel coating was found to maintain attachment in these two lines and so was also used for ARPE-19 so that culture conditions were comparable. Based on visual observation this multilayering was present within a couple of weeks of plating, suggesting that it was not a consequence of the extended 85-day incubation.

The variation in ARPE-19 cell morphology could explain the difference between the two (707A>G) (C-terminal FLAG) lines in X-VIVO 10 medium, one of which showed lateral localisation and one of which did not, but which contained four and two cells respectively. However this cannot explain the difference between the wild-type lines (N-terminal FLAG), which contained over a dozen BEST1-positive cells in each. In that case it is possible that taking the images at different areas of the culture wells may have had a systematic effect, with cells at the edge and the centre differing in layering and density. Alternatively the difference could be the result of clonal expansion of a single BEST1-positive cell to occupy the entire field of view. While this is unlikely to have happened after plating of the cells on the chamber slides (unless the BEST1-positive cell had a significant selective advantage due to the location of the retroviral insertion), the G418 selection of the cell lines prior to this may have created a severe evolutionary bottleneck such that the positive cells on plating onto the chamber slides were descendants of

a very small number of starting cells. The fact that in most cases the transfected ARPE-19 cells showed a very low percentage of BEST1-positive cells even after strong G418 selection implies that the cells that were BEST1-positive were atypical in some manner that meant they had survived and continued to express *BEST1* while the vast majority of the others had not. This could be due to the number of copies of the retroviral insertion, the genomic location of the insertion(s), or some property of those particular ARPE-19 cells within the transfected population.

4.5.6 Retroviral transfection of ARPE-19 with *BEST1* constructs may cause cell death in a Best-mutation-dependent manner. Transfection of ADVIRC mutants appears to cause vesicle-like structures in ARPE-19 cells

The reason that there were so few BEST1-positive cells in the confocal images of the ARPE-19 cells is that it proved difficult to produce stable lines after transfection. In fact after several attempts no viable V86M (256G>A) was ever produced. It was noted that sometimes a few days after transfection some lines would show catastrophic cell death quite suddenly. It was hypothesised that the cells were becoming infected with a bacterium or fungus during the transfection procedure. However, there appeared to be a link between the plasmid that had been transfected and the lines that were lost. Closer examination using light microscopy revealed that following transfection some lines showed structures with the appearance of bubbles and that these vesicle-like structures were only seen in the cells transfected with ADVIRC mutation-containing constructs, although the effect varied greatly between lines. Staining of these cells revealed no co-localisation of the vesicle structures with markers for acidic compartments, lysosomes, or BEST1. This suggests that the structures do not represent lysosomal formation for the degradation of overexpressed BEST1, or mis-trafficked BEST1 causing fluid entry into cytoplasmic vesicles.

Calcium signalling have been associated with the autophagocytosis pathway (reviewed by Rovere *et al.,* 2016(La Rovere et al. 2016)), so one possibility is that the ADVIRC BEST1 overexpression is disrupting calcium signalling and causing the formation of autophagosomes, which would not be expected to stain for lysosomal markers prior to fusion with lysosomes into autolysosomes. Another possibility is that the 'vesicles' are actually subcellular, forming between the cell membrane and the culture plastic. This would explain why they did not co-localise with the stains, and also why they tended to mostly vanish when the cells were fixed for staining. Another possibility is that they internalised cell membrane and may contain extracellular medium. The structures disappeared after several weeks in culture, or much faster if the cells were replated and so actively dividing. It is not clear whether this was due to death of the cells that contained the vesicular structures or due to loss of the structures from within

cells over time, therefore it is not clear whether the vesicular structures are directly related to cell death in lines. It is also not clear if transfection of V235A (704T>C) BEST1 into HEK293 or MDCK cells also produced these vesicle-like structures. Still it seems unlikely to be a coincidence that they were only seen in lines transfected with ADVIRC mutant BEST1 and does suggest something particular occurs in these cases relative to the wild-type or ARB mutants. Stains for cytoskeletal components or cell plasma membrane markers might illuminate the identity of the structures. It seems possible that this effect requires high levels of expression of the BEST1 protein, and so represents an *in vitro* artefact. Still, it may be relevant to the nature of ADVIRC pathology *in vivo*. Transfections of a greater range of Bestrophinopathy mutants into the ARPE-19 cell line would illuminate whether this effect is reproducible and particular to ADVIRC mutations.

PCR analysis suggested that every transfected ARPE-19 line assayed contained the transfected plasmid NEO^R resistance gene, even those with no detectable BEST1 protein. All these lines had been through strong G418 selection that had killed off untransfected cells. This suggests that many cells were expressing NEO^R, but not BEST1. This is possible as they have separate promoters and so the *BEST1* CMV promoter could be selectively silenced. It suggests that while NEO^R expression was selected for, BEST1 expression was selected against. It is possible that this negative selection applies only to high levels of BEST1 expression, which would explain why the BEST1 staining that was present was frequently extremely dim. However, the fact that three RPE-derived cell lines, ARPE-19, D407, and RPE-J, all show a lack of endogenous BEST1 protein(Marmorstein et al. 2000) suggests that BEST1 expression may be generally selected against *in vitro*.

Why then were there any BEST1-expressing ARPE-19 cells at all after 85 days in DMEM or X-VIVO 10 medium? One reason could be that expression levels were generally low, as already pointed out. Another possibility is that a BEST1-expressing cell is more likely to survive when surrounded by non-expressing cells. Another possibility is that BEST1 expression only confers a mild growth disadvantage and so once the cells are confluent and stop dividing the ratio of expressing and non-expressing cells does not change.

As for the catastrophic cell death seen after some transfections and not others? Perhaps the time it takes to downregulate the BEST1 CMV promoter means that if transfection efficiency is too high then the cells die before this can occur. In any case experimental work that involves creating stable cell lines of BEST1 expressing ARPE-19 should consider placing the selection gene under the same promoter as the *BEST1* gene.

It is also possible that that BEST1 expression did not reduce cellular fitness. Instead it could be the case that transcription of *BEST1* did occur and that there was strong control at the level of translation, as suggested by Bakall *et al*.(Bakall et al. 2003). In the same study that found a lack of BEST1 protein in ARPE-19, D407, and RPE-J lines it was also found that mRNA for *BEST1* could be detected, supporting the idea of translational control(Marmorstein et al. 2000). *BEST1* transcript has also been detected in MDCK cells, which do not show the presence of BEST1 protein(Doumanov et al. 2013). Quantitative PCR analysis for the level of *BEST1* mRNA could illuminate whether *BEST1* transcription is occurring in these ARPE-19 lines.

4.5.7 It is unclear if having a C-terminal or N-terminal FLAG tag affects localisation of wild-type BEST1 in ARPE-19 cells

Based on the results presented, the effect of the C- or N-terminal FLAG tag on localisation are not clear. The reason for including the C-terminal FLAG was that transfected BEST1 could be distinguished from any endogenous BEST1 that was expressed. However, the FLAG antibody staining was unreliable. When it did work it appeared to be identical to the BEST1 antibody staining only even less intense. For this reason and the limited number of samples for staining it was not used to stain the cells after long term culture. The N-terminal FLAG was included in order that the localisation of the premature stop codon mutant R200X (598C>T) might be detected. No N-terminal FLAG staining was ever seen, suggesting that this site was not available for antibody binding.

Only two mutants were used for transfection of ARPE-19 cells with both versions (one with C- and one with N-terminal FLAG). One was the premature stop codon R200X (598C>T) ARB mutant, which was undetectable using either the BEST1 or FLAG antibody for reasons already given. The other was the wild-type BEST1. In this case the BEST1 (C-terminal) was slightly lateral in some cells in the DMEM condition and lateral in the X-VIVO 10 condition. Two BEST1 (N-terminal) lines were made, both of which were not lateral in the DMEM condition and one of which was lateral in the X-VIVO 10 condition. This data is not enough to draw firm conclusions from, but both the C- and N-terminal FLAG versions of the wild-type BEST1 are capable of being laterally localised, which suggests neither FLAG location fundamentally disrupts localisation relative to the other. Repeating transfections for the other mutant constructs with both the C- and N-terminal FLAG, and comparing those to a retroviral plasmid version with no FLAG would illuminate the disruptive effect (if any) of these terminal epitope tags.

4.5.8 ADVIRC mutations appear to affect cellular localisation of BEST1 in ARPE-19 cells incubated in X-VIVO 10 for 85 days

As already stated, after 85 days in DMEM medium only two ARPE-19 lines showed any suggestion of lateral localisation of BEST1: the wild-type (C-terminal FLAG) line and one of the

two silent mutation P233P (699A>T) (C-terminal) lines. On the other hand, after 85 days in X-VIVO 10 those wild-type and silent mutation lines showed definite lateral localisation, as did one of the two wild-type (N-terminal) lines. This suggests that the ARPE-19 cells in X-VIVO were showing BEST1 localisation at least partially similar to native RPE and that these could be used to compare the localisation of BEST1 in the ADVIRC lines.

The G83D (248G>A) X-VIVO 10 sample was lost during staining, and the DMEM control sample suggested a lack of BEST1 staining anyway. The V86M (256G>A) line was never successfully produced. Both of the V235A (704T>C) lines did not show staining at greater intensity than the negative controls. One of the two Y236C (707A>G) lines showed lateral localisation. The V239M (715G>A) line showed a suggestion of some lateral localisation. Together this picture is far from clear, but suggests that ADVIRC mutations may affect BEST1 localisation in some cases. The fact that both of the V235A (704T>C) lines did not show positive staining at a greater intensity than the negative controls means that these results cannot be compared with the report of mis-localisation of this ADVIRC mutant in iPS-RPE cells(Carter et al. 2016).

Note that the M325T (974T>C) ARB mutation lines in X-VIVO 10 medium showed only a hint of lateral localisation in one of the two lines, consistent with previous reports of mis-localisation for this mutation in MDCK cells(Davidson et al. 2011; Johnson et al. 2014).

4.5.9 Implications for future research on ADVIRC and other Bestrophinopathies

The results presented here are not inconsistent with the hypothesis that ADVIRC mutations may affect cellular localisation of BEST1, as seen in a study using iPS-RPE to investigate one of these AVIRC mutations, V235A (704T>C) (Carter et al. 2016). However, the lack of consistent detectable BEST1 expression in the ARPE-19 cell lines produced in this study means that no conclusions can be drawn.

Previous work examining the pathology of ADVIRC mutations have suggested a role for altered splicing(Yardley et al. 2004; Burgess et al. 2009), which was inconsistent with the lack of altered splicing seen in the iPS-RPE study. This suggested that the effects of ADVIRC mutations (and likely *BEST1* mutations generally) are dependent on the cell line used. Here these preliminary results show suggestion that the localisation of the wild-type BEST1 and V235A (704T>C) BEST1 depend in part on whether the constructs are expressed in MCDK cells, HEK293 cells, or naïve ARPE-19 cells. This supports the view that results from model cell lines will not always apply to native RPE, a unique and highly specialised cell type.

Whether mis-localisation of BEST1 is pathological *in vivo* is an entirely different question. Investigation of ARB mutant BEST1 found that most were mis-localised in MDCK cells and caused mis-localisation of co-expressed wild-type BEST1 as well(Johnson et al. 2014). As ARB is recessive

this implies that a heterozygous carrier will have significantly mis-localised BEST1 without showing any dysfunction, further suggesting that mis-localisation *per se* doesn't cause disease. Alternatively this may be an effect specific to overexpression in MDCK cells that does not apply to native RPE.

The discovery of iPS cells and the increasing efficiency of producing RPE cells from them should make it easier to conduct studies of BEST1 function in cells that more closely resemble native RPE. Development of more efficient gene-editing techniques will complement this approach, allowing known disease-causing mutations to be introduced or removed selectively in human iPS-RPE lines. In the meantime, results from non-RPE cell lines should only be taken as suggestive as to the role of BEST1 in native RPE. Using multiple cell models, including epithelial lines such as MDCK and HEK293 as well as RPE-derived lines such as ARPE-19 can increase confidence in consistent results.

Of course even iPS-RPE may not represent a perfect *in vitro* model. Even if iPS-RPE were exactly equivalent to native RPE, any cell line grown in a plastic dish in artificial medium is going to show some differences from its native counterpart. This may be particularly true of RPE cells that interact so heavily with their cellular neighbours. As an example, native RPE phagocytose many thousands of photoreceptor outer segments every day. How might a complete lack of outer segment exposure or phagocytosis affect RPE cells grown *in vitro*? One exciting development in the stem-cell ophthalmology is the production of optic cups, small organoids that contain multiple retinal cell types in a partially organised state(Meyer et al. 2009; Parfitt et al. 2016). This promises to allow study of human RPE-photoreceptor interactions *in vitro*.

The question of the mechanism of Bestrophinopathies is important not just for understanding the function of BEST1 in RPE, but also for future treatment development. As already stated there are no therapies for Bestrophinopathies beyond reducing neovascularisation and replacing cataracts. Areas of healthier RPE can be transplanted from other parts of the retina and it may soon be possible to replace diseased RPE with stem-cell derived RPE(Da Cruz et al. 2018). However, the former does not solve the underlying problem and the latter will be an expensive surgical procedure if and when it is approved.

However, if a simple mechanism such as nonsense-mediated decay, mis-localisation, or splice variation can be confirmed for particular patient mutations then there are already potential drug interventions known. For example the proteasome inhibitor bortezomib, and the chemical chaperone 4-phenylbutyrate (4PBA) both restored localisation of 4 ARB mutant BEST1 proteins that were otherwise mis-localised and degraded(Uggenti et al. 2016). Both of these drugs are already approved for use in humans. However this paper used overexpression in MDCK cells and

so the mis-localisation may not occur in native RPE, and if it is it may not be the mis-localisation that is actually causing the disease.

Read-through inducing drugs can allow a full-length protein to be produced from a transcript containing a nonsense substitution. For example, PTC124 has been shown to restore expression of MERTK and rescue some phagocytosis function in an iPS-RPE line derived from a patient with a nonsense mutation(Ramsden et al. 2017).

There are many known chemicals that are known to affect splicing. For example Kinetin has been shown to partially correct mutation-induced splicing errors assays of the neurofibromatosis type 1 (NF1) gene in patient-derived cells(Pros et al. 2010). Additionally antisense morpholino treatment has been demonstrated to block a disease-causing mis-splicing of the cilia-related gene CEP290 in IPS-derived optic cups derived from a patient with Leber congenital amaurosis (LCA)(Parfitt et al. 2016). If ADVIRC mutations causes mis-splicing then these approaches could be viable clinical approaches. However if the mis-splicing is an artefact of the HEK293 cell line then it would provide no benefit.

If the mutation is a null, as is suspected for cases of ARB, then gene therapy could be used to introduce a functional version of the *BEST1* gene in the RPE cells. This could also apply to recessive compound heterozygote mutations. This gene therapy approach, using a viral vector, has been applied in clinical trials to introduce healthy version of the RPE65 gene into the RPE of LCA patients(Bainbridge et al. 2008; Maguire et al. 2008).

The key to the approaches described above is knowing the nature of the dysfunction that the mutation of interest causes. The results presented in this chapter suggest that ADVIRC BEST1 localisation defects occur in a cell-type specific manner. Therefore results acquired from BEST1 overexpression in a single non-RPE cell line should be treated with caution until they are replicated in multiple model lines, including at least cells derived from RPE and ideally RPE derived from iPS cells.

Chapter 5 – Final conclusions

In the first chapter of this thesis four aims were outlined for the work that was to be presented. Below these aims will be revisited and broader implications of the presented work will be briefly considered.

5.1 Fulfilling the thesis aims

The first experimental chapter aimed to address the question as to whether the circadian clock is an active 'driver' of the progression of the cell cycle or whether it 'gates' cell cycle progression to particular times of day. The results presented in that chapter strongly supported a gating model of regulation. In addition, the discussion of these results in the context of the published literature produced testable explanatory theories for the conflict in results seen using different model systems.

The aim of the second experimental chapter was to assess cell density as a meaningful hidden variable in the circadian regulation of the cell cycle, and then to use this framework to provide plausible and testable explanations for apparently contradictory results in the published literature. In this chapter variation in cell density was shown to affect the relative phase lengths of G1 and SG2M, explaining the statistically significant difference seen in SG2M lengths between T-cycle experiments. Going beyond this, the variable density dataset was analysed and found to suggest a role for cell density in the coupling between the circadian clock and cell cycle itself. The implications of this effect were again discussed in the context of the published literature and testable explanatory theories were produced for the conflict in results seen using different model systems.

The aim of the third experimental chapter was to address the question as to whether contradictory results in the published literature as to the effects of specific mutations are due in part to the choice of cell line model. The results presented suggest that the cell model line and culture conditions both may affect localisation of Bestrophin-1 protein in a disease mutant-dependent fashion. However, the inconsistent and low levels of BEST1 construct expression prevent mean that firm conclusions cannot be drawn. The implications of these results for conclusions drawn from studying RPE pathology in general, and BEST1 function in particular, using epithelial model cells lines was discussed.

The final aim of this thesis was to actively consider what properties of these models, and others in the published literature, may be unrepresentative of the organ or organism-level biological systems that they are being used to represent. In all three experimental chapters the impact of the model used on the results has been considered and placed into the context of differing model systems used in these fields.

5.2 The importance of considering hidden variables

If this author was asked to provide a single principle or theme that could be extracted from the work presented in this thesis it would be the importance of considering hidden variables when designing and interpreting experimental protocols. This final section considers this theme in the context of circadian biology and beyond.

5.2.1 Cell density as a hidden variable

In the second experimental chapter data was presented that suggests that both mitosis period and rhythmicity are density-dependent, and that this density effect could explain conflicting findings in terms of the circadian influence on cell cycle timing. If confirmed as a generally-applicable effect across cell lines then this density-dependence is something that needs to be considered during the experimental design and data analysis of studies that probe the coupling between the circadian clock and the cell cycle.

It has been demonstrated that in NIH 3T3 cells mitotic events robustly phase-shift the circadian clock by around 5 hours(Bieler et al. 2014). This effect, if found to be generalise to other cell types, suggests that the effect of cell cycle progression on clock phase is something circadian cell biologists should be aware of in their own experiments. This is particularly the case if experiments are conducted on dilute un-entrained cells, as many are. One likely consequence of this effect is that clock rhythmicity at a population level will dampen more quickly when free-running if the cells are proliferating than if they are not.

5.2.2 The circadian clock as a hidden variable

Outside the field of circadian biology the role that the circadian clock might play in experimental results is almost never considered. However, a self-sustaining cellular circadian clock appears to be near universal for all cell types studied. This means that an un-entrained cell population under study will contain cells with randomised circadian phases. At a population level this will average out, but at a single cell level it could significantly affect cell behaviour. As only a single example, cell cycle phase is known to influence the propensity to differentiate in stem cells(Calder et al. 2012), and cell cycle phase timing is known to be influenced by circadian phase. Therefore one explanation for why only a subset of stem cells respond to a differentiation cue could be due to their circadian clock phase – a hidden variable.

Even worse, it is known that treatments as universal as the serum pulse from changing cell culture medium are sufficient to synchronise the circadian phase of a cells *in vitro*(Balsalobre et al. 1998; Welsh et al. 2004). Combine this with the extensive and tissue-specific clock regulation of gene expression and it is easy to see how the influence of the circadian clock could

significantly affect experimental results. For example if an experiment was performed comparing cells kept in culture for 1 week vs 1 month, and the 1 week samples were collected one hour after feeding and the 1 month 3 hours after feeding, significant effects could be found between the two that have nothing to do with length of time in culture. Alternatively, if an experimental protocol involves pulsing cells with some kind of chemical agent and measuring their response then the response measured may be due to synchronisation of the circadian clocks of the cell population rather than any effect of the treatment.

5.2.3 Hidden variables vs stochasticity

The word 'stochastic' is often used incorrectly to explain variation in collected data. Technically speaking a stochastic variation is one that is due to a random effect, and thus is inherently unpredictable in principle. More often though variation is described as stochastic when no plausible explanation will be offered by the authors. Above it has been described why both cell density and circadian clock influences are likely to cause variability in experimental results that might be considered stochastic to those not looking for them.

An example of the consideration of whether an effect is due to stochastic variation or a deterministic hidden variable can be found in Sandler *et al.,* 2015(Sandler et al. 2015). Here they address the question of the cousin-mother inequality. It had previously been observed in many cell types that the correlation in cell cycle length between mother and daughter cells is close to zero, while that between sister cells is much higher. This could be due to a factor that is inherited at birth and determines cell cycle length, but that is stochastic and therefore reset each generation. However, it was also observed that the correlation between cousin cells is also much higher than between mother and daughter. This implies instead a deterministic factor that is not reset each generation.

They suggested that this factor could be the circadian clock and demonstrate a circadian phase influence on cell cycle length using data collected from cyanobacteria(Yang et al. 2010), fitting their theory and their model.

They suggest this explanation could also apply to mammalian cells. This could be addressed using a cell cycle and circadian clock dual reporter system and assessing whether cell cycle length correlates with clock phase. Alternatively, though less ideally, just a cell cycle reporter could be used in an entrained cell line such as the zebrafish PAC2 line used in this thesis.

Chapter 6 – Appendix

Whole cell cycle

Group	n	Mean	s.d.	total x	total x^2
T16	28	68.76786	16.51457	1925.5	139776.3
T18	107	67.00467	14.87328	7169.5	503838.8
T24	51	61.78431	13.28881	3151	203512
T32	46	64.01087	14.38961	2944.5	197797.8

total n	232
k	4
total x	15190.5
total x^2	1044924.75

	Sum of Squares	d.f.	MS
Total	50307.11961	231	
Between group	1347.258861	3	449.0863
Within group	48959.86075	228	214.7362
F value	2.091339147		
d.f.	3, 228		
p value	0.102151		

G1 length

Group	n	Mean	s.d.	total x	total x^2
T16	142	46.95775	17.36217	6668	355618
T18	100	43.39	17.73024	4339	219391
T24	78	49.61538	22.30965	3870	230336

total n	320
k	3
total x	14877
total x^2	805345

	Sum of Squares	d.f.	MS
total	113703.9719	319	
Between group	1753.973858	2	876.9869
Within group	111949.998	317	353.1546
F value	2.483294876		
d.f.	2, 317		
p value	0.08509		

SG2M length

Group	n	Mean	s.d.	total x	total x^2
T16	100	21.13	7.736383	2113	50573
T18	100	24.49	6.886519	2449	64671
T24	100	22	4.51037	2200	50414

total n	300
k	3
total x	6762
total x^2	165658

	Sum of Squares	d.f.	MS
total	13242.52	299	
Between group	608.22	2	304.11
Within group	12634.3	297	42.53973
F value	7.148846394		
d.f.	2, 297		
p value	0.000928		

Table 6.1 ANOVA analyses comparing cell cycle length, G1 length, and SG2M length between T-cycle groups.

	$\bar{x}i-\bar{x}j$	Critical q $q(\alpha,r,dfW)$	Standardised error	95% confidence interval for ui-uj		Significant at 0.05%?
T18-T24	-3.36	3.33	0.65222489	-5.531909	-1.1881	YES
T18-T32	-0.87	3.33	0.65222489	-3.041909	1.30191	NO
T24-T32	2.49	3.33	0.65222489	0.3180911	4.66191	YES
critical q from http://www.vassarstats.net/tabs.html#q, k=3, dfW = 297						
standardised error	root((MSw/2)*(1/ni+1/nj))					
	is the same for all as n is the same					
checked with http://astatsa.com/OneWay_Anova_with_TukeyHSD/_result/						
	result is that 1 and 3 are significant at 0.05, but not 2					
Tukey HSD results						
treatments	Tukey HSD	Tukey HSD	Tukey HSD			
pair	Q statistic	p-value	inferfence			
A vs B	5.1516	0.0010053	** p<0.01			
A vs C	1.3339	0.6046232	insignificant			
B vs C	3.8177	0.0200237	* p<0.05			
checked using https://brownmath.com/stat/anova1.htm#ANOVAdo						

Table 6.2 Tukey Post-Hoc HSD test comparing SG2M lengths in T-cycle groups.

Welch's t-test	Dataset	cell cycle phase length	mean	standard deviation	n	s.e.m.
sample 1	T24 (T-cycle)	Cell cycle length	41.18954	8.8592086	51	1.240537339
sample 2	T24 (Var-den)	Cell cycle length	56.38842	16.18332	295	0.942229328
t	-9.756652131					
d.f. (Welch-Scatterthwaite)	117.6692404	rounds down to	117			
checked with https://www.graphpad.com/quickcalcs/ttest2/						
The two-tailed P value is less than 0.0001						
Welch's t-test	Dataset	cell cycle phase length	mean	standard deviation	n	s.e.m.
sample 1	T24 (T-cycle)	G1 length	28.92667	11.820162	100	1.182016197
sample 2	T24 (Var-den)	G1 length	33.47704	17.044637	265	1.047043721
t	-2.8816814					
d.f. (Welch-Scatterthwaite)	256.1707852	rounds down to	256			
checked with https://www.graphpad.com/quickcalcs/ttest2/						
The two-tailed P value equals 0.0043						
Welch's t-test	Dataset	cell cycle phase length	mean	standard deviation	n	s.e.m.
sample 1	T24 (T-cycle)	SG2M length	16.32667	4.5910125	100	0.459101254
sample 2	T24 (Var-den)	SG2M length	21.26687	9.4271054	252	0.593851818
t	-6.581469731					
d.f. (Welch-Scatterthwaite)	336.2051654	rounds down to	336			
checked with https://www.graphpad.com/quickcalcs/ttest2/						
The two-tailed P value is less than 0.0001						

Table 6.3 Welch's t-test comparing cell cycle and phase length data between T24 fixed-density and T24 variable-density.

Welch's t-test	Dataset	cell cycle phase length	mean	standard deviation	n	s.e.m.
sample 1	Denser than T-cycle	cell cycle length	50.175	12.5082281	40	1.977724508
sample 2	Less dense than T-cycle	Cell cycle length	52.3451	15.2851675	255	0.957194315
t	-0.98767266					
d.f. (Welch-Scatterthwaite)	58.91462613	rounds down to	58			
checked with https://www.graphpad.com/quickcalcs/ttest2/						
The two-tailed P value equals 0.3274						
Welch's t-test	Dataset	cell cycle phase length	mean	standard deviation	n	s.e.m.
sample 1	Denser than T-cycle	G1 length	36.07843	13.9008534	51	1.946508818
sample 2	Less dense than T-cycle	G1 length	29.66822	15.9219699	214	1.088403457
t	2.87435353					
d.f. (Welch-Scatterthwaite)	84.22071115	rounds down to	84			
checked with https://www.graphpad.com/quickcalcs/ttest2/						
The two-tailed P value equals 0.0051						
Welch's t-test	Dataset	cell cycle phase length	mean	standard deviation	n	s.e.m.
sample 1	Denser than T-cycle	SG2M length	15.23438	3.97908096	64	0.49738512
sample 2	Less dense than T-cycle	SG2M length	21.14815	9.33018775	189	0.678671296
t	-7.028329534					
d.f. (Welch-Scatterthwaite)	238.6976133	rounds down to	238			
checked with https://www.graphpad.com/quickcalcs/ttest2/						
The two-tailed P value is less than 0.0001						

Table 6.4 Welch's t-test comparing cell cycle and phase lengths between dense and dilute cells.

		R-squared of regression	
Y variable	X variable	Linear	Power
Start count	Plating density	0.5071	0.5983
End count	Plating density	0.1679	0.2603
End count	Start count	0.7484	0.7947
Proliferation index	Plating density	0.2105	0.6699
All calculated using Microsoft Excel			

Table 6.5 R-squared values for linear and power regressions relating different measures of cell density.

eurofins mwg|operon

pEX-K vector map, multiple cloning site and sequence

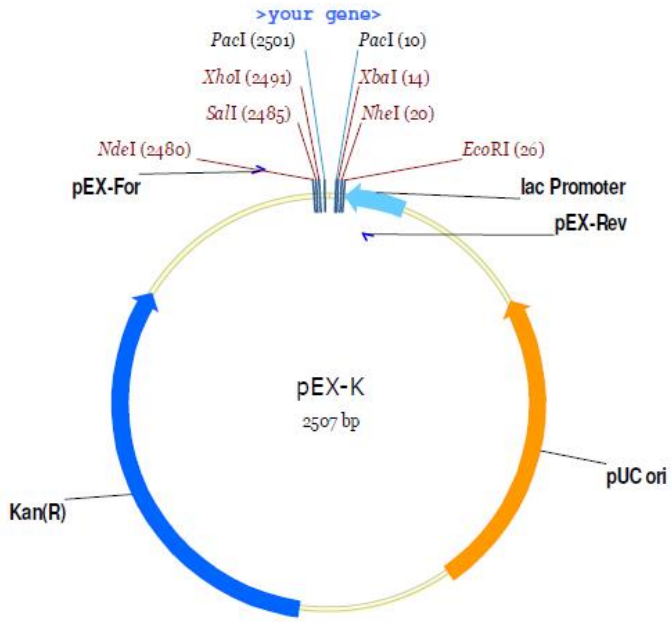

MCS of pEX-K

Sequencing primers and *PacI* restriction sites underlined

GGAGCAGACAAGCCCGTCAGGGCGCGTCAGCGGGTGTTGGCGGGTGTCGGGGC

TGGCTTAACTATGCGGCATCAGAGCAGATTGTACTGAGAGTGCACCATATGgt

cgacCTCGAGttaattaaCGTA >your gene> GTGGttaattaaTCTAGA

gctagcGAATTCCTGTGTGAAATTGTTATCCGCTCACAATTCCACACAACATA

CGAGCCGGAAGCATAAAGTGTAAAGCCTGGGGTGCCTAATGA

Figure 6.1 Details of cloning plasmid pEX-K from Eurofins mwg|operon.

For PAC2 cell qPCR			
Forward	Reverse	target	
CGCAAATACTCCGTCTGGAT	GGGCCAGACTCATCGTACTC	β-Actin	
CAGCTGATCGTTGGAGTCAA	TGTATGCGCTGACTTCCTTG	EF1-α	
TCGCTAGTTGGCATCGTTTATG	CGGAGGTTCGAAGACGATCA	18s	
ATCCAGACCCCAATACAAC	GGGAGACTCTGCTCCTTCT	PER1	
AGGCTTACACAGCAGCATCA	CTGCACTGCCTCTGGACTTT	CRY1a	
for sequencing pEX.Best1			
GTTTCTGAACCCAGCCAAGG			
TAAAGGAGGCTCGACGGAAC			
GTCGGGGCTGGCTTAACTAT			
CTTCCGGCTCGTATGTTGTG			
TCATTTCAGGTCCTTGGGGCAC			
GCCATCCACGCTGTTTTGAC			
AGCAGGCTTTATGACTCCGG			
CTGATACAGTGGGGCAGACT			
for pCLNC-Best1-FLAG cloning			
GTAACGCGTCTCGAGGAAGCCATGACCATCACT	to amplify Best1 gene from pEX-K4.Best1 with NotI and MluI and overhangs		
CGGCGGCCGCTGAGGAATGTGCTTCATCCCTGT			
AGCTTACGCGTGCGGCCGCGGACTACAAAGACGATGACGACAAGTAAAT	to anneal to form MCS-FLAG with HindIII and ClaI compatible overhangs		
CGATTTACTTGTCGTCATCGTCTTTGTAGTCCGCGGCCGCACGCGT			
for pCLNC-FLAG-BEST1 cloning			
GCTTGCGGCCGCTTCTATGACCATCACTTACACAAG	to amplify Best1 gene from pEX-K4.Best1 with NotI and MluI overhangs		
CGATACGCGTTTAGGAATGTGCTTCATCCC			
AGCTTGCCATGGACTACAAAGACGATGACGACAAGGCGGCCGCACGCGTAT	to anneal to form KOZAK-MET-FLAG-MCS with HindIII and ClaI compatible overhangs		
CGATACGCGTGCGGCCGCCTTGTCGTCATCGTCTTTGTAGTCCATGGCA			
for site-directed mutagenesis			
Primer	to produce the base change in BEST1	Protein substitution	Disease
CATTTCCTTCGTGCTGGACTTCTACGTGACGCTGG			
CCAGCGTCACGTAGAAGTCCAGCACGAAGGAAATG	248 G>A	pGly83Asp	ADVIRC
TCGTGCTGGGCTTCTACATGACGCTGGTCGTGACC			
GGTCACGACCAGCGTCATGTAGAAGCCCAGCACGA	256 G>A	pV86M	ADVIRC
GATTAGTATCCCACTGGCGTATACACAGGTGGTGA			
TCACCACCTGTGTATACGCCAGTGGGATACTAATC	704 T>C	pV235A	ADVIRC
TAGTATCCCACTGGTGTGTACACAGGTGGTGACTG			
CAGTCACCACCTGTGTACACACCAGTGGGATACTA	707 A>G	pY236C	ADVIRC
CACTGGTGTATACACAGATGGTGACTGTGGCGGTG			
CACCGCCACAGTCACCATCTGTGTATACACCAGTG	715 G>A	pV239M	ADVIRC
AGGCGTGGCTTGGAGGTTGAATCCGGGACCCTATC			
GATAGGGTCCCGGATTCAACCTCCAAGCCACGCCT	598 C>T	pR200X	ARB
GTTGGCTGTGGATGAGACGCACCAGGACCTGCCTC			
GAGGCAGGTCCTGGTGCGTCTCATCCACAGCCAAC	974 T>C	pM325T	ARB
GACTGGATTAGTATCCCTCTGGTGTATACACAGGT			SILENT
ACCTGTGTATACACCAGAGGGATACTAATCCAGTC	699 A>T	-	MUTATION

Table 6.6 A list of primers and oligonucleotides used in this thesis.

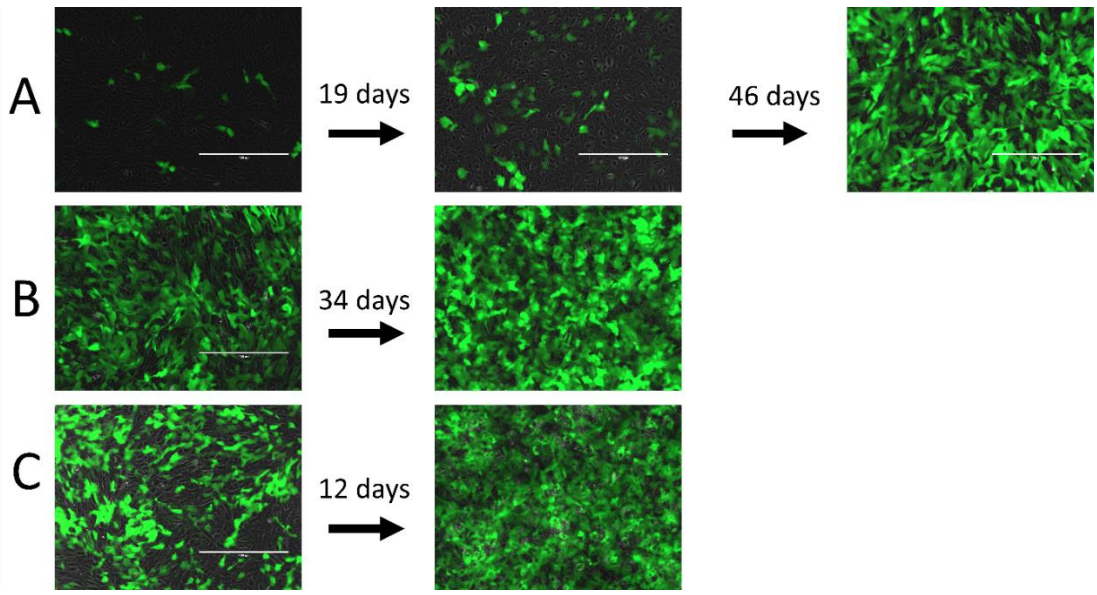

Figure 6.2 Action of G418 selection on GFP expression in pCLNC-GFP transfected ARPE19 cells over time.

Shown are the pCLNC-GFP control lines for three separate transfections of ARPE19 cells. Each is shown as

a composite brightfield and GFP image taken with the EVOS. The intervals between images in days is indicated. G418 selection concentration as well as replating interval and splitting ratio were not standardised between the different transfections. A, B and C show GFP control lines from separate transfection dates.

					Approximate number of Best1-positive cells per		
Cell type	**Best1 mutation**	**Terminal flag tag**	**Disease**	**Transfection**	**X-VIVO**	**DMEM**	**Notes**
ARPE19	Wild-type	C	-	B	**70**	**9**	
	248 G>A	C	ADVIRC	B	**Well was lost**	**No clear cellular staining**	No clear cellular staining
	256 G>A	C	ADVIRC	-	**No viable cell line was produced**	**No viable cell line was produced**	No viable cell line was produced
	704 T>C	C	ADVIRC	A	**9**	**5**	
				C	**2**	**1**	
	707 A>G	C	ADVIRC	A	**4**	**4**	
				C	**2**	**1**	
	715 G>A	C	ADVIRC	C	**14**	**1**	
	598 C>T	C	ARB	C	**No clear cellular staining**	**No clear cellular staining**	No clear cellular staining
	974 T>C	C	ARB	A	**7**	**1**	
				C	**30**	**3**	
	699 A>T	C	-	A	**40**	**15**	
				C	**40**	**20**	
	Wild-type	N	-	A	**16**	**15**	
				C	**20**	**4**	
	598 C>T	N	ARB	A	**No clear cellular staining**	**No clear cellular staining**	No clear cellular staining
	GFP control	-	-	C	**No clear cellular staining**	**No clear cellular staining**	Negative control lines

Table 6.7 Estimated number of BEST1-positive cells in each confocal imaging stack taken of ARPE19 cell lines transfected with retroviral BEST1 expression vectors and grown in X-VIVO or DMEM medium. *The table shows (from left to right) the transfected cell line; the Best1 mutation contained in the transfected plasmid; whether the construct had a C or N-terminal FLAG tag; the disease associated with the mutation; whether the line was created in transfection A, B, or C; a visual estimate of total BEST1-positive cells in the field of view in each line grown in X-VIVO medium; a visual estimate of total BEST1-positive cells in the field of view in each line grown in DMEM medium; notes on BEST1-negative images.*

					Peak mean BEST1 staining intensity (0-255)		
Cell type	**Best1 mutation**	**Terminal flag tag**	**Disease**	**Transfection**	**X-VIVO**	**DMEM**	**Clear staing of some cells and not others?**
ARPE19	Wild-type	C	-	B	16.78	15.343	Yes
	248 G>A	C	ADVIRC	B	Well was lost	3.123	No
	256 G>A	C	ADVIRC	-	No viable cell line was produced	No viable cell line was produced	No viable cell line was produced
	704 T>C	C	ADVIRC	A	2.222	4.163	Yes
				C	2.031	1.925	Yes
	707 A>G	C	ADVIRC	A	2.439	3.352	Yes
				C	3.978	2.496	Yes
	715 G>A	C	ADVIRC	C	4.616	3.55	Yes for XVIVO, No for DMEM
	598 C>T	C	ARB	C	3.468	7.775	No
	974 T>C	C	ARB	A	1.638	2.607	Yes
				C	18.963	7.157	Yes
	699 A>T	C	-	A	11.817	6.481	Yes
				C	39.694	7.976	Yes
	Wild-type	N	-	A	3.152	9.938	Yes
				C	7.685	6.303	Yes
	598 C>T	N	ARB	A	1.505	1.832	No
	GFP control	-	-	C	4.022	4.831	No

Table 6.8 BEST1 staining maximum mean intensity in retrovirally transfected AREP19 cell lines, based on BEST1 and DAPI staining of fixed cells imaged at 40x with a confocal microscope. *The table shows (from left to right) the transfected cell line; the Best1 mutation contained in the transfected plasmid; whether the construct had a C or N-terminal FLAG tag; the disease associated with the mutation; whether the line was created in transfection A, B, or C; the mean intensity of BEST1 staining in the z-slice with the highest mean BEST1 intensity in the stack for the cell lines in X-VIVO medium; ; the mean intensity of BEST1 staining in the z-slice with the highest mean BEST1 intensity in the stack for the cell lines in DMEM medium; whether the confocal stack showed clearly visible stained cells alongside clearly visible unstained cells. Red cells show intensities that are less than the GFP negative control and cells that have no clear staining of visible cells. Green cells show intensities that are more than the GFP negative control and cells that have clear staining of visible cells.*

					Number of layers of cells in the stack		
Cell type	**Best1 mutation**	**Terminal flag tag**	**Disease**	**Transfection**	**X-VIVO**	**DMEM**	**Notes**
ARPE19	Wild-type	C	-	B	1	2	
	248 G>A	C	ADVIRC	B	Well was lost	2	No clear cellular staining
	256 G>A	C	ADVIRC	-	No viable cell line was produced	No viable cell line was produced	No viable cell line was produced
	704 T>C	C	ADVIRC	A	2	2	
				C	1	2	
	707 A>G	C	ADVIRC	A	1	2	
				C	2	2	
	715 G>A	C	ADVIRC	C	2	2	
	598 C>T	C	ARB	C	1	2 or 3	No clear cellular staining
	974 T>C	C	ARB	A	2	2	
				C	2	2	
	699 A>T	C	-	A	1	2	
				C	2	2 or 3	
	Wild-type	N	-	A	1	2	
				C	2	2 or 3	
	598 C>T	N	ARB	A	1	2 or 3	No clear cellular staining
	GFP control	-	-	C	2	3	Negative control lines

Table 6.9 Layering of cells in retrovirally transfected AREP19 cell lines, based DAPI staining of fixed cells imaged at 40x with a confocal microscope. *The table shows (from left to right) the transfected cell line; the Best1 mutation contained in the transfected plasmid; whether the construct had a C or N-terminal FLAG tag; the disease associated with the mutation; whether the line was created in transfection A, B, or C; approximately how many cell layers existed after culture in X-VIVO medium; approximately how many cell layers existed after culture in DMEM medium; notes on some of the cell lines. Layering was estimated by eye based on stacking of DAPI stained nuclei in confocal stacks. A layer did not have to be complete across the field of view to be counted, only clearly distinct from nuclei above or below it.*

					Localisation of BEST1 positive cells within cell		
Cell type	**Best1 mutation**	**Terminal flag tag**	**Disease**	**Transfection**	**X-VIVO**	**DMEM**	**Notes**
ARPE19	Wild-type	C	-	B	1 of 1	Apical of 2	
	248 G>A	C	ADVIRC	B	Well was lost	No clear cellular staining	No clear cellular staining
	256 G>A	C	ADVIRC	-	No viable cell line was produced	No viable cell line was produced	No viable cell line was produced
	704 T>C	C	ADVIRC	A	Basal of 2	Both of 2	
				C	1 of 1	Apical of 2	
	707 A>G	C	ADVIRC	A	1 of 1	Apical of 2	
				C	Apical of 2	Apical of 2	
	715 G>A	C	ADVIRC	C	Apical of 2	No clear cellular staining	
	598 C>T	C	ARB	C	No clear cellular staining	No clear cellular staining	No clear cellular staining
	974 T>C	C	ARB	A	Basal of 2	Apical of 2	
				C	Basal of 2	Apical of 2	
	699 A>T	C	-	A	1 of 1	Apical of 2	
				C	Apical of 2, and a little basal	Apical and basal, but not middle of 3	
	Wild-type	N	-	A	1 of 1	Primarily apical of 2	
				C	Basal of 2	Primarily apical of 2 or 3	
	598 C>T	N	ARB	A	No clear cellular staining	No clear cellular staining	No clear cellular staining
	GFP control	-	-	C	No clear cellular staining	No clear cellular staining	Negative control lines

Table 6.10 Localisation of BEST1-positive cells within layering of cells in retrovirally transfected AREP19 cell lines, based DAPI staining of fixed cells imaged at 40x with a confocal microscope. *The table shows (from left to right) the transfected cell line; the Best1 mutation contained in the transfected plasmid; whether the construct had a C or N-terminal FLAG tag; the disease associated with the mutation; whether the line was created in transfection A, B, or C; approximately which cell layer the BEST1-positive cells existed in after culture in X-VIVO medium; approximately which cell layer the BEST1-positive cells existed in after culture in DMEM medium; notes on some of the cell lines. Layering and localisation was estimated by eye based on stacking of BEST1 cells and DAPI stained nuclei in confocal stacks. A layer did not have to be complete across the field of view to be counted, only clearly distinct from nuclei above or below it.*

								8-bit threshold of 7					
line ID	Cell line	Best1 mutation	Terminal FLAG tag	magnification (x)	Z-slice width (micrometres)	negative control?	average pixel intensity in stack (8-bit value)	intensity 255 pixels	intensity 0 pixels	total pixels	%positive pixels	lateral staining	estimated BEST1 apical distance (um)
61	HEK293	Wild-type	C	20	2.043			962805	85771	1048576	91.82	2	4.086
62	HEK293	704T>C	C	20	2.043			419716	628860	1048576	40.03	2	4.086
63	HEK293	GFP	-	20	2.643	y	1.365	43	1048533	1048576	0.00		
65	MDCK	Wild-type	C	20	2.643			367698	680878	1048576	35.07	2	0
66	MDCK	704T>C	C	20	2.643			29594	1018982	1048576	2.82	0	2.643
54	ARPE19	704T>C	C	20	2.043			43781	1004795	1048576	4.18	0	0
55	ARPE19	707A>G	C	20	2.043			344488	704088	1048576	32.85	0	0
56	ARPE19	715G>A	C	20	2.043			184547	864029	1048576	17.60	0	0
512	ARPE19	GFP	-	20	2.043	y	1.019	3158	1045418	1048576	0.30		-
24	ARPE19	704T>C	C	20	1.043			49954	998622	1048576	4.76	0	0
25	ARPE19	707A>G	C	20	1.043			20196	1028380	1048576	1.93	0	2.086
26	ARPE19	715G>A	C	20	1.043			16282	1032294	1048576	1.55	0	2.086
27	ARPE19	598C>T	C	20	1.043	y	1.549	20022	1028554	1048576	1.91		-
28	ARPE19	974T>C	C	20	1.043			76551	972025	1048576	7.30	0	1.043
29	ARPE19	699A>T	C	20	1.043			182961	865615	1048576	17.45	1	1.043
210	ARPE19	Wild-type	N	20	1.043			26014	1022562	1048576	2.48	0	1.043
211	ARPE19	598C>T	N	20	1.043	y	1.934	15271	1033305	1048576	1.46	0	1.043
212	ARPE19	GFP	-	20	1.043	y	1.137	277	1048299	1048576	0.03		-
41	ARPE19	Wild-type	C	20	1.043			124981	923595	1048576	11.92	0	1.043
42	ARPE19	248G>A	C	20	1.043			6848	1041728	1048576	0.65	0	1.043
57	ARPE19	598C>T	C	20	1.043	y	1.137	5183	1043393	1048576	0.49		-
58	ARPE19	974T>C	C	20	1.043			43638	1004938	1048576	4.16	0	1.043
59	ARPE19	699A>T	C	20	2.043			181711	866865	1048576	17.33	0	0
510	ARPE19	Wild-type	N	20	2.043			6814	1041762	1048576	0.65	0	2.043
511	ARPE19	598C>T	N	20	2.043	y	1.023	4023	1044553	1048576	0.38		4.086
			mean average pixel intensity of negative controls				1.309						

Table 6.11 Data used to produce estimates for the percentage of BEST1 positive pixels in confocal stacks taken of transfected ARPE-19, MDCK and HEK293 cells. The average pixel intensity for the image stacks

is shown for the negative control lines (in orange). Below the table is shown the mean of these values, 1.309. Based on this value a thresholding value of 7 out of 255 was chosen and the test stack projections were subjected to this thresholding. The percentage of pixels in the test images that passed this threshold were measured and used to produce an estimate for percentage positive pixels. Any that lay below the value calculated for the negative controls were defined as negative for BEST1 staining and excluded from further analysis (shown in red).

									8-bit threshold of 12					
Culture Medium	line ID	Cell line	Best1 mutation	Terminal FLAG tag	magnification (X)	Z-slice width (micrometres)	negative control	average pixel intensity (8-bit value)	intensity 255 pixels	intensity 0 pixels	total pixels	%positive pixels	lateral staining	estimated BEST1 apical distance (um)
X-VIVO	24	arpe19	704T>C	C	40	2			4937	1043639	1048576	0.471	0	4
	25	arpe19	707A>G	C	40	2			27489	1021087	1048576	2.622	2	-2
	28	arpe19	974T>C	C	40	2			23	1048553	1048576	0.002	0	6
	29	arpe19	699A>T	C	40	2			160174	888402	1048576	15.275	2	-4
	210	arpe19	wildtype	N	40	2			7765	1040811	1048576	0.741	0	0
	211	arpe19	598C>T	N	40	2	Y	0.819	253	1048423	1048676	0.024		-4
	41	arpe19	wildtype	C	40	2			199595	848981	1048576	19.035	2	4
	42	arpe19	248G>A	C	40	2	No image acquired							
	54	arpe19	704T>C	C	40	2			506	1048070	1048576	0.048	0	6
	55	arpe19	707A>G	C	40	2			18803	1029773	1048576	1.793	0	2
	56	arpe19	715G>A	C	40	2			8611	1039965	1048576	0.821	1	6
	57	arpe19	598C>T	C	40	2	Y	2.461	2722	1045854	1048576	0.260		0
	58	arpe19	974T>C	C	40	2			290878	757698	1048576	27.740	1	4
	59	arpe19	699A>T	C	40	2			614251	434325	1048576	58.580	2	2
	510	arpe19	wildtype	N	40	2			113316	935260	1048576	10.807	2	-4
	512	arpe19	gfp		40	2	Y	3.185	1292	1047284	1048576	0.123		10
DMEM	24	arpe19	704T>C	C	40	2			13506	1035070	1048576	1.288	0	0
	25	arpe19	707A>G	C	40	2			1071	1047505	1048576	0.102	0	2
	28	arpe19	974T>C	C	40	2			9610	1038966	1048576	0.916	0	2
	29	arpe19	699A>T	C	40	2			18703	1029873	1048576	1.784	0	0
	210	arpe19	wildtype	N	40	2			44510	1004066	1048576	4.245	0	2
	211	arpe19	598C>T	N	40	2	Y	0.798	100	1048476	1048576	0.010		0
	41	arpe19	wildtype	C	40	2			161844	886732	1048576	15.435	1	4
	42	arpe19	248G>A	C	40	2			5808	1042768	1048576	0.554	0	-6
	54	arpe19	704T>C	C	40	2			2498	1046078	1048576	0.238	0	0
	55	arpe19	707A>G	C	40	2			361	1048215	1048576	0.034	0	-6
	56	arpe19	715G>A	C	40	2			3626	1044950	1048576	0.346	0	-8
	57	arpe19	598C>T	C	40	2	Y	3.646	5044	1043532	1048576	0.481		2
	58	arpe19	974T>C	C	40	2			35980	1012596	1048576	3.431	0	0
	59	arpe19	699A>T	C	40	2			57232	991344	1048576	5.458	1	2
	510	arpe19	wildtype	N	40	2			23156	1025420	1048576	2.208	0	4
	512	arpe19	gfp		40	2	Y	2.519	1203	1047373	1048576	0.115		6
							mean	2.238						

Table 6.12 Data used to produce estimates for the percentage of BEST1 positive pixels in confocal stacks taken of transfected ARPE-19 cells after 85-day incubation in XVIVO or DMEM medium. The average pixel intensity for the image stacks is shown for the negative control lines (in orange). Below the table is shown the mean of these values, 2.238. Based on this value a thresholding value of 12 out of 255 was chosen and the test stack projections were subjected to this thresholding. The percentage of pixels in the test images that passed this threshold were measured and used to produce an estimate for percentage positive pixels. Any that lay below the value calculated for the negative controls were defined as negative for BEST1 staining and excluded from further analysis (shown in red).

Chapter 7 - References

Ablonczy, Z. et al., 2011. Human Retinal Pigment Epithelium Cells as Functional Models for the RPE In Vivo. *Investigative Opthalmology & Visual Science*, 52(12), p.8614. Available at: http://iovs.arvojournals.org/article.aspx?doi=10.1167/iovs.11-8021.

Adams, J., 1883. Adams JE 1883.

Adijanto, J. et al., 2009. CO2-induced ion and fluid transport in human retinal pigment

epithelium. *The Journal of General Physiology*, 133(6), pp.603–622. Available at: http://www.jgp.org/lookup/doi/10.1085/jgp.200810169.

Adler, R. & Canto-Soler, M.V., 2007. Molecular mechanisms of optic vesicle development: Complexities, ambiguities and controversies. *Developmental Biology*, 305(1), pp.1–13.

Adli, M., 2018. The CRISPR tool kit for genome editing and beyond. *Nature Communications*, 9(1). Available at: http://dx.doi.org/10.1038/s41467-018-04252-2.

Ahmado, A. et al., 2011. Induction of differentiation by pyruvate and DMEM in the human retinal pigment epithelium cell line ARPE-19. *Investigative Ophthalmology and Visual Science*, 52(10), pp.7148–7159.

Akashi, M. et al., 2002. Control of Intracellular Dynamics of Mammalian Period Proteins by Casein Kinase I ε (CKI ε) and CKI in Cultured Cells. *Molecular and Cellular Biology*, 22(6), pp.1693–1703.

Akashi, M. & Nishida, E., 2000. Involvement of the MAP kinase cascade in resetting of the mammalian circadian clock. *Genes Dev*, 14(6), pp.645–649.

Akashi, M. & Takumi, T., 2005. The orphan nuclear receptor RORalpha regulates circadian transcription of the mammalian core-clock Bmal1. *Nature structural & molecular biology*, 12(5), pp.441–448.

Akhtar, R.A. et al., 2002. Circadian cycling of the mouse liver transcriptome, as revealed by cDNA microarray, is driven by the suprachiasmatic nucleus. *Current Biology*, 12(7), pp.540–550.

Allada, R. et al., 1998. A mutant Drosophila homolog of mammalian clock disrupts circadian rhythms and transcription of period and timeless. *Cell*, 93(5), pp.791–804.

Anderson, D.H. et al., 1980. Rod and Cone Disc Shedding in the Rhesus Monkey Retina : A Quantitative Study. *Exp. Eye Res.*, 30, pp.559–574.

Anderson, D.H. & Fisher, S.K., 1979. The relationship of primate foveal cones to the pigment epithelium. *Journal of Ultrasructure Research*, 67(1), pp.23–32.

Antoch, M.P. et al., 2013. Deficiency in PER proteins has no effect on the rate of spontaneous and radiation-induced carcinogenesis. *Cell Cycle*, 12(23), pp.3673–3680.

Antoch, M.P. et al., 2008. Disruption of the circadian clock due to the Clock mutation has discrete effects on aging and carcinogenesis. *Cell Cycle*, 7(9), pp.1197–1204.

Arden, G.B., Barrada, A. & Kelsey, J.H., 1962. New clinical test of retinal function based upon the standing potential of the eye. *British Journal of Ophthalmology*, 46(8), pp.449–467.

Arden, G.B. & Constable, P.A., 2006. The electro-oculogram. *Progress in Retinal and Eye Research*, 25(2), pp.207–248.

Argos, P., 1990. An investigation of oligopeptides linking domains in protein tertiary structures and possible candidates for general gene fusion. *Journal of Molecular Biology*, 211(4), pp.943–958.

Aschoff, J., 1983. Circadian control of body temperature. *Journal of Thermal Biology*, 8(1–2), pp.143–147.

Aymerich, M.S. et al., 2001. Evidence for pigment epithelium-derived factor receptors in the neural retina. *Invest Ophthalmol Vis Sci*, 42(13), pp.3287–3293. Available at: http://www.ncbi.nlm.nih.gov/entrez/query.fcgi?cmd=Retrieve&db=PubMed&dopt=Citation&list_uids=11726635.

Baca, W. et al., 1994. Dark adaptation in patients with Best vitelliform macular dystrophy. ,

pp.430–432.

Baek, A. et al., 2017. Autophagy and KRT8/keratin 8 protect degeneration of retinal pigment epithelium under oxidative stress. *Autophagy*, 13(2), pp.248–263. Available at: http://dx.doi.org/10.1080/15548627.2016.1256932.

Bainbridge, J.W.B. et al., 2008. Effect of gene therapy on visual function in Leber's congenital amaurosis. *New England Journal of Medicine*, 358(21), pp.2231–2239. Available at: http://www.nejm.org/doi/full/10.1056/NEJMoa0802268.

Bakall, B. et al., 2003. Expression and localization of bestrophin during normal mouse development. *Investigative Ophthalmology and Visual Science*, 44(8), pp.3622–3628.

Balsalobre, A. et al., 2000. Resetting of circadian time in peripheral tissues by glucocorticoid signaling. *Science*, 289(5488), pp.2344–2347.

Balsalobre, A., Damiola, F. & Schibler, U., 1998. A serum shock induces circadian gene expression in mammalian tissue culture cells. *Cell*, 93(6), pp.929–937.

Balsalobre, A., Marcacci, L. & Schibler, U., 2000. Multiple signaling pathways elicit circadian gene expression in cultured Rat-1 fibroblasts. *Current Biology*, 10(20), pp.1291–1294.

Ban, Y. & Rizzolo, L.J., 2000. Regulation of glucose transporters during development of the retinal pigment epithelium. *Developmental Brain Research*, 121(1), pp.89–95.

Bargiello, T.A., Jackson, F.R. & Young, M.W., 1984. Restoration of circadian behavioural rhythms by gene transfer in Drosophila. *Nature*, 312, pp.752–754.

Barrett, R.K. & Takahashi, J.S., 1995. Temperature compensation and temperature entrainment of the chick pineal cell circadian clock. *The Journal of neuroscience : the official journal of the Society for Neuroscience*, 15(8), pp.5681–5692.

Barro-Soria, R., Schreiber, R. & Kunzelmann, K., 2008. Bestrophin 1 and 2 are components of the Ca2+activated Cl-conductance in mouse airways. *Biochimica et Biophysica Acta - Molecular Cell Research*, 1783(10), pp.1993–2000.

Bee, L. et al., 2015. Nucleotide excision repair efficiency in quiescent human fibroblasts is modulated by circadian clock. *Nucleic Acids Research*, 43(4), pp.2126–2137.

Van Der Beek, E.M. et al., 1997. Evidence for a Direct Neuronal Pathway From the Suprachiasmatic Nucleus to the Gonadotropin-Releasing Hormone System : Combined Tracing and Light and Electron Microscopic Immunocytochemical Studies. , 579(April 1996), pp.569–579.

Bellingham, J. et al., 2002. Zebrafish melanopsin: Isolation, tissue localisation and phylogenetic position. *Molecular Brain Research*, 107(2), pp.128–136.

Berson, D.M., Dunn, F.A. & Takao, M., 2002. Photoransduction by retinal ganglion cells that set the circadian clock. *Science*, 295(557), pp.1070–1073. Available at: %5C%5CRoot%5Cgroups%5CElectronic Library%5C300040.

Berthet, C. et al., 2003. Cdk2 Knockout Mice Are Viable. *Current Biology*, 13(20), pp.1775–1785.

Best, F., 1905. Über eine hereditäre Muskelaffektion. Beiträge zur Vererbungslehre. *Z Augenheilkd*, 13, pp.199–212.

Bieler, J. et al., 2014. Robust synchronization of coupled circadian and cell cycle oscillators in single mammalian cells. *Molecular systems biology*, 10(7), p.739. Available at: http://www.ncbi.nlm.nih.gov/pubmed/25028488.

Birndorf, L.A. & Dawson, W.W., 1973. A normal electrooculogram in a patient with a typical

vitelliform macular lesion. *Invest Ophthalmol*, 12(11), pp.830–833.

Bitner, H. et al., 2011. A homozygous frameshift mutation in BEST1 causes the classical form of best disease in an autosomal recessive mode. *Investigative Ophthalmology and Visual Science*, 52(8), pp.5332–5338.

Blaauwgeers, H.G.T. et al., 1999. Polarized vascular endothelial growth factor secretion by human retinal pigment epithelium and localization of vascular endothelial growth factor receptors on the inner choriocapillaris: Evidence for a trophic paracrine relation. *American Journal of Pathology*, 155(2), pp.421–428.

Blair, N.P. et al., 1984. Autosomal Dominant vitreoretinochoroidopathy (ADVIRC). *Encyclopedia of Otolaryngology, Head and Neck …*, 68, pp.2–9. Available at: http://link.springer.com/content/pdf/10.1007/978-3-642-23499-6_200017.pdf.

Bloom, J. & Cross, F.R., 2007. Multiple levels of cyclin specificity in cell-cycle control. *Nature Reviews Molecular Cell Biology*, 8(2), pp.149–160.

Bolige, A., Kiyota, M. & Goto, K., 2005. Circadian rhythms of resistance to UV-C and UV-B radiation in Euglena as related to “escape from light” and “resistance to light.” *Journal of Photochemistry and Photobiology B: Biology*, 81(1), pp.43–54.

Booij, J.C. et al., 2010. The dynamic nature of Bruch’s membrane. *Progress in Retinal and Eye Research*, 29(1), pp.1–18. Available at: http://dx.doi.org/10.1016/j.preteyeres.2009.08.003.

Boon, C.J.F. et al., 2009. The spectrum of ocular phenotypes caused by mutations in the BEST1 gene. *Progress in Retinal and Eye Research*, 28(3), pp.187–205. Available at: http://dx.doi.org/10.1016/j.preteyeres.2009.04.002.

Brecher, R. & Bird, A.C., 1990. Adult vitelliform macular dystrophy. *Eye (Basingstoke)*, 4(1), pp.210–215.

Bressler, S.B., 2009. Introduction: Understanding the Role of Angiogenesis and Antiangiogenic Agents in Age-Related Macular Degeneration. *Ophthalmology*, 116(10 SUPPL.), pp.S1–S7. Available at: http://dx.doi.org/10.1016/j.ophtha.2009.06.045.

Brosh, R.M., 2013. DNA helicases involved in DNA repair and their roles in cancer cancer. *Nat Rev Cancer*, 18(8), pp.542–558.

Brown, M. et al., 2006. ISCEV Standard for Clinical Electro-oculography (EOG) 2006. *Documenta Ophthalmologica*, 113(3), pp.205–212.

Brown, S. a, 2014. Circadian clock-mediated control of stem cell division and differentiation: beyond night and day. *Development (Cambridge, England)*, 141(16), pp.3105–11. Available at: http://www.ncbi.nlm.nih.gov/pubmed/25100653.

Brown, S.A. et al., 2002. Rhythms of mammalian body temperature can sustain peripheral circadian clocks. *Current Biology*, 12(02), pp.1574–1583.

Brown, S.A., Ripperger, J. & Kadener, S., 2005. PERIOD1-Associated Proteins Modulate the Negative Limb of the Mammalian Circadian Oscillator. *Science*, 308, pp.693–697.

Buchholz, D. et al., 2009. Derivation of Functional Retinal Pigmented Epithelium from Induced Pluripotent Stem Cells. *Stem Cells*, 27, pp.2427–2434.

Buijs, R.M. et al., 2003. The suprachiasmatic nucleus balances sympathetic and parasympathetic output to peripheral organs through separate preautonomic neurons. *Journal of Comparative Neurology*, 464(1), pp.36–48.

Bullough, W.S., 1947. Mitotic activity in the adult male mouse, Mus musculus L. The diurnal cycles and their relation to waking and sleeping. *Proc R Soc B*, 135, pp.212–242.

Bunt-Milam, A.H. & Saari, J.C., 1983. Immunocytochemical localization of two retinoid-binding proteins in vertebrate retina. *Journal of Cell Biology*, 97(3), pp.703–712.

Burgess, R. et al., 2009. ADVIRC is caused by distinct mutations in BEST1 that alter pre-mRNA splicing. *Journal of Medical Genetics*, 46(9), pp.620–625. Available at: http://jmg.bmj.com/cgi/doi/10.1136/jmg.2008.059881.

Burgess, R. et al., 2008. Biallelic Mutation of BEST1 Causes a Distinct Retinopathy in Humans. *American Journal of Human Genetics*, 82(1), pp.19–31.

Burke, J.M. et al., 2007. Photobleaching of melanosomes from retinal pigment epithelium: I. Effects on protein oxidation. *Photochemistry and Photobiology*, 83(4), pp.920–924.

Busino, L. et al., 2007. SCFFbxl3 Controls the Oscillation of the Circadian Clock by Directing the Degradation of Cryptochrome Proteins. *Science*, 316(May), pp.900–905.

Calder, A. et al., 2012. Lengthened G1 Phase Indicates Differentiation Status in Human Embryonic Stem Cells. *Stem Cells and Development*, 22(2), p.120829080827006.

Caldwell, G.M. et al., 1999. Bestrophin gene mutations in patients with best vitelliform macular dystrophy. *Genomics*, 58(1), pp.98–101.

Caplan, M.J. et al., 1986. Intracellular sorting and polarized cell surface delivery of (Na+,K+)ATPase, an endogenous component of MDCK cell basolateral plasma membranes. *Cell*, 46(4), pp.623–631.

Cardone, L. et al., 2005. Circadian Clock Control by SUMOylation of BMAL1. *Science*, 309(5739), pp.1390–1394. Available at: http://www.sciencemag.org/cgi/doi/10.1126/science.1110689.

Carr, A.-J., Vugler, A., et al., 2009. Molecular characterization and functional analysis of phagocytosis by human embryonic stem cell-derived RPE cells using a novel human retinal assay. *Molecular vision*, 15(January), pp.283–95. Available at: http://www.pubmedcentral.nih.gov/articlerender.fcgi?artid=2635847&tool=pmcentrez&rendertype=abstract.

Carr, A.-J., Vugler, A.A., et al., 2009. Protective Effects of Human iPS-Derived Retinal Pigment Epithelium Cell Transplantation in the Retinal Dystrophic Rat. *PLoS ONE*, 4(12), p.e8152. Available at: http://dx.plos.org/10.1371/journal.pone.0008152.

Carr, A.-J.F. & Whitmore, D., 2005. Imaging of single light-responsive clock cells reveals fluctuating free-running periods. *Nature Cell Biology*, 7(3), pp.319–321. Available at: http://www.nature.com/doifinder/10.1038/ncb1232.

Carr, A.J.F. et al., 2006. Light reaches the very heart of the zebrafish clock. *Chronobiology International*, 23(1–2), pp.91–100.

Carter, D.A. et al., 2016. Mislocalisation of BEST1 in iPSC-derived retinal pigment epithelial cells from a family with autosomal dominant vitreoretinochoroidopathy (ADVIRC). *Scientific reports*, 6(August), p.33792. Available at: http://www.ncbi.nlm.nih.gov/pubmed/27653836%5Cnhttp://www.pubmedcentral.nih.gov/articlerender.fcgi?artid=PMC5031956.

Cashmore, A.R. et al., 1999. Cryptochromes: blue-light receptors for plants and animals. *Science*, 284(5415), pp.760–765. Available at: http://www.sciencemag.org/cgi/doi/10.1126/science.284.5415.760.

Catterall, W. a, 2000. Structure and Regulation of Voltage-Gated Ca2+ Channels. *Annual Reviews of Cell and Developmental Biology*, 16(521), p.555.

Cavallari, N. et al., 2011. A blind circadian clock in cavefish reveals that opsins mediate peripheral clock photoreception. *PLoS Biology*, 9(9).

Chaya, T. et al., 2017. Versatile functional roles of horizontal cells in the retinal circuit. *Scientific Reports*, 7(1), pp.1–15. Available at: http://dx.doi.org/10.1038/s41598-017-05543-2.

Chen, C.J. et al., 2016. Long-Term Macular Changes in the First Proband of Autosomal Dominant Vitreoretinochoroidopathy (ADVIRC) Due to a Newly Identified Mutation in BEST1. *Ophthalmic Genetics*, 37(1), pp.102–108. Available at: http://dx.doi.org/10.3109/13816810.2015.1039893.

Chen, S.T. et al., 2005. Deregulated expression of the PER1, PER2 and PER3 genes in breast cancers. *Carcinogenesis*, 26(7), pp.1241–1246.

Chen, X. et al., 2013. Targeted sequencing of 179 genes associated with hereditary retinal dystrophies and 10 candidate genes identifies novel and known mutations in patients with various retinal diseases. *Investigative ophthalmology & visual science*, 54(3), pp.2186–2197.

Chi, L. et al., 2017. TIMELESS contributes to the progression of breast cancer through activation of MYC. *Breast Cancer Research*, 19(1), pp.1–10.

Chien, L.-T. & Hartzell, H.C., 2008. Rescue of volume-regulated anion current by bestrophin mutants with altered charge selectivity. *The Journal of general physiology*, 132(5), pp.537–546.

Chien, L.-T., Zhang, Z.-R. & Hartzell, H.C., 2006. Single Cl^- Channels Activated by Ca^{2+} in *Drosophila* S2 Cells Are Mediated By Bestrophins. *The Journal of General Physiology*, 128(3), pp.247–259. Available at: http://www.jgp.org/lookup/doi/10.1085/jgp.200609581.

Clemett, R., 1991. Vitelliform dystrophy : long-term observations on New Zealand pedigrees. *Australian and New Zealand Journal of Ophthalmology*, 19(3), pp.221–227.

Cordeiro, S. et al., 2010. Heat-sensitive TRPV channels in retinal pigment epithelial cells: Regulation of VEGF-A secretion. *Investigative Ophthalmology and Visual Science*, 51(11), pp.6001–6008.

Da Cruz, L. et al., 2018. Phase 1 clinical study of an embryonic stem cell-derived retinal pigment epithelium patch in age-related macular degeneration. *Nature Biotechnology*, 36(4), pp.1–10. Available at: http://dx.doi.org/10.1038/nbt.4114.

D'Cruz, P.M. et al., 2000. Mutation of the receptor tyrosine kinase gene Mertk in the retinal dystrophic RCS rat. *Human molecular genetics*, 9(4), pp.645–651. Available at: http://www.ncbi.nlm.nih.gov/pubmed/10699188.

Daan, S. & Aschoff, J., 1975. Circadian rhythms of locomotor activity in captive birds and mammals: Their variations with season and latitude. *Oecologia*, 18(4), pp.269–316.

Dai, J. et al., 1998. Postmortem tracing reveals the organization of hypothalamic projections of the suprachiasmatic nucleus in the human brain. *Journal of Comparative Neurology*, 400(1), pp.87–102.

Damiola, F. et al., 2000. Restricted feeding uncouples circadian oscillators in peripheral tissues from the central pacemaker in the suprachiasmatic nucleus. *Genes and Development*, 14(23), pp.2950–2961.

Davidson, A.E. et al., 2010. A synonymous codon variant in two patients with autosomal recessive bestrophinopathy alters in vitro splicing of BEST1. *Molecular vision*, 16(December), pp.2916–2922. Available at: http://www.pubmedcentral.nih.gov/articlerender.fcgi?artid=3013070&tool=pmcentrez&rendertype=abstract.

Davidson, A.E. et al., 2011. Functional characterization of bestrophin-1 missense mutations associated with autosomal recessive bestrophinopathy. *Investigative Ophthalmology and Visual Science*, 52(6), pp.3730–3736.

Davidson, A.E. et al., 2009. Missense Mutations in a Retinal Pigment Epithelium Protein, Bestrophin-1, Cause Retinitis Pigmentosa. *American Journal of Human Genetics*, 85(5), pp.581–592. Available at: http://dx.doi.org/10.1016/j.ajhg.2009.09.015.

Davies, W.I.L. et al., 2011. Functional diversity of melanopsins and their global expression in the teleost retina. *Cellular and Molecular Life Sciences*, 68(24), pp.4115–4132.

Davis, S., Mirich, D.K. & Stevens, R.G., 2001. Night shift work, light at night and risk of breast cancer. *Journal of the National Cancer Institute*, 93(20), pp.1557–62.

Dawson, D.W., 1999. Pigment Epithelium-Derived Factor: A Potent Inhibitor of Angiogenesis. *Science*, 285(5425), pp.245–248. Available at: http://www.sciencemag.org/cgi/doi/10.1126/science.285.5425.245.

Dekens, M.P.S. et al., 2003. Light Regulates the Cell Cycle in Zebrafish. *Current Biology*, 13(23), pp.2051–2057.

Destici, E. et al., 2011. Mammalian cryptochromes impinge on cell cycle progression in a circadian clock-independent manner. *Cell Cycle*, 10(21), pp.3788–3797.

Dickson, V.K., Pedi, L. & Long, S.B., 2014. Structure and insights into the function of a Ca2+-activated Cl− channel. *Nature*, 516(7530), pp.213–218. Available at: http://dx.doi.org/10.1038/nature13913.

Diernfellner, A.C.R. et al., 2005. Molecular mechanism of temperature sensing by the circadian clock of Neurospora crassa. , pp.1968–1973.

Doumanov, J.A. et al., 2013. Disease-causing mutations in BEST1 gene are associated with altered sorting of bestrophin-1 protein. *International Journal of Molecular Sciences*, 14(7), pp.15121–15140.

Downey, M.J. et al., 2011. Extracting fluorescent reporter time courses of cell lineages from high-throughput microscopy at low temporal resolution. *PLoS ONE*, 6(12).

Dunn, K.C. et al., 1996. ARPE-19, a human retinal pigment epithelial cell line with differentiated properties. *Experimental eye research*, 62(2), pp.155–169.

Dyson, N., 1998. The regulation of E2F by pRB-family?proteins. *Genes and Development*, 12(617), pp.2245–2262.

Eckel-Mahan, K.L. et al., 2008. Circadian oscillation of hippocampal MAPK activity and cAMP: Implications for memory persistence. *Nature Neuroscience*, 11(9), pp.1074–1082.

Eide, E.J. et al., 2005. Control of Mammalian Circadian Rhythm by CKI ε -Regulated Proteasome-Mediated PER2 Degradation Control of Mammalian Circadian Rhythm by CKI ε -Regulated Proteasome-Mediated PER2 Degradation. *Molecular and cellular biology*, 25(7), pp.2795–2807.

Einthoven, W. & Jolly, W.A., 1908. the Form and Magnitude of the Electrical Response of the Eye To Stimulation By Light At Various Intensities. *Quarterly Journal of Experimental*

Physiology, 1(4), pp.373–416.

Eksandh, L. et al., 2001. Best's vitelliform macular dystrophy caused by a new mutation (Val89Ala) in the VMD2 gene. *Ophthalmic Genetics*, 22(2), pp.107–115. Available at: http://www.tandfonline.com/doi/full/10.1076/opge.22.2.107.2226.

Ellingsen, T., Bener, A. & Gehani, A.A., 2007. Study of shift work and risk of coronary events. *Journal of The Royal Society for the Promotion of Health*, 127(6), pp.265–267.

Esumi, N. et al., 2009. BEST1 expression in the retinal pigment epithelium is modulated by OTX family members. *Human Molecular Genetics*, 18(1), pp.128–141.

Esumi, N. et al., 2007. VMD2 promoter requires two proximal E-box sites for its activity in vivo and is regulated by the MITF-TFE family. *Journal of Biological Chemistry*, 282(3), pp.1838–1850.

Evans, M.J. & Kaufman, M.H., 1981. Establishment in culture of pluripotential cells from mouse embryos. *Nature*, 292(5819), pp.154–156.

Farkas, M.H. et al., 2013. Transcriptome analyses of the human retina identify unprecedented transcript diversity and 3.5 Mb of novel transcribed sequence via significant alternative splicing and novel genes. *BMC Genomics*, 14(1).

Fasler-Kan, E. et al., 2018. The Retinal Pigment Epithelial Cell Line (ARPE-19) Displays Mosaic Structural Chromosomal Aberrations. In N. S. Barteneva & I. A. Vorobjev, eds. *Cellular Heterogeneity: Methods and Protocols*. New York, NY: Springer New York, pp. 305–314. Available at: https://doi.org/10.1007/978-1-4939-7680-5_17.

Faundez, V. & Hartzell, H.C., 2004. Intracellular Chloride Channels: Determinants of Function in the Endosomal Pathway. *Science Signaling*, 2004(233), pp.re8-re8. Available at: http://stke.sciencemag.org/cgi/doi/10.1126/stke.2332004re8.

Feillet, C. et al., 2015. Coupling between the Circadian Clock and Cell Cycle Oscillators: Implication for Healthy Cells and Malignant Growth. *Frontiers in Neurology*, 6, p.96. Available at: http://www.pubmedcentral.nih.gov/articlerender.fcgi?artid=4426821&tool=pmcentrez&rendertype=abstract [Accessed May 12, 2015].

Feillet, C. et al., 2014. Phase locking and multiple oscillating attractors for the coupled mammalian clock and cell cycle. *Proceedings of the National Academy of Sciences of the United States of America*, 111(27), pp.9828–9833. Available at: http://www.pnas.org/content/early/2014/06/18/1320474111.abstract.html?etoc.

Felbor, U., Schilling, H. & Weber, B.H.F., 1997. Adult vitelliform macular dystrophy is frequently associated with mutations in the peripherin/RDS gene. *Human Mutation*, 10(4), pp.301–309.

Filipski, E. et al., 2009. Circadian disruption accelerates liver carcinogenesis in mice. *Mutation Research - Genetic Toxicology and Environmental Mutagenesis*, 680(1–2), pp.95–105.

Filipski, E. et al., 2004. Effects of Chronic Jet Lag on Tumor Progression in Mice. , (20), pp.7879–7885.

Filipski, E. et al., 2002. Host circadian clock as a control point in tumor progression. *Journal of the National Cancer Institute*, 94(9), pp.690–697.

Filipski, E., Li, X.M. & Lévi, F., 2006. Disruption of circadian coordination and malignant growth. *Cancer Causes and Control*, 17(4), pp.509–514.

Fischer, R.M. et al., 2013. Co-Expression of VAL- and TMT-Opsins Uncovers Ancient

Photosensory Interneurons and Motorneurons in the Vertebrate Brain. *PLoS Biology*, 11(6).

Fischmeister, R. & Hartzell, H.C., 2005. Volume sensitivity of the bestrophin family of chloride channels. *Journal of Physiology*, 562(2), pp.477–491.

Forsman, K. et al., 1992. The gene for Best's macular dystrophy is located at 11q13 in a Swedish family. *Clin Genet.*, 42(3), pp.156–159.

Fowles, C., Akhtar, M. & Cohen, P., 1989. Interplay of Phosphorylation and Dephosphorylation in Vision : Protein Phosphatases of Bovine Rod Outer Segments1 '. *Biochemistry*, 28(1987), pp.9385–9391.

Fu, L. et al., 2002. The Circadian Gene Period2 Plays an Important Role in Tumor Suppression and DNA-Damage Response In Vivo. *Cell*, 111(7), p.1055.

Gallemore, R.P., Hughes, B.A. & Miller, S.S., 1997. Retinal pigment epithelial transport mechanisms and their contributions to the electroretinogram. *Progress in Retinal and Eye Research*, 16(4), pp.509–566.

Gallemore, R.P. & Steinberg, R.H., 1989. Effects of DIDS on the chick retinal pigment epithelium. II. Mechanism of the light peak and other responses originating at the basal membrane. *J Neurosci*, 9(6), pp.1977–1984. Available at: http://www.ncbi.nlm.nih.gov/entrez/query.fcgi?cmd=Retrieve&db=PubMed&dopt=Citation&list_uids=2723762.

Gao, H. & Hollyfield, J.G., 1992. Aging of the human retina. Differential loss of neurons and retinal pigment epithelial cells. *Investigative ophthalmology & visual science*, 33(1), pp.1–17.

Gardner, J.M. et al., 1992. The mouse pink-eyed dilution gene; association with human Prader-Willi and Angelmann syndromes. *Science*, 257(5073), pp.1121–1124.

Gass, J.D., 1974. A clinicopathologic study of a peculiar foveomacular dystrophy. *Transactions of the American Ophthalmological Society*, 72, pp.139–156.

Gauger, M. a. & Sancar, A., 2005. Cryptochrome, circadian cycle, cell cycle checkpoints, and cancer. *Cancer Research*, 65(15), pp.6828–6834.

Gehrs, K.M. et al., 2006. Age-related macular degeneration - Emerging pathogenetic and therapeutic concepts. *Annals of Medicine*, 38(7), pp.450–471.

Gekakis, N. et al., 1998. Role of the CLOCK Protein in the Mammalian Circadian Mechanism. , 280(June), p.6.

George, L.F. et al., 2019. Ion channel contributions to wing development in Drosophila melanogaster. *G3: GENES, GENOMES, GENETICS*.

Gerth, C. et al., 2009. Detailed analysis of retinal function and morphology in a patient with autosomal recessive bestrophinopathy (ARB). *Documenta ophthalmologica*, 118(3), pp.239–246. Available at: http://link.springer.com/article/10.1007/s10633-008-9154-5.

Gery, S. et al., 2007. Epigenetic Silencing of the Candidate Tumor Suppressor Gene Per1 in Non-Small Cell Lung Cancer. *Clinical Cancer Research*, 13(5), pp.1399–1404. Available at: http://clincancerres.aacrjournals.org/cgi/doi/10.1158/1078-0432.CCR-06-1730.

Gery, S. et al., 2005. Transcription profiling of C / EBP targets identifies Per2 as a gene implicated in myeloid leukemia Transcription profiling of C / EBP targets identifies Per2 as a gene implicated in myeloid leukemia. *Blood*, 106(8), pp.2827–2836.

Godinho, S.I.H. et al., 2007. The After-Hours Mutant Reveals a Role for Fbxl3 in Determining

Mammalian Circadian Period. *Science*, 316(May), pp.897–900.

Goldberg, M.F. et al., 1989. Histopathologic Study of Autosomal Dominant Vitreoretinochoroidopathy: Peripheral Annular Pigmentary Dystrophy of the Retina. *Ophthalmology*, 96(12), pp.1736–1746. Available at: http://dx.doi.org/10.1016/S0161-6420(89)32663-7.

Gordon, E., Brautigan, D.L. & Zimmerman, A.L., 1992. Protein Phosphatases Modulate the Apparent Agonist Affinity of the Light-Regulated Ion Channel in Retinal Rods. *Neuron*, 9, pp.739–748.

Gottesfeld, J.M. & Forbes, D.J., 1997. Mitotic repression of the transcriptional machinery. *Trends in Biochemical Sciences*, 22(6), pp.197–202.

Graziotto, J.J. et al., 2011. Three gene-targeted mouse models of RNA splicing factor RP show late-onset RPE and retinal degeneration. *Investigative Ophthalmology and Visual Science*, 52(1), pp.190–198.

Gréchez-Cassiau, A. et al., 2008. The circadian clock component BMAL1 is a critical regulator of p21 WAF1/CIP1 expression and hepatocyte proliferation. *Journal of Biological Chemistry*, 283(8), pp.4535–4542.

Guillaumond, F. et al., 2005. Differential control of Bmal1 circadian transcription by REV-ERB and ROR nuclear receptors. *Journal of Biological Rhythms*, 20(5), pp.391–403.

Gundersen, D., Orlowski, J. & Rodriguez-Boulan, E., 1991. Apical polarity of Na,K-ATPase in retinal pigment epithelium is linked to a reversal of the Ankyrin-Fodrin submembrane cytoskeleton. *Journal of Cell Biology*, 112(5), pp.863–872.

Guziewicz, K.E. et al., 2011. Molecular consequences of BEST1 gene mutations in canine multifocal retinopathy predict functional implications for human bestrophinopathies. *Investigative Ophthalmology and Visual Science*, 52(7), pp.4497–4505.

Haeseleer, F. et al., 1998. Molecular characterization of a novel short-chain dehydrorgenase/reductase that reduces all-trans-retinal. *J. Biol. Chem.*, 21(34), pp.21790–21799.

Hagiwara, S. et al., 2002. Circadian Gating of Photoinduction of Commitment to Cell-cycle Transitions in Relation to Photoperiodic Control of Cell Reproductiopn in Euglena. *Photochemistry and Photobiology*, 76(1), pp.105–115.

Hamann, S. et al., 2003. Cotransport of H+, lactate, and H2O in porcine retinal pigment epithelial cells. *Experimental Eye Research*, 76(4), pp.493–504.

Hamblen-Coyle, M.J. et al., 1992. Behavior of period-altered circadian rhythm mutants of Drosophila in light: Dark cycles (Diptera: Drosophilidae). *Journal of Insect Behavior*, 5(4), pp.417–446.

Hamel, C.P. et al., 1993. Molecular cloning and expression of RPE65, a novel retinal pigment epithelium-specific microsomal protein that is post-transcriptionally regulated in vitro. *Journal of Biological Chemistry*, 268(21), pp.15751–15757.

Hammerton, R.W. et al., 1991. Mechanism for regulating cell surface distributuion of Na+, K+-ATPase in polarized epithelial cells. *Science*, 254, pp.847–850.

Hanahan, D., Weinberg, R.A. & Francisco, S., 2000. The Hallmarks of Cancer Review University of California at San Francisco. , 100, pp.57–70.

Hansen, L.L., van den Burg, H.A. & van Ooijen, G., 2017. Sumoylation Contributes to Timekeeping and Temperature Compensation of the Plant Circadian Clock. *Journal of Biological*

Rhythms, 32(6), pp.560–569.

Harper, J.W. et al., 1993. The p21 Cdk-interacting protein Cip1 is a potent inhibitor of G1 cyclin-dependent kinases. *Cell*, 75(4), pp.805–816.

Hartong, D.T., Berson, E.L. & Dryja, T.P., 2006. Retinitis pigmentosa. *Lancet*, 368(9549), pp.1795–1809.

Hartzell, C., Qu, Z. & Chien, L., 2005. Looking Chloride Channels Straight in the Eye : Best Disease May Be a Model. *PHYSIOLOGY*, 20, pp.292–302.

Hartzell, H.C. et al., 2008. Molecular Physiology of Bestrophins: Multifunctional Membrane Proteins Linked to Best Disease and Other Retinopathies. *Physiological Reviews*, 88(2), pp.639–672. Available at: http://physrev.physiology.org/cgi/doi/10.1152/physrev.00022.2007.

Hastings, J.W. & Sweeney, B.M., 1957. On the Mechanism of Temperature Independence in a Biological Clock. *Proceedings of the National Academy of Sciences of the United States of America*, 43(9), pp.804–811.

Hattar, S. et al., 2003. Melanopsin and rod—cone photoreceptive systems account for all major accessory visual functions in mice. *Nature*, 424(6944), pp.76–81.

Haus, E. & Smolensky, M., 2006. Biological clocks and shift work: Circadian dysregulation and potential long-term effects. *Cancer Causes and Control*, 17(4), pp.489–500.

Hergott, G.J., Sandig, M. & Kainins, V.I., 1994. Cytoskeletal organization of retinal pigment epithelial cells during repair of small wounds in organ culture. *Invest. Ophthalmol. Vis. Sci.*, 35(4), p.1764.

Hirami, Y. et al., 2009. Generation of retinal cells from mouse and human induced pluripotent stem cells. *Neuroscience Letters*, 458(3), pp.126–131.

Hirayama, J. et al., 2005. Common pathways in circadian and cell cycle clocks: Light-dependent activation of Fos/AP-1 in zebrafish controls CRY-1a and WEE-1. *Proceedings of the National Academy of Sciences*, 102(29), pp.10194–10199. Available at: http://www.pnas.org/cgi/doi/10.1073/pnas.0502610102.

Hirayama, J., Cho, S. & Sassone-Corsi, P., 2007. Circadian control by the reduction/oxidation pathway: catalase represses light-dependent clock gene expression in the zebrafish. *Proceedings of the National Academy of Sciences of the United States of America*, 104(40), pp.15747–52. Available at: http://www.ncbi.nlm.nih.gov/pubmed/17898172%5Cnhttp://www.pubmedcentral.nih.gov/articlerender.fcgi?artid=PMC2000381.

Holmes, M.G. & Klein, W.H., 1986. Photocontrol of Dark Circadian Rhythms in Stomata of Phaseolus vulgaris L. *Plant Physiology*, 82(1), pp.28–33.

Van Der Horst, G.T.J. et al., 1999. Mammalian Cry1 and Cry2 are essential for maintenance of circadian rhythms. *Nature*, 398(6728), pp.627–630.

Hu, D.N., Simon, J.D. & Sarna, T., 2008. Role of ocular melanin in ophthalmic physiology and pathology. *Photochemistry and Photobiology*, 84(3), pp.639–644.

Hu, J.G. et al., 1994. Localization of NaK ATPase on cultured human retinal pigment epithelium. *Invest Ophthalmol Vis Sci*, 35(10), pp.3582–3588. Available at: http://www.ncbi.nlm.nih.gov/entrez/query.fcgi?cmd=Retrieve&db=PubMed&dopt=Citation&list_uids=8088949.

Hua, H. et al., 2006. Circadian gene mPer2 overexpression induces cancer cell apoptosis. *Cancer*

Science, 97(7), pp.589–596.

Hua, J. et al., 2018. MITF acts as an anti-oxidant transcription factor to regulate mitochondrial biogenesis and redox signaling in retinal pigment epithelial cells. *Experimental Eye Research*, 170(January), pp.138–147. Available at: https://doi.org/10.1016/j.exer.2018.02.023.

Huang, J., Possin, D.E. & Saari, J.C., 2009. Localizations of visual cycle components in retinal pigment epithelium. *Molecular vision*, 15(December 2008), pp.223–234.

Hughes, M.E. et al., 2012. Brain-specific rescue of Clock reveals system-driven transcriptional rhythms in peripheral tissue. *PLoS Genetics*, 8(7).

Idda, M.L. et al., 2012. Circadian timing of injury-induced cell proliferation in zebrafish. *PLoS ONE*, 7(3).

Ishikawa, K. & Shimazu, T., 1980. Circadian rhythm of liver glycogen metabolism in rats: Effects of hypothalamic lesions. *American Journal of Physiology - Endocrinology and Metabolism*, 1(1).

Iyer, R. et al., 2002. A biological role for prokaryotic ClC chloride channels. *Nature*, 419(October), pp.715–718.

Jeffrey D. Plautz, Maki Kaneko, Jeffrey C. Hall, S.A.K., 1997. Independent Photoreceptive Circadian Clocks Throughout Drosophila. *Science*, 278(5343), pp.1632–1635. Available at: http://www.sciencemag.org/cgi/doi/10.1126/science.278.5343.1632.

Jentsch, T.J.J. et al., 2002. Molecular structure and physiological function of chloride channels. *Physiological Reviews*, 82(2), p.503.

Jin, M. et al., 2005. Rpe65 is the retinoid isomerase in bovine retinal pigment epithelium. *Cell*, 122(3), pp.449–459.

Johnson, A.A. et al., 2013. Differential effects of best disease causing missense mutations on bestrophin-1 trafficking. *Human Molecular Genetics*, 22(23), pp.4688–4697.

Johnson, A.A. et al., 2014. Disease-causing mutations associated with four bestrophinopathies exhibit disparate effects on the localization, but not the oligomerization, of Bestrophin-1. *Exp Eye Res*, 121, pp.74–85.

Johnson, C.H., 1999. *Forty years of PRCs - What have we learned?*,

Kaeffer, B. & Pardini, L., 2005. Clock genes of Mammalian cells: practical implications in tissue culture. *I Vitro Cell. Dev. Biol - Animals*, 41(10), pp.311–320.

Kalsbeek, A. et al., 2006. SCN outputs and the hypothalamic balance of life. *Journal of Biological Rhythms*, 21(6), pp.458–469.

Karakashian, M.W., 1968. The Rhythm of Mating in Paramecium aurelia, Syngen 3'. *J. Cell. Physiol.*, 71, pp.197–210.

Karlin, A. & Akabas, M.H., 1998. Substituted-cysteine accessibility method. *Methods in Enzymology*, 293(1986), pp.123–145.

Karlsson, B., Knutsson, A. & Lindahl, B., 2001. Is there an association between shift work and having a metabolic syndrome? Results from a population based study of 27,485 people. *Occupational and environmental medicine*, 58(11), pp.747–52.

Karlsson, B.H. et al., 2003. Metabolic disturbances in male workers with rotating three-shift work. Result of the WOLF study. *International Archives of Occupational and Environmental Health*, 76(6), pp.424–430.

Kaufman, S.J. et al., 1982. Autosomal dominant vitreoretinochoroidopathy. *Archives of Ophthalmology*, 100(2), pp.272–278. Available at: http://dx.doi.org/10.1001/archopht.1982.01030030274008.

Kellner, U. et al., 1998. Autosomal dominant vitreoretinochoroidopathy with normal electrooculogram in a German family. *Graefe's Archive for Clinical and Experimental Ophthalmology*, 236(2), pp.109–114.

Kevany, B. & Palczewski, K., 2010. Phagocytosis of retinal rod and cone photoreceptors. *Physiology*, 25(1), pp.8–15. Available at: http://scholar.google.com/scholar?hl=en&btnG=Search&q=intitle:Phagocytosis+of+Retinal+Rod+and+Cone+Photoreceptors#0.

Kidd, P.B., Young, M.W. & Siggia, E.D., 2015. Temperature compensation and temperature sensation in the circadian clock. *Proceedings of the National Academy of Sciences*, 112(46), pp.E6284–E6292. Available at: http://www.pnas.org/lookup/doi/10.1073/pnas.1511215112.

Kiessling, S. et al., 2017. Enhancing circadian clock function in cancer cells inhibits tumor growth. *BMC Biology*, 15(1), p.13. Available at: http://bmcbiol.biomedcentral.com/articles/10.1186/s12915-017-0349-7.

Kim, D. et al., 2013. TopHat2: accurate alignment of transcriptomes in the presence of insertions, deletions and gene fusions. *Genome Biology*, 14(4).

King, D.P. et al., 1997. Positional cloning of the mouse circadian clock gene. *Cell*, 89(4), pp.641–53. Available at: http://www.ncbi.nlm.nih.gov/pubmed/9160755%5Cnhttp://www.pubmedcentral.nih.gov/articlerender.fcgi?artid=PMC3815553.

Klimanskaya, I. et al., 2004. Derivation and Comparative Assessment of Retinal Pigment Epithelium from Human Embryonic Stem Cells Using Transcriptomics. *Cloning and Stem Cells*, 6(3), pp.217–245. Available at: http://www.liebertonline.com/doi/abs/10.1089/clo.2004.6.217.

Konari, K. et al., 1995. Development of the blood-retinal barrier in vitro: Formation of tight junctions as revealed by occludin and ZO-1 correlates with the barrier function of chick retinal pigment epithelial cells. *Experimental Eye Research*, 61(1), pp.99–108.

Kondo, T. et al., 1993. Circadian rhythms in prokaryotes: luciferase as a reporter of circadian gene expression in cyanobacteria. *Proceedings of the National Academy of Sciences*, 90(12), pp.5672–5676. Available at: http://www.pnas.org/cgi/doi/10.1073/pnas.90.12.5672.

Kondratov, R. V et al., 2006. Early aging and age-related pathologies in mice deficient in BMAL1 , the core component of the circadian clock. *GENES & DEVELOPMENT*, 20, pp.1868–1873.

Konopka, R.J. & Benzer, S., 1971. Clock mutants of Drosophila melanogaster. *Proceedings of the National Academy of Sciences of the United States of America*, 68(9), pp.2112–6. Available at: http://www.pubmedcentral.nih.gov/articlerender.fcgi?artid=389363&tool=pmcentrez&rendertype=abstract.

Konrad, M. et al., 2006. Mutations in the Tight-Junction Gene Claudin 19 (CLDN19) Are Associated with Renal Magnesium Wasting, Renal Failure, and Severe Ocular Involvement. *The American Journal of Human Genetics*, 79(5), pp.949–957.

Kornmann, B. et al., 2001. Analysis of circadian liver gene expression by ADDER, a highly sensitive method for the display of differentially expressed mRNAs. *Nucleic acids research*, 29(11),

pp.E51-1. Available at: http://www.ncbi.nlm.nih.gov/pubmed/11376163.

Kornmann, B. et al., 2007. System-driven and oscillator-dependent circadian transcription in mice with a conditionally active liver clock. *PLoS Biology*, 5(2), pp.0179–0189.

Kowalska, E. et al., 2013. NONO couples the circadian clock to the cell cycle. *Proceedings of the National Academy of Sciences of the United States of America*, 110(5), pp.1592–9. Available at: http://www.pubmedcentral.nih.gov/articlerender.fcgi?artid=3562797&tool=pmcentrez&rendertype=abstract.

Kozak, M., 1987. An analysis of 5'-noncoding sequences from 699 vertebrate messenger RNAs. *Nucleic Acids Research*, 15(20), pp.8125–8148.

Krämer, F. et al., 2000. Mutations in the VMD2 gene are associated with juvenile-onset vitelliform macular dystrophy (Best disease) and adult vitelliform macular dystrophy but not age-related macular degeneration. *European Journal of Human Genetics*, 8(4), pp.286–292.

Kume, K. et al., 1999. mCRY1 and mCRY2 are essential components of the negative limb of the circadian clock feedback loop. *Cell*, 98(2), pp.193–205.

Kuo, Y.-H. et al., 2014. Effects of alternative splicing on the function of bestrophin-1 calcium-activated chloride channels. *The Biochemical journal*, 458(3), pp.575–83. Available at: http://www.pubmedcentral.nih.gov/articlerender.fcgi?artid=4145631&tool=pmcentrez&rendertype=abstract.

Kurabayashi, N. et al., 2010. DYRK1A and Glycogen Synthase Kinase 3 , a Dual-Kinase Mechanism Directing Proteasomal Degradation of CRY2 for Circadian Timekeeping. *Molecular and Cellular Biology*, 30(7), pp.1757–1768. Available at: http://mcb.asm.org/cgi/doi/10.1128/MCB.01047-09.

Kurosawa, G. & Iwasa, Y., 2005. Temperature compensation in circadian clock models. *Journal of Theoretical Biology*, 233(4), pp.453–468.

Kuznetsova, A. V. et al., 2014. Cell Models to Study Regulation of Cell Transformation in Pathologies of Retinal Pigment Epithelium. *Journal of Ophthalmology*, 2014, pp.1–18. Available at: http://www.hindawi.com/journals/joph/2014/801787/.

Lafaut, B. et al., 2001. Clinical and electrophysiological findings in autosomal dominant vitreoretinochoroidopathy: Report of a new pedigree. *Graefe's Archive for Clinical and Experimental Ophthalmology*, 239(8), pp.575–582.

Lahti, T.A. et al., 2008. Night-time work predisposes to non-Hodgkin lymphoma. *International Journal of Cancer*, 123(9), pp.2148–2151.

Lamia, K.A. et al., 2009. AMPK Regulates the Circadian Clock by Cryptochrome Phosphorylation and Degradation. *Science*, 326(5951), pp.437–440.

Landers, A., Alvarez, A. & Bridges, C.D., 1984. Purification Synthesized and Characterization of a Retinol-binding and Secreted by Bovine Neural Retina * Glycoprotein. , 259(10), pp.6534–6542.

Lane, A. et al., 2014. Engineering Efficient Retinal Pigment Epithelium Differentiation From Human Pluripotent Stem Cells. *Stem Cells Translational Medicine*, 3, pp.1295–1304.

Laranjeiro, R. et al., 2018. Circadian Clock Synchronization of the Cell Cycle in Zebrafish Occurs through a Gating Mechanism Rather Than a Period-phase Locking Process. *Journal of Biological Rhythms*, XX(X), p.074873041875558. Available at:

http://journals.sagepub.com/doi/10.1177/0748730418755583.

Laranjeiro, R. et al., 2013. Cyclin-dependent kinase inhibitor p20 controls circadian cell-cycle timing. *Proceedings of the National Academy of Sciences of the United States of America*, 110(17), pp.6835–40. Available at: http://www.pubmedcentral.nih.gov/articlerender.fcgi?artid=3637774&tool=pmcentrez&rendertype=abstract.

Lee, C.S. et al., 2015. A novel BEST1 mutation in autosomal recessive bestrophinopathy. *Investigative Ophthalmology and Visual Science*, 56(13), pp.8141–8150.

Lee, S. et al., 2010. Disrupting circadian homeostasis of sympathetic signaling promotes tumor development in mice. *PLoS ONE*, 5(6).

Lévi, F. et al., 2007. Cross-talks between circadian timing system and cell division cycle determine cancerbiology and therapeutics. *CSH Symposio*, 72, pp.465–475.

Li, X.M. et al., 2013. A circadian clock transcription model for the personalization of cancer chronotherapy. *Cancer Research*, 73(24), pp.7176–7188.

Lian, X. et al., 2014. Cell-Cycle Control of Bivalent Epigenetic Domains Regulates the Exit from Pluripotency. *Stem Cell Reports*, 3, pp.323–336.

Liao, J.L. et al., 2010. Molecular signature of primary retinal pigment epithelium and stem-cell-derived RPE cells. *Human Molecular Genetics*, 19(21), pp.4229–4238.

Liskay, R.M., 1977. Absence of a measurable G2 phase in two Chinese hamster cell lines. *Proceedings of the National Academy of Sciences of the United States of America*, 74(4), pp.1622–5. Available at: http://www.pubmedcentral.nih.gov/articlerender.fcgi?artid=430843&tool=pmcentrez&rendertype=abstract.

Liu, Y. et al., 1998. How temperature changes reset a circadian oscillator. *Science*, 281(5378), pp.825–829.

Livak, K.J. & Schmittgen, T.D., 2001. Analysis of Relative Gene Expression Data Using Real- Time Quantitative PCR and the 2 Χ ⬡⬡ C T Method. *Methods*, 25(4), pp.402–408.

López-Olmeda, J.F., Madrid, J.A. & Sánchez-Vázquez, F.J., 2006. Light and temperature cycles as zeitgebers of zebrafish (Danio rerio) circadian activity rhythms. *Chronobiology International*, 23(3), pp.537–550.

Lotery, A.J. et al., 2000. Allelic Variation in the VMD2 Gene in Best Disease and Age-Related Macular Degeneration. *Investigative Ophthalmology & Visual Science*, 41(6), pp.1291–1296.

Low, S. et al., 2011. Autosomal dominant Best disease with an unusual electrooculographic light rise and risk of angle-closure glaucoma: a clinical and molecular genetic study. *Molecular vision*, 17(March 2010), pp.2272–2282.

Lowery, P. et al., 2000. Positional synthetic cloning and functional charicterization of the mammalian circadian mutation tau. *Science*, 288(5465), pp.483–491.

Lowrey, P.L. & Takahashi, J.S., 2004. MAMMALIAN CIRCADIAN BIOLOGY: Elucidating Genome-Wide Levels of Temporal Organization. *Annual Review of Genomics and Human Genetics*, 5(1), pp.407–441. Available at: http://www.annualreviews.org/doi/10.1146/annurev.genom.5.061903.175925.

Lucas, R.J. et al., 2003. Diminished Pupillary Light Reflex at High Irradiances in Melanopsin -

Knockout Mice. *Science*, 299(5604), pp.245–247.

Lund, R.D. et al., 2001. Subretinal transplantation of genetically modified human cell lines attenuates loss of visual function in dystrophic rats. *Proceedings of the National Academy of Sciences of the United States of America*, 98(17), pp.9942–9947.

Luo, Y. et al., 2012. Deregulated expression of Cry1 and Cry2 in human gliomas. *Asian Pacific Journal of Cancer Prevention*, 13(11), pp.5725–5728.

Luo, Y. et al., 2006. Effects of culture conditions on heterogeneity and the apical junctional complex of the ARPE-19 cell line. *Investigative Ophthalmology and Visual Science*, 47(8), pp.3644–3655.

Ma, J.-X. et al., 2005. RPE65 is the isomerohydrolase in the retinoid visual cycle. *Investigative Ophthalmology & Visual Science*, 46(E-Abstract), p.1057.

Maguire, A.M. et al., 2008. Safety and Efficacy of Gene Transfer for Leber's Congenital Amaurosis. *New England Journal of Medicine*, 358(21), pp.2240–2248. Available at: http://www.nejm.org/doi/abs/10.1056/NEJMoa0802315.

Malumbres, M. et al., 2004. Mammalian cells cycle without the D-type cyclin-dependent kinases Cdk4 and Cdk6. *Cell*, 118(4), pp.493–504.

Maminishkis, A. et al., 2006. Confluent Monolayers of Cultured Human Fetal Retinal Pigment Epithelium Exhibit Morphology and Physiology of Native Tissue. *Invest Ophthalmol Vis Sci.*, 47(8), pp.3612–3624.

Manila, N.G. et al., 2018. Insulin-like growth factor I receptor regulates the radiation-induced G2/M checkpoint in HeLa cells. *Biochemical and Biophysical Research Communications*, pp.1–7. Available at: https://linkinghub.elsevier.com/retrieve/pii/S0006291X18317625.

Maniscalco, M. et al., 2014. Light-dependent expression of four cryptic archaeal circadian gene homologs. , 5(March), pp.1–10.

Marmorstein, a D. et al., 2000. Bestrophin, the product of the Best vitelliform macular dystrophy gene (VMD2), localizes to the basolateral plasma membrane of the retinal pigment epithelium. *Proceedings of the National Academy of Sciences of the United States of America*, 97(23), pp.12758–12763.

Marmorstein, A.D., 2001. The polarity of the retinal pigment epithelium. *Traffic (Copenhagen, Denmark)*, 2(12), pp.867–872.

Marmorstein, A.D., Cross, H.E. & Peachey, N.S., 2009. Functional roles of bestrophins in ocular epithelia. *Progress in Retinal and Eye Research*, 28(3), pp.206–226. Available at: http://dx.doi.org/10.1016/j.preteyeres.2009.04.004.

Marmorstein, L.Y. et al., 2002. Bestrophin Interacts Physically and Functionally with Protein Phosphatase 2A*. , 277(34), pp.30591–30597.

Marmorstein, L.Y. et al., 2006. The Light Peak of the Electroretinogram Is Dependent on Voltage-gated Calcium Channels and Antagonized by Bestrophin (Best-1). *The Journal of General Physiology*, 127(5), pp.577–589. Available at: http://www.jgp.org/lookup/doi/10.1085/jgp.200509473.

Marquardt, A. et al., 1998. Mutations in a novel gene, VMD2, encoding a protein of unknown properties cause juvenile-onset vitelliform macular dystrophy (Best's disease). *Human Molecular Genetics*, 7(9), pp.1517–1525.

Martin, G.R., 1981. Isolation of a pluripotent cell line from early mouse embryos cultured in medium conditioned by teratocarcinoma stem cells. *Proceedings of the National Academy*

of Sciences, 78(12), pp.7634–7638. Available at: http://www.pnas.org/cgi/doi/10.1073/pnas.78.12.7634.

Martínez-Morales, J.R. et al., 2003. OTX2 activates the molecular network underlying retina pigment epithelium differentiation. *Journal of Biological Chemistry*, 278(24), pp.21721–21731.

Matson, Ja.P. & Cook, J.G., 2017. Cell cycle proliferation decisions: the impact of single cell analyses. *FEBS J.*, 284(3), pp.362–375.

Matsuo, T. et al., 2003. Control mechanism of the circadian clock for timing of cell division in vivo. *Science (New York, N.Y.)*, 302(5643), pp.255–259.

Maw, M.A. et al., 1997. Mutation of the gene encoding cellular retinaldehyde-binding protein in autosomal recessive retinitis pigmentosa. *Nature Genetics*, 17(2), p.200.

Mazzoni, F., Safa, H. & Finnemann, S.C., 2014. Understanding photoreceptor outer segment phagocytosis: Use and utility of RPE cells in culture. *Experimental Eye Research*, 126, pp.51–60.

McCarthy, D.J., Chen, Y. & Smyth, G.K., 2012. Differential expression analysis of multifactor RNA-Seq experiments with respect to biological variation. *Nucleic Acids Research*, 40(10), pp.4288–4297.

Megdal, S.P. et al., 2005. Night work and breast cancer risk: A systematic review and meta-analysis. *European Journal of Cancer*, 41(13), pp.2023–2032.

Mellman, I., 1992. The importance of being acid: the role of acidification in intracellular membrane traffic. *The Journal of experimental biology*, 172, pp.39–45.

Meunier, I. et al., 2011. Systematic screening of BEST1 and PRPH2 in juvenile and adult vitelliform macular dystrophies: A rationale for molecular analysis. *Ophthalmology*, 118(6), pp.1130–1136. Available at: http://dx.doi.org/10.1016/j.ophtha.2010.10.010.

Meyer, J.S. et al., 2009. Modeling early retinal development with human embryonic and induced pluripotent stem cells. *Proceedings of the National Academy of Sciences of the United States of America*, 106(39), pp.16698–16703.

Milenkovic, A. et al., 2015. Bestrophin 1 is indispensable for volume regulation in human retinal pigment epithelium cells. *Proceedings of the National Academy of Sciences*, 112(20), pp.E2630–E2639. Available at: http://www.pnas.org/lookup/doi/10.1073/pnas.1418840112.

Milenkovic, V.M., Röhrl, E., et al., 2011. Disease-associated missense mutations in bestrophin-1 affect cellular trafficking and anion conductance. *Journal of Cell Science*, 124(17), pp.2988–2996. Available at: http://jcs.biologists.org/lookup/doi/10.1242/jcs.085878.

Milenkovic, V.M. et al., 2007. Insertion and topology of normal and mutant bestrophin-1 in the endoplasmic reticulum membrane. *Journal of Biological Chemistry*, 282(2), pp.1313–1321.

Milenkovic, V.M., Krejcova, S., et al., 2011. Interaction of bestrophin-1 and Ca2+ channel β-subunits: Identification of new binding domains on the bestrophin-1 C-terminus. *PLoS ONE*, 6(4).

Millar-Craig, M.W., Bishop, C.N. & Raftery, E.B., 1978. Circadian Variation of Blood-Pressure. *The Lancet*, 311(8068), pp.795–797.

Mohawk, jennifer A., Green, C.B. & Takahashi, J.S., 2012. Central and Peripheral Circadian Clocks in Mammals. *Annu Rev Neurosci*, 35, pp.445–462.

Moore, R.Y. & Eichler, V.B., 1972. Loss of a circadian adrenal corticosterone rhythm following suprachiasmatic lesions in the rat. *Brain Research*, 42, pp.201–206.

Moore, R.Y. & Lenn, N.J., 1972. A Retinohypothalamic Projection in the Rat. *J. Comp. Neur.*, 146, pp.1–14.

Morgan, D.O., 1997. CYCLIN-DEPENDENT KINASES : Engines , Clocks , and Microprocessors. *Annu. Rev. Cell Dev. Biol*, 13, pp.261–291.

Mori, T., Binder, B. & Johnson, C.H., 1996. Circadian gating of cell division in cyanobacteria growing with average doubling times of less than 24 hours. *Proceedings of the National Academy of Sciences of the United States of America*, 93(19), pp.10183–10188.

Mormont, M.C. & Levi, F., 2003. Cancer chronotherapy: Principles, applications, and perspectives. *Cancer*, 97(1), pp.155–169.

Moshfegh, Y. et al., 2016. BESTROPHIN1 mutations cause defective chloride conductance in patient stem cell-derived RPE. *Human Molecular Genetics*, 25(13), pp.2672–2680.

Moutsaki, P. et al., 2003. Teleost multiple tissue (tmt) opsin: A candidate photopigment regulating the peripheral clocks of zebrafish? *Molecular Brain Research*, 112(1–2), pp.135–145.

Mrosovsky, N., 1999. Masking: History, definitions, and measurement. *Chronobiology International*, 16(4), pp.415–429.

Mteyrek, A. et al., 2016. Clock gene Per2 as a controller of liver carcinogenesis. *Oncotarget*.

Mukherjee, P.K. et al., 2007. Neurotrophins enhance retinal pigment epithelial cell survival through neuroprotectin D1 signaling. *Proceedings of the National Academy of Sciences*, 104(32), pp.13152–13157. Available at: http://www.pnas.org/cgi/doi/10.1073/pnas.0705949104.

Müller, C. et al., 2014. CaV1.3 L-type channels, maxiK Ca2+-dependent K+channels and bestrophin-1 regulate rhythmic photoreceptor outer segment phagocytosis by retinal pigment epithelial cells. *Cellular Signalling*, 26(5), pp.968–978. Available at: http://dx.doi.org/10.1016/j.cellsig.2013.12.021.

Mullins, R.F. et al., 2007. Differential Macular and Peripheral Expression of Bestrophin in Human Eyes and Its Implication for Best Disease. *Investigative Ophthalmology & Visual Science*, 48(7), pp.3372–3380.

Mullins, R.F. et al., 2005. Late development of vitelliform lesions and flecks in a patient with best disease: Clinicopathologic correlation. *Archives of Ophthalmology*, 123(11), pp.1588–1594.

Muniz, A. et al., 2007. A novel cone visual cycle in the cone-dominated retina. *Experimental Eye Research*, 85(2), pp.175–184.

Muñiz, A. et al., 2014. Retinoid uptake, processing, and secretion in human iPSRPE support the visual cycle. *Investigative Ophthalmology and Visual Science*, 55(1), pp.198–209.

Nabi, I.R. et al., 1993. Immortalization of polarized rat retinal pigment epithelium. *J Cell Sci*, 104 (Pt 1, pp.37–49. Available at: http://www.ncbi.nlm.nih.gov/pubmed/8383696.

Nagoshi, E. et al., 2004. Circadian gene expression in individual fibroblasts: cell-autonomous and self-sustained oscillators pass time to daughter cells. *Cell*, 119(5), pp.693–705. Available at: http://www.ncbi.nlm.nih.gov/pubmed/15550250 [Accessed June 22, 2015].

Nakajima, M. et al., 2005. Reconstitution of circadian oscillation of cyanobacterial KaiC. , 308(April), pp.414–416.

Neussert, R. et al., 2010. The presence of bestrophin-1 modulates the Ca2+ recruitment from Ca2+ stores in the ER. *Pflügers Archiv - European Journal of Physiology*, 460(1), pp.163–175. Available at: https://doi.org/10.1007/s00424-010-0840-2.

O'Neill, J.S. et al., 2011. Circadian rhythms persist without transcription in a eukaryote. *Nature*, 469(7331), pp.554–558. Available at: http://dx.doi.org/10.1038/nature09654.

O'Neill, J.S. & Reddy, A.B., 2011. Circadian clocks in human red blood cells. *Nature*, 469(7331), pp.498–503. Available at: http://dx.doi.org/10.1038/nature09702.

Ogryzko, V. V, Wong, P. & Howard, B.H., 1997. WAF1 retards S-phase progression primarily by inhibition of cyclin-dependent kinases. *Molecular and cellular biology*, 17(8), pp.4877–82. Available at: http://www.pubmedcentral.nih.gov/articlerender.fcgi?artid=232340&tool=pmcentrez&rendertype=abstract%0Ahttp://www.ncbi.nlm.nih.gov/pubmed/9234744%0Ahttp://www.pubmedcentral.nih.gov/articlerender.fcgi?artid=PMC232340.

Oh, S.-J. & Lee, C.J., 2017. Distribution and Function of the Bestrophin-1 (Best1) Channel in the Brain. *Experimental Neurobiology*, 26(3), p.113. Available at: http://www.ncbi.nlm.nih.gov/pubmed/28680296%0Ahttp://www.pubmedcentral.nih.gov/articlerender.fcgi?artid=PMC5491579%0Ahttps://synapse.koreamed.org/DOIx.php?id=10.5607/en.2017.26.3.113.

Ortega, S. et al., 2003. Cyclin-dependent kinase 2 is essential for meiosis but not for mitotic cell division in mice. *Nature Genetics*, 35(1), pp.25–31.

Osafune, K. et al., 2008. Marked differences in differentiation propensity among human embryonic stem cell lines. *Nature Biotechnology*, 26(3), pp.313–315.

Osakada, F. et al., 2009. In vitro differentiation of retinal cells from human pluripotent stem cells by small-molecule induction. *Journal of Cell Science*, 122(17), pp.3169–3179. Available at: http://jcs.biologists.org/cgi/doi/10.1242/jcs.050393.

Oshlack, A., Robinson, M.D. & Young, M.D., 2010. From RNA-seq reads to differential expression results. *Genome Biology*, 11(12), pp.1–10.

Ozturk, N. et al., 2009. Loss of cryptochrome reduces cancer risk in p53 mutant mice. *Proceedings of the National Academy of Sciences of the United States of America*, 106(8), pp.2841–2846.

Pacha, J. & Sumova, A., 2013. Circadian regulation of epithelial functions in the intestine. *Acta Physiologica*, 208(1), pp.11–24.

Palczewski, K. et al., 1989. The Catalytic Subunit of Phosphatase 2A Dephosphorylates Phosphoopsin1. *The American Chemical Society*, 28, pp.415–419.

Panda, S. et al., 2002. Coordinated transcription of key pathways in the mouse by the circadian clock. *Cell*, 109(3), pp.307–320.

Panda, S. et al., 2003. Melanopsin Is Required for Non – Image-Forming Photic Responses in Blind Mice. , 301(JULY), pp.525–528.

Parfitt, D.A. et al., 2016. Identification and Correction of Mechanisms Underlying Inherited Blindness in Human iPSC-Derived Optic Cups. *Cell Stem Cell*, 18(6), pp.769–781. Available at: http://dx.doi.org/10.1016/j.stem.2016.03.021.

Parker, L.L., Atherton-Fessler, S. & Piwnica-Worms, H., 1992. P107Wee1 Is a Dual-Specificity Kinase That Phosphorylates P34Cdc2 on Tyrosine 15. *Proceedings of the National Academy of Sciences*, 89(7), pp.2917–2921. Available at:

http://www.pnas.org/cgi/doi/10.1073/pnas.89.7.2917.

Parker, L.L. & Piwnica-Worms, H., 1992. Inactivation of the p34cdc2-Cyclin B Complex by the Human WEE1 Tyrosine Kinase. *Science*, 257(1989), pp.1955–1957.

Pendergast, J.S. et al., 2010. Disconnected circadian and cell cycles in a tumor-driven cell line. *Communicative & Integrative Biology*, 3(6), pp.536–539. Available at: http://www.tandfonline.com/doi/abs/10.4161/cib.3.6.12841.

Peng, S., Rahner, C. & Rizzolo, L.J., 2003. Apical and basal regulation of the permeability of the retinal pigment epithelium. *Investigative Ophthalmology and Visual Science*, 44(2), pp.808–817.

Petrukhin, K. et al., 1998. Identification of the gene responsible for Best macular dystrophy. *Nat Genet*, 19(3), pp.241–247. Available at: http://www.ncbi.nlm.nih.gov/entrez/query.fcgi?cmd=Retrieve&db=PubMed&dopt=Citation&list_uids=9662395%5Cnhttp://www.nature.com/ng/journal/v19/n3/pdf/ng0798_241.pdf.

Peyric, E., Moore, H.A. & Whitmore, D., 2013. Circadian Clock Regulation of the Cell Cycle in the Zebrafish Intestine. *PLoS ONE*, 8(8), pp.1–12.

Philp, N.J. & Nachmias, V.T., 1987. Polarized distribution of integrin and fibronectin in retinal pigment epithelium. *Investigative Ophthalmology and Visual Science*, 28(8), pp.1275–1280.

Pittendrigh, C.S., 1960. Circadian rhythms and the circadian organization of living systems. *Cold Spring Harbor symposia on quantitative biology*, 25, pp.159–184.

Pittendrigh, C.S. & Daan, S., 1976a. A functional analysis of circadian pacemakers in nocturnal rodents. IV. Entrainment: Pacemaker as Clock. *Journal of Comparative Physiology*, 106, pp.291–331.

Pittendrigh, C.S. & Daan, S., 1976b. A functional analysis of circadian pacemakers in nocturnal rodents. *Journal of comparative physiology A*, 106(3), pp.333–355. Available at: http://link.springer.com/article/10.1007/BF01417860%5Cnhttp://link.springer.com/content/pdf/10.1007/BF01417860.pdf%5Cnhttp://link.springer.com/10.1007/BF01417860.

Pittendrigh, C.S. & Daan, S., 1976c. A functional analysis of circadian pacemakers in nocturnal rodents V. Pacemaker Structure: A Clock for All Seasons. *Journal of comparative physiology A*, 106(3), pp.333–355. Available at: http://link.springer.com/article/10.1007/BF01417860%5Cnhttp://link.springer.com/content/pdf/10.1007/BF01417860.pdf%5Cnhttp://link.springer.com/10.1007/BF01417860.

Pittendrigh, C.S. & Minis, D.H., 1964. The Entrainment of Circadian Oscillations by Light and Their Role as Photoperiodic Clocks. *The American Naturalist*, 98(902), pp.261–294.

Pomares, E. et al., 2012. Nonsense-mediated decay as the molecular cause for autosomal recessive bestrophinopathy in two unrelated families. *Investigative Ophthalmology and Visual Science*, 53(1), pp.532–537.

Potapova, T.A. et al., 2009. Fine Tuning the Cell Cycle: Activation of the Cdk1 Inhibitory Phosphorylation Pathway during Mitotic Exit. *Molecular Biology of the Cell*, 20(March), pp.1737–1748.

Preitner, N. et al., 2002. The orphan nuclear receptor REV-ERBalpha controls circadian transcription within the positive limb of the mammalian circadian oscillator. *Cell*, 110(2), pp.251–260.

Del Priore, L. V., Kuo, Y.H. & Tezel, T.H., 2002. Age-related changes in human RPE cell density and apoptosis proportion in situ. *Investigative Ophthalmology and Visual Science*, 43(10), pp.3312–3318.

Pros, E. et al., 2010. Modulation of aberrant NF1 pre-mRNA splicing by kinetin treatment. *European Journal of Human Genetics*, 18(5), pp.614–617.

Qi, C. et al., 2009. A role for the clock gene Per1 in prostate cancer. *Cancer Research*, 69(19), pp.7619–7625.

Qiu, C. et al., 2016. Differential expression of TYRP1 in adult human retinal pigment epithelium and uveal melanoma cells. *Oncology Letters*, 11(4), pp.2379–2383.

Qu, Z., 2006. The Anion-Selective Pore of the Bestrophins, a Family of Chloride Channels Associated with Retinal Degeneration. *Journal of Neuroscience*, 26(20), pp.5411–5419. Available at: http://www.jneurosci.org/cgi/doi/10.1523/JNEUROSCI.5500-05.2006.

Qu, Z. et al., 2003. Two bestrophins cloned from Xenopus laevis oocytes express Ca(2+)-activated Cl(-) currents. *The Journal of biological chemistry*, 278(49), pp.49563–49572.

Qu, Z.Q. et al., 2007. Activation of Bestrophin Cl Channels Is Regulated by. *The Journal of biological chemistry*, 282(24), pp.17460–17467.

Ralph, M.R., Foster, R.G. & Davis, F.C., 1990. Transplanted Suprachiasmatic Nucleus Determines Circadian Period. *Science*, 247, pp.975–978.

Ralph, M.R. & Menaker, M., 1988. A Mutation of the Circadian System in Golden Hamsters. *Science*, 241, pp.1225–1227.

Ramsden, C.M. et al., 2017. Rescue of the MERTK phagocytic defect in a human iPSC disease model using translational readthrough inducing drugs. *Scientific Reports*, 7(1), pp.1–9. Available at: http://dx.doi.org/10.1038/s41598-017-00142-7.

Reddy, A.B. et al., 2006. Circadian Orchestration of the Hepatic Proteome. *Current Biology*, 16(11), pp.1107–1115.

Reebs, S.G., 1994. The anticipation of night by fry-retrieving cichlids. *Amin. Behav.*, 48, pp.89–95.

Reichhart, N. et al., 2010. Effect of bestrophin-1 on L-type Ca 2 þ channel activity depends on the Ca 2 þ channel beta-subunit. *Experimental Eye Research*, 91(5), pp.630–639. Available at: http://dx.doi.org/10.1016/j.exer.2010.08.001.

Reichhart, N. & Strauß, O., 2014. Ion channels and transporters of the retinal pigment epithelium. *Experimental Eye Research*, 126, pp.27–37.

Resnikoff, S. et al., 2004. Global data on visual impairment in the year 2002. *Bulletin of the World Health Organization*, 82(11), pp.844–51. Available at: http://www.pubmedcentral.nih.gov/articlerender.fcgi?artid=2623053&tool=pmcentrez&rendertype=abstract.

Rieke, F. & Baylor, D.A., 1998. Single photon detection by rod cells of the retina. *Rev. Mod. Phys*, 70(3), pp.1027–1036.

Rinchik, E.M. et al., 1993. A gene for the mouse pink-eyed dilution locus and for human type II oculocutaneous albinism. *Nature*, 361(6407), pp.72–6. Available at: http://dx.doi.org/10.1038/361072a0.

Rizzolo, L.J., 2007. Development and Role of Tight Junctions in the Retinal Pigment Epithelium. *International Review of Cytology*, 258(07), pp.195–234.

Robinson, M.D., McCarthy, D.J. & Smyth, G.K., 2009. edgeR: A Bioconductor package for differential expression analysis of digital gene expression data. *Bioinformatics*, 26(1), pp.139–140.

Robson, J.G. & Frishman, L.J., 2014. The rod-driven a-wave of the dark-adapted mammalian electroretinogram. *Progress in Retinal and Eye Research*, 39, pp.1–22. Available at: http://dx.doi.org/10.1016/j.preteyeres.2013.12.003.

Roccio, M. et al., 2013. Predicting stem cell fate changes by differential cell cycle progression patterns. *Development*, 140(2), pp.459–470. Available at: http://dev.biologists.org/cgi/doi/10.1242/dev.086215.

Rodriguez, G. et al., 2013. Forskolin-inducible cAMP pathway negatively regulates T-cell proliferation by uncoupling the interleukin-2 receptor complex. *Journal of Biological Chemistry*, 288(10), pp.7137–7146.

Rosenthal, R. et al., 2006. Expression of bestrophin-1, the product of the VMD2 gene, modulates voltage-dependent Ca2+ channels in retinal pigment epithelial cells. *FASEB*, 20(1), pp.178–80. Available at: http://www.ncbi.nlm.nih.gov/pubmed/16282372.

La Rovere, R.M.L. et al., 2016. Intracellular Ca2+signaling and Ca2+microdomains in the control of cell survival, apoptosis and autophagy. *Cell Calcium*, 60(2), pp.74–87. Available at: http://dx.doi.org/10.1016/j.ceca.2016.04.005.

Rymer, J. & Wildsoet, C.F., 2005. The role of the retinal pigment epithelium in eye growth regulation and myopia: A review. *Visual Neuroscience*, 22(3), pp.251–261.

Sakaue-Sawano, A. et al., 2008. Visualizing Spatiotemporal Dynamics of Multicellular Cell-Cycle Progression. *Cell*, 132(3), pp.487–498.

Sandler, O. et al., 2015. Lineage correlations of single cell division time as a probe of cell-cycle dynamics. *Nature*, 519(7544), pp.468–471. Available at: http://www.nature.com/doifinder/10.1038/nature14318.

Santamaría, D. et al., 2007. Cdk1 is sufficient to drive the mammalian cell cycle. *Nature*, 448(7155), pp.811–815.

Sato, T.K. et al., 2004. A functional genomics strategy reveals rora as a component of the mammalian circadian clock. *Neuron*, 43(4), pp.527–537.

Sato, T.K. et al., 2006. Feedback repression is required for mammalian circadian clock function. *Nature Genetics*, 38(3), pp.312–319.

Satyanarayana, A. & Kaldis, P., 2009. Mammalian cell-cycle regulation : several Cdks , numerous cyclins and diverse compensatory mechanisms. , 28(33), pp.2925–2939. Available at: http://dx.doi.org/10.1038/onc.2009.170.

Schernhammer, E.S. et al., 2003. Night-shift work and risk of colorectal cancer in the nurses' health study. *Journal of the National Cancer Institute*, 95(11), pp.825–828.

Schernhammer, E.S. et al., 2001. Rotating Night Shifts and Risk of Breast Cancer in Women Participating in the Nurses ' Health Study. *Jornal of the Nationa Cancer Institute*, 93(20), pp.1563–1568.

Seddon, J.M. et al., 2001. Assessment of mutations in the Best macular dystrophy (VMD2) gene in patients with adult-onset foveomacular vitelliform dystrophy, age-related maculopathy, and bull's-eye maculopathy. *Ophthalmology*, 108(11), pp.2060–2067.

Seddon, J.M. et al., 2003. Phenotype and Genotype Correlations in Two Best Families. , 6420(03), pp.1724–1731.

Serrano, M., Hannon, G.J. & Beach, D., 1993. A new regulatory motif in cell-cycle control causing specific inhibition of cyclin D/CDK4. *Nature*, 366(6456), pp.704–707. Available at: http://www.nature.com/doifinder/10.1038/366704a0.

Shi, S.Q. et al., 2013. Circadian disruption leads to insulin resistance and obesity. *Current Biology*, 23(5), pp.372–381. Available at: http://dx.doi.org/10.1016/j.cub.2013.01.048.

Shinohara, Y. et al., 2017. Temperature-Sensitive Substrate and Product Binding Underlie Temperature-Compensated Phosphorylation in the Clock. *Molecular Cell*, 67(5), p.783–798.e20.

Siepka, S.M. et al., 2007. Circadian mutant Overtime reveals F-box protein FBXL3 regulation of Cryptochrome and Period gene expression. *Cell*, 129(5), pp.1011–1023.

Simoni, A. et al., 2014. A Mechanosensory Pathway to the Drosophila Circadian Clock. *Science*, 343(January), pp.525–528.

Singh, A.M. et al., 2015. Utilizing FUCCI reporters to understand pluripotent stem cell biology. *Methods*, 2, pp.1–7. Available at: http://linkinghub.elsevier.com/retrieve/pii/S1046202315301031.

Singh, R. et al., 2013. iPS cell modeling of best disease: Insights into the pathophysiology of an inherited macular degeneration. *Human Molecular Genetics*, 22(3), pp.593–607.

Skeie, J.M. & Mahajan, V.B., 2014. Proteomic Landscape of the Human Choroid–Retinal Pigment Epithelial Complex. *JAMA Ophthalmology*, 52242(11), pp.1271–1281.

Soria, R.B. et al., 2009. Bestrophin-1 enables Ca2+-activated Cl- conductance in Epithelia. *Journal of Biological Chemistry*, 284(43), pp.29405–29412.

Stamer, W.D. et al., 2003. Aquaporin-1 Channels in Human Retinal Pigment Epithelium: Role in Transepithelial Water Movement. *Investigative Opthalmology & Visual Science*, 44(6), p.2803. Available at: http://iovs.arvojournals.org/article.aspx?doi=10.1167/iovs.03-0001.

Stanton, C.M. et al., 2017. Novel pathogenic mutations in C1QTNF5 support a dominant negative disease mechanism in late-onset retinal degeneration. *Scientific Reports*, 7(1), pp.1–15. Available at: http://dx.doi.org/10.1038/s41598-017-11898-3.

Stanton, J.B. et al., 2006. Hydrodynamic properties of porcine bestrophin-1 in Triton X-100. *Biochimica et Biophysica Acta - Biomembranes*, 1758(2), pp.241–247.

Stephan, F.K. & Zucker, I., 1972. Circadian rhythms in drinking behavior and locomotor activity of rats are eliminated by hypothalamic lesions. *Proceedings of the National Academy of Sciences of the United States of America*, 69(6), pp.1583–1586.

Stöhr, H. et al., 2002. Three novel human VMD2-like genes are members of the evolutionary highly conserved RFP-TM family. *European Journal of Human Genetics*, 10(4), pp.281–284.

Stokkan, K.-A. et al., 2001. Feeding Entrainment of the Circadian Clock in the Liver by Feeding. *Science*, 291(490–493), pp.2686–279. Available at: http://www.sciencemag.org/cgi/content/full/291/5503/490.

Stone, E.M. et al., 1992. Genetic linkage of vitelliform macular degeneration (Best's disease) to chromosome 11q13. *Nature genetics*, 1, pp.246–250.

Stone, E.M., Sheffield, V.C. & Hageman, G.S., 2001. Molecular genetics of age-related macular degeneration. *Human Molecular Genetics*, 10(20), pp.2285–2292.

Storch, K.-F. et al., 2002. Extensive and divergent circadian gene expression in liver and heart. *Nature*, 417(6884), pp.78–83.

Straley, S.C. & Bruce, V.G., 1979. Stickiness to Glass CIRCADIAN CHANGES IN THE CELL SURFACE OF CHLAMYDOMONAS REINHARDI. *Pkant Physiol.*, 63, pp.1175–1181.

Strauss, O. et al., 2000. Activation of neuroendocrine L-type channels (α1D subunits) in retinal pigment epithelial cells and brain neurons by pp60(c-src). *Biochemical and Biophysical Research Communications*, 270(3), pp.806–810.

Strauss, O., 2005. The Retinal Pigment Epithelium in Visual Function. *Physiological Reviews*, 85, pp.845–881.

Subrizi, A. et al., 2012. Generation of hESC-derived retinal pigment epithelium on biopolymer coated polyimide membranes. *Biomaterials*, 33(32), pp.8047–8054. Available at: http://dx.doi.org/10.1016/j.biomaterials.2012.07.033.

Sugiyama, M. et al., 2009. Illuminating cell-cycle progression in the developing zebrafish embryo. *Proceedings of the National Academy of Sciences of the United States of America*, 106(49), pp.20812–20817.

Sujino, M. et al., 2003. Suprachiasmatic Nucleus Grafts Restore Circadian Behavioral Rhythms of Genetically Arrhythmic Mice. *Current biology : CB*, 13(7), pp.568–74. Available at: http://www.ncbi.nlm.nih.gov/pubmed/12676087.

Sun, C., Huang, S. & Zeng, J., 2010. Per2 Inhibits K562 Leukemia Cell Growth In Vitro and In Vivo Through Cell Cycle Arrest and Apoptosis Induction. *Pathol. Oncol. Res.*, 16, pp.403–411.

Sun, H. et al., 2002. The vitelliform macular dystrophy protein defines a new family of chloride channels. *Proceedings of the National Academy of Sciences of the United States of America*, 99(6), pp.4008–13. Available at: http://www.pnas.org/content/99/6/4008.abstract%5Cnhttp://www.ncbi.nlm.nih.gov/pubmed/11904445%5Cnhttp://www.pubmedcentral.nih.gov/articlerender.fcgi?artid=PMC122639%5Cnhttp://www.pnas.org/cgi/doi/10.1073/pnas.052692999.

Sweeney, B.M. & Hastings, J.W., 1958. Rhythmic Cell Division in Populations of Gonyaulax polyedra. *J. Protozool.*, 5(3), pp.217–224.

Takahashi, K. & Yamanaka, S., 2006. Induction of Pluripotent Stem Cells from Mouse Embryonic and Adult Fibroblast Cultures by Defined Factors. *Cell*, 126(4), pp.663–676.

Takata, K., 1996. Glucose transporters in the transepithelial transport of glucose. *Journal of Electron Microscopy*, 45(4), pp.275–284.

Takeda, K. et al., 2003. OTX2 regulates expression of DOPAchrome tautomerase in human retinal pigment epithelium. *Biochemical and Biophysical Research Communications*, 300(4), pp.908–914.

Tamai, T.K. et al., 2012. Light Acts on the Zebrafish Circadian Clock to Suppress Rhythmic Mitosis and Cell Proliferation. *Journal of Biological Rhythms*, 27(3), pp.226–236.

Tamai, T.K., Young, L.C. & Whitmore, D., 2007. Light signaling to the zebrafish circadian clock by Cryptochrome 1a. *Proceedings of the National Academy of Sciences of the United States of America*, 104(37), pp.14712–14717. Available at: http://www.pnas.org/cgi/doi/10.1073/pnas.0704588104.

Tavsanli, B.C. et al., 2001. dbest1 , a Drosophila Homolog of Human Bestrophin , Is Not Required for Viability or Photoreceptor Integrity. , 136, pp.130–136.

Taylor, S.R. et al., 2010. Velocity response curves support the role of continuous entrainment in circadian clocks. *Journal of biological rhythms*, 25(2), pp.138–149.

Thomson, J.A. et al., 1998. Embryonic Stem Cell Lines Derived from Human Blastocysts. *Science*,

282(5391), pp.1145–1148.

Todo, T., 1999. Functional diversity of the DNA photolyaserblue light receptor family. *Mutation Research*, 434(2), pp.89–97.

Todo, T. et al., 1996. Similarity Among the Drosophila (6-4)Photolyase, a Human Photolyase Homolog, and the DNA Photolyase-Blue-Light Photoreceptor Family. *Science*, 272(5258), pp.109–112. Available at: http://www.sciencemag.org/cgi/doi/10.1126/science.272.5258.109.

Toyoshima, H. & Hunter, T., 1994. p27, a novel inhibitor of G1 cyclin-Cdk protein kinase activity, is related to p21. *Cell*, 78(1), pp.67–74.

Traboulsi, E.I. & Payne, J.W., 1993. Autosomal dominant vitreoretinochoroidopathy: Report of the third family. *Archives of Ophthalmology*, 111(2), pp.194–196. Available at: http://dx.doi.org/10.1001/archopht.1993.01090020048021.

Tsin, A., Betts-Obregon, B. & Grigsby, J.G., 2018. Visual cycle proteins: structure, function, and roles in human retinal disease. *Journal of Biological Chemistry*, 65, p.jbc.AW118.003228. Available at: http://www.jbc.org/lookup/doi/10.1074/jbc.AW118.003228.

Tsuchiya, Y., Akashi, M. & Nishida, E., 2003. Temperature compensation and temperature resetting of circadian rhythms in mammalian cultured fibroblasts. *Genes to Cells*, 8(8), pp.713–720.

Tsunenari, T. et al., 2003. Structure-Function Analysis of the Bestrophin Family of Anion Channels. *Journal of Biological Chemistry*, 278(42), pp.41114–41125.

Tsunenari, T., Nathans, J. & Yau, K.-W., 2006. Ca2+-activated Cl− Current from Human Bestrophin-4 in Excised Membrane Patches. *Journal of General Physiology*, 127(4), pp.191–204. Available at: http://www.jgp.org/cgi/doi/10.1085/jgp.200609490.

Turek, F.W. et al., 2013. Obesity and Metabolic Syndrome in Circadian Clock Mutant Mice. , 1043(2005), pp.1043–1045.

Uggenti, C. et al., 2016. Restoration of mutant bestrophin-1 expression, localisation and function. *Disease models & mechanisms*, (August). Available at: http://www.ncbi.nlm.nih.gov/pubmed/27519691.

Vallone, D. et al., 2004. E-box function in a period gene repressed by light. *Proceedings of the National Academy of Sciences of the United States of America*, 101(12), pp.4106–4111.

Vatine, G. et al., 2009. Light directs zebrafish period2 expression via conserved D and E boxes. *PLoS Biology*, 7(10).

Vitaterna, M. et al., 1994. Mutagenesis and mapping of a mouse gene, Clock, essential for circadian behavior. *Science*, 264(5159), pp.719–725. Available at: http://www.sciencemag.org/cgi/doi/10.1126/science.8171325.

Vitaterna, M.H. et al., 1999. Differential regulation of mammalian Period genes and circadian rhythmicity by cryptochromes 1 and 2. *Proceedings of the National Academy of Sciences*, 96(21), pp.12114–12119. Available at: http://www.pnas.org/cgi/doi/10.1073/pnas.96.21.12114.

Vugler, A. et al., 2008. Elucidating the phenomenon of HESC-derived RPE: Anatomy of cell genesis, expansion and retinal transplantation. *Experimental Neurology*, 214(2), pp.347–361. Available at: http://dx.doi.org/10.1016/j.expneurol.2008.09.007.

Wald, B.Y.G., 1935. CAROTENOIDS AND THE VISUAL CYCLE. *The Journal of General Physiology*.

Weber, B.H.F., Walker, D. & Muller, B., 1994. Molecular evidence for non-penetrance in Best ' s disease. *J Med Genet*, 31, pp.388–392.

Weinberg, R.A., 1995. The retinoblastoma protein and cell cycle control. *Cell*, 81(3), pp.323–330.

Wells, J. et al., 1993. Mutations in the human retinal degeneration slow (RDS) gene can cause either retinitis pigmentosa or macular dystrophy. *Nat Genet*, 3(3), pp.213–218. Available at: http://www.ncbi.nlm.nih.gov/entrez/query.fcgi?cmd=Retrieve&db=PubMed&dopt=Citation&list_uids=8485576%5Cnhttp://www.nature.com/ng/journal/v3/n3/pdf/ng0393-213.pdf.

Welsh, D.K. et al., 2004. Bioluminescence imaging of individual fibroblasts reveals persistent, independently phased circadian rhythms of clock gene expression. *Current biology : CB*, 14(24), pp.2289–95. Available at: http://www.sciencedirect.com/science/article/pii/S0960982204009157.

Whitehead, K. et al., 2009. Diurnally entrained anticipatory behavior in archaea. *PloS one*, 4(5), p.e5485. Available at: http://www.pubmedcentral.nih.gov/articlerender.fcgi?artid=2675056&tool=pmcentrez&rendertype=abstract.

Whitmore, D. et al., 1998. Zebrafish Clock rhythmic expression reveals independent peripheral circadian oscillators. , (C).

Whitmore, D., Foulkes, N.S. & Sassone-Corsi, P., 2000. Light acts directly on organs and cells in culture to set the vertebrate circadian clock. *Nature*, 404(6773), pp.87–91.

Wooten, B.R. & Hammond, B.R., 2002. Macular pigment: Influences on visual acuity and visibility. *Progress in Retinal and Eye Research*, 21(2), pp.225–240.

Wright, K.P., Lowry, C.A. & LeBourgeois, M.K., 2012. Circadian and wakefulness-sleep modulation of cognition in humans. *Frontiers in Molecular Neuroscience*, 5(April), pp.1–12. Available at: http://journal.frontiersin.org/article/10.3389/fnmol.2012.00050/abstract.

Wu, M. et al., 2012. Experimental chronic jet lag promotes growth and lung metastasis of Lewis lung carcinoma in C57BL / 6 mice. *Oncology Reports*, 27, pp.1417–1428.

Xiao, Q. et al., 2008. Regulation of Bestrophin Cl Channels by Calcium : Role of the C Terminus. , pp.681–692.

Xiong, Y. et al., 1993. P21 Is a Universal Inhibitor of Cyclin Kinases. *Nature*, 366(6456), pp.701–704. Available at: http://www.nature.com/doifinder/10.1038/366701a0.

Yang, Q. et al., 2010. Circadian gating of the cell cycle revealed in single cyanobacterial cells. *Science*, 327(5972), pp.1522–1526.

Yang, T. et al., 2014. Structure and selectivity in bestrophin ion channels. *Science*, 346(6207), pp.355–359. Available at: http://www.sciencemag.org/content/346/6207/355%5Cnhttp://www.ncbi.nlm.nih.gov/pubmed/25324390%5Cnhttp://www.sciencemag.org/content/346/6207/355.full.pdf%5Cnhttp://www.sciencemag.org/content/346/6207/355.long.

Yardley, J. et al., 2004. Mutations of VMD2 splicing regulators cause nanophthalmos and autosomal dominant vitreoretinochoroidopathy (ADVIRC). *Investigative Ophthalmology and Visual Science*, 45(10), pp.3683–3689.

Yeh, K. et al., 2005. Abnormal expression of Period 1 (PER1) in endometrial carcinoma. , 1, pp.111–120.

Yeom, M. et al., 2010. Circadian-independent cell mitosis in immortalized fibroblasts. *Proceedings of the National Academy of Sciences*, 107(21), pp.9665–9670. Available at: http://www.pnas.org/cgi/doi/10.1073/pnas.0914078107.

Yoo, S.-H. et al., 2004. PERIOD2::LUCIFERASE real-time reporting of circadian dynamics reveals persistent circadian oscillations in mouse peripheral tissues. *Proceedings of the National Academy of Sciences of the United States of America*, 101(15), pp.5339–46. Available at: http://www.pnas.org/content/101/15/5339.full [Accessed May 13, 2015].

Young, R.W., 1967. The renewal of photoreceptor cell outer segments. *J cell Biol.*, 33(1), pp.61–72.

Young, R.W. & Bok, D., 1969. Participation of the retinal pigment epithelium in the rod outer segment renewal process. *The Journal of cell biology*, 42(2), pp.392–403.

Yu, K., Cui, Y. & Hartzell, H.C., 2006. The bestrophin mutation A243V, linked to adult-onset vitelliform macular dystrophy, impairs its chloride channel function. *Investigative Ophthalmology and Visual Science*, 47(11), pp.4956–4961.

Yvon, C. et al., 2015. Using Stem Cells to Model Diseases of the Outer Retina. *Computational and Structural Biotechnology Journal*, 13, pp.382–389. Available at: http://linkinghub.elsevier.com/retrieve/pii/S2001037015000276.

Zadlo, A. et al., 2007. Photobleaching of retinal pigment epithelium melanosomes reduces their ability to inhibit iron-induced peroxidation of lipids. *Pigment Cell Research*, 20(1), pp.52–60.

Zhang, R. et al., 2014. A circadian gene expression atlas in mammals: Implications for biology and medicine. *Proceedings of the National Academy of Sciences*, 111(45), pp.16219–16224. Available at: http://www.pnas.org/lookup/doi/10.1073/pnas.1408886111.

Zhao, L. et al., 2012. A novel compound heterozygous mutation in the BEST1 gene causes autosomal recessive Best vitelliform macular dystrophy. *Eye*, 26, pp.866–871.

Zhao, P.Y. et al., 2015. TRP Channels Localize to Subdomains of the Apical Plasma Membrane in Human Fetal Retinal Pigment Epithelium. *Investigative Opthalmology & Visual Science*, 56(3), p.1916. Available at: http://iovs.arvojournals.org/article.aspx?doi=10.1167/iovs.14-15738.

Zheng, B. et al., 2001. Nonredundant roles of the mPer1 and mPer2 genes in the mammalian circadian clock. *Cell*, 105(5), pp.683–694.

Zhu, M. et al., 2010. Unexpected Transcriptional Activity of the Human VMD2 Promoter in Retinal Development. In R. E. Anderson, J. G. Hollyfield, & M. M. LaVail, eds. *Retinal Degenerative Diseases: Laboratory and Therapeutic Investigations*. New York, NY: Springer New York, pp. 211–216. Available at: https://doi.org/10.1007/978-1-4419-1399-9_24.

Zielinski, T. et al., 2014. Strengths and limitations of period estimation methods for circadian data. *PLoS ONE*, 9(5).

Zimmerman, W., Pittendrigh, C. & Pavlidis, T., 1968. Temperature Compensation of the Circadian Oscillation in Drosophila Psuedoobscura and its Entrainment by Temperature Cycles. *J. Insect Physiol.*, 14, pp.669–684. Available at: http://www.ncbi.nlm.nih.gov/pubmed/12676087.